Zbornik 4. Študentske konference Mednarodne podiplomske šole Jožefa Stefana

Proceedings of 4th Jožef Stefan International Postgraduate School Students Conference

# ZBORNIK
Proceedings of
# IPSSC

## 1. DEL
## Part I

**25. maj 2012, Ljubljana, Slovenija**

Zbornik 4. Študentske konference Mednarodne podiplomske šole Jožefa Stefana
(Proceedings of the 4th Jožef Stefan International Postgraduate School Students Conference)

Uredniki:
Dejan Patelin
Aleš Tavčar
Boštjan Kaluža

Založnik:
Mednarodna podiplomska šola Jožefa Stefana, Ljubljana

Tisk:
Franc Jagodic, s.p. - Jagraf

Naklada:
150 izvodov

Ljubljana, maj 2012

IPSSC organizira študentski svet Mednarodne podiplomske šole Jožefa Štefana
(IPSSC is organized by Jožef Stefan International Postgraduate School - IPS student council)

CIP - Katložni zapis o publikaciji
Narodna in univerzitetna knjižnica, Ljubljana

5/6(082)
378.046-021.68:001.891(497.4)(082)

MEDNARODNA podiplomska šola Jožefa Stefana. Študentska konferenca (4 ; 2012 ; Ljubljana)
Zbornik prispevkov = Proceedings / 4. študentska konferenca
Mednarodne podiplomske šole Jožefa Stefana = 4th Jožef Stefan
International Postgraduate School Students Conference, 25. maj
2012, Ljubljana, Slovenija ; [organizira študentski svet Mednarodne
podiplomske šole Jožefa Štefana = organized by Jožef Stefan
International Postgraduate School - IPS Student Council] ; uredili,
edited by Dejan Petelin, Aleš Tavčar, Boštjan Kaluža. - Ljubljana : Mednarodna
podiplomska šola Jožefa Stefana, 2012

ISBN 978-961-92871-4-9
1. Petelin, Dejan 2. Mednarodna podiplomska šola Jožefa Stefana (Ljubljana)

261775360

# 4. ŠTUDENTSKA KONFERENCA MEDNARODNE PODIPLOMSKE ŠOLE JOŽEFA STEFANA

## 4TH JOŽEF STEFAN INTERNATIONAL POSTGRADUATE SCHOOL STUDENTS CONFERENCE

## Zbornik - 1. del

## Proceedings - part 1

Uredili / Edited by

Dejan Petelin, Aleš Tavčar in Boštjan Kaluža

25. maj 2012, Ljubljana, Slovenija

## Organizacijski odbor / Organising Committee

## Redakcijski odbor / Technical Review Committee

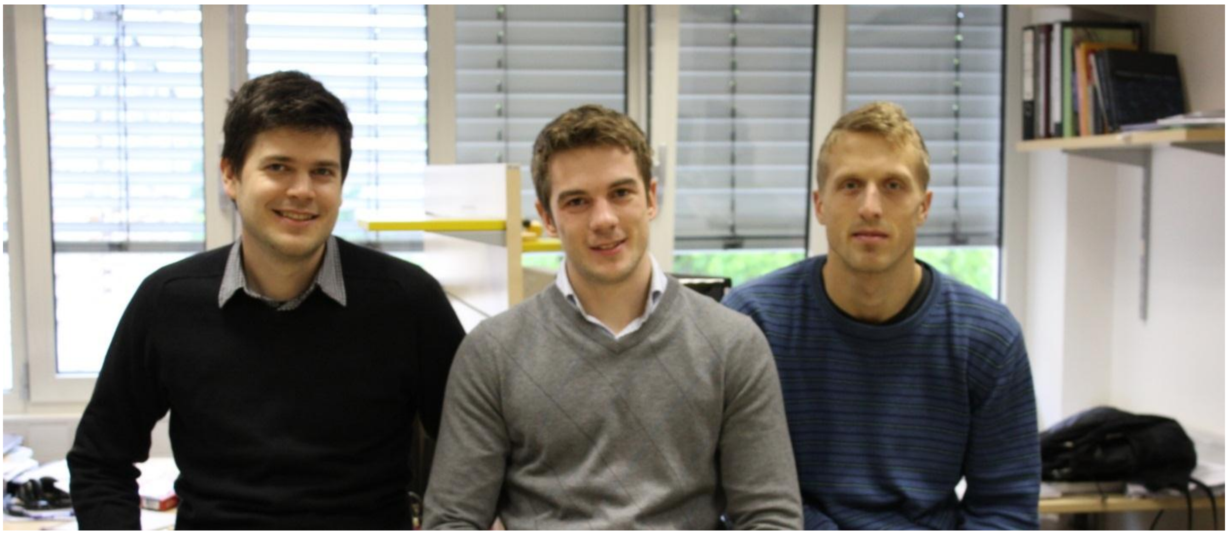

# Z inovativnimi raziskavami do tesnejšega sodelovanja z gospodarstvom

Z lanskoletnim odličnim odzivom številnih uspešnih visokotehnoloških podjetij smo dobili potrditev, da študentska konferenca napreduje in je vedno bolj zanimiva tako za podjetja kot za študente. Tako smo se z velikim veseljem in zagonom ter v želji po novih presežkih lotili organizacije že 4. študentske konference Mednarodne podiplomske šole Jožefa Stefana, namenjene predstaviti naših raziskav širšemu občinstvu in podjetjem ter s tem krepitvi povezav z gospodarstvom.

Ob začetku študijskega leta smo izdali knjižico s splošnim opisom študentske konference, njenim namenom, dosedanjimi nagrajenci ter navodili za pripravo prispevkov za sodelovanje na konferenci. Organizirali smo tudi sestanek z mentorji, na katerem smo jim podrobno predstavili študentsko konferenco in poslanstvo le-te. Vse te zgodnje priprave so se obrestovale, saj smo letos prejeli rekordnih 53 prispevkov. S tem smo dobili tudi potrditev študentov, da se zavedajo pomembnosti konference in si želijo sodelovanja s podjetji.

Pri tako številnih prispevkih smo želeli zagotoviti visoko kvaliteto le teh, zato smo v letošnjem letu uvedli redakcijski odbor v sestavi sedmih članov. Vsak prispevek sta temeljito pregledala dva člana odbora. Recenzenti so se poleg kakovosti prispevkov osredotočali tudi na pravilnost in razumljivost besedila, še posebej splošnega povzetka, ki je namenjen širšemu občinstvu, saj je le ta bistvenega pomena za razumevanje naših raziskav s strani podjetij in s tem posledično vzpostavljanje stikov.

Za dodaten pretok informacij in vzpostavljanje stikov med študenti in podjetji smo letos pripravili tudi okroglo mizo, na kateri sodelujejo tako predstavniki podjetij kot predstavniki študentov. Pri tem si želimo, da bi se srečanje razvilo v aktivno razpravo, ki bo zbližala poglede na povezovanje gospodarstva z raziskovalci tako predstavnikom podjetij kot raziskovalcem in tako pripomogla k tesnejšemu in uspešnejšemu sodelovanju.

Vsem študentom in njihovim mentorjem se zahvaljujemo za sodelovanje in s tem izkazano zaupanje ter zavedanje pomembnosti sodelovanja z gospodarstvom. Zahvala gre tudi vsem podjetjem, ki so kljub ne prav prijaznim časom za gospodarstvo pokazala veliko mero razumevanja in želje po sodelovanju. Iskreno se jim zahvaljujemo tako za finančno podporo, brez katere konference zagotovo ne bi uspeli organizirati, kot za pripravljenost na sodelovanje. Predvsem pa se zahvaljujemo celotnemu osebju na Mednarodni podiplomski šoli Jožefa Stefana za vso pomoč in podporo. Še posebej gre velika zahvala dekanji prof. dr. Aleksandri Kornhauser Frazer, ki ogromno prispeva tako k sami konferenci kot stalnemu napredku le te, ter mag. Sergeji Vogrinčič, ki nam je pomagala prav pri vseh nalogah in težavah. Prav tako se iskreno zahvaljujemo vsem članom redakcijskega odbora, ki so temeljito pregledali vse prispevke in tako bistveno prispevali k še višji kvaliteti konference.

Uredniški odbor

## Beseda dekana MPŠ

V uvodu k prvi Študentski konferenci MPŠ je bila poudarjena želja, da bi te letne prireditve postale tradicija šole. Zdaj – ob zaporedni četrti, doslej daleč največji – čutimo, da se ta žlahtna tradicija uresničuje.

In taka tradicija je velika dragocenost, še posebej v svetu, ki ga pretresajo krize. Hude krize so kot viharji – odnesejo vse, kar ni trdno ukoreninjeno. Tradicija, ki razvija korenine, v takih dneh ni le obet za boljše pogoje, velikokrat je kar pogoj preživetja.

Mladi raziskovalci sprejemajo te konference kot svoj mladostno zagnani, a tudi že samokritično izpostavljeni korak. Svoje začetne raziskovalne pobude, večkrat komaj več kot sanje, v raziskovanju soočajo z eksperimentalnim preverjanjem in zahtevo o ponovljivosti rezultatov. Predstavitev terja globlje razumevanje vpetosti rezultatov v poznavanje sistemov in procesov. Zanesljivo se želi prepoznati njihov prispevek k znanstvenim ugotovitvam, naj bo to trditvam ali dvomom.

V času, ko je gospodarsko preživetje razvitega sveta, še posebej Evrope, odvisno predvsem od visokih tehnologij, se polagajo veliki upi na znanost. Ni več časa za zaporedno postopnost v prenosu novega znanja v trajnostno razvijano proizvodnjo, Novi temeljni znanstveni dosežki se morajo sproti prenašati v razvojne procese. Gospodarske organizacije, zlasti partnerji MPŠ, sodelujejo v pripravah in izvedbi teh konferenc in tako omogočajo, da se svetova znanosti in gospodarstva vsaj na majhnih področjih zlivata v celoto.

To nalaga mladim raziskovalcem in še posebej njihovim mentorjem tudi zahtevno skrb za iskanje možnosti neposredne ali posredne uporabe raziskovalnih dosežkov za razvoj proizvodnje in varovanje okolja. Znanstveno razmišljati pomeni danes celostno: od porajanja originalnih zamisli in njihovega preverjanja in dopolnjevanja ter poglabljanja znanja, preko oblikovanja novega znanja za prenos v uporabo, do izumov in prek njih do inovacij. Te naj zvišujejo dodano vrednost, da bi lahko dvignili kakovost življenja, ki bo omogočila tudi, da bi lahko še več in bolje raziskovali.

Da bi to dosegli, moramo spremeniti večkrat okostenelo miselnost, da je znanost varna samo, če je povsem ločena od prakse. Naučiti se moramo tudi takega izražanja, ki bo hkrati znanstveno dognano in širše razumljivo. Tak jezik ni le pogoj za najširše možno razumevanje, je tudi bistveni del sodobne znanstvene kulture.

Čas je, da podiplomcem, ki predstavljajo svoje originalne zamisli ob vključevanju vseh teh vidikov, ter njihovim mentorjem, ki jih spodbujajo in usmerjajo na tej strmi poti na goro, ki se imenuje znanost, vsi čestitamo! Dolgujemo jim tudi zahvalo, da na študentskih konferencah Mednarodne podiplomske šole Jožefa Stefana delijo z nami svoje mladostne načrte, svoja iskanja, svoje dosežke in dvome ter zlasti svoja upanja, da bodo kot raziskovalci prispevali k višji kakovosti življenja.

Prof. dr. Aleksandra Kornhauser Frazer
Dekan MPŠ

# Beseda predsednika MPŠ

Priča smo svetovni gospodarski recesiji, ki sovpada z ekonomsko krizo in krizo družbenih vrednot, klimatskimi spremembami, problemi zdravja in zdrave prehrane, pomanjkanja vode, ohranitve biodiverzitete in še kaj bi lahko dodali. Tej krizi so se v dobri meri izognile države, ki so pravočasno zaznale te globalne probleme ter pričele vlagati velika sredstva v znanost in raziskave, kot so npr. Nemčija, Skandinavske države, Avstralija, Kitajska, Brazilija, Južna Afrika in še nekatere druge. Vse to delajo z namenom, da bi zgradili kompetitivno, dinamično ter na znanju temelječo ekonomijo. Osnova temu so odličnost v znanju, mednarodno povezovanje, hrabrost pri odločanju ter svoboda. Vse naštete ekonomije so in še vedno zvišujejo finančna vlaganja v znanost, ki je temelj inovacijam. V tej smeri deluje tudi vzpostavljeni Evropski raziskovalni prostor – ERA, ki naj bi omogočal boljšo integracijo nacionalnih raziskav v širšem evropskem prostoru ter s tem večjo konkurenčnost evropskega gospodarstva. Vsako zaostajanje pomeni ekonomsko nestabilnost in izgubo samostojnosti.

Slovenija se je znašla v gospodarski recesiji. Za vrsto reševanja nakopičenih problemov rabimo med drugim višja vlaganja v izobraževanje kvalitetnih kadrov. Še posebej morajo biti napori usmerjeni v promocijo visokošolskega izobraževanja ter raziskovalno dejavnost, kar omogoča in pospešuje zdravo tekmovalnost. Le to daje odlične zaposlitvene možnosti, za kar je odgovornost deljena: politika, gospodarstvo, univerze in raziskovalni instituti. To so izzivi za nove generacije, ki so upravičene do boljše prihodnosti, kot jim jo ponuja sedanjost. Dolžni smo prihajajočim generacijam omogočati, da se uspešno spopadejo z izzivi v domačem okolju, ne pa da iščejo izpolnitve svojih ambicij in eksistenčnih možnosti z "begom možganov" v tujino.

S temi razmišljanji je Institut "Jožef Stefan" (IJS), najbolj elitna slovenska raziskovalna organizacija na področju naravoslovnih in tehničnih ved, sprejel odločitev o ustanovitvi Mednarodne podiplomske šole Jožefa Stefana (MPŠ). Po večletnih prizadevanjih in s podporo uspešnih slovenskih gospodarskih podjetij je leta 2004 ustanovil samostojni visokošolski zavod. Študijske usmeritve zajemajo nova področja, kot so nanotehnologije in nanoznanosti, informacijske in komunikacijske tehnologije, ekotehnologije ter s tem povezan menedžment. Upravičenost ustanovitve te podiplomske šole potrjuje dejstvo, da narašča zanimanje za študij. Tako je bilo v šolskem letu 2011/2012 vpisanih 200 podiplomcev. Od ustanovitve šole pa do danes je bilo podeljenih preko 90 doktoratov in 40 magisterijev.

IJS in MPŠ v tesni sodelavi izkoriščata odlično raziskovalno opremo vključno s Centri odličnosti. Vrhunski kadrovski potenciali ter mednarodne povezave vključno s projekti 7. OP EU omogočajo usposabljanje na najvišji ravni ter prenašanje odličnega sodobnega znanja, pridobljenega na temeljnih raziskavah, tudi v gospodarstvo. To je misija naše Mednarodne podiplomske šole ter prispevek k pospešenemu zagonu slovenskega gospodarstva ter hitrejšemu prehodu v družbo znanja.

Znanje je vrednota, ki omogoča narodu ekonomski razvoj in obstoj. Mladi vrhunski raziskovalci, ki so pogoj za uspešen gospodarski razvoj, pa so srce družbe znanja.

Prof. dr. Vito Turk
Predsednik MPŠ

# Beseda predstavnice gospodarstva

Slovenska izvozno naravnana industrija se na globalnih trgih srečuje s svetovno konkurenco. Za uvrščanje med vodilne ponudnike na ozkih programskih področjih potrebuje vrhunske rešitve. Le-te pa lahko ustvarjajo samo razvojni timi v sodelovanju z vztrajnimi, radovednimi raziskovalci z ambicijo, da se njihova dognanja iz znanstvenih člankov prelijejo v iskane konkurenčne rešitve. Inovativnost, kreativnost, znanje, pogum in vztrajnost v tekmi s konkurenco na svetovnih trgih so dejavniki, ki omogočajo preboj v sam svetovni vrh. S prilagoditvijo vsebin podiplomskega izobraževanja tudi raziskovalnim ciljem industrije, vključevanjem podiplomskih študentov v mednarodne raziskovalne kroge in vrhunskim raziskovalnim okoljem na IJS, se znanje pretvarja v izdelke z visoko dodano vrednostjo. Znanje omogoča trajnostni razvoj podjetij ter posledično tudi nadaljnje raziskave. Raziskovalci MPŠ s svojimi rezultati potrjujejo pravilnost vizionarske odločitve o ustanovitvi mednarodne podiplomske šole.

dr. Jožica Rejec
Predsednica uprave Domel d.d.

Kazalo (Table of Contents)

# Ekotehnologija (Ecotechnology) 1

## Nanoznanosti in nanotehnologije (Nanosciences and Nanotechnologies) 195

# Ekotehnologija (Ecotechnology)

# The role of human activities on number concentration and size distribution of particles in indoor air

**Mateja Bezek**[1,2], **Janja Vaupotič**[1]

[1] Department of Environmental Sciences, Jožef Stefan Institute, Ljubljana, Slovenia
[2] Jožef Stefan International Postgraduate School, Ljubljana, Slovenia
mateja.bezek@ijs.si

**Abstract.** Particle number concentrations and size distributions have been monitored in the kitchen during candle burning and smoking a cigarette with a Scanning Mobility Particle Sizer. Burning a candle produces particles in size range of 6–15 nm, whereas during smoking a cigarette, larger particles are formed in size range of 40–150 nm. Total concentration of particles increased up to 1,341,000 and 423,000 $cm^{-3}$ during burning a candle and smoking a cigarette, respectively.

**Keywords**: indoor air, nanoparticles, particle size distribution, total particle concentration

## 1 Introduction

Particles are emitted in the atmosphere by a number of various human activities [1, 2]. Important indoor particle sources in homes include cooking exhaust [3], cigarette smoke [4], candles and other sorts of flames [2, 5] and solvents. At workplaces many processes form particles, such as smelting, welding, soldering, laser ablation, grinding and others[6]. Furthermore, huge amount of particles is released to the atmosphere by biomass burning and traffic emissions [7]. Engineered nanoparticles are produced intentionally to be used in electronics, medicines, pharmaceuticals, cosmetics, paints and a variety of other consumers' products [8, 9].

Ultrafine particles (UFPs) or nanoparticles, defined as particles with aerodynamic diameter <100 nm [10], are widely believed to be responsible for the adverse health effects. During breathing of air, certain fraction of particles is deposited on the walls of the respiratory tract. Strongly depending on the particle size, significant amounts of particles are deposited in nasopharyngeal, traheobronhial and alveolar region of respiratory tract [11]. Smaller particles are chemically and biochemically more reactive and potentially more toxic than larger ones, due to large surface area. With dropping particle size, the probability of deposition in respiratory system is increasing [11, 12]. It has been recognised that nanoparticles cause oxidation stress, pulmonary inflammation and cardiovascular events [11, 13]. Factors that influence nanoparticle toxicity include size, number, surface characteristics, shape, chemical composition, surface treatment and potential for agglomeration [14, 15].

In this paper characterization of particles formed during burning a candle and smoking a cigarette is given. We have focused on fraction below 100 nm, comparing fractions of particles below 20 and 10 nm, which are potentially more toxic due to deeper penetration in respiratory tract.

## 2 Experimental

Indoor measurements were performed in the kitchen of the basement flat in the suburb of Ljubljana during two experiments, burning a candle and smoking a cigarette. Particle number concentrations and size distributions during these experiments were measured with a Scanning Mobility Particle Sizer + Counter (SMPS+C, Series 5.400, Grimm, Germany). Differential Mobility Analyzer (DMA) unit separates charged particles into 44 channels based on their electrical mobility ($d$), which depends on the particle size and electrical charge. Afterwards, in the Condensation Particle Counter (CPC) they are enhanced and counted.

The frequency of measurement with medium DMA unit is one in four minutes for size range 5–350 nm. The instrument gives the total number concentration of particles $C$(tot), the geometric mean of their diameters $d_{\mathrm{GM}}$, and the number size distribution. In addition, fractions of particles below 10, 20 and 100 nm ($x$(<10), $x$(<20) and $x$(<100)) were calculated.

## 3 Results and Discussion

Particle size distributions during burning a candle and smoking a cigarette are presented in Figure 1. During burning a candle (Figure 1a) high particle concentration in a narrow size range of 6–15 nm was observed, whereas during smoking a cigarette (Figure 1b) much larger particles in size range of 40–200 nm were formed.

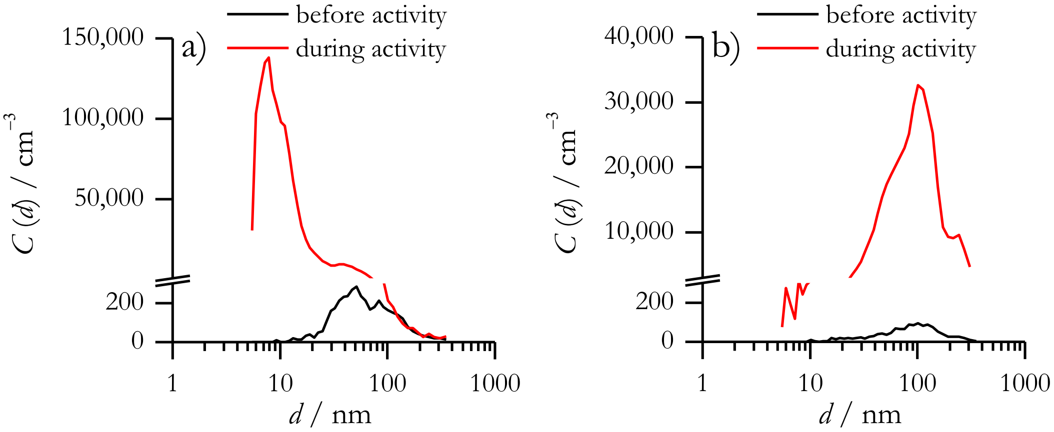

**Figure 1**: Particle size distribution during a) burning a candle and b) smoking a cigarette

During burning a candle particle concentration extremely increased, up to 1,341,000 cm$^{-3}$, with $d_{GM}$ of 10 nm. Candle smoke produces in average $5.52 \times 10^{11}$ particles min$^{-1}$ [1]. As seen in Figure 2a, more than 90 % of the particles were smaller than 20 nm during burning. Afterwards $C$(tot) rapidly decreased and $d_{GM}$ increased due to agglomeration of particles. During burning the candle $x$(<100) was practically 1.0. Later, six hours after the experiment, the levels of $C$ (tot) and $x$(<10) dropped, whereas $x$(<100) was still above 0.9 which is comparable to values of 0.6 and 0.9 for $x$(<10) and $x$(<20), respectively, obtained in previous experiments [16].

During smoking a cigarette total particle concentration increased up to 423,000 cm$^{-3}$ with $d_{GM}$ of 83 nm (Figure 2b). Although the duration of smoking was only five minutes, newly formed particles have been present in the air for more than six hours after the event. $C$(tot) rapidly decreased and $d_{GM}$ increased due to agglomeration, what is evident also from the increase of $d_{GM}$. There was no increase of $x$(<10) and $x$(<20) (Figure 2b), because larger particles in the size range 40–150 nm were formed. Emission rate of smoking is reported to be $1.91 \times 10^{11}$ particles min$^{-1}$ [1], and about 2–4 times lower emission rates are also evident at total particle concentration, which was during smoking three times lower than during burning a candle.

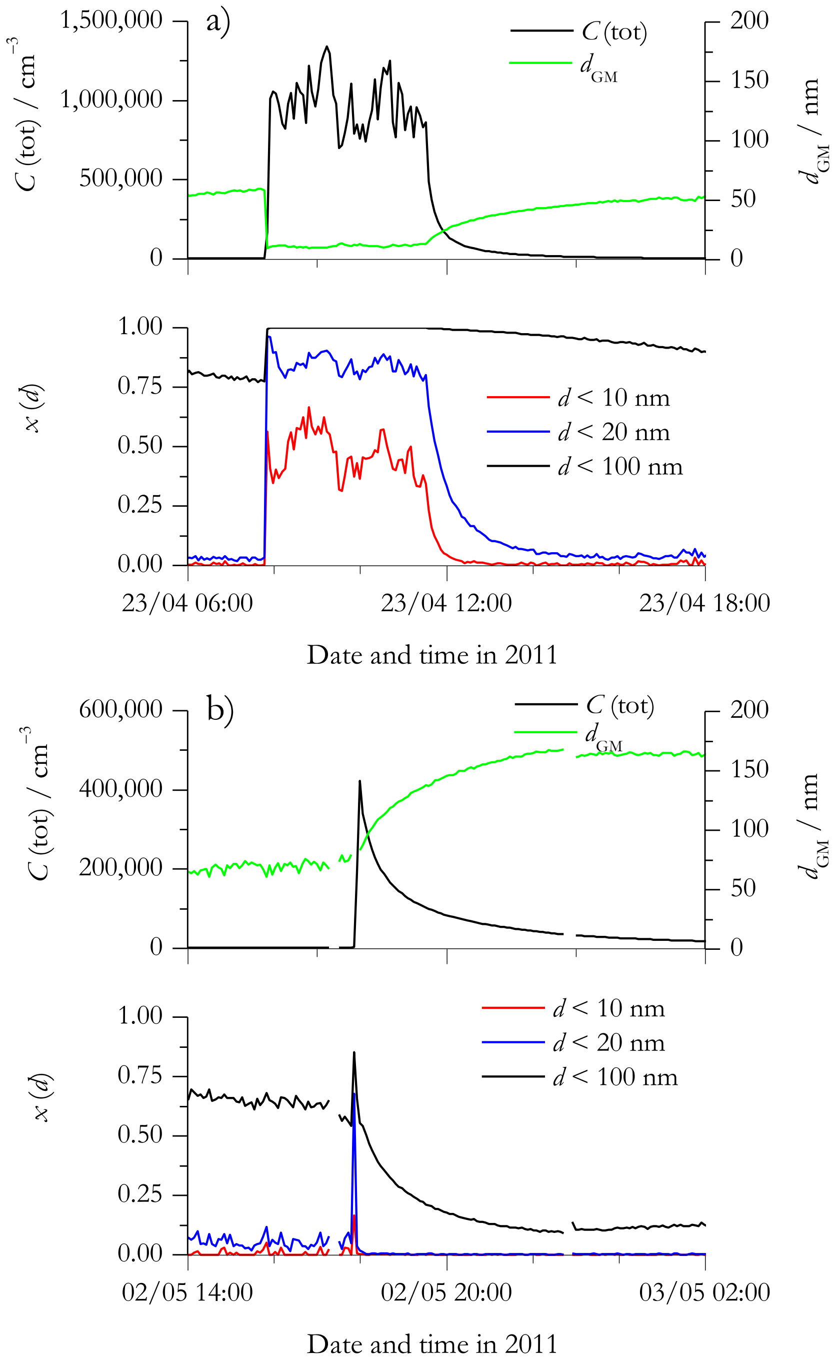

**Figure 2**: Time run of $C$(tot), $d_{GM}$, $x$(<10), $x$(<20) and $x$(<100) for a) burning a candle and b) smoking a cigarette

## 4 Conclusions

Particle concentration and size distribution has been monitored in the kitchen during two human activities generating particles. Taking into account only number particle concentration and its size distribution, without chemical composition, burning a candle can be potentially more toxic than smoking a cigarette, because it produces significantly smaller particles and higher number concentration of particles. Furthermore longer retention time of particles formed during burning a candle in the air leads to longer exposure time. In our future work, analyses of particle shape, morphology and chemical composition are foreseen.

## References

[1] C. He, L. Morawska, J. Hitchins, and D. Gilbert, Contribution from indoor sources to particle number and mass concentrations in residential houses. *Atmospheric Environment*, 38(21):3405–3415, 2004

[2] W. R. Ott and H. C. Siegmann, Using multiple continuous fine particle monitors to characterize tobacco, incense, candle, cooking, wood burning, and vehicular sources in indoor, outdoor, and in-transit settings. *Atmospheric Environment*, 40(5):821–843, 2006

[3] G. Buonanno, L. Morawska, and L. Stabile, Particle emission factors during cooking activities. *Atmospheric Environment*, 43(20):3235–3242, 2009

[4] H. Sohn and K. Lee, Impact of smoking on in-vehicle fine particle exposure during driving. *Atmospheric Environment*, 44(28):3465–3468, 2010

[5] S. Zai, H. Zhen, and W. Jia-song, Studies on the size distribution, number and mass emission factors of candle particles characterized by modes of burning. *Journal of Aerosol Science*, 37(11):1484–1496, 2006

[6] D. H. Brouwer, J. H. J. Gijsbers, and M. W. M. Lurvink, Personal exposure to ultrafine particles in the workplace: exploring sampling techniques and strategies. *Annals of Occupational Hygiene*, 48(5):439–453, 2004

[7] P. R. Buseck and K. Adachi, Nanoparticles in the atmosphere. *Elements*, 4(6):389–394, 2008

[8] P. Kumar, P. Fennell, and A. Robins, Comparison of the behaviour of manufactured and other airborne nanoparticles and the consequences for prioritising research and regulation activities. *Journal of Nanoparticle Research*, 12(5):1523–1530, 2010

[9] C. E. Mackay and K. H. Henry, Environmental fate and transport, in Nanotechnology and the Environment., CRC Press, Taylor & Francis Group: Boca Raton, USA, 2009

[10] U.S. Environmental Protection Agency (EPA), *Air quality criteria for particulate matter.*,: Washington, USA, 2004

[11] G. Oberdörster, E. Oberdörster, and J. Oberdörster, Nanotoxicology: an emerging discipline evolving from studies of ultrafine particles. *Environmental Health Perspectives*, 113(7):823–839, 2005

[12] International Commission on Radiological Protection (ICRP), Human respiratory model for radiological protection, ICRP Publication 24, Oxford, UK, 1994.

[13] P. Andujar, S. Lanone, P. Brochard, and J. Boczkowski, Respiratory effects of manufactored nanoparticles. *Revue des Maladies Respiratoires*, 28:e66–e75, 2011

[14] B. Nowack and T. D. Bucheli, Occurrence, behavior and effects of nanoparticles in the environment. *Environmental Pollution*, 150(1):5–22, 2007

[15] P. Kumar, A. Robins, S. Vardoulakis, and R. Britter, A review of the characteristics of nanoparticles in the urban atmosphere and the prospects for developing regulatory controls. *Atmospheric Environment*, 44(39):5035–5052, 2010

[16] M. Smerajec and J. Vaupotič, Nano-aerosols including radon decay products in outdoor and indoor air at a suburban site. *Journal of Toxicology*, ID 510876, 2012:1–31, 2012

## For wider interest

Nanoparticles contribute importantly to the pollution of ambient air and thus to the resulting adverse effects on human health. There are number of various natural and anthropogenic sources of indoor particles from engineered nanoparticles used in cosmetology, industry and medicine to unintentionally produced nanoparticles by biomass burning and traffic emissions. Important indoor sources include cooking exhaust, cigarette smoke, candles and other sorts of flames, and solvents.

Smaller particles are chemically and biochemically more reactive and potentially more toxic than larger ones, due to large surface area. With dropping particle size, the probability of deposition in respiratory system is increasing. It has been now recognised that nanoparticles cause oxidation stress, pulmonary inflammation and cardiovascular events. Factors that influence nanoparticle toxicity include size, number, surface characteristics, shape, chemical composition, surface treatment and potential for aggregation/agglomeration. Currently, there are no legal thresholds for nanoparticle number concentrations in ambient air, nevertheless, it is acknowledged that mass based particle concentration limits do not effectively control smaller particles. Therefore, particle number concentrations are likely to be considered within future air quality regulation.

The aim of our research is to contribute to the improvement of knowledge on nanoparticles characteristics, sources, and transport by monitoring outdoor and indoor air and to evaluate its influence on human health. In this contribution, measurements of particle concentrations and size distributions during two human activities of generating particles, burning a candle and smoking a cigarette, are described. Characterisation of newly formed particles and their abundance in air afterwards are presented. Taking into account only number particle concentration and its size distribution, without chemical composition, burning a candle can be potentially more toxic than smoking a cigarette, because it produces significantly smaller particles and higher number concentration of particles. Furthermore longer retention time of particles formed during burning a candle in the air leads to longer exposure time.

# Cytostatics cyclophosphamide and ifosfamide – do they occur in Slovene wastewaters and surface waters?

**Marjeta Česen[1,2], Tina Kosjek[1], Ester Heath[1,2]**

[1] Department of Environmental Sciences, Jožef Stefan Institute, Ljubljana, Slovenia

[2] Jožef Stefan International Postgraduate School, Ljubljana, Slovenia

marjeta.cesen@ijs.si

**Abstract.** To assess pollution of the Slovene aquatic environment by the cytostatics cyclophosphamide (CF) and ifosfamide (IF), we developed an analytical method for their analysis in wastewater and surface water by gas chromatography-mass spectrometry (GC-MS). Samples were collected and analyzed from the Institute of Oncology Ljubljana, the Central Wastewater Treatment Plant in Ljubljana and from the Ljubljanica River downstream from the WWTP discharge. Results revealed concentrations in wastewater from the Institute of Oncology of 12.1 μg $L^{-1}$ and 10.5 μg $L^{-1}$ for CF and IF, respectively. At other locations the concentrations of CF and IF were under their detection limits. In the future the method will be further optimized in order to detect lower concentrations of CF and IF. In addition, the study will be extended to include wastewaters and surface waters from other locations in Slovenia as well as the main metabolites of CF and IF.

**Keywords**: cyclophosphamide, ifosfamide, wastewater, Institute of Oncology Ljubljana, Central Wastewater Treatment Plant Ljubljana, gas chromatography-mass spectrometry

## 1 Introduction

Cyclophosphamide (CF) and ifosfamide (IF) are cytostatic compounds used in chemotherapy to treat patients with cancer and certain autoimmune diseases (Figure 1). Since their action is based on alkylation of nucleophilic compounds, they have the potential to cause genotoxic effects on non-target organisms in the environment [1].

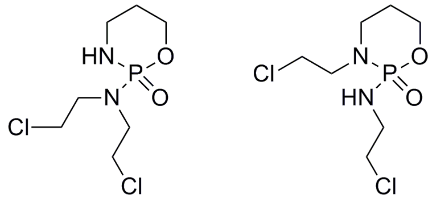

**Figure 1:** Structures of cyclophosphamide and ifosfamide.

To obtain data concerning their effects, it is necessary to asses their environmental occurrence in wastewaters and surface waters. Therefore, we developed an analytical method to determine these compounds in environmental samples. Wastewater samples were collected from the Institute of Oncology Ljubljana (IO Ljubljana) as well as influent and effluent samples from the Central Wastewater Treatment Plant in Ljubljana (CWTP Ljubljana) [2]. Samples were also collected from the Ljubljanica River downstream from the WWTP discharge.

## 2 Methods and techniques

### 2.1 Optimization of analytical method and sample preparation

The developed analytical technique was based on gas chromatography-mass spectrometry (GC-MS). HP 6890 series (Hewlett-Packard, Waldbron, Germany) gas chromatograph with a single quadrupole mass selective detector was used. The programme of GC oven was following: an initial temperature 65 °C was held for 2 min, then ramped at 30 °C min$^{-1}$ to 180 °C, at 15 °C min$^{-1}$ to 280 °C, at 30 °C min$^{-1}$ to 305 °C and finally held for 3 min. Total GC-MS runtime was 13.17 min. A capillary column, with He as the carrier gas, was a DB-5 MS 30 m × 0.25 mm × 0.25 μm (Agilent J&W, CA, USA). Aliquots (1 μL) of the samples were injected in splitless mode at 280 °C. The MS was operated in EI ionisation mode at 70 eV. The GC-MS used Chemstation software for instrumental control and data processing. All measurements were complied with an internal standard (4-methylcyclophosphamide). Since selected cytostatics are not sufficiently volatile for GC, they had to be derivatized first. This was performed using different derivatizing agents including acetic anhydride, heptafluorobutyric anhydride, trifluoroacetic anhydride (TFAA), N-(tert-butyldimethylsilyl)-N-methyltrifluoroacetamide and N-methyl-N-(trimethylsilyl)trifluoroacetamide).

Different derivatization times and temperatures were also investigated. Optimal derivatization was achieved by addition of 100 μL of TFAA to the sample, which was then derivatized for 0.5 h at 60 °C. For extraction, HLB Oasis$^{TM}$ cartridges (3cc, 60 mg) were used. Cartridges were conditioned using 3 mL of ethyl acetate, 3 mL of methanol and 3 mL of tap water. Optimal elution was achieved with 3 mL of ethyl acetate.

Grab samples were taken from the wastewater collection basin at IO Ljubljana and at Ljubljanica River (downstream from the WWTP discharge). Time-proportional samples (24 hours) were collected from the WWTP's influent and effluent. All samples were immediately transported on ice to the laboratory, where they were filtered (0.45 μm cellulose nitrate filters) and stored at - 20°C until analysis.

### 2.2 Sample analysis

To estimate the concentration range of CF and IF, different volumes of the samples were extracted and analyzed (200 mL, 500 mL and 1000 mL). For this purpose we used wastewater influent from laboratory-scale biological treatment plant (V = 200 mL). Recovery (%) was determined using 0.5 μgL$^{-1}$ of CF and IF and was calculated as ratio between peak areas of spiked amount of analyte, which was added prior to extraction (n = 3), and peak areas of same amount of analyte, added post extraction (n = 3). A six point calibration was performed (n = 3). Linear regression was used to obtain the $r^2$ values. LOD (limit of detection) and LOQ (limit of quantification) were determined as 3-times (LOD) and 10-times (LOQ) standard deviations of the peak areas of the baseline from the blanks (n = 6) divided by the slope of calibration curve. Repeatability was calculated as RSD at three concentration levels (500 ng L$^{-1}$ , 5000 ng L$^{-1}$ , 10000 ng L$^{-1}$; n = 3)

## 3 Results and discussion

Optimal volume for analysis of wastewater from IO Ljubljana was 200 mL, while samples of influent and effluent of CWTP Ljubljana and Ljubljanica River contained undetectable concentrations of CF and IF at these volumes and specified conditions of analytical method. The linear range, recoveries (%), LOD, LOQ, $r^2$ values and repeatability (RSD values) for CF and IF are shown in Table 1.

**Table 1:** Validation parameters for CF and IF.

| **Validation parameters** | **CF (± sd)** | **IF (± sd)** |
|---|---|---|
| linear range | 750 ng $L^{-1}$ - 12500 ng $L^{-1}$ | |
| recovery (%) (n = 3) | 92.0 ± 2.3 % | 99.6 ± 2.3 % |
| LOD (n = 6) | 11.2 ng $L^{-1}$ | 34.7 ng $L^{-1}$ |
| LOQ ( n = 6) | 37.2 ng $L^{-1}$ | 115.7 ng $L^{-1}$ |
| $r^2$ values (6 conc. points, n = 3) | 0.984 | 0.997 |
| RSD (%) (3 conc. points, n = 3) | 2.1 | 5.7 |

Concentrations of CF and IF in wastewater samples from IO Ljubljana were 12.1 μg $L^{-1}$ and 10.5 μg $L^{-1}$ for CF and IF, respectively. In the remaining samples (influent and effluent of CWTP Ljubljana and Ljubljanica River) CF and IF were below the LOD. Future work will involve extracting a higher number of samples, extracting larger volumes and the use of higher capacity cartridges (6cc, 150 mg). In addition, the analytical method will be optimized for lower LOD and LOQ and revalidated. Grab samples will also be obtained from IO Ljubjana and the Ljubljanica River on an hourly basis to investigate hourly, daily and weekly variations.

In addition, samples will be collected from other wastewaters of Slovenian institutions where CF and IF are used and followed through WWTP to receiving surface water. Furthermore, we will also compare our data with other European countries, which are participating in the EU FP7 CytoThreat project. Because pharmaceuticals undergo metabolism after ingestion, we will extend our research also to the analysis of the main metabolites of CF and IF in wastewaters and surface waters [3].

## Acknowledgements

This work was financially supported by the EU through the EU FP7 project CytoThreat (Fate and effects of cytostatic pharmaceuticals in the environment and the identification of biomarkers for and improved risk assessment on environmental exposure, grant agreement No.: 265264) and by the Slovenian Research Agency (Program Group P1-0143 and Young Researcher grant to M. Č.). We would also like to thank IO Ljubljana and JP Vodovod-Kanalizacija d.o.o. Ljubljana for their collaboration.

## References:

[1]I. J. Buerge. Occurrence and Fate of the Cytostatic Drugs Cyclophosphamide and Ifosfamide in Wastewater and Surface Waters. *Environmental Science and Technology*, 40(23):7242-7250, 2006

[2]Javni holding Ljubljana, Vodovod-kanalizacija official home page. http://www.jhl.si/en/vo-ka/about, 2012

[3]S. Mompelat. Occurrence and fate of pharmaceutical products and by-products, from resource to drinking water. *Environment International,* 35(5):803-814,2009

# For wider interest

Pharmaceuticals contribute greatly to our wellbeing, but their residues are finding their way into the environment where they can have unintended consequences, often at very low concentrations. The aim of this study is to evaluate the presence of cytostatics, potent pharmaceuticals used in chemotherapy. Samples of wastewater from Institute of Oncology Ljubljana, Central Wastewater Treatment Plant Ljubljana and receiving surface water (Ljubljanica River) were analysed for the presence of two commonly prescribed cytostatics: cyclophosphamide and ifosfamide. By using gas chromatography-mass spectrometry, we found 12.1 $\mu g\ L^{-1}$ of cyclophosphamide and 10.5 $\mu g\ L^{-1}$ of ifosfamide in samples of wastewater from Institute of Oncology Ljubljana. The concentrations of both compounds in the influent and effluent of the Central Wastewater Treatment Plant Ljubljana and in the Ljubljanica River were under limits of detection ($LOD_{(CF)} = 11.2\ ng\ L^{-1}$, $LOD_{(IF)} = 34.7\ ng\ L^{-1}$) due to the dilution effect of the sewerage system, which collects wastewater from a wide region of Ljubljana and returns it after treatment to Ljubljanica River. In the future, a more sensitive analytical method will be developed that will allow us to detect the presence of cytostatics at lower concentrations ($ng\ L^{-1}$). In addition, sampling will be repeated so that hourly, daily and weekly variations will be identified and the study of their occurrence will be extended to other waste and environmental waters.

# Karakterizacija slovenskega oljčnega olja z uporabo stabilnih izotopov

**Marinka Gams Petrišič**[1,2], **Milena Bučar-Miklavčič**[3,4], **Nives Ogrinc**[1,2]

[1] Odsek za znanosti o okolju, Institut Jožef Stefan, Ljubljana, Slovenija

[2] Mednarodna podiplomska šola Jožef Stefan, Ljubljana, Slovenija

[3] UP ZRS LPOO – Univerza na Primorskem, Znanstveno-raziskovalno središče, Laboratorij za preskušanje oljčnega olja, Izola, Slovenija

[4] LABS d.o.o., Inštitut za ekologijo, oljčno olje in kontrolo, Izola, Slovenija

marinka.petrisic@ijs.si

**Povzetek.** V Evropski uniji posvečajo veliko pozornost kakovosti in kontroli prehrambnih izdelkov. Pri našem delu smo se osredotočili na oljčno olje, kjer smo dokazovali potvorjenost oljčnega olja z uporabo metode stabilnih izotopov. V vzorcih oljčnega olja smo določevali vsebnost in izotopsko sestavo maščobnih kislin (FA). Meritve izotopske sestave ogljika v posameznih FA smo izvedli z GC-C-IRMS. Izkušnje iz prejšnjih raziskav [3] so pokazale, da se potvorjenost oljčnega olja lahko določa z meritvami izotopske sestave ogljika v palmitinski ($C_{16:0}$) in oleinski ($C_{18:1}$) kislini pri čemer naj bi bile vrednosti $\delta^{13}C_{16:0}$:$\delta^{13}C_{18:1}$ v razmerju 1:1, odstopanje od teh vrednosti pa naj bi pomenilo potvorjenost olja. Z našimi raziskavami smo nadgradili bazo podatkov pristnih slovenskih oljčnih olj, vendar nam vseh potvorjenosti ni uspelo dokazati na osnovi izotopske sestave maščobnih kislin, zato je potrebno raziskave razširiti še na druge elemente kot sta O in H.

**Ključne besede**: oljčno olje, stabilni izotopi ogljika, GC-C-IRMS; maščobne kisline

## 1 Uvod

Potvarjanje prehrambnih izdelkov predstavlja velik ekonomski dobiček za živilsko industrijo, predvsem pa za manjše podjetnike. Glede na vrsto tehnološkega postopka ločimo deviška oljčna olja, rafinirana oljčna olja in olja iz oljčnih tropin.

Glede na tehnologijo predelave in kakovost se v skladu z Uredbo Komisije (EU) št. 29/2012 lahko tržijo v maloprodaji le naslednja oljčna olja: ekstra deviško oljčno olje, deviško oljčno olje, oljčno olje, sestavljeno iz rafiniranih oljčnih olj in deviških oljčnih olj in olje iz oljčnih tropin.

Ker so analizne metode za ugotavljanje kakovosti in pristnosti oljčnega olja dolgotrajne in zahtevne, smo za ugotavljanje pristnosti uvedli novo metodo, ki temelji na analizi stabilnih izotopov ogljika v maščobnih kislinah. Za ugotavljanje potvojenosti prehrambenih izdelkov je potrebno najprej izdelati bazo podatkov pristnih oljčnih olj iz različnih področjih in le-te primerjati z domnevno potvorjenimi oljčnimi olji.

Meritve stabilnih izotopov ogljika v maščobnih kislinah smo uporabili v različne namene. Z meritvami avtentičnih oljčnih olj iz različnih območij smo najprej dopolnili bazo podatkov za leto 2006, 2007 in 2008 in testirali uporabo stabilnih izotopov ogljika pri določanju geografskega porekla oljčnega olja. Nadalje smo metodo testirali na potvorjenih vzorcih oljčnega olja.

# 2 Metode

Meritve smo izvedli na 238 vzorcih pristnega oljčnega olja iz različnih slovenskih območij (Slovenska Istra, Brda) in drugih državah proizvajalk oljčnega olja letnikov 2006, 2007 in 2008. Meritve smo izvedli v celokupnem vzorcu oljčnega olja, nato pa še v posameznih maščobnih kislinah. Vzorce iz Slovenije smo uporabili pri dopolnitvi baze podatkov pristnih oljčnih olj, ostale vzorce pa smo uporabili pri statistični obdelavi, ko smo testirali uporabnost analiz pri določanju geografskega porekla oljčnega olja.

## 2.1 Priprava vzorcev in analiza

V vzorcih oljčnega olja smo določevali maščobne kisline, ki imajo kislost manjšo ali enako 0,8 ut.%. V vialo smo dali 100 μl vzorca oljčnega olja, dodali 2 ml heksana in 200 μl metanolnega KOH s koncentracijo 2 mol/L. Vialo smo dobro zaprli z zamaškom in 30 s močno stresali. Pustili smo, da se plasti ločita in da se zgornja plast zbistri. Zgornjo plast, ki vsebuje metilne estre smo oddekantirali v vialo za avtomatski vzorčevalnik in jo zaprli. Tako pripravljeno raztopino metilnih estrov maščobnih kislin v heksanu je bilo potrebno analizirati v 12h urah.

## 2.2 Analiza vzorcev

Meritve izotopske sestave ogljika v posameznih maščobnih kislinah smo izvedli na masnem spektrometru za stabilne izotope IsoPrime GV Instruments s plinskim kromatografom Agilent 6890N s FID detektorjem ter s sežigno enoto in vmesnikom (CIRMS). Meritve izotopske sestave ogljika so podane z vrednostmi delta – δ v promilih (‰) glede na Vienna Pee Dee Belemnite limestone (VPDB) standard. Pravilnost in potek meritev smo spremljali z uporabo laboratorijskega standarda FAME – Fatty acid methyl ester z vrednostjo $\delta^{13}C$ -29,8 ‰. Napaka meritev tako določene izotopske sestave ogljika v maščobnih kislinah izmerjena na dveh vzporednih ponovitvah znaša ±0,2 ‰. Pri meritvah smo poleg izotopske sestave ogljika spremljali tudi površino posameznih pikov, na podlagi katerih smo lahko določili razmerja vsebnosti posameznih maščobnih kislin in jih primerjali z razmerji določenimi na podlagi plinske kromatografije (GC/MS).

# 3 Rezultati in diskusija

## 3.1. Pristna oljčna olja, baza podatkov, geografsko poreklo

Vrednost $\delta^{13}C$ v celokupnem oljčnem olju in posameznih FA se spreminja med –31,6 ‰ in –29,1 ‰, kar je tipično za C3 rastline. Izkušnje iz prejšnjih raziskav so pokazale, da se potvorjenost oljčnega olja lahko določa z meritvami izotopske sestave ogljika v palmitinski ($C_{16:0}$) in oleinski ($C_{18:1}$) kislini, pri čemer naj bi bile vrednosti $\delta^{13}C_{16:0}$:$\delta^{13}C_{18:1}$ v razmerju 1:1 v avtentičnih vzorcih, odstopanje od teh vrednosti pa naj bi pomenilo potvorjenost olja [3].

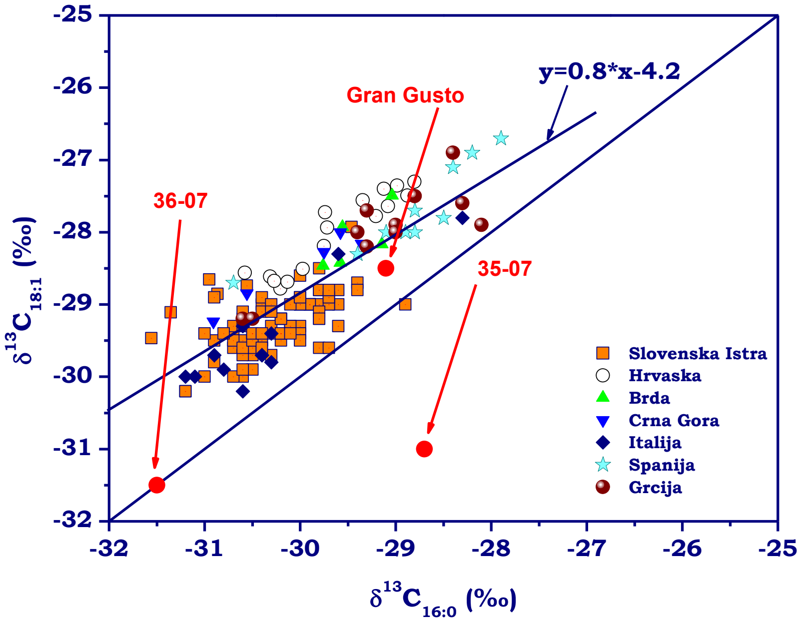

Slika 1. Odvisnost $\delta^{13}C_{18:1}$ od $\delta^{13}C_{16:1}$ v pristnih vzorcih iz leta 2006 (Slovenska Istra, Hrvaška, Brda, Črna Gora, Italija, Španija in Grčija) in treh izbranih potvorjenih vzorcih oljčnega olja (36-07, Gran Gusto in 35-07).

Naše trenutne meritve (Slika 1) ne potrjujejo omenjene predpostavke. Dobili smo dobro korelacijo med vrednostmi $\delta^{13}C_{16:0}$ in $\delta^{13}C_{18:1}$ ($r^2 = 0.94$; $p < 0.0001$), vendar so vrednosti $\delta^{13}C_{18:1}$ v povprečju za 1,7 ‰ višje kot $\delta^{13}C_{16:0}$. Razlogi za odstopanja so lahko različni in jih je potrebno še nadalje raziskati. Eden od glavnih razlogov je vpliv sprememb klimatskih pogojev, ki se letno spreminjajo in vplivajo na naravne vsebnosti ogljikovih izotopov.

Rezultate smo statistično obdelati in testirati uporabnost analiz pri določanju geografskega porekla oljčnega olja. Kemometrijske metode, ki se uporabljajo pri ugotavljanju podskupin/razredov med podatki, so običajno metoda glavnih osi (Principal Component Analysis – PCA) in različne metode grupiranja. Kot je razvidno iz slike 2, že koncentracije in izotopska sestava maščobnih kislin daje zadovoljive rezultate pri ločljivosti oljčnih olj z različnih geografskih področij. Veliko boljšo ločljivost med posameznimi področjih bi po podatkih iz literature dosegli z uporabo meritev izotopske sestave O in H v oljčnem olju.

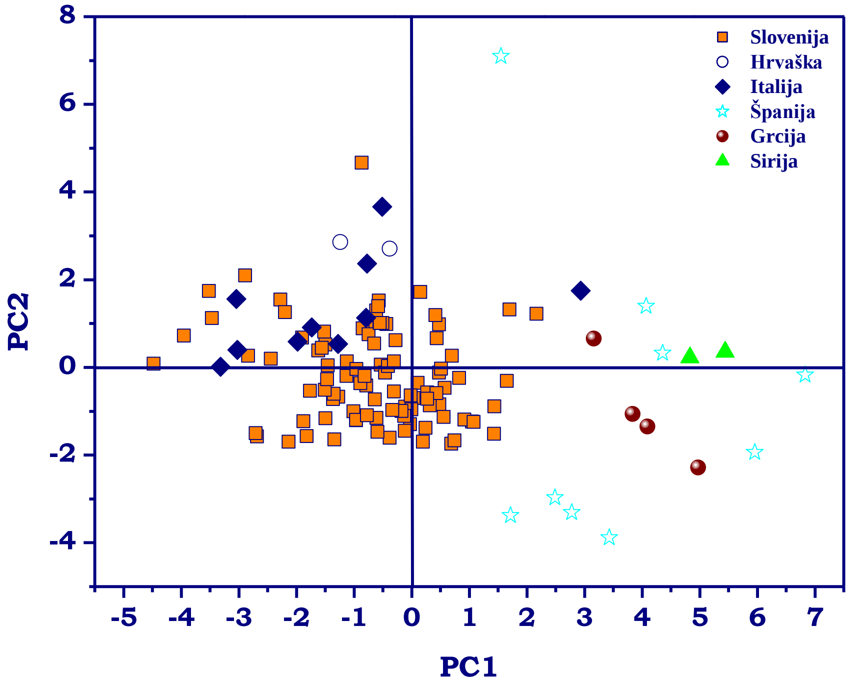

Slika 2. Projekcija oljčnih olj v ravnini, definirani z dvema glavnima osema PC1/PC2 po metodi glavnih osi (Principal Component Analysis – PCA)

### 3.2 Določanje potvorjenosti izdelkov iz oljčnega olja

Uporabo stabilnih izotopov ogljika v maščobnih kislinah za ugotavljanje potvorjenosti smo testirali tudi v treh različnih potvorjenih vzorcih oljčnega olja. Vzorec z oznako Gran Gusto, mešanici olja z naslednjima oznakama in sestavo - COI 035-07: 70 % deviškega oljčnega olja, 10 % rafiniranega olja iz oljčnih tropin , 20 % sončničnega olja z visoko vsebnostjo oleinske kisline in COI 036-07: 80 % deviškega oljčnega olja z visoko vsebnostjo kampesterola in 20 % palmovega olja z visoko vsebnostjo oleinske kisline. V vzorcu Gran Gusto potvorjenost opazimo pri analizi vsebnosti maščobnih kislin. Vsebnost linolne kisline 57,6 % je višja kot v pristnem oljčnem olju, medtem ko sta vsebnosti palmitinske in stearinske kisline nižji kot v pristnem oljčnem olju. Vrednosti $\delta^{13}C_{16:0}$ =-29,1 ‰ in $\delta^{13}C_{18:1}$ = -28,5 ‰ sovpadata z vrednostmi pristnega oljčnega olja in na podlagi le teh meritev potvorjenosti ne moremo dokazati. Nasprotno kažejo rezultati mešanice olja COI 035-07. Vsebnost posameznih maščobnih kislin je podobna kot v pristnem oljčnem olju, vendar pa se vrednosti $\delta^{13}C_{16:0}$ in $\delta^{13}C_{18:1}$ znatno razlikujeta med sabo. Vrednost $\delta^{13}C_{18:1}$ je kar za 2,3 ‰ nižja kot $\delta^{13}C_{16:0}$.

V pristnem oljčnem olju so vrednosti $\delta^{13}C_{18:1}$ v povprečju za 1,7 ‰ višje kot $\delta^{13}C_{16:0}$. Rezultati tretjega vzorca pa nakazujejo, da tovrstno potvorjenost dokazujemo lahko z meritvami vsebnosti posameznih maščobnih kislin kot tudi z meritvami izotopske sestave ogljika v maščobnih kislinah. Vrednosti $\delta^{13}C_{16:0}$ in $\delta^{13}C_{18:1}$ sta enaki. Rezultati meritev $\delta^{13}C_{16:0}$ in $\delta^{13}C_{18:1}$ v potvorjenih vzorcih so prikazani na sliki 1.

## 4 Zaključek

Z meritvami avtentičnih oljčnih olj iz različnih območij smo dopolnili bazo podatkov za leto 2006,2007 in 2008 in testirali uporabo stabilnih izotopov ogljika pri določanju geografskega porekla oljčnega olja. Ugotovili smo, da le na podlagi izotopske sestave maščobnih kislin določenih potvorb ne moremo dokazati, zato je potrebno v raziskave vključiti izotopsko sestavo drugih elementov kot sta O in H. Ker imamo na voljo in dostop tudi do teh meritev, bomo v nadaljevanju izbrali reprezentativne vzorce pristnih oljčnih olj iz različnih področij in jim določili $\delta^{18}O$ in $\delta^{2}H$ vrednosti. Izkazalo se je, da $\delta^{18}O$ in $\delta^{2}H$ vrednosti pripomorejo k boljši ločitvi oljčnega olja glede na geografsko poreklo in možnost dokazovanja potvorjenosti oljlnega olja z lešnikovim oljem, kar predstavlja pereč problem tudi na tržišču.

Tovrstne raziskave podpirajo razvoj sistema za monitoring prehrambnih proizvodov in razvoj metod za izvajanje kontrole živil. Z možnostjo dokazovanja avtentičnosti oljčnega olja v prehrambnih izdelkih bodo pristojni organi zaščitili in zavarovali kakovost oljčnih proizvodov hkrati pa tudi zaščitili potrošnika pred morebitnimi potvorbami.

## Literatura

[1] http://www.oljcno-olje.com/index.php?option=com_content&view=article&id=49&Itemid=64

[2] N. Ogrinc in sod.. Primerjava in razvoj novih metod za določanje avtentičnosti olja in prehrambenih izdelkov; zaključno poročilo o rezultatih opravljenega raziskovalnega dela *elektronski vir*, 2008.

[3] J. E. Spangenberg, N. Ogrinc. Authentication of vegetable oils by bulk and molecular carbon isotope analyses with emphasis on olive oil and pumpkin seed oil, J. Agric. Food Chem. 1534-1540 (49), 2001.

[4] N. Ogrinc, M. Gams Petrišič, M. Bučar-Miklavčič. Uporaba stabilnih izotopov ogljika pri določanju geografskega porekla in pristnosti oljčnega olja. *Knjiga povzetkov /15. mednarodni simpozij Spektroskopija v teoriji in praksi, Nova Gorica, Slovenija, 18.-21. april 2007*

## Za širši interes

Potreba po spremljanju avtentičnosti in kakovosti prehrambnih izdelkov je povzročila, da se je pojavilo povpraševanje po metodah, s katerimi bi dokazali potvorjenost. Za odkrivanje ponarejanja živil se torej lahko poslužujemo tako imenovanega globalnega pristopa, pri katerem določamo oporečnost na osnovi fizikalno-kemijskih lastnostih vzorca. Te metode temeljijo na tako imenovanem izotopskem prstnem odtisu ali »fingerprintingu«. Z njimi ne določamo le stopnjo in način potvorjenosti, temveč tudi geografsko poreklo in celo leto proizvodnje izdelka. Poleg oljčnega olja smo v raziskave avtentičnosti prehrambnih izdelkov vključili tudi vina, med, sladkor, sadne sokove, ustekleničene vode in mleko ter mlečne izdelke. Omenjene analize prispevajo h kakovosti oziroma certificiranju določenih prehrambnih izdelkov in s tem k okrepitvi konkurenčne sposobnosti agro-živilske industrije.

# Results of coal gas desorption experiments, laboratory sorption experiments on lignite samples and in-situ seam gas pressure - rock stress measurements

**Sergej Jamnikar**[1], **Jerneja Lazar**[1], **Simon Zavšek**[1], **Ludvik Golob**[1]

[1] Coal Mine Velenje, Partizanska 78, Velenje, Slovenia
sergej.jamnikar@rlv.si

**Abstract.** Understanding the principles of coal seam gas behaviour require a great number of experimental tests, monitoring campaigns, equipment design and numerous correlations between gained data. Research work on Velenje lignite and "in-situ" monitoring on long-wall faces consisted of coal's gas content experiments and mine monitoring campaigns. Gas content is commonly measured with standard desorption methods by using direct method which measures actual released gas volume from sample. According to some widely-known methods (US Bureau of Mines direct method, Australian Standard method), gas content determination methodology for Velenje lignite was developed. Mine monitoring included seam gas pressure and rock stress measurements, accompanied by gas sampling for composition and isotopic analysis. Observations showed definite correlations between listed parameters when measured results were combined into combined analysis.

**Keywords**: Coal seam gas, desorption experiments, seam gas pressure, rock stress.

## 1 Introduction

Coal mining in thick lignite seams by using long-wall mining methodologies is an approach towards efficient and effective way of coal deposits extraction. By expanding the size of long-wall face, the amount of crushed coal often cause increased additional releases of coal seam gases (carbon dioxide, methane) and possible rock bursts, often accompanied by gas outbursts [1]. Lignite seam at Coal Mine Velenje represents large volume reservoir for coal seam gases. Carbon dioxide represents major share in total gas balance and is mostly adsorbed to coal or is trapped in micro-pores of the coal structure, while methane is accumulated by the

surface of coal seam, just under the roof-strata clay seam [2]. It is obvious that free methane is present also in lover sections of the coal seam as its presence is detected and concentrations are monitored in return air of every working long-wall face [3].
Experimental work as laboratory desorption experiments (gas content determination), adsorption experiments and continuous mine monitoring (coal seam gas behaviour, geotechnical monitoring) result in understanding the interaction between events of gas releases accompanied by geotechnical factors.

## 1.1 Coal seam outline

Lignite deposit in Velenje basin is amongst the thickest in worlds scale with maximum thickness of over 160 metres and depth of 150 – 500 m below ground level. Its size spreads over an area of 8,3 km × 2,5 km and contains about 130 millions of mineable coal reserves.
Coal seam is placed on floor strata of andesitic rocks, sands, breccia and Triassic dolomite. Above coal deposit there is a thick layer of isolative clay, sand and interchangeable layers of clay, silt, sand, mud-stone and under surface alluvial deposits.

## 1.2 Velenje mining method outline

The Velenje long-wall mining method was developed on classical coal faces equipped with friction legs and iron beams. A true revolution in the support system development was represented by hydraulic support system with a conveyor sitting on a base, lemniscate-guided shield, an option of total control (prevention) of caving-in in the foot-line section and electro-hydraulic control system. The entire long-wall excavation process is based on the consideration of natural characteristics, provision of adequate safety and the prediction of impacts on the environment. According to Velenje mining method coal face is divided in the foot-line section (lower excavation section) and the hanging wall (upper excavation section) section (Figure 1). The allowed face height at the long-wall depends on the thickness of clay insulating layers in the hanging wall, which protect the face from the inrush of running sand and water. Following the criteria of „Safe mining below water bearing strata at Velenje Coal Mine" the allowed working height is calculated according to preliminary stated variations.

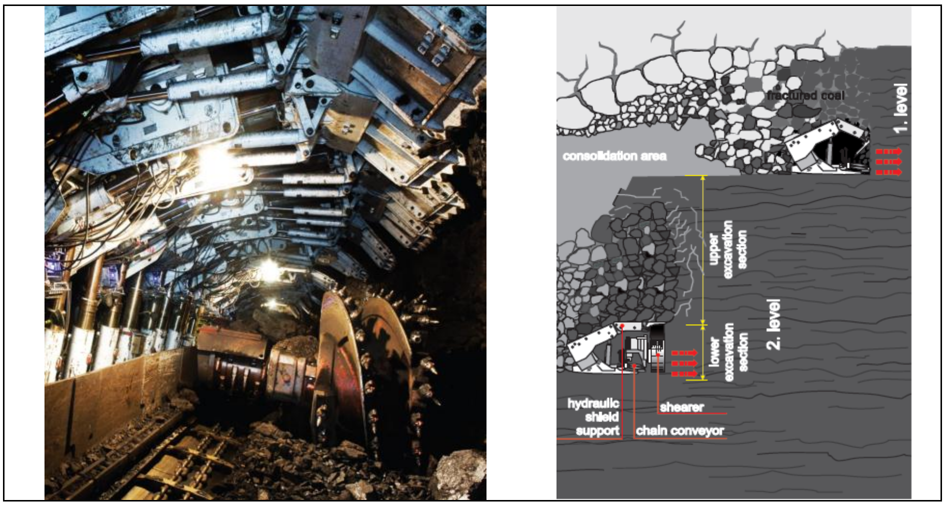

**Figure 1:** Long-wall face with hydraulic steel shield support, shearer and chain conveyor (left) and schematic presentation of lignite seam division into levels, together with sequence of sub-caving excavation in levels (left) (Premogovnik Velenje, 2011)

## 2 Experimental work

Gas content in coal is determined by variations of desorption experiments amongst which US Bureau of Mines direct method and Australian Standard method [4] represent direct gas content determination method that uses physical principles of gas release from coal samples.

Proposed direct experimental methods measures actual desorbed gas from core coal samples by using desorbed gas over-pressure in canister where sample is kept to supplant desorption solution in an inverted graduated cylinder. The volume of supplanted solution is the actual desorbed gas volume from the sample.

Literature [4] usually suggest desorption experiments as sequence driven test in steps to determine total desorbed gas content as follows:

$$Q_{total} = Q_{lost} + Q_{desorbed} + Q_{residual} \tag{1}$$

Total desorbed gas content consists of lost gas ($Q_{lost}$) which is determined analiticaly basing on initial quantities of actual desorbed gas ($Q_{desorbed}$). Residual gas ($Q_{residual}$) is quantity of gas that stays adsorbed to coal micro-structure and could be released only after crushing the sample.

Based on observation and results of previous desorption experiments [5], [6], [7], [8], [9], [10] research of lost gas content, litho-type influence and equipment design (Figure 2) that answers Velenje lignite desorption properties started.

a) b)

**Figure 2:** Modified equipment for desorption experiments. Lost gas content determination equipment (left), laboratory desorption equipment (right) (Jamnikar, 2011-2012).

Desorption experiments continued in April 2012 when equipment was successfully tested. First samples were taken from bore-hole jgm 55 (-2°)/12 in Mine Preloge.

### 2.1 Gas content determination experiment 2/2012

Sample brief litho-type analysis: fine dethrite (dD) [11]
Lost gas content determination, Laboratory desorption experiment

Gas content determination - Desorption test 2/2012 started as lost gas content determination experiment in mine (Figure 3) and continued in laboratory by monitoring gas release together with sampling of desorbed gas. Figure 3 shows graphical presentation of desorption measurements within more than 78 minutes after sample coring. Gas release stopped after that time at volume 170 ml. In processing, a tangent was added to time-volume curve to determine lost gas volume, shown as crossing of tangent with negative Y-axis. The crossing value represents approximate lost gas value of 470 ml. Sample was transferred to laboratory after lost gas content determination for standard two-month experiment time.

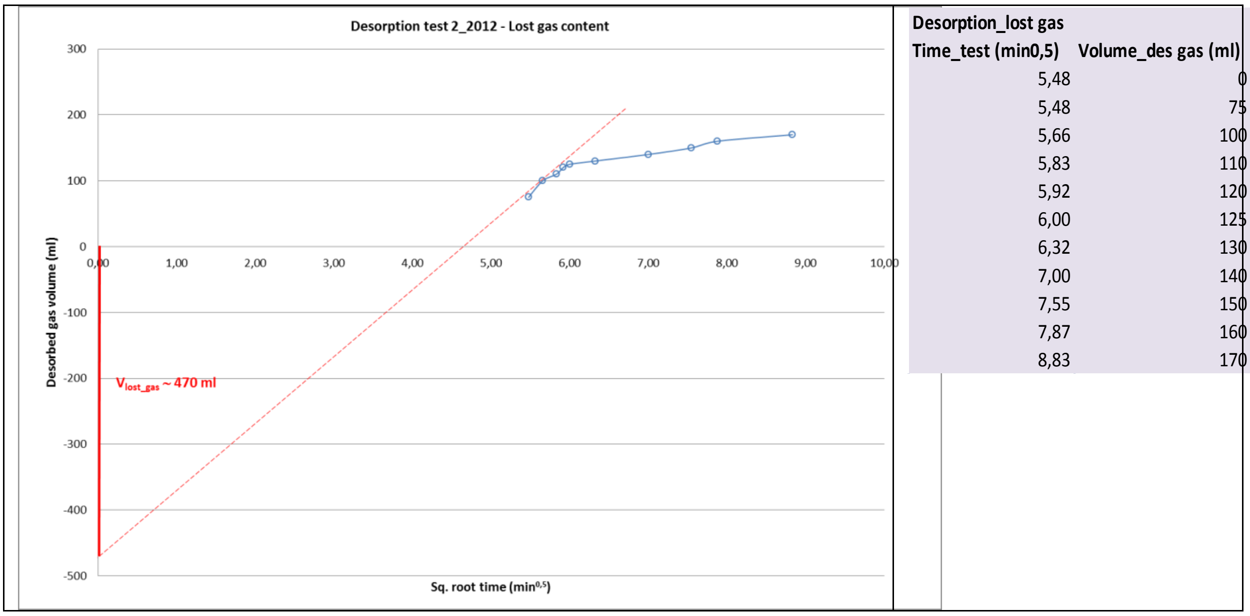

Desorption_lost gas

| Time_test (min0,5) | Volume_des gas (ml) |
|---|---|
| 5,48 | 0 |
| 5,48 | 75 |
| 5,66 | 100 |
| 5,83 | 110 |
| 5,92 | 120 |
| 6,00 | 125 |
| 6,32 | 130 |
| 7,00 | 140 |
| 7,55 | 150 |
| 7,87 | 160 |
| 8,83 | 170 |

**Figure 3:** Desorption experiment 2/2012 – Lost gas content

# 3 Mine monitoring

## 3.1 Seam gas pressure monitoring

Seam gas pressure monitoring was established with purpose to correlate gas pressure behaviour in dependence of long-wall face approach with geotechnical monitoring, especially stress measurements. Geotechnical monitoring over past years showed certain dynamics of rock stress manifestation in dependence of distance to long-wall face. Presumably, wave of rock stress increase caused changes in permeability of coal seam which was described also as “opening and closing” of fault and crack system. Described effect of stress caused permeability changes of coal, observed in laboratory experiments was discussed in papers [12], [13]. An emphasis was put on measuring well construction (Figure 4) for seam gas pressure monitoring. Its construction and sequence of drilling are targeting total tightness to prevent gas leakage from coal seam and well.

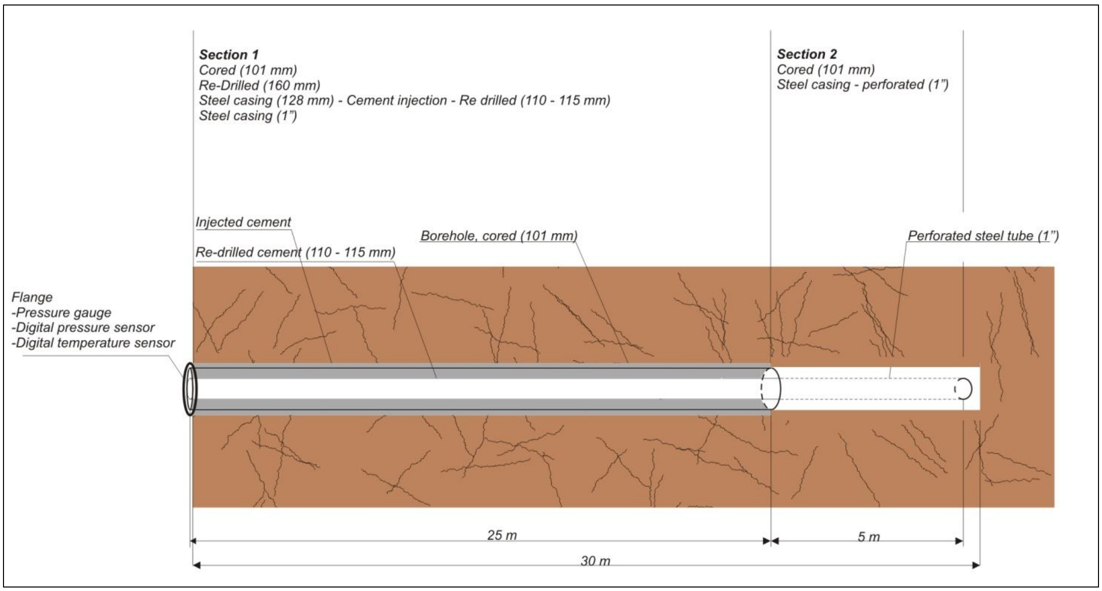

**Figure 4:** Scheme of seam gas monitoring well construction (Jamnikar, 2010)

## 3.2 Rock stress monitoring

Rock stress monitoring is an established methodology on long-wall face influence observations. Stress cells are built into bore-holes which are drilled with different orientations and inclinations. Rock stress monitoring design normally dictates bore-holes drilling into excavation pillars in order to detect influence of advancing long-wall face.

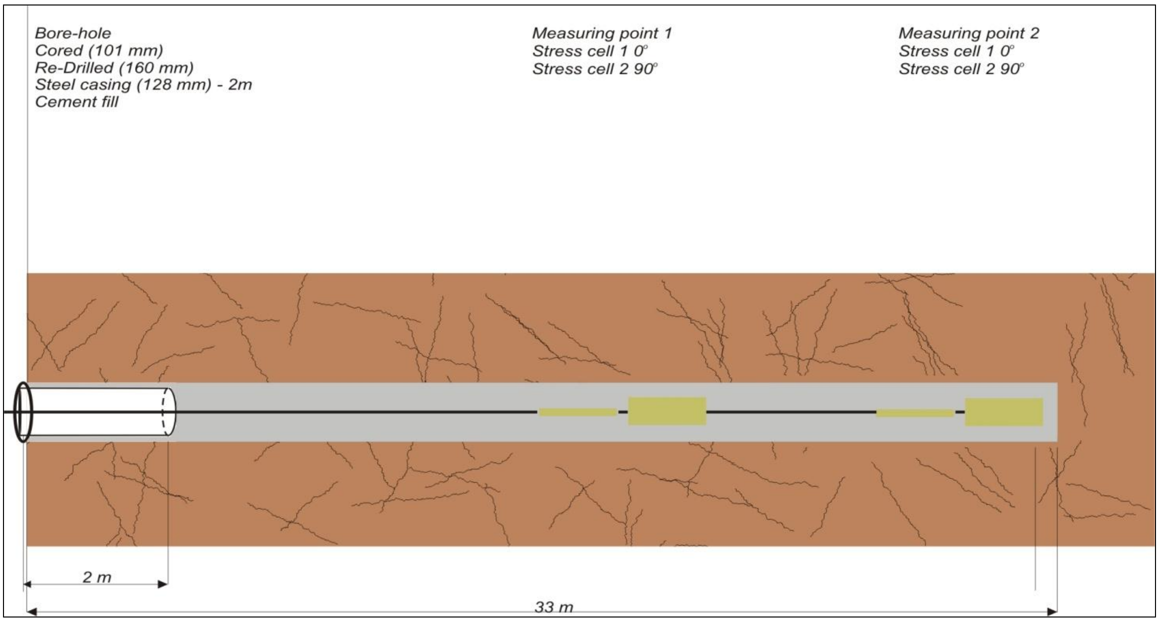

**Figure 2:** Scheme of rock stress monitoring well construction (Jamnikar, 2012)

## 3.3 Mine monitoring at long-wall face K. -50 C (Mine Pesje)

Long-wall face K. -50 C (Figure 6) was chosen for multiple – monitoring field because of its specific location in the coal seam. Due to general CM-Velenje excavation concept, sub-caving methodology and geological features, excavation pillar was divided into two sections with different gas and stress state properties. NW part of excavation pillar was located directly under solid (virgin) coal and intact roof strata whereas SE part was located under pre-mined coal and deformed roof strata. Historical recordings of excavation results show increased gas accumulations and increased rock stress in excavation areas where mining is performed for the first time.

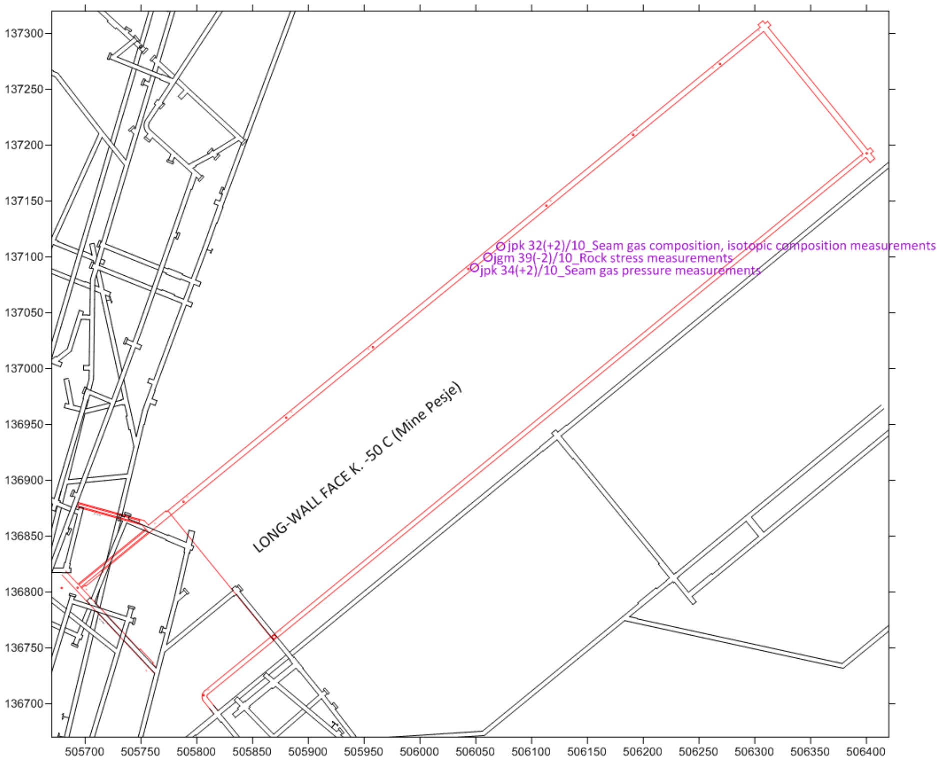

**Figure 6:** Location of seam gas pressure and rock stress measurements at long-wall face K. -50 C (Mine Pesje)

Combined presentation of seam gas pressure and rock stress measurement results are shown on Figure 20 below. Measuring point at long-wall face K. -50 C was equipped with seam gas pressure monitoring well (jpk 34 (+2°)/10), rock stress monitoring well (jgm 39 (-2°)/10) and gas sampling and isotopic composition analysis well (jpk 32 (+2°)/10) (Figure 6).

Well jgm 39 (-2°)/10 was equipped with two pairs of stress cells, amongst which pair of cells at 25m depth was chosen for further discussions due to better recordings of dynamic stress changes ahead of the advancing long-wall face.

Results from rock stress monitoring (jgm 39 (-2°)/10) and seam gas pressure monitoring (jpk 34 (+2°)/10) are combined together on a single chart. Figure 7 represents comparison of stress and gas pressure changes. Stress change is shown in MPa while gas pressure is scaled in bars. Values of stress and gas pressure changes are presented in dependence of long-wall face advance.

In the chart influence of stress state changes and gas pressure dynamics is presumably explained by "cleat system opening and closing". When long-wall face distance to monitoring point is more than approximately 70 meters, stress influence causes several in-seam deformations. Seam gas is allowed to move freely through seam and measured gas pressure decreases. When long-wall face approaches towards monitoring point, rock stress rises, the cleats are closing and seam gas is trapped into closed volume. This phenomenon is recorded in seam gas pressure rise. Seam gas pressure rises until the peak of maximum coal strength is achieved (50 – 30 m). After stress peak is achieved (30 – 0 m), deformations of excavation pillar rises and seam gas escapes from cleat system.

Additional gas behaviour is observed in isotopic composition of carbon isotope $^{13}C$ in carbon dioxide and methane as it was discussed in papers [14], [15], [16]. Figure 7 show changes in isotopic composition of carbon isotope $^{13}C$ in carbon dioxide and methane analysed (Institute Jožef Stefan) from gas samples taken at well jpk 32 (+2˚)/10 and represent further study and research task.

Values of isotopic composition $CO_2$ ($\delta\ ^{13}C_{CO2}$) from gas sampling in long borehole jpk 32 (+2°)/10 were changing in time of LW advancing from 1,0 to -9,7 ‰. Values $\delta\ ^{13}C_{CO2}$ between -10 to -5 ‰ are typical for coal gases with higher amount of $CO_2$ concentration and correlate with endogenic source of $CO_2$. Higher values of CDMI index (Carbon dioxide – Methane Index) and positive values of isotopic composition of $\delta\ ^{13}C_{CO2}$ show mixed origin of carbon dioxide between biogenic ($CO_2$ reduction) and endogenic $CO_2$.

Initial values of methane isotope $\delta\ ^{13}C_{CH4}$ were varying around -60 ‰ which indicated origin of methane in coal seam as reduction of $CO_2$. At the distance from the LW face around 300 m we observed the change in the methane isotope composition in coal gas samples. Values of methane isotope $\delta\ ^{13}C_{CH4}$ became lower from -45 to -31 ‰ that alternative type of methane – microbic methane, migrated through the coal seam. As discussed before, stress influenced permeability changes were seen in seam gas pressure changes and also in gas migrations in coal seam.

Alternative values remained the same until methane escape through the rock stress caused cleat/ porous system. After structure deformation, original gas state with low values of isotopes δ $^{13}C_{CH4}$ was observed [3].

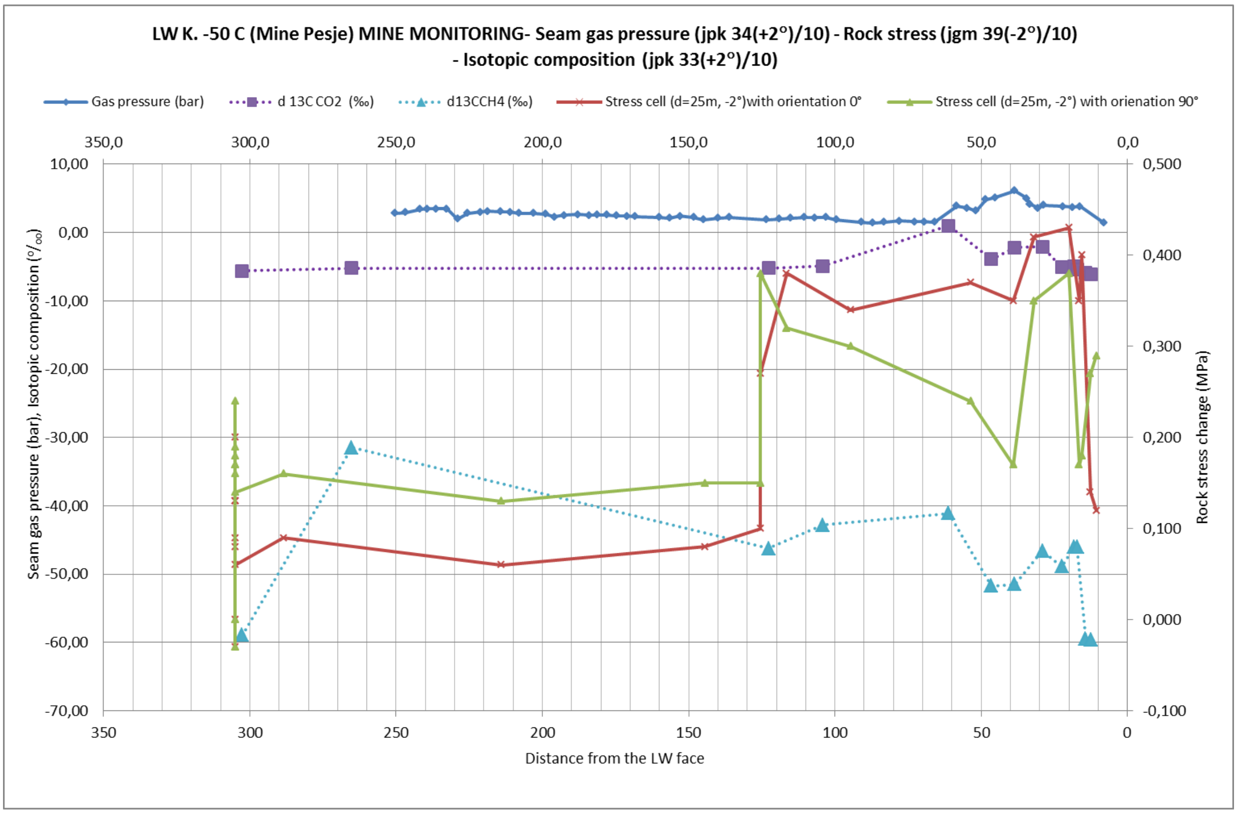

**Figure 7:** Relation between seam gas pressure and rock stress state change in dependence of distance to long-wall face. Rapid increase of stress at distances 305 m and 125 m represent stress cell settings with additional fluid injection.

## 4 Conclusions and future work

Investigation in field of desorption and gas content determination included review of knowledge, experiments and methodology on field in world's scale, experiments, performed on samples from Coal Mine Velenje and methodology and equipment design that match Velenje lignite properties.

Desorption experiments included repetitions of experiments from previous campaigns, followed by modifications in sample treatment (crushing) and lost gas content determinations.

Mine monitoring was divided into seam gas pressure measurements and rock stress measurements for which dedicated measurement methodology and monitoring objects were developed. Results of both were combined after data interpretations showed possible correlations that were assumed even before seam gas pressure monitoring was established.

In addition, seam gas pressure and rock stress measurements interpretations were accompanied with seam gas and isotopic composition results that describe migration principles of coal seam gases.

## References:

[1]J. Likar. Analiza mehanizmov nenadnih izbruhov premoga in plina v premogovnikih, 1995. Univerza v Ljubljani, Fakulteta za naravoslovje in tehnologijo, Oddelek za montanistiko. *Ph.D. Dissertation.*

[2]T. Kanduč. Izotopske značilnosti premogovega plina v velenjskem bazenu, (2004). University of Ljubljana, Faculty of natural sciences and engineering department of geology. *M. Sc. Dissertation.*

[3]S. Jamnikar, J. Lazar, R. Lah, J. Žula, E. Burič, S. Zavšek. Poročila o spremljanju tehnoloških, plinskih in geotehničnih parametrov na odkopih G2/B, K. -50 A, K. -120 B, K. -50 B, G 2/C, K.-50 C. 2008 – 2012. Premogovnik Velenje. *Report.*

[4]W.P. Diamond, S. Schatzel. Measuring the gas content of coal: A review., 1986. *International Journal of Coal Geology 35 (1998), 311-331.* Paper.

[5]J. Likar, M. Ulrich-Obal. Poročilo o kontrolnem testiranju desorbimetrov z mešali, 1997. IRGO, Ljubljana. *Report.*

[6]J. Likar, M. Ulrich, M. Zahornik. Laboratorijski desorbimeter, 1997. IRGO, Ljubljana. *Report.*

[7]J. Pezdič, M. Markič, M. Letič, A. Popovič, S. Zavšek. Laboratory simulation of desorption – desorption processes on different lignite lithotypes from Velenje lignite mine, 1999, *RMZ – Materials and Geoenviroment, Vol. 46, No. 3, 555-568, Paper.*

[8]A. Zapušek, D. Dimec, M. Videmšek, E. Burič, J. Jezeršek. Vrtina 933 T/96: Rezultati meritev desorbiranih plinov, 1997. ERICo, Velenje. *Report.*

[9]A. Zapušek, V. Landekar, E. Burič. Vrtini 759 T/98 in 770-K/98: Rezultati meritev desorbiranih plinov, 1999. ERICo, Velenje. *Report.*

[10]S. Jamnikar. Desorption properties of Velenje lignite and measurement methodology development, 2011. 4th Balkan Mining Congress, *Paper's book*, 165 – 172. Paper.

[11]M. Markič. Petrology and genesis of the Velenje lignite, (2009). University of Ljubljana, Faculty of natural sciences and engineering department of geology. *Ph.D. Dissertation.*

[12]S. Durucan, and J.S. Edwards. The Effects of Stress and Fracturing on Permeability of Coal, 1986. *Mining Science and Technology, 3, 205-216.* Paper.

[13]R. Konečny, jr., A. Kožušnikova, P. Martinec. Rock mass as a porous medium: Gas filtration ability in triaxial state of stress. Institute of Geonics ASCR, Ostrava, Czech Republic. *Proceedings of the International Congress on Rock Mechanics, Paris, 1999.* Paper.

[14]T. Kanduč. Izotopske značilnosti premogovega plina v velenjskem bazenu, (2004). University of Ljubljana, Faculty of natural sciences and engineering department of geology. *M. Sc. Dissertation.*

[15]T. Kanduč, J. Pezdič. Origin and distribution of coalbed gases from the Velenje basin, Slovenia, 2005. Geochemical Journal, Vol.39.

[16]T. Kanduč, J. Pezdič, S. Lojen, S. Zavšek. Study of the gas composition ahead of the working face in a lignite seam from the Velenje basin. *RMZ – Materials and Geoenviroment.* Paper.

## For wider interest

Underground coal mining still represents hazardous operations and dealing with natural forces amongst which coal and rock-bursts represent possible threats for miner's safety.

Research into hazardous events prevention precautions consists from coal gas content determination experiments and mine monitoring campaigns of gas behaviour analysis and coal excavation influence on surrounding coal masses.

Mine monitoring included seam gas pressure and rock stress measurements, accompanied by gas sampling for composition and isotopic analysis. Observations showed definite correlations between listed parameters when measured results were combined into combined analysis.

Research work is targeting final result - understanding coal seam properties concerning gas behaviour and rock stress distribution influence that answers challenge of underground gas drainage of coal seam.

# Jedkanje PET filmov v poznem porazelektritvenem delu kisikove plazme

**Metod Kolar**[1,2,3], **Darij Kreuh**[1], **Alenka Vesel**[2,3], **Miran Mozetič**[2,3], **Karin Stana - Kleinschek**[4]

[1] Ekliptik d.o.o., Teslova ulica 30, 1000 Ljubljana

[2] Odsek za tehnologijo površin in optoelektroniko, Institut "Jožef Stefan", Jamova 39, 1000 Ljubljana,

[3] Mednarodna podiplomska šola Jožefa Stefana, Jamova 39, 1000 Ljubljana

[4] Fakulteta za strojništvo, Univerza v Mariboru, Smetanova ul. 17, 2000 Maribor

metod.kolar@ijs.si

**Povzetek.** Praktična uporaba polimernih materialov v medicini je še vedno omejena s specifičnimi lastnostmi teh materialov. Pri uporabi polietilen tereftalata (PET) za umetne žile in katetre se soočamo s problemom vezave bioloških substanc na površino polimernih materialov. Po naši hipotezi lahko ta problem bistveno zmanjšamo z uporabo reaktivnih plazemskih delcev. Delci reagirajo s površino polimera tako, da odstranijo sledove organskih nečistoč, obenem pa zmanjšajo vezavo proteinov. Za razvoj ustreznega industrijskega postopka pa ključno težavo predstavlja jedkanje materiala. Da bi natančno določili vpliv nevtralnih kisikovih atomov na jedkanje PET-a smo opravili raziskave, ki so opisane v tem prispevku. Z zelo natančno metodo kremenove mikrotehtnice z enoto merjenja dušenja nihanja (QCM-D) smo izmerili hitrost jedkanja PET materiala v porazelektritvenem delu kisikove plazme in ugotovili, da je le ta odvisna od vzbujevalne moči in postane pri večjih močeh konstantna z vrednostjo okoli 1 nm/min. Rezultati kažejo, da je tovrstna obdelava uporabna v medicinski praksi, saj je hitrost jedkanja bistveno manjša za polimer kot za organske nečistoče.

**Ključne besede**: jedkanje, organski materiali, plazma, PET.

## 1 Uvod

Plazma je stanje plina, v katerem je znatni del molekul disociiran in ioniziran. Prehod plina v stanje plazme lahko dosežemo na dva načina in sicer tako, da plin segrejemo do tako visoke temperature, da znatni del atomov razpade na pozitivne ione in elektrone, ali pa tako, da plin namestimo v močno električno polje, kjer se prosti elektroni, ki so v vsakem primeru v plinu v majhnih gostotah, pospešijo in ob neprožnih trkih z atomi ali molekulami le-te ionizirajo.

Obdelava materialov z nizko-temperaturno plazmo velja za eno najbolj vsestranskih tehnik za pridobivanje edinstvenih lastnosti površin materialov, še posebej polimernih. Zadnje čase poteka vse več raziskav obdelave organskih materialov z neravnovesnimi nizko-temperaturnimi plinskimi plazmami, predvsem zaradi možne uporabe v biomedicini. Znano je, da se pri obdelavi s kisikovo plazmo na površini ustvarijo polarne funkcionalne skupine, površina materiala se jedka, posledično se zato poveča hrapavost površine [1-5]. Čeprav je jedkanje s plazmo znano že desetletja, natančen mehanizem tega pojava še ni znan. Bistven razlog je v dejstvu, da v plazmi vselej nastajajo različne vrste reaktivnih delcev, kot so molekularni in atomarni ioni, nevtralni atomi v osnovnem in vzbujenih stanjih, ter nevtralne molekule v metastabilnih vzbujenih stanjih. Plazemska obdelava polimerov je pogosto preveč agresivna, saj je zelo težko zagotoviti obdelavo pri sobni temperaturi. Da bi rešili ta tehnološki problem, smo postavili hipotezo, po kateri za dosego primernih učinkov kisikove plazme sploh ne potrebujemo, ampak potrebujemo zgolj eno vrsto reaktivnih delcev, to so nevtralni kisikovi atomi v osnovnem stanju. Predhodne raziskave v naši raziskovalni skupini so pokazale, da lahko zagotovimo obdelavo materialov z nevtralnimi atomi tako, da obdelovanec namestimo v pozni porazelektritveni del kisikove plazme [6, 7]. V porazelektritvenem delu namreč električno nabiti delci in visoko vzbujeni atomi niso prisotni, saj se na poti od plazme do porazelektritvenega dela nevtralizirajo oz. deekscitirajo. Po naši hipotezi je interakcija atomov s površino obdelovanca dovolj intenzivna, da odstranimo organske nečistoče in funkcionaliziramo površino polimera, obenem pa dovolj šibka, da prepreči intenzivno jedkanje.

# 2 Metode in materiali

## 2.1 Priprava vzorcev

Modelne filme PET smo nanašali na kremenove substrate s tehniko vrtenja (spin-coating). Folijo amorfnega polietilen tereftalata (Goodfellow, Cambridge, Velika

Britanija) visoke čistosti smo raztopili v 1,1,2,2-tetrakloretanu (Sigma-Aldrich, St. Louis, ZDA) pri temperaturi okoli 150 °C. Ko se je raztopina ohladila na sobno temperaturo, smo jo filtrirali skozi 0,2 µm Acrodisc GHP filter (Pall Life Sciences, Portsmouth, Velika Britanija). Na kremenove kristale (QSense AB, Göteborg, Švedska) s premerom 14 mm smo nanesli 30 µl raztopine in jih vrteli 1 minuto z 2.000 vrtljaji na minuto. Kristali so bili po sušenju v pečici (105 ° C, 30 min) pripravljeni za nadaljnjo uporabo.

## 2.2 Obdelava v porazelektritvenem delu

Modelne filme PET-a smo obdelali v porazelektritveni komori prikazani na Sliki 1. Eksperimentalna komora je steklena cev dolžine 80 cm in premera 4 cm. Povezana je z ozko stekleno cevjo, na katero smo priključili generator mikrovalov, ki deluje na standardni frekvenci 2,45 GHz z nastavljivo močjo do 300 W.

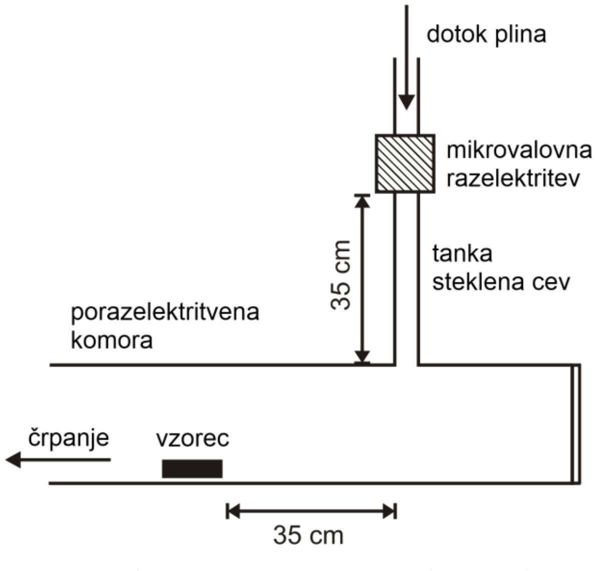

**Slika 1**: Shema eksperimentalnega vakuumskega sistema.

Tlak kisika v sistemu smo ohranjali pri 50 Pa s pomočjo vakuumske črpalke. Gostoto atomov kisika na mestu, kamor smo namestili vzorce, smo izmerili s katalitično sondo.

## 2.3 QCM meritve

Debelino polimernega filma v odvisnosti od časa plazemske obdelave smo določili s pomočjo kremenove mikrotehtnice z enoto merjenja dušenja nihanja, QCM-D (Model E4, QSense AB, Göteborg, Švedska). S QCM-D napravo merimo maso tankega filma odloženega na kremenov kristal, ki je stisnjen med dvema elektrodama. Elektrodi sta priključeni na vir napetosti, tako da kremenov kristal niha z osnovno resonančno frekvenco in njenimi nadtoni (večkratniki osnovne resonančne frekvence). Frekvenca kristala se manjša z naraščajočo maso kristala oz. na kristal odloženim polimerom. Debelina odloženega filma se izračuna iz spremembe frekvence, pri čemer upoštevamo gostoto odloženega filma na osnovi literaturnih podatkov (1300 kg/m$^3$) [8].

## 3 Rezultati

Hitrost jedkanja smo določili tako, da smo najprej izmerili debelino prvotno nanesenega filma. Kristal smo izpostavili delovanju kisikovih atomov in ponovno izmerili debelino filma. Postopek smo ponavljali toliko časa, da je postala debelina filma nemerljivo tanka. Značilen rezultat je prikazan na Sliki 2. Opazimo, da je debelina linearno odvisna od časa obdelave. Iz nagiba premice na Sliki 2 lahko izračunamo hitrost jedkanja. Za izbran primer je le ta 0,9 nm/min.

Eksperiment smo ponovili pri več izbranih močeh. Na Sliki 3 je prikazana odvisnost hitrosti jedkanja od moči mikrovalovnega generatorja. Opazimo lahko, da hitrost jedkanja sprva narašča, pri moči okoli 150 W pa se ustali pri konstantni vrednosti okoli 1 nm/min. Opažen pojav razložimo z nasičenjem stopnje disociiranosti kisikovih molekul znotraj mikrovalovne votline.

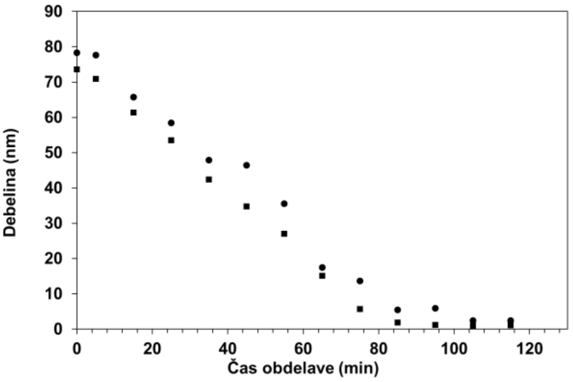

**Slika 2**: Debelina PET filma v odvisnosti od časa obdelave pri moči 150 W.

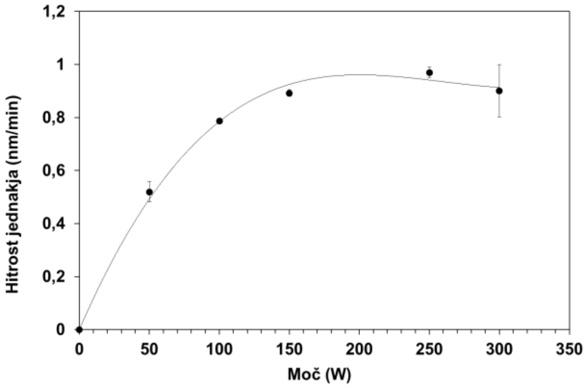

**Slika 3**: Hitrost jedkanja v odvisnosti od moči.

# 4 Zaključek

Rezultati naših meritev kažejo, da je izbrani polimerni material dobro odporen na jedkanje z nevtralnimi kisikovimi atomi. Za razliko od obdelave v plazmi, kjer smo opazili izredno agresivno jedkanje [9-11], je hitrost jedkanja v porazelektritvenem delu za dva velikostna reda manjša. Ker je hitrost jedkanja organskih nečistoč [12], ki se značilno nahajajo na površini katetrov, bistveno večja, lahko sklepamo, da je metoda obdelave v porazelektritvenem delu primerna za čiščenje katetrov po uporabi v medicinski praksi. Z atomi kisika lahko torej odstranimo nečistoče, ne da bi bistveno spremenili prvotne lastnosti katetra.

Operacijo delno financira Evropska unija, in sicer iz Evropskega socialnega sklada.

## Literatura:

[1] A. Vesel, K. Elersič, I. Junkar, in B. Malič. Modification of a polyethylene naphthalate polymer using an oxygen plasma treatment. Mater. Tehnol., 43(6): 323-326, 2009.

[2] C. M. Chan, T. M. Ko, H. Hiraoka. Polymer surface modification by plasmas and photons. Surface Science Reports, 24(1-2): 1-54, 1996.

[3] A. Vesel, M. Mozetic, A. Hladnik, J. Dolenc, J. Zule, S. Milosevic, N. Krstulovic, M. Klanjšek-Gunde, N. Hauptmann. Modification of ink-jet paper by oxygen-plasma treatment. Journal of Physics D: Applied Physics, 40(12): 3689-3696, 2007.

[4] V. Hody, T. Belmonte, T. Czerwiec, G. Henrion, J. M. Thiebaut. Oxygen grafting and etching of hexatriacontane in late $N_2$–$O_2$ post-discharges. Thin Solid Films, 506-507: 212-216, 2006.

[5] T. Belmonte, C. D. Pintassilgo, T. Czerwiec, G. Henrion, V. Hody, J. M. Thiebaut, J. Loureiro. Oxygen plasma surface interaction in treatments of polyolefines. Surf. Coat. Technol., 200(1-4): 26-30, 2005.

[6] G. Primc, R. Zaplotnik, A. Vesel, M. Mozetic. Microwave discharge as a remote source of neutral oxygen atoms. AIP Advances, 1(2): 022129, 2011.

[7] M. Mozetič. Surface modification of materials using an extremely non-equilibrium oxygen plasma. Mater. Tehnol., 44(4): 165-171, 2010.

[8] Polyethylene terephthalate - online catalogue source - supplier of research materials in small quantities - Goodfellow, http://www.goodfellow.com/E/Polyethylene-terephthalate.html, 2012.

[9] A. Doliška, A. Vesel, M. Kolar, K. Stana-Kleinschek, M. Mozetič. Interaction between model poly(ethylene terephthalate) thin films and weakly ionised oxygen plasma. Surf. Int. Anal., 44(1): 56-61, 2012.

[10] I. Junkar, A. Vesel, U. Cvelbar, M. Mozetic, S. Strnad. Influence of oxygen and nitrogen plasma treatment on polyethylene terephthalate (PET) polymers. Vacuum, 84(1): 83-85, 2009.

[11] I. Junkar, U. Cvelbar, A. Vesel, N. Hauptman, M. Mozetič. The Role of Crystallinity on Polymer Interaction with Oxygen Plasma. Plasma Processes Polym., 6(10): 667-675, 2009.

[12] U. Cvelbar, M. Mozetič, N. Hauptman, M. Klanjšek-Gunde. Degradation of Staphylococcus aureus bacteria by neutral oxygen atoms. J. Appl. Phys., 106(10): 103303, 2009.

## Za širši interes

Na odseku za tehnologijo površin in optoelektroniko Instituta "Jožef Stefan" raziskovalci razvijajo metode za modifikacijo površin različnih materialov s termodinamsko zelo neravnovesno plinsko plazmo. Industrijski partnerji potrebujejo tovrstne tehnologije za izboljšanje kakovosti svojih izdelkov in nadomeščanje okolju neprijaznih tehnoloških postopkov. Za različne partnerje so razvili tehnološke postopke plazemskega čiščenja, selektivnega plazemskega jedkanja, površinske funkcionalizacije in hladnega upepeljevanja. V zadnjem času se predvsem ukvarjajo z modifikacijo površinskih lastnosti polimernih materialov, ki se uporabljajo v medicini. Originalne tehnološke postopke zaščitijo z mednarodnimi patenti, znanstvena odkritja pa objavljajo v vrhunskih specializiranih revijah.

Moja vloga v raziskovalni skupini, ki je izrazito interdisciplinarna, je razvoj postopkov za modifikacijo površine umetnih žil, s ciljem izboljšanja biokompatibilnosti. Umetne žile, ki se trenutno uporabljajo, imajo sicer odlične kemijske in mehanske lastnosti, žal pa prepogosto povzročajo različne po-operativne zaplete, kamor v prvi vrsti sodi tromboza. Preliminarne raziskave so pokazale, da je mogoče s primerno funkcionalizacijo notranje površine umetnih žil bistveno zmanjšati aktivacijo trombocitov in s tem nastajanje krvnih strdkov. Da bi inovativni tehnološki postopek uporabili v medicinski praksi, je potrebno opraviti obsežne temeljne raziskave, ki bi omogočile vpogled v izredno zahteven pojav kopičenja krvnih proteinov. V okviru svojega doktorskega izobraževanja je moja naloga natančno določiti vpliv različnih reaktivnih kisikovih delcev na funkcionalizacijo polimernih materialov za umetne žile, določiti intenzivnost interakcije izbranih reaktivnih delcev s krvnimi proteini in določiti morebitne poškodbe umetnih žil, ki so posledica interakcije obdelovancev z reaktivnimi delci.

Končni cilj mojih raziskav je optimizacija površinske modifikacije umetnih žil, ki bi omogočila minimalno depozicijo krvnih proteinov ob hkratni izboljšani biokompatibilnosti za pravilno vezavo endotelija na umetne žile.

# Entirely renewable and self-sufficient municipal energy system

**Anja Kostevšek**[1,2], **Leon Cizelj**[3], **Janez Petek**[4], **Boris Sučić**[5], **Matevž Pušnik**[5], **Aleksandra Pivec**[1]

[1] Scientific Research Centre Bistra Ptuj, Ptuj, Slovenia

[2] Jožef Stefan International Postgraduate School, Ljubljana, Slovenia

[3] Reactor Engineering Division, Jožef Stefan Institute, Ljubljana, Slovenia

[4] Local Energy Agency Spodnje Podravje, Ptuj, Slovenia

[5] Energy Efficiency Centre, Jožef Stefan Institute, Ljubljana, Slovenia

anja.kostevsek@gmail.com

**Abstract.** Municipal energy system is recognized as the one of the major development engines in greening the energy system. Integration of renewable resources into the energy system is the most appropriate choice in an attempt to decrease negative impacts on the environment. Various energy policies define targets with inclusion of different shares of renewable resources in specific time horizons. However, energy systems on 100% renewable supply still represent a challenge. The main objective of this paper is to demonstrate feasibility of the proposed renewable and self-sufficient municipal energy system. Energy model is used for setting the reference energy system and calculation of the scenarios. Performance of biomass, solar and renewable mix scenarios were conducted for this research. The paper discusses only technical aspects of the 100% renewable energy system.

**Keywords**: municipal energy system, renewable energy sources, renewable and self-sufficient energy systems

## 1 Introduction

Decarbonisation of energy systems represents a major issue in today's society. A variety of possible pathways is being proposed. With energy policies on European level additional targets were proposed, such as a 20% share of energy from renewable sources in the gross final energy consumption by 2020, and a 10% share of renewable energy specifically in the transport sector [1]. On the other hand, some proposals are drafted to reach an 80% share from renewable energy sources (RES) by 2050. In the frame of the European Union energy climate package Slovenia set ambitious target by 2020 to achieve 25% renewable energy in the gross final energy consumption. According to the new National Renewable Energy Action Plan Slovenia[1] would play an active role in the development and promotion of the new technologies and solutions, which would enable wider usage of the renewable energy sources in industry, public, residential and transport sectors [2].

In order to accomplish future energy objectives on European and national level, additional work on local level has to be performed. The draft of Slovenian Energy Program[2] encourages the use of 100% renewable energy systems in five municipalities by 2020 and twenty municipalities by 2030. The importance of creation of a 100% renewable municipal energy system (MES) has also been recognized elsewhere [3]. This paper presents performance of energy scenarios to provide suitable structure of a 100% renewable and self-sufficient MES. The main focus is to demonstrate the technical eligibility of the 100% renewable MES.

## 2 Methodology

### 2.1 Model development

The following step presents the selection of adequate energy planning tool for generating future scenarios of MES. Several modeling tools are available for local energy planning. In the Slovenian case, the decision was made on various assumptions and experiences from the constitution of previous energy models. MESAP (Modular Energy-System Analysis and Planning Environment) toolbox was brought up because it covers all the relevant tools for building an appropriate model for municipalities. The Reference Energy Environmental Model for Municipalities (REES-MOL), which was created for the city of Ljubljana, the capital of Slovenia, was transformed and adapted to calculate scenarios for renewable energy system of Podlehnik municipality. The REES-MOL is energy

---

[1] National Renewable Energy Action Plan Slovenia – National renewable energy action plan 2010-2020 (NREAP) Slovenia, Ljubljana, July 2010.

[2] Slovenian Energy Program – Proposal of the National Energy Programme of the Republic of Slovenia for the 2010-2030 Period, draft, Ljubljana, June 2010.

system model which enables the analysis of energy policies on both the end-use and supply side. Model provides calculations of optimal combination of the local energy efficiency measures in all energy sectors and use of renewable sources for heat supply, distributed electricity generation, and wider usage of the combined heat and power production units [4].

### 2.2 Scenario performance

Calculations of numerous energy scenarios provide support to decision makers. By defining trade-offs among versatile parameters, an optimal solution must be identified based on an in-depth scenario analysis. A decision was made for processing three scenarios, based on two most important perspectives: the MES must implement the 100% renewable principle and the 100% self-sufficiency principle. At first, a reference energy scenario for year 2008 was performed. Through further research work the calculations of following scenarios were considered: biomass scenario (BIO), solar scenario (SOL) and RES mix scenario (MIX). Specific assumptions for each scenario are presented in Table 1.

Table 1: Main assumptions of different scenarios

| Various assumptions | BIO | SOL | MIX |
|---|---|---|---|
| Individual heating: | | | |
| heat pumps | 10% | 10% | 15% |
| solar thermal | 5% | 10% | 5% |
| biomass boilers | 45% | 40% | 40% |
| district heating | biomass (40%) | biomass (40%) | biomass (40%) |
| Industry: | biomass | biomass | biomass |
| Electricity production mix | 60% solar, 20% biomass, 20% biogas | 80% solar, 10% biomass, 10% biogas | 70% solar, 15% biomass, 15% biogas |

## 3 Practical applications in the Podlehnik municipality

Different supply mixes of renewable sources are provided at the basis of feasibility studies of every local renewable resource. Natural, economic, technological, social and political barriers put decision makers of future energy systems in a difficult position. Potentials for RES deployment in the Podlehnik municipality were defined from previous analysis and are shown in Table 2.

Table 2: RES potentials for Podlehnik municipality

| Types of RES | Potential for future RES deployment |
|---|---|
| Biomass | 18.230 MWh/a |
| Biogas from crops | 7.737 MWh/a |
| Biogas from manure | 2.378 MWh/a |
| Solar | 38.850 MWh/a |
| Geothermal | 5.392 MWh/a |
| Total potential | 72.587 MWh/a |

Data for the present state and share of renewable resources are presented in Table 3 for year 2008.

Table 3: Energy consumption for the Podlehnik municipality in 2008

| Heat [MWh] | | Electricity [MWh] | | Total energy consumption [MWh] | RES share [%] |
|---|---|---|---|---|---|
| Conventional energy sources | RES | Conventional energy sources | RES | | |
| 4.145 | 5.378 | 3.224 | 1.746 | 14.493 | 49,15 |

After the scenario calculations the results for the final energy consumption in year 2050 were provided and are shown in Table 4.

Table 4: Final energy consumption for the Podlehnik municipality in 2050

| Heat energy [MWh] | Electricity energy [MWh] | Total energy consumption [MWh] | RES share [%] |
|---|---|---|---|
| RES | RES | | |
| 5.647 | 5.949 | 11.596 | 100,0 |

Scenario simulations indicate higher electricity consumption and lower heat demand in 100% RES municipal energy system. Overall energy consumption in year 2050 will be decreased in comparison to year 2008 in accordance to various energy efficiency assumptions adopted in the model.

## 4 Discussion and conclusion

A modern MES with renewable supply mix differs in routes from present fossil based energy systems. Integration of 100% renewable and self-sufficient principles into MES presents the future goal of fighting climate change. The study confirmed technical feasibility of constituting a 100% renewable and self-sufficient MES. Assessment of scenarios should be performed on the basis of local conditions. On behalf of presented scenarios, decision makers may be able to depict the proper solution. For Podlehnik municipality the RES feasibility studies were included in the Local Energy Concept. Only general predictions from various previous analyses were presented. Further research would take place in defining more in-depth studies for specific RES potentials. This research considers only technical aspects of a 100% renewable MES. In the future perspective, also environmental, social and economic aspects need to be included. Penetration of new technologies and R&D activities in the field of renewable technologies will make an enormous impact on the outlook of the 2050 MES. To conclude with, transfer towards a 100% renewable MES would require a sequential adaptation process in different time horizons.

## Acknowledgements

The research work of the corresponding author is supported by the European Slovenian Technology Agency under tender Young researchers from industry. Operation is partly financed by the European Union (European Social Fund).

## References:

[1] The European Parliament and the Council of the European Union. Directive 2009/28/EC of the European Parliament and of the council of 23 April 2009 on the promotion of the use of energy from renewable sources, 2009.

[2] National Renewable Energy Action Plan 2010-2020. http://ec.europa.eu/energy/renewables/transparency_platform/doc/national_renewable_energy_action_plan_slovenia_en.pdf, 2010

[3] P. A. Østergaard, B. V. Mathiesen, B. Möller and H. Lund. A renewable energy scenario for Aalborg Municipality based on low-temperature geothermal heat, wind power and biomass. *Energy*, 35(12): 4892-4901, 2010

[4] Energy Efficiency Centre, Jozef Stefan Institute. *Sustainable urban infrastructure-Ljubljana-Prospectives by 2050*. IJS, 2011.

## For wider interest

Climate change mitigation activities support usage of renewable resources due to their neutral impact on the environment. Various legislative acts stress the important role of municipalities in accomplishing the energy targets. This is why focus on municipality energy system and its development present a promising future orientation. Forming energy system on entirely renewable resources presents the new pathway, where the whole energy supply could be based on local supply facilities. In practice, the results could be applied for other municipalities, smaller local community, a district or a group of buildings. In addition, for concretizing the system more technical studies should be revealed.

The case study was presented for Podlehnik municipal energy system. Analyses of three different scenarios leading to entirely renewable energy system with mixes of biomass, solar and electricity confirmed on the sufficiency of renewable resources. The results confirmed the technical feasibility to develop an independent renewable municipal energy system. Demonstration of possibilities to develop energy systems on a 100% renewable and 100% local supply represents added value. In the future several research activities should be focused in providing detailed analysis of integration of renewable resources into energy supply chain from technical, environmental, economic and social aspect.

# Selenium and its distribution in edible mussel *Mytilus galloprovincialis* collected from different locations

**Urška Kristan**[1,2], **Vekoslava Stibilj**[1]

[1] Department of Environmental Sciences, Jožef Stefan Institute, Jamova 39, SI-1000 Ljubljana

[2] Jožef Stefan International Postgraduate School, Ljubljana, Slovenia

`vekoslava.stibilj@ijs.si`

**Abstract.** Mussels *Mytilus galloprovincialis* collected and bought from different locations (Slovenian coastline, Italy and NE Pacific) were analysed by techniques of hydride generation atomic fluorescence spectrometry (HG-AFS) and liquid chromatography coupled to inductively coupled plasma mass spectrometry (HPLC-ICP-MS) in order to assess selenium (Se), its distribution and Se species in raw and cooked soft tissue. Total Se concentration in raw mussels ranged between 3.15 to 8.27 µg/g, while in cooked ones, Se concentration were half lower. Selenium species identified were selenomethione (SeMet) and selenocystine (SeCys$_2$).

**Keywords**: Selenium, mussel, ICP-MS, HG-AFS, speciation

## 1. Introduction

Selenium (Se) is an essential trace element with a very complex impact on human and animals. Furthermore, the line between essentiality and toxicity is very narrow; less than 0.1 µg Se/g can cause Se deficiency, while 0.5 µg Se/g toxicity. The principal source of trace elements for humans is diet. Some special nutrients, such as Se is known as antagonist to some toxic elements especially to Hg, protect organism against cancer. Furthermore, it has a very important role as part of the active site in selenoproteins such as glutathione peroxidase [1, 2]. The minimum selenium daily requirements for Slovenia have been summarized from the values accepted in Austria, Germany and Switzerland from the year of 2004. The Dietary Reference Intake (DRI) recommendations for Se intake were set between 30 to 70 µg/day for men and women. [3].

Speciation of Se is of particular interest since bioavailability of the element is important and mostly depends on its chemical form [4]. Selenium intake generally occurs via plant food and seafood, where most of Se has been associated with organic forms, such as selenomethionine (SeMet) and trimethylselenonium ion ($TMSe^+$) both found in mussel, while inorganic Se was not found in mussel tissue [5]. Mediterranean mussels *Mytilus galloprovincialis* lives attached on hard substrata, being filter feeders exposed to ambient seawater. The mussels are primarily used as food and also as indicators of environmental pollution, due to their ability to accumulate high levels of different contaminants (heavy metals, hydrocarbons and pesticides) [6]. The aim of this study was to determine total concentration of selenium and its species in marine mussel *Mytilus Galloprovincialis* from different locations (Slovenia, Italy and NE Pacific). Furthermore, we compared Se concentration in fresh and cooked mussel tissue in order to see the change in amount of bioavailable Se.

## 2. Materials and methods

### 2.1 Samples

Mussel samples used in this analysis were brought from Italy and also collected from Slovenian mussel breeder. Mussels were cleaned by removing soft tissue from shell, except for the mussels which were used in cooking procedure. These mussels were first cleaned under the tap water and furthermore cooked in white vine (we followed typical cooking procedure of mussel in Slovenia) in order to see the change between Se and its species in raw and cooked mussel. Another set of samples represented the mussels which were bought in the supermarket (fishing area FAO87, NE Pacific). These mussels were bought frozen and were previously removed from shell and cleaned by the producer, that means that the mussels were subjected to higher temperatures. Soft tissue of fresh and cooked mussel were dried in a freeze dryer at -46 °C for 172h to constant weight, homogenized firstly in agate mill and later on with the mill Pulverisete 7 (Fritsch) at a rotational speed of 18,000 rpm. Samples were stored in polyethylene containers at – 18 °C.

### 2.2 Procedures and methods

*Determination of total Se concentration by hydride generation atomic fluorescence spectrometry (HG-AFS):* Approximately 0.2 g of dry mussel sample was weighed in a Teflon® tube, in which mineralisation of the sample was performed using 0.5 ml of concentrated $H_2SO_4$ and 1.5 ml of concentrated $HNO_3$ by heating the tube on aluminium block for 24 h at 80 °C, then increasing the temperature to 130 °C and maintaining for 60 min. After cooling the solution to room temperature, 2 ml of 30 % $H_2O_2$ was added and the solution reheated for 10 min at 115 °C. This step was repeated. After cooling, addition of 0.150 ml $V_2O_5$ in $H_2SO_4$ followed and the solution was heated at 115 °C for approximately 20 min until the solution became blue in colour (in order to eliminate the surplus of $H_2O_2$). Reduction of $Se^{6+}$ to $Se^{4+}$ was made by addition of concentrated HCl to a final concentration around 6M, and heating for 10 min at 90 °C. Samples were then diluted with MiliQ water, depending on the foreseen Se concentration in the samples. HG-AFS was used for Se detection [7].

*Enzymatic extraction*: All samples of fresh and cooked soft mussel tissue were extracted in duplicate as described by Mazej et al. [8]. The supernatant was filtered successively through 0.45 and 0.22 μm filters and then subjected to selenium speciation analysis by liquid chromatography coupled to inductively coupled plasma mass spectrometry (HPLC-ICP-MS). Supernatants and sediments were stored at -20 °C until analysis for total Se in sediments and supernatants by HG-AFS was carried out.

*Sediments and supernatants:* Selenium in the sediments (residue) after enzymatic extraction was determined by the same procedure as that for total selenium determination described above. The Se content in supernatant was digested by $HNO_3$. 1 ml of concentrated $HNO_3$ was added to 0.5 of supernatant in a 50 ml Teflon tube and heated for 30 min at 80 °C and then for 15 min at 160 °C. After cooling, addition of 0.5 ml of $H_2O_2$ followed and the solution was evaporated at 120 °C to 0.5 g. This step was repeated twice. For reduction of $Se^{6+}$ to $Se^{4+}$ concentrated HCl was added. After dilution, selenium was determined by continuous HG-AFS.

*Separation and detection of Se species:* For selenium species determination in supernatants, an ion exchange HPLC system coupled directly to an ICP-MS set-up was used. For Se species separation, a Hamilton PRP-X 100 anion-exchange column and a Zorbax 300-SCX cation-exchange column were used. The flow rate was 0.5 ml/min, and the volume of the sample injected was 100 μl. The method and operating conditions are described in details elsewhere [9]. Selenium species in supernatants were confirmed by the standard addition method.

## 3. Results and discussion

Selenium concentrations determined in soft mussel tissue were variable between different locations from 3.15 to 8.27 µg/g dry matter (DM) (Table 1). The highest concentrations obtained were in mussels collected from Italy, where the amount of Se ranged between 7.7 and 8.8 µg/g, while in cooked mussel Se concentration was around half the amount; from 4.1 to 4.4 µg/g, so we could conclude that the rest of Se remained in liquid where mussels were cooked. Mussels bought from Slovenian breeders contained from 5.5 to 6.1 µg/g DM of Se, whilst in cooked ones Se ranged between 3.3 to 3.6 µg/g DM. The lowest concentration obtained was in mussels from NE Pacific, where average concentration was around 3.2 µg/g DM. The accuracy of Se determination was checked by analysing the certified reference material SRM 2976 and good agreement was found between the total value obtained of 1.74 ± 0.07 µg/g and certified of 1.80 ± 0.15 µg/g, while there is no data about Se species. After enzymatic extraction the proportion of soluble Se was similar in all samples, around 63, 67 and 76 % for mussel from NE Pacific, Slovenia and Italy, respectively. As is it seen in the table cooking indeed have the

Table 1: Se and its distribution in raw and cooked mussel from different locations

|  |  | Mussel tissue DM a |  |  |  |  |  |
|---|---|---|---|---|---|---|---|
| Sample (n) |  | Total Se µg g-1 | Soluble Se µg g-1 | Average solubility (%) | Selenium species identified |  |  |
|  |  |  |  |  | SeCys2 (µg Se/g) | SeMet (µg Se/g) | Se as $TMSe^+$ |
| Mussel from Slovenian breeders (4) | raw | 5.81 ± 0.33 | 4.32 ± 0.39 | 76.49 | 0.22 ± 0.03 (4.7) | 0.09 ± 0.01 (1.9) | 0.65 ± 0.08 (13.7) |
|  | cooked | 3.52 ± 0.21 | 2.70 ± 0.11 | 74.15 | 0.72 ± 0.09 (24.9) | 0.27 ± 0.02 (9.8) | 0.83 ± 0.04 (28.7) |
| Mussel from Italy (4) | raw | 8.27 ± 0.34 | 5.58 ± 0.57 | 67.37 | 0.36 ± 0.03 (7.1) | 0.33 ± 0.03 (6.5) | 0.86 ± 0.06 (16.6) |
|  | cooked | 4.24 ± 0.20 | 2.64 ± 0.16 | 66.75 | 0.35 ± 0.09 (13.1) | 0.37 ± 0.03 (14.1) | 0.48 ± 0.14 (17.8) |
| Mussel FAO87 (5) | raw | 3.15 ± 0.04 | 1.98 ± 0.15 | 62.77 | 0.45 ± 0.04 (22.8) | 0.30 ± 0.02 (14.9) | 0.47 ± 0.01 (23.4) |
| SRM 2976 (3) |  | 1.74 ± 0.07 | 1.04 ± 0.07 | 58.4 | 0.15 ± 0.03 (14.8) | 0.07 ± 0.01 (6.9) | 0.13 ± 0.01 (15.1) |

(n) Number of samples analysed

[a] Results are given as the average ± standard deviation on dry matter basis (DM)

[b] (% of identified soluble Se)

effect on Se concentration since the amount of Se was almost half lower in cooked mussels, nevertheless the percentage of Se solubility stayed the same. Liquid where mussels from Italia were cooked was also analysed; the amount of Se was around 3.6 µg /g DM. Although a lot of Se stayed in liquid where mussels are cooked, we need to take into account that by typical preparation of mussels liquid is also included in the meal. In order to determine whether losses of selenium occur during sample preparation (extraction and separation), a mass balance was drawn up between the total selenium in the sample and the amount of selenium in the supernatant and residue. The mass balance obtained for all mussel samples was around 100 %, showing that there was no loss of Se. After enzymatic extraction, chromatographic analysis of the supernatant was performed. Two selenium species were identified and confirmed, $SeCys_2$ and SeMet. In all chromatograms we obtained one peak, which could not be identified due to the lack of Se standards. We compared the peak with literature data, where authors identified $TMSe^+$, and found that the retention time on cationic column (with the same conditions as ours) are the same, so we can conclude that the unknown Se species could be $TMSe^+$ [10].

## References:

[1] M. Plessi, D. Bertelli, A. Monzani. Mercury and selenium content in selected seafood. *Journal of Food Composition and Analysis*, 14: 461-467, 2001

[2] M. Angeles Quijano, P. Moreno, A. M. Gutierrez, M. Concepcion Perez-Conde, C. Camara. Selenium speciation in animal tissues after enzymatic digestion by high-performance liquid chromatography coupled to inductively coupled plasma mass spectrometry. *Journal of Mass Spectrometry,* 35: 878-884, 2000

[3] German Nutrition Society (DGE), Austrian Nutrition Society (ÖGE), Swiss Society for Nutrition Research (SGE), Swiss Nutrition Association (SVE). *Reference Values for Nutrient Intake, 1st ed.* Druckerei V+V, Bonn, 2002.

[4] C. Thiry, A. Ruttens, L. De Temmerman, Y. J. Scheinder, L. Pussemier. Current knowledge in species-related bioavailability of selenium in food. *Food Chemistry*, 130: 767-784, 2012

[5] L. Hinojosa Reyes, J. L. Guzman Mar, G. M. Mizanur Rahman, B. Seybert, T. Fahrenholtz, H.M. Skip Kingston. Simultaneous determination of arsenic and selenium species in fish tissues using microwave-assisted enzymatic extraction and ion chromatography-inductively coupled plasma mass spectrometry. *Talanta*, 78: 983-990, 2009

[6] A. Osterc, T. Kanduč, Z. Šlejkovec, V. Stibilj, A. Ramšak. *Mytilus Galloprovincialis* as an indicator of environmental pollution along NE coast of Adriatic. In *Proceedings of the tenth international conference on the Mediterranean coastal environment, MEDCOAST 11,* Rhodes, Greece, 2011

[7] P. Smrkolj, V. Stibilj. Determination of selenium in vegetables by hydride generation atomic fluorescence spectrometry. *Analytica Chimica Acta,* 512: 11-17, 2004

[8] D. Mazej, I. Falnoga, M. Veber, V. Stibilj. Determination of selenium species in plant leaves by HPLC-UV-HG-AFS. *Talanta,* 68: 558-568, 2006

[9] P. Cuderman, I. Kreft, M. Germ, M. Kovačecič, V. Stibilj. Selenium species in selenium-enriched and drought exposed potatoes. *Jornal of Agricultural and Food Chemistry,* 56: 9114-9120, 2008

[10] P. Moreno, M. A. Quijano, A. M. Gutierrez, M. C. Perez-Conde, C. Camara. Fractionation studies of selenium compounds from oysters, and their determination by high-performance liquid chromatography coupled to inductively coupled plasma mass spectrometry. *Journal of Analytical Atomic Spectrometry,* 16: 1044-1050, 2001

## For wider interest

Selenium (Se) is a complex, essential trace element for animal and human. It has numerous important biological functions that depend on the activity of certain Se-containing proteins. It is essential for the body because it forms seleno-enzymes that carry out redox reactions such as glutathione peroxidase (GPx), thioredoxin reductase, and thyroid hormone deiodinase families. However, Se is also considered to be a toxic element at high concentrations. Function and bioavailability of this element are strongly correlated with its chemical form, so it is necessary to control the selenium intake to avoid deficiency diseases and toxicity problems. Therefore it is important to determine the selenium species in foods, especially in seafood, because of its known accumulation capacity. Our aim in this work was to investigate selenium and its species with different analytical techniques in edible mussel *Mytilus galloprovincialis* collected from different locations (Slovenian coastline, Italy, Udine and NE Pacific). Furthermore we wanted to see if cooking of mussel has any effect on selenium concentration and its distribution. In this experiment we followed typical cooking procedure which is mostly used in Slovenia. To determine total concentration of Se, hydride generation atomic fluorescence spectroscopy (HG-AFS) was used. Total Se concentrations in mussels differ between the locations where mussels were bred. The lowest concentrations obtained were in mussel that comes from NE Pacific, but here we need to take into account that mussels were already cleaned and removed from shell when we bought them from the supermarket, while the mussels from Slovenia and Italy were cleaned in our laboratory. Selenium speciation was performed by a liquid chromatography as separation system and coupled to mass spectrometer as detector system (HPLC-ICP-MS). Two selenium species were determined, while future work will involve further species identification.

# Research of innovative technologies for degasification of lignite seam

**Jerneja Lazar,** Simon Zavšek, Sergej Jamnikar, Janja Žula, Gregor Uranjek, Ludvik Golob

Premogovnik Velenje d.d., Partizanska 78, Velenje

jerneja.lazar@rlv.si

**Abstract.** Gas outbursts are great problem in coal mines, especially in coal mining of thick coal seams. In Velenje Coal mine up to 160 m thick coal seam presents a large volume reservoir of coal gas. An average gas mixture ratio in Velenje coal gas is approximately $CO_2$:$CH_4$ $\geq$ 2:1 from which high proportion of carbon dioxide is adsorbed on lignite structure, while methane is free in coal fractures. "In-situ" monitoring is provided in the mine with the support of laboratory analysis, such as desorption and adsorption laboratory tests, and coupled numerical modelling of gas migration under the influence of stress change is also performed. Individual research work is focused on coupled geomechanical modelling of coal pillar. Modelling is performed with two programs – Flac3D and TOUGH2. Different models in Flac3D were prepared. Further on, the focus will be on the modelling of gas pressure changes and gas migration around the borehole at the longwall Pesje K. -50/C.

**Keywords:** gas outbursts, thick coal seam, coal gas, Flac3D modelling, TOUGH2 modelling

## 1 Introduction

Gas outbursts present high risk by the coal mining of thick coal seam, where thick coal seam up to 160 m in Velenje Coal Mine presents a large volume reservoir for coal gas and production of coal causes changes in stress and pore pressure around the longwall coal face and coal gas can emit. When outburst occurs, the rock/coal/gas system changed from a stable to an unstable state with the release of a significant volume of gas over the duration of the outburst [1]. Outbursts with $CO_2$ are more violent, more difficult to control and more dangerous because of the greater sorption capacity of carbon dioxide [2]. At Velenje Coal Mine, coal seam has an average gas mixture ratio of approximately $CO_2:CH_4 \geq 2:1$ with high proportion of carbon dioxide which is adsorbed on lignite structure or it is captured in the coals matrix and methane, which is free in coal fractures.

Coal gas concentrations has been monitored in various boreholes that were drilled in coal pillars at different areas in coal mine. Also, coal gas pressure inside boreholes has been measured under the influence of the retreating longwall coal face. For determination of the detailed gas content, sorption (adsorption and desorption) tests were performed on coal samples coupled with numerical modelling of gas migration under the influence of stress change.

My individual research work mainly concerns the coupling geomechanical modelling of coal pillar, which is under dynamic stresses of longwall top coal caving. Modelling is performed with two programs – Flac3D and TOUGH2. Numerical modelling is widely used in coal mining for understanding the behaviour of coal under dynamic stresses. With coupling we will be able to understand how the coal gas is migrating under dynamic stresses and how the gas migration is influencing the gas outbursts. Flac3D is a three-dimensional explicit finite-difference program for engineering mechanics computation. With the TOUGH2 we will be able to model behaviour of the coal gas under different permeability changes. TOUGH2 is a general-purpose numerical simulator for multi-dimensional fluid and heat flows of multiphase, multicomponent fluid mixtures in porous and fractured media [3].

## 1.1 Coal geology

The Velenje coal seam is one of the thickest coal seams in the world and is located in N Slovenia near the town Velenje. The lignite seam is lens-shaped with thickness up to 165 m in the central part and the seam pinches out towards the margins and lies in the Velenje basin. Under the lignite seam lays coal-bearing strata, which consists of shales, clayey coal and lignite and is up to 50 m thick. The footwall lies on more than 250 m thick green sandy silts. Above the coal seam, a thin layer of marls with lacustrine molluscs was detected and after that thin layer is up to 350 m thick lacustrine strata consisting of clays, marls and silts. This strata is overlain with 90 m thick sandy-silty formation. The most upper part of the basin consists of terrestrial silts, overlain by recent fluvial sediments [4].

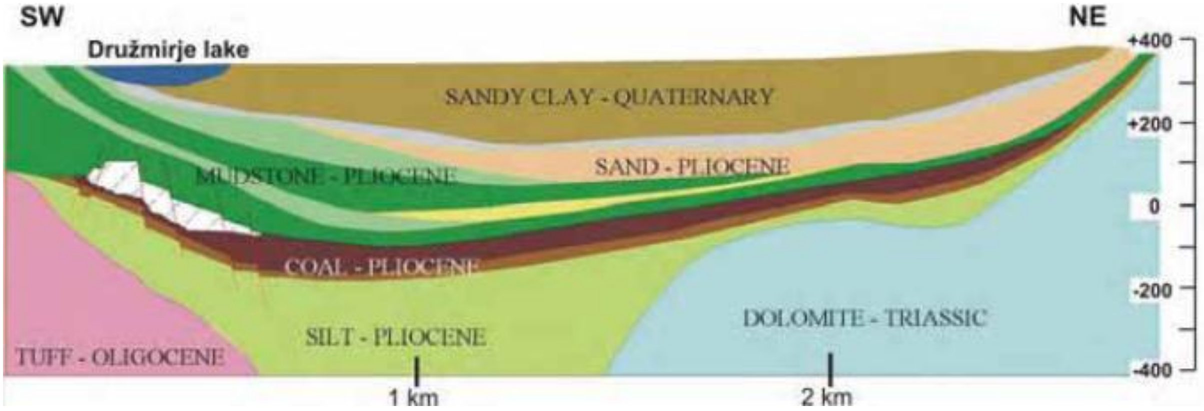

**Figure 1:** Shematic geological cross-section SW-NE (Veber and Dervarič, 2004)

## 2 Experimental

### 2.1 Coal gas origin and migration

Coal gas in Velenje lignite has three main gas components: $CO_2$, $CH_4$ and nitrogen. Table 1 represents concentrations of separate gas components in coal gas. The main causes of the changing concentrations are numerous origins of the coalbed gas and chemical processes, meanwhile the gas is being transported by diffusion, adsorption and desorption processes [5].

**Table 1:** Coal gas components and their concentration distribution

| Gas | Concentration (min, max) [vol. %] |
|---|---|
| $CO_2$ | 18 – 98.8 |
| $CH_4$ | 1.1 – 100 |
| $N_2$ | 7.2 – 67.3 |

Movement of gas through coal is widely believed to occur under two processes, starting with diffusion in which gas is desorbed from the coal matrix into the fracture network (Fick`s diffusion law), and movement within the fracture network according to pressure difference as described by Darcy`s law [6].

### 2.2 Coal permeability

The longwall top coal caving (LTCC) method with high productivity, which is found in Velenje Coal Mine, causes large stress releases which increases the rock mass permeability in surrounding coal. Increase in coal permeability could cause coal gas to migrate from the surrounding coal into roadways. To prevent gas outburst the task is to drain the coal gas from the coal panels before it is excavated.

Coal seam has in the first place natural fractures or cleats, which act as a major system for gas flow inside a coal seam. Advanced numerical model presents an opportunity to realistically simulate rock mass response to longwall operations, the associated gas liberation and flow through the fractured rock mass without resorting to field experimentation [7].

Durucan and Edwards in 1986 developed an exponential equation which can give the best fit to the stress – permeability correlation:

$$K = (1{,}12 - 0{,}03\sigma_3)K_i e^{-(1{,}12-0{,}03\sigma_3)C\sigma_3} \qquad (1)$$

Where, $K_i$ and C are constants, $\sigma_3$ is the radial stress applied and K is the permeability at stress $\sigma_3$. Constant C, which represent the compressibility of coal (i.e. the degree of reduction in permeability under stress), is the behaviour of the micro-structure of coal under stress and it can be determined individually for each seam. Constant $K_i$ defines the relative incidence of existing fissures and fractures in coal. [8]. Coal with higher value of $K_i$ would have higher permeability.

### 2.3 Numerical modelling of longwall face in Velenje coal mine

Numerical modelling is widely used in coal mining for understanding the behaviour of coal under dynamic stresses. When the stress results are known then with stress-permeability correlation by Durucan and Edwards the permeability can be defined which is used for data in the coupled geomechanical program TOUGH2. The objective for the model analysis in Flac3D is to gather stress changes around the pressure borehole for monitoring gas pressure changing in dependence of advanced longwall face. First, the geometry of the model was defined. The geometry of the longwall face Pesje K.-50/C was chosen due to the fact that the pressure measurements were successful at this longwall face and due to its half of the planned excavate coal pillar lying under fresh hanging wall and the second half lying under pre-mined longwall faces. Longwall face Pesje K. -50/C was 150 m wide and 684 m long. The mining method is divided into coal face slicing in height of 4 m and top coal caving in average height of 11 m.

The model was simplified and Mohr-Coulomb constitutive model was chosen. The Mohr-Coulomb model is the conventional model used to represent shear failure in soils and rocks [9]. The Mohr-Coulomb criterion is represented with the principal stresses $\sigma_1$, $\sigma_2$, $\sigma_3$. In Table 2 rock properties which were used for the modelling and which correspond to the geology of the Velenje basin where coal seam lies are represented.

**Table 2:** Rock properties of the modelled material

| Rock type | Density [kg/m$^3$] | Bulk module [Pa] | Shear module [Pa] | Cohesion [Pa] | Angle of friction [°] | Tension [Pa] |
|---|---|---|---|---|---|---|
| Overburden | 2260 | 5.2*10$^8$ | 2.17*10$^8$ | 2*10$^6$ | 35 | 0.23*10$^8$ |
| Hanging wall | 1870 | 4.8*10$^8$ | 2*10$^8$ | 7*10$^5$ | 30 | 0.08*10$^8$ |
| Coal | 1260 | 4.51*10$^8$ | 1.68*10$^8$ | 1.5*10$^6$ | 30 | 0.92*10$^8$ |
| Floor strata | 1870 | 4.7*10$^8$ | 2*10$^8$ | 7*10$^5$ | 30 | 0.44*10$^8$ |

## 2.4 Results of the modelling

After 17827 steps equilibrium was reached and the distribution of maximal principal stresses vary from 7.75 MPa at the bottom of the model and to 1 MPa from the surface down (Figure 2).

In the second step excavated area of the longwall face K. -50/C was modeled. To represent an excavation, a null model is used. The stresses within a null model zone are automatically set to zero [9]:

$$\sigma_{ij}^{N} = 0 \quad (2)$$

After 1000 steps, maximal principal stresses around the coal face were 10.4 MPa (blue colour in the grid).

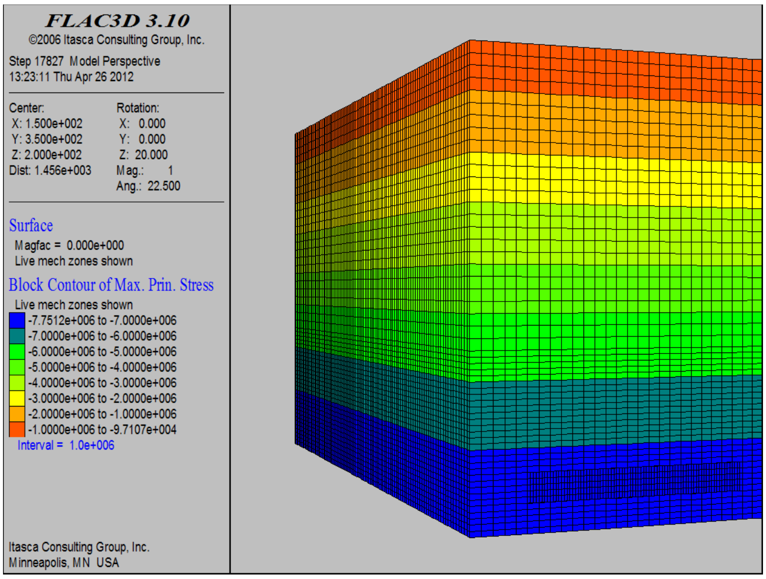

**Figure 2:** Maximal principal stresses (Pa)

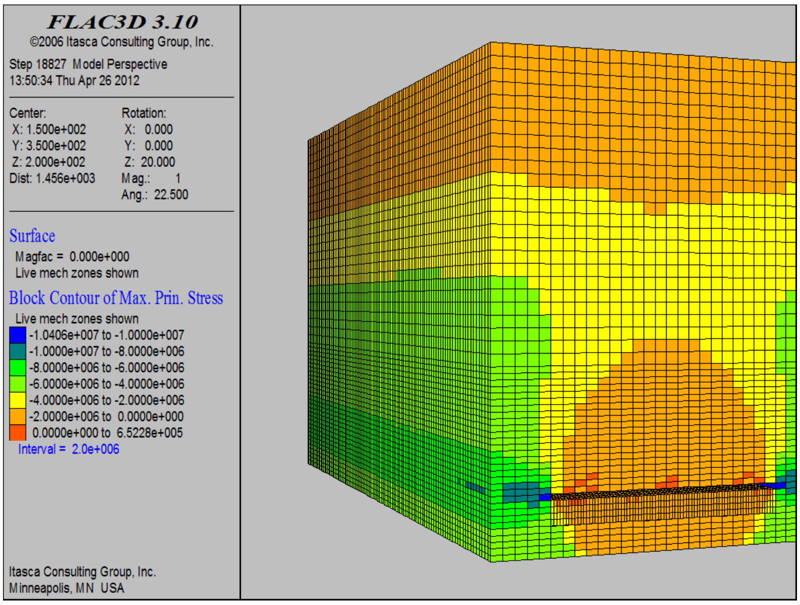

**Figure 3:** Maximal principal stresses after the excavation (Pa)

## 3 Conclusions

The future work will be focused on the modelling with Hoek-Brown constitutive model. More complex models will be defined. Material properties will be converted into rock mass data using empirical relationships widely used in geomechanics. Modelling of the caved area is another important step that affects the accuracy of obtained results [10]. Therefore, this step needs to be taken into detail. Analysis of the consolidation tests in the goaf will be studied.

Also, the dynamic model will be used at the location of the gas pressure borehole JPK 34/10 where we successfully monitored the coal seam pressure under the influence of the longwall dynamic.

Geomechanical modelling with TOUGH2 will be performed. For the input data it is needed to characterize fluid hydrogeological parameters and relations of the permeable media with permeability, porosity and capillary pressure, thermo-physical properties of the fluids, initial and boundary conditions of the system with sink and sources.

# 4 References

[1] Choi, X. and Wold, M., Study of the Mechanism of Coal and Gas Outbursts Using a New Numerical Modeling Approach ,2004. *Underground Coal Operators´ Conference.* Paper 142.

[2] Lama, R. and Saghafi, A., Overview of Gas Outbursts and Unusual Emissions, 2002. *Underground Coal Operators´ Conference.* Paper 196.

[3] Prues, K., Oldenburg, C. and Moridis, G., TOUGH2 User`s Guide, Version 2.0, 1999. *Ernest Orlando Lawrence Berkeley National Laboratory.*

[4] Kanduc, T., Pezdic, J., Origin and distribution of coalbed gases from the Velenje basin, Slovenia, 2005. *Geochemical Journal, Vol.39.*

[5] Pezdič, J., Markič, M., Letič, M., Popovič, A., Zavšek, S., Laboratory simulation of desorption – desorption processes on different lignite lithotypes from Velenje lignite mine,1999, *RMZ – Materials and Geoenviroment, Vol. 46, No. 3, 555-568, Paper.*

[6] Williams, R.J. and Weissman, J.J., Gas emission and outburst assessment in mixed $CO_2$ and $CH_4$ environments, 1995. *ACIRL Undeground Mining Seminar Brisbane,* Paper.

[7] Esterhuinzen, G.S., Karacan, C.O., Development of Numerical Models to Investigate Permeability Changes and Gas Emissions around Longwall Mining Panel, paper.

[8] Durucan, S. and Edwards, J.S., The Effects of Stress and Fracturing on Permeability of Coal, 1986. *Mining Science and Technology, 3, 205-216.* Paper.

[9] Itasca, Flac3D: Fast Lagrangian Analysis of Continua in 3 Dimensions, Online Manual.

[10] Yatsili, N.E., and Unver, B., 3-D numerical modelling of stresses around a longwall panel with top coal caving, 2005. *The Journal of The South African Institute of Mining and Metallurgy,* Paper.

## For wider interest

In the last few years the importance of coal as an energy source is raising again, due to development of Clean Coal Technologies (CCT). However, coal combustion produces billions of tonnes of carbon dioxide each year and all of that is released to the atmosphere. Because of the problems with greenhouse gas emissions at Velenje Coal Mine we launched a research group on Clean Coal Technologies (at the end of year 2007). The task of the research group is to find new technologies for cleaner use of coal. Clean Coal Technologies research group also applied for two international projects. First is Development of Novel Technologies for Predicting and Combating Gas Outbursts and Uncontrolled Emissions in Thick Seam Coal Mining, which will improve coal excavation, safety and working conditions in the mine (CoGasOUT). The project is partially founded by Research Fund for Coal and Steel. The second project entitled Greenhouse Gas Recovery from Coal mines and Coalbeds for Conversion to Energy (GHG2E) is funded within the 7th framework programme. During both projects, “in-situ” monitoring is provided in the mine with the support of laboratory analysis, such as desorption and adsorption laboratory tests, coupled with numerical modelling of gas migration under the influence of stress change. Results will improve mines around the world with new technology to combat outbursts and high gas emissions.

# Use of monolithic chromatography for speciation of Pt based chemotherapeutic drugs

**Anže Martinčič**[1,2], **Radmila Milačič**[1,2], **Maja Čemažar**[3], **Gregor Serša**[3], **and Janez Ščančar**[1,2]

[1] Department of Environmental sciences, Jožef Stefan Institute, Ljubljana, Slovenia

[2] Jožef Stefan International Postgraduate School, Ljubljana, Slovenia

[3] Institute of Oncology, Department of Experimental Oncology, Ljubljana, Slovenia

anze.martincic@ijs.si

**Abstract.** Distribution of Pt-based chemo-therapeutic drugs; cisplatin, carboplatin and oxaliplatin was studied using monolithic chromatography coupled to inductively coupled plasma mass spectrometry (ICP-MS). Previously developed method for speciation of cisplatin was successfully used for pharmacokinetic studies of oxaliplatin and carboplatin in human serum.

**Keywords**: cisplatin, carboplatin, oxaliplatin, monolithic chromatography, ICP-MS

## 1 Introduction

Pt-based chemotherapeutic drugs: cisplatin (CDDP), carboplatin and oxaliplatin, are applied worldwide in clinical practice. [1] The cytotoxicity of these drugs is a consequence of Pt's binding to DNA which results in cellular death by apoptosis or necrosis. [2] CDDP is used for treating numerous types of tumours (testicular, ovarian, cervical, bladder, etc.) but its use is limited by severe side effects. [2] Carboplatin exhibits fewer side effects but is also less effective than CDDP. It is mainly used to treat ovarian carcinoma, lung, head and neck cancers. [3] Oxaliplatin was approved in 1996 and is mainly used to treat colorectal cancer.

Analytical chemistry is today essentially involved in research in life sciences. Inductively coupled plasma mass spectrometry (ICP-MS) is an elemental MS technique characterized by its isotope specificity, versatility, high sensitivity, large linear dynamic range and robustness. Coupled to high pressure liquid chromatography (HPLC) it is the method of choice for speciation analysis. [4] In our previous work an analytical method for speciation of CDDP in human blood serum was developed. [5] In this paper we present the applicability of the developed method for studying pharmacokinetics of other Pt based chemotherapeutic drugs.

## 1.1 Materials and methods

HPLC separations were performed with an Agilent (Tokyo, Japan) series 1200 quaternary system on a weak anion-exchange CIM DEAE-1 monolithic column (Bia Separations, Ljubljana, Slovenia). Protein signals were followed online with UV-Vis detector at 278 nm and $^{195}$Pt signals with Agilent 7700x ICP-MS.

The chromatographic run was carried out at a flow rate of 1 mL min$^{-1}$. Linear gradient elution from 100% buffer A (50 mM TRIS HCl + 30 mM $HCO_3^-$ at pH 7.4) to 100% buffer B (buffer A + 1 M $NH_4Cl$) was applied for 10.5 min. The column was then regenerated by rinsing with 100% buffer C (2 M $NH_4Cl$) for 2 min at flow rate 10 mL min$^{-1}$, followed by elution with buffer D (0.2 M TRIS HCl at pH 7.4) for 3 min at flow rate 10 mL min$^{-1}$. After that, the column was equilibrated with buffer A at a flow rate of 10 mL min$^{-1}$ for 2 min and at flow rate of 1 mL min$^{-1}$ from 17.5 to 19.5 min.

Human serum was spiked with the equivalent of 200 ng Pt mL$^{-1}$ of each drug separately and incubated for 24 h at 37 °C. For kinetic studies human serum was first warmed to 37 °C and than spiked with the equivalent of 200 ng Pt mL$^{-1}$ of each drug. 0.1 mL of serum was taken for speciation analysis at 5 min, 1 h, 3 h, 5 h, 24 h and 48 h. Before analysis each sample was diluted five times with buffer A.

## 1.2 **Results**

In our previous work we showed that the main binding site for CDDP in human serum was human serum albumin (HSA) on to which 83 % of all CDDP was bound while 3 % of all CDDP was bound to transferrin (Tf) and 14 % remained unbound (Fig.1). Unbound drug elutes at the retention volume of immunoglobulins (IgG), but it was shown that it is not bound to IgG. [5] Molar ratio of HSA/Tf is ~10/1 while Pt ratio between them is ~28/1. We found that oxaliplatin behaves similarly to CDDP; 63 % of all oxaliplatin was bound to HSA, 10 % was bound to Tf and 27 % remained unbound. Carboplatin on the other hand remains predominantly unbound (74.5 %) and only 7.5 % was bound to Tf and 18 % to HSA.

Kinetics of binding to human serum proteins was also studied. Results show that CDDP and oxaliplatin bind quickly to serum proteins. (Fig. 2) After only 3 h most of CDDP and oxaliplatin is already bound to HSA. A significant amount of carboplatin bound to HSA can only be observed after 24 h.

Kinetic studies were done in one day for all three compounds which would be impossible with a standard HPLC column. In our experience those columns require a thorough cleaning after 5 or 6 serum injections. [5] But with CIM columns up to a hundred separations of serum can be made without the need for cleaning.

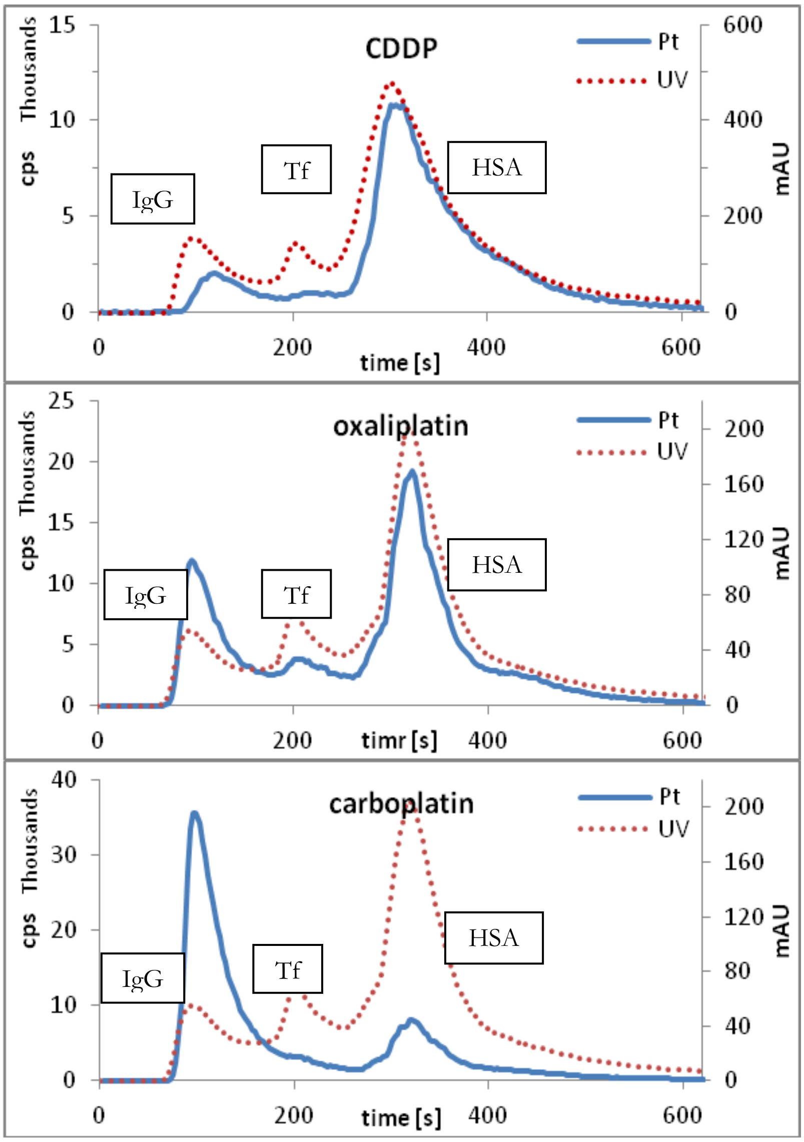

**Figure 1**: Chromatograms showing binding of tested drugs to human serum proteins after 24 h incubation.

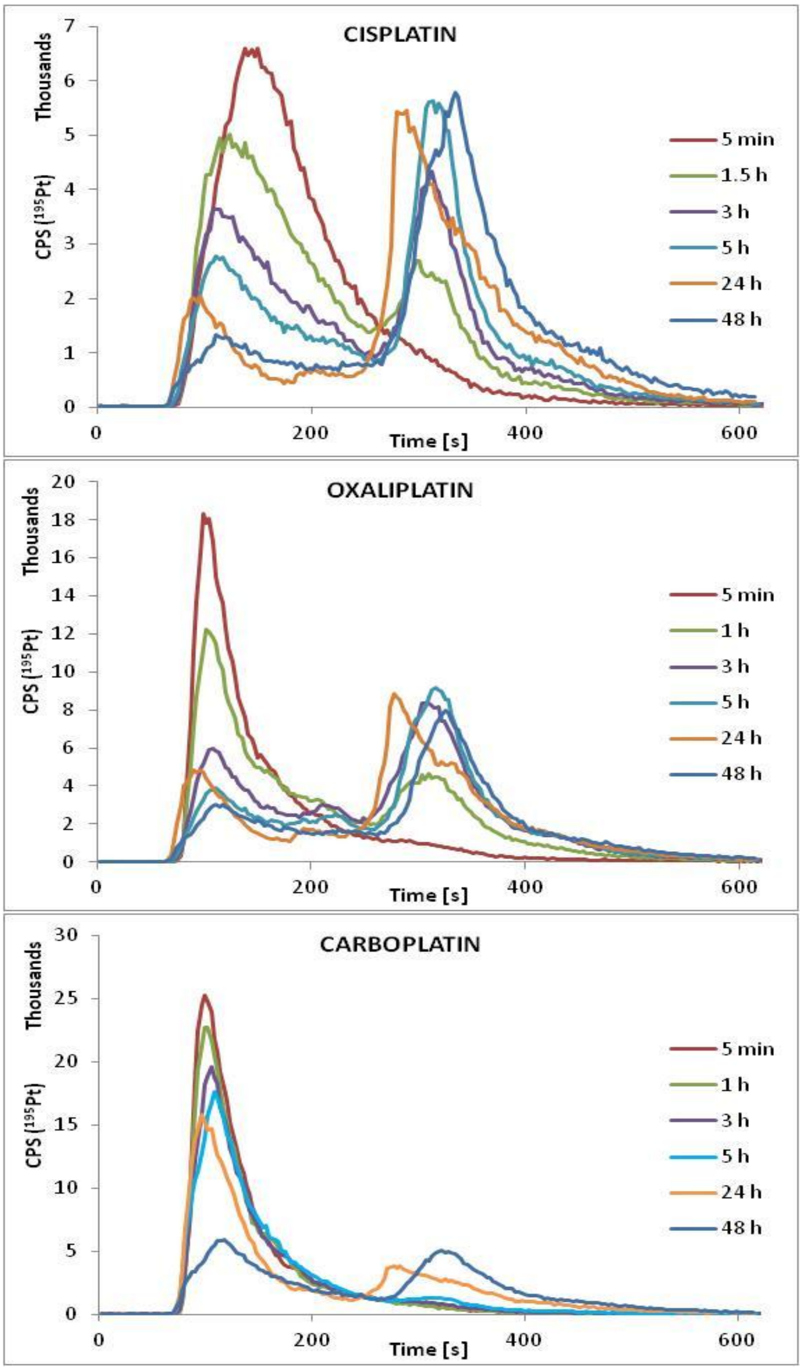

**Figure 2**: Chromatograms showing kinetics studies of binding of tested drugs to human serum proteins.

## 2 Conclusion

In this work we further extend the applicability of our method for separating different Pt species in human blood. Method is based on monolithic chromatography which has several advantages over standard (particle packed) chromatographic columns. In our future work will further develop this method for speciation of Ru-based compounds.

## References:

[1]F. Huq, J. Q. Yu, P. Beale, in A. Boneti, R. Leone, F. M. Muggia, S. B. Howell (ed.), *Platinum and Other Heavy Metal Compounds in Cancer Chemotherapy*, Humana Press Inc., New York, 2009.

[2]D. Esteban-Fernandez, E. Moreno-Gordaliza, B. Canas, M. A. Palacios and M. M. Gomez-Gomez, *Metallomics*, 2, 19–38, 2010.

[3]NJ. Wheate, S. Walker, GE. Craig, R. Oun., *Dalton Trans*, 39, 8113-27, 2010.

[4]D. M. Templeton, F. Ariese, R. Cornelis, L.-G. Danielsson, H. Muntau, H. P. Van Leeuwen and R. Lobinski, *Pure Appl. Chem.*, 72, 1453–1470, 2000.

[5]A. Martinčič, R. Milačič, M. Čemažar, G. Serša, J. Ščančar, *Anal. Methods*, 4, 780-790, 2012.

## For wider interest

Our work is based on monolithic chromatography which offers several advantages over standard (particle packed) chromatographic columns. Monolithic supports have high permeability and therefore allow thorough cleaning during regeneration after each separation run. This enables great robustness of such chromatographic columns which in turn enables higher throughput of samples. Monolithic supports are also cheaper and offer possibilities to be applied in numerous chromatographic separations of compounds in environmental and biological samples.

# Determnation of Cr(VI) in corrosion protection coatings by speciated isotope dilution ICP-MS

**Breda Novotnik**[1,2], **Tea Zuliani**[1], **Janez Ščančar**[1,2] **and Radmila Milačič**[1,2]
[1] Department of Environmental sciences, Jožef Stefan Institute, Ljubljana, Slovenia
[2] Jožef Stefan International Postgraduate School, Ljubljana, Slovenia
breda.novotnik@ijs.si

**Abstract:** Chromium conversion coatings are used as decorative finishes and to improve the corrosion protection and strengthen the wear resistance of metallic surfaces. Chromium electroplating frequently involves the use of hexavalent chromium (Cr). To reduce environmental impacts, several EU directives restricted its use to threshold values of 0.1 % Cr(VI) by weight per homogenous material in vehicles, and 1000 mg kg$^{-1}$ of Cr(VI) in electronic and electrical equipment. In a view of these demands the aim of our work was to develop a selective and quantitative analytical procedure for determination of Cr(VI) in corrosion protection coatings. The results have proven that for efficient extraction of Cr(VI), 2 % NaOH + 3 % $Na_2CO_3$ with addition of $MgCl_2$ as extraction solution and ultrasonic extraction at 70 °C for 30 min should be applied. Several consecutive extractions are necessary to quantitatively extract Cr(VI) from corrosion prevention coatings.

**Key words**: corrosion protection coatings, chromium(VI), speciated isotope dilution, Inductively Coupled Plasma Mass Spectrometry

## 1 Introduction

The amount of Cr(VI) in corrosion protection coatings and electrical equipment is of environmental concern and is restricted by several legislation directives [1-3]. To date, determination of Cr(VI) in corrosion protection coatings was mainly performed by hot water extraction and spectrophotometric 1,5 diphenylcharbazide detection (EN 15205, [4]) or by the use of slightly alkaline ammonia extracting solution (pH 9) and quantification of Cr(VI) by HPLC-ICP-MS [5]. Since hot water and alkaline buffers with low ionic strength are not powerful leaching agents, the aim of our work was to develop a method based on alkaline extraction, that would enable selective and quantitative determination of Cr(VI) in corrosion protection coatings. Species interconversions during the extraction procedure were followed by the use of stable isotopes. Cr(VI) was quantified by isotope dilution inductively coupled plasma mass spectrometry (ID-FPLC-ICP-MS) procedure.

## 2 Materials and methods

### Preparation of enriched isotopic standard solutions

$^{50}$Cr(VI) standard solution was prepared by alkaline melting from $Cr_2O_3$ ($^{50}$Cr enriched isotope). $^{53}$Cr(III) standard solution was prepared from $Cr_2O_3$ ($^{53}$Cr enriched isotope) by microwave assisted digestion. Determination of the concentrations of enriched $^{53}$Cr(III) and $^{50}$Cr(VI) standard solutions was performed by reverse ID-ICP-MS. A dead time of 46 ns was used. The mass bias was determined daily by chromatographic separation of $^{nat}$Cr(VI) at concentrations that were close to Cr concentrations in the samples investigated.

### Sample preparation

Chromium conversion or hard chrome coatings on electroplated copper (10 μm) or zinc (10 μm) steel surfaces (metallic plates 10 mm x 10 mm x 1.5 mm) of 5 or 10 μm thickness of homogenously coated chromium layer were prepared in a galvanization workshop.

### Extraction procedure

A final volume of 10 mL of extraction solution was prepared from 2 % NaOH+3 % $Na_2CO_3$, 1 mL of $MgCl_2$ (1 mol $L^{-1}$) and enriched isotopic spike solutions of $^{50}$Cr(VI) and $^{53}$Cr(III) (20 ng Cr $mL^{-1}$). Ultrasonic extraction was applied at 70 °C for 30 min. Six consecutive extractions were performed. Analysis of Cr(VI) in extracts was performed by high performance liquid chromatography HPLC-ICP-MS. Concentrations of Cr(VI) were calculated by speciated isotope dilution ICP-MS, based on determining the signal intensities ratio between $^{50}$Cr(VI) enriched spike and $^{52}$Cr(VI) present in the sample ($R^{VI}_{50/52}$ ratio).

## 3 Results and discussion

### Optimisation of the extraction procedure

To check whether any oxidation and/or reduction occurs during the extraction of chromium from plates, a double isotopically enriched spike of $^{50}$Cr(VI) and $^{53}$Cr(III) was added to extracting solution. As can be seen from Fig. 1A, noticeable oxidation of $^{53}$Cr(III) is observed, when alkaline extraction is performed. To prevent Cr(III) oxidation during the extraction procedure, TRIS, EDTA or $MgCl_2$ were tested in a time span of 90 min (Fig. 1). When TRIS was added to the extraction solution, $^{53}$Cr(VI) was detected, indicating that TRIS was not able to prevent Cr(III) oxidation (Fig. 1B). When EDTA was used, a reduction of $^{50}$Cr(VI) was observed (Fig. 1C). From Fig. 1D it is evident that $MgCl_2$ can prevent oxidation of $^{53}$Cr(III) and does not provoke $^{50}$Cr(VI) reduction during 30 min extraction. Therefore, $MgCl_2$ was used in all further experiments to prevent Cr(III) oxidation.

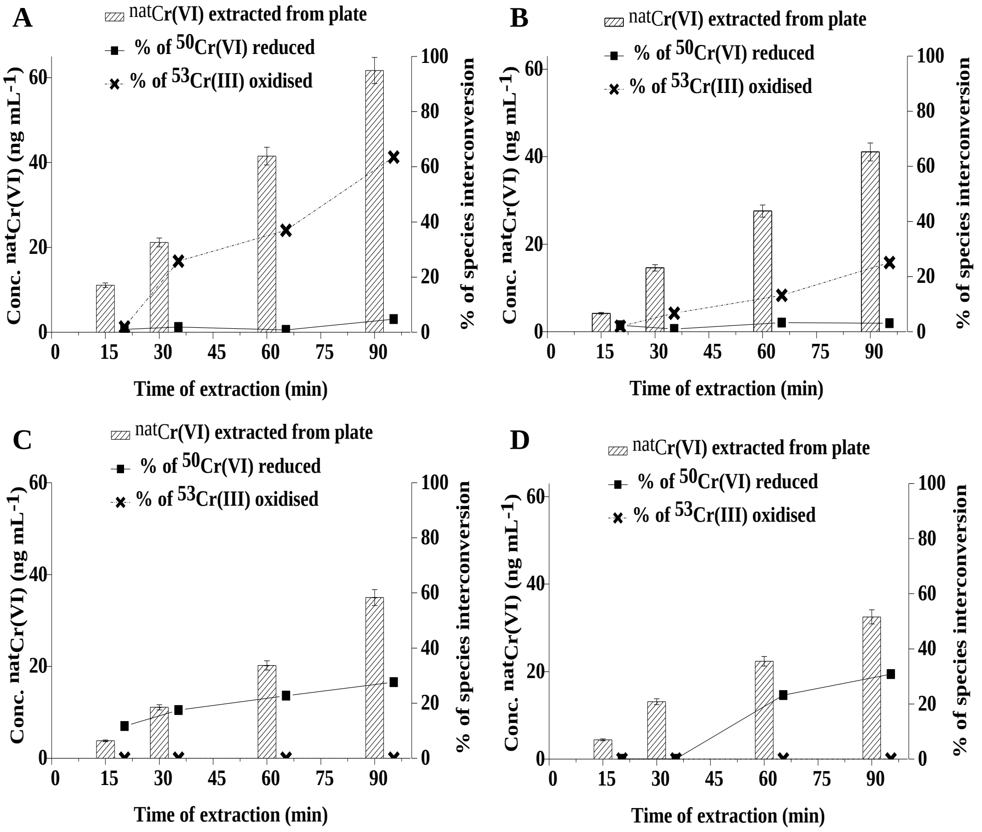

**Figure 1**: Extraction of Cr(VI) from 5 µm hard chrome coating on copper electroplated metallic plate in a time span of 90 min using A: 2 % NaOH + 3 % $Na_2CO_3$, B: 2 % NaOH + 3 % $Na_2CO_3$+ 0.05 mol $L^{-1}$ TRIS, C: 2 % NaOH + 3 % $Na_2CO_3$ + 0.1 mol $L^{-1}$ EDTA and D: 2 % NaOH + 3 % $Na_2CO_3$ + 0.1 mol $L^{-1}$ $MgCl_2$. To each extraction solution, a double isotopically enriched spike of 20 ng $mL^{-1}$ $^{50}$Cr(VI) and 20 ng $mL^{-1}$ $^{53}$Cr(III) was added.

## Consecutive extractions

In order to study whether Cr(VI) is efficiently extracted from the plates, several consecutive extractions were performed. 5 different metallic plates were analysed (Fig. 2). The amount of total Cr(VI) extracted from plates (6 consecutive extractions) depended on the thickness and type of coating and roughly ranged from 2 to 7 ng mm$^{-2}$. The highest concentration (ng mm$^{-2}$) of Cr(VI) was extracted with first extraction.

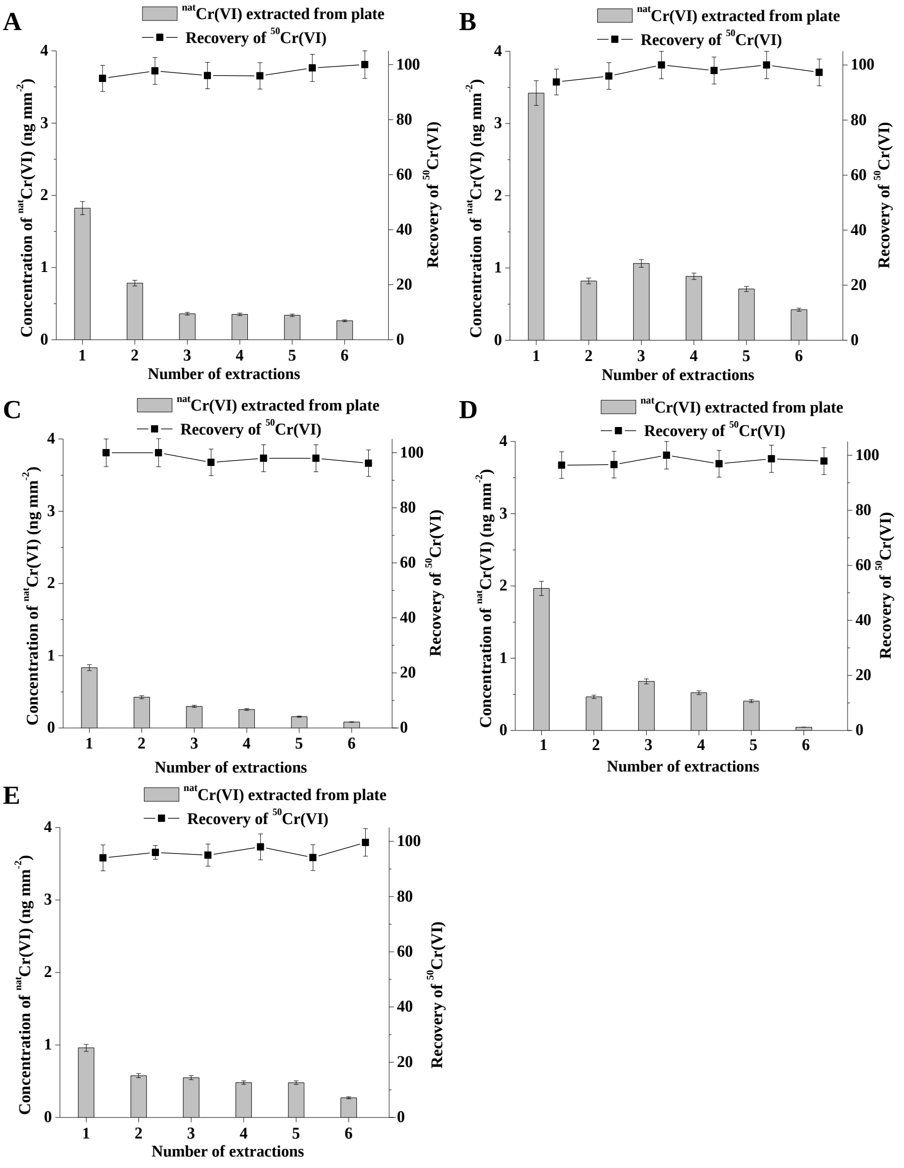

**Figure 2**: Extraction of Cr(VI) from plates 1A: 10 µm Cu+5 µm Cr; B: 10 µm Cu+10 µm Cr; C: 10 µm Cu+5 µm HCr; D: 10 µm Cu+10 µm HCr; E: 10 µm Zn + 5 µm Cr

## Influence of copper and zinc on species interconversions during extraction

To check the influence of copper and zinc on species interconversions during extraction, copper or zinc electroplated metallic plates without chromium coatings were subjected to consecutive extractions. As before, each extraction solution was spiked with isotopically enriched $^{50}$Cr(VI) and $^{53}$Cr(III). This experimental data proved that no oxidation of $^{53}$Cr(III) occurred during consecutive extractions. $^{50}$Cr(VI) was not reduced during consecutive extractions from copper electroplated metallic plates, but significant reduction of $^{50}$Cr(VI) was observed after the first extraction from zinc electroplated plates. Meaning that zinc in the following extractions acted as a reducing agent. From the analytical point of view, this means that any mechanical damage to the chromium coatings on electroplated zinc surfaces may consequently cause the reduction of Cr(VI) during extraction.

In conclusion, 30 min ultrasonic extraction at 70 °C using 2 % NaOH + 3 % $Na_2CO_3$ + $MgCl_2$ as extracting agent and 6 consecutive extractions were necessary to quantitatively extract Cr(VI) from protective layers. The use of enriched isotopic solutions of $^{50}$Cr(VI) and $^{53}$Cr(III) enabled to control species interconverstions during the analytical procedure and to quantify Cr(VI) by speciatied ID-ICP-MS. However, once the analytical procedure was optimised, quantification of Cr(VI) is also possible by ICP-MS, using external calibration. The method developed is highly sensitive. Limit of quantification (LOQ) was found to be 0.0107 ng Cr(VI) $mm^{-2}$ if the coating surface was 250 $mm^2$. The possibility to use external calibration for quantification of separated Cr(VI) instead of ID-ICP-MS, extends the application of the developed procedure to routine laboratory use.

## References

[1.] The Council of the European Union, 2000, European Directive 2000/53/EC on end-of life vehicles. Official Journal of European Union

[2.] The Council of the European Union, 2002, European Directive 2002/95/EC on the restriction of the use of certain hazardous substances in electrical and electronic equipment. Official Journal of European Union

[3.] The Council of the European Union, 2002, European Directive 2002/96/EC on waste electrical and electronic equipment (WEEE). Official Journal of European Union

[4.] ISO (1995) EN ISO 3613. ISO, Geneva

[5.] F. Séby, A. Castetbon, R. Ortega, C. Guimon, F. Niveau, N. Barrois-Oudin, H. Garraud and O.F.X. Donard. Development of analytical procedures for the determination of hexavalent chromium in corrosion prevention coatings used in the automotive industry. *Analitical and Bioanalitical Chemistry,*391: 587-597, 2008

## Za širši interes

Evropska unija je sprejela številne predpise s katerimi določa kritične meje Cr(VI) v protikorozijskih premazih, ki se uporabljajo v avtomobilski industriji (2000/53/EC) in elektronski opremi (2002/95/EC) ter v recikliranih izdelkih (2002/96/EC). Postopki, ki so trenutno v uporabi za analizo Cr(VI) vključujejo ekstrakcijo z vrelo vodo ali rahlo alkalno amonijevo raztopino, ter spektrofotometrično določitev Cr(VI) v ekstraktu oziroma določitev z ICP-MS. Ker omenjeni ekstrakcijski sredstvi nista dovolj učinkoviti, je bil naš cilj razviti novo analizno metodo, ki temelji na alkalni ekstrakciji. Pri razvoju ekstrakcijskega postopka smo uporabili stabilne izotope kroma (50Cr(VI) in 53Cr(III)) s katerimi smo sledili oksidaciji in redukciji kromovih zvrsti med samim ekstrakcijskih postopkom. Ugotovili smo, da alkalna ekstrakcija povzroči oksidacijo Cr(III) v vzorčku. Da bi preprečili oksidacijo kroma med ekstrakcijo, smo preverili v kakšni meri TRIS, EDTA in MgCl2 preprečijo oksidacijo Cr(III). Poskusi so pokazali, da TRIS ni sposoben preprečiti oksidacije in, da se pri dodatku EDTA pojavi redukcija Cr(VI). MgCl2 se je tako izkazal kot najustreznejši, saj pri 30 min ekstrakcije nismo zasledili oksidacije Cr(III) ali redukcije Cr(VI). Tako smo v vseh nadaljnjih poskusih za ekstrakcijo Cr(VI) uporabili ultrazvočno ekstrakcijo (30 min, 70 °C) in kot ekstrakcijsko sredstvo 2 % NaOH + 3 % Na2CO3 z dodatkom MgCl2. Omenjeni postopek ekstrakcije je zagotovil pogoje, pri katerih ni prišlo do pretvorb kromovih zvrsti, kar smo dodatno sledili med vsako ekstrakcijo z uporabo obogatenih stabilnih izotopov kroma 50Cr(VI) in 53Cr(III). Cr(VI) v ekstraktu smo določili z izredno občutljivo kvantitativno metodo izotopskega redčenja z ICP-MS. Ugotovili smo, da je bilo pri preučevanih vzorcih za ekstrakcijo celotnega Cr(VI) iz površine nanosa protikorozijskih prevlek potrebnih šest zaporednih ekstrakcij.

# Optimization of distillation separation procedure for methyl mercury in natural waters

**Kristina Obu[1,4], Neža Koron[2], Arne Bratkič[3,4], Mitja Vahčič[3], Milena Horvat[3,4]**

[1]Ecological Engineering Institute, Maribor, Slovenia

[2]Marine Biology Station Piran, National Institute of Biology, Ljubljana, Slovenia

[3]Department of Environmental Sciences, 'Jozef Stefan' Institute, Ljubljana, Slovenia

[4]Jožef Stefan International Postgraduate School, Ljubljana, Slovenia

kristina.obu@iei.si

## Abstract

Mercury in the aquatic environment is present at very low levels and its determination can be a subject to losses and/or contamination during sampling, sample preparation and analysis. Speciation of chemical forms of mercury in natural waters is even more demanding. The monomethyl mercury form (MeHg) is persistent, it accumulates and biomagnifies in the food webs. MeHg is formed in the nature, particularly in the aquatic environment. Therefore, the accurate determination is of great importance. The aim of this study was to optimize a simple and efficient separation technique for MeHg determination in natural waters using aqueous phase distillation followed by derivatisation using ethylation, purging and room temperature adsorption on Tenax, gas chromatography, pyrolysis and detection by cold vapour atomic fluorescence spectrometry (CV AFS). Optimisation steps included temperature of distillation unit, duration of distillation, purging with nitrogen ($N_2$) and addition of reagents prior distillation. Due to the absence of Certified reference Materials (CRM), the accuracy of the results was compared with an independent separation technique based on solvent extraction. Optimal conditions were found and the Limit of Detection (LOD) achieved was 0.42 pg/L based on 50 mL of natural water sample taken for distillation. The method was used for the samples taken from the Mediterranean Sea, where values from 1.4 to 72.5 pg/L were determined.

**Keywords:** Distillation, methyl mercury, sea water

# 1 Introduction

Mercury (Hg) is a toxic metal for humans and the ecosystem. It is a natural element, but during the last century of human activities increased its presence in the global atmosphere for about a factor of three [1, 2]. The main anthropogenic activities include burning of fossils fuels, high temperature processes (ore, metal industry, cement kilns) and the use of mercury in industrial processes and products [3]. In the environment different forms of mercury (elementary $Hg^0$, inorganic $Hg^{2+}$ and $Hg_2^{2+}$, organic MeHg) are present, of which elemental Hg is volatile at room temperature. Transformation of these forms under natural conditions form the basis for the local, regional and global biogeochemical cycle. Due to its volatile nature it can travel long distances and can be deposited far from its source and it is therefore characterized as a **global pollutant**. Oceans play very important role in the global mercury cycle. Due to reduction/oxidation processes oceans can be a source and/or sink of mercury from the global atmosphere. In the water and sediments mercury can be transformed to MeHg, which is one of the most toxic Hg compound and accumulates and biomagnifies in the aquatic food webs. Therefore, it is of paramount importance to obtain accurate information about the presence and formation of this compound in the aquatic environment [3].

The concentrations of mercury in natural waters are low, and range from 0.2 to a few ng/L. In natural waters, especially in sea water, MeHg occurs in very low concentrations; typically, less than 10 % of total Hg in water exists as MeHg [3]. The analysis is therefore demanding and can be a subject to losses and/or contamination during sampling, sample handling and analysis. For the purpose of MeHg isolation from the matrix, two methods are commonly used. The first is based on extraction procedure using organic solvents (methylene chloride) and the second is based on aqueous phase distillation [1]. Both methods are followed by a derivatisation procedure and CV AFS detection [1] which is sensitive enough to measure sub picogram levels of MeHg. Although the distillation technique has been in use for a long time [1], it is very important to optimize the procedure to achieve required precision, good recoveries and contamination-free conditions. In order to achieve suitable LOD, the procedure should be simple, involving limited number of steps, and reagents. The aim of this work was to optimize the distillation technique that can achieve suitable LODs (lower then 1 pg/L) for studies of mercury behavior in the marine environment.

## 2 Methods

The distillation procedure used is based on the protocol described by Horvat et al [1].

Step 1: Initially, 50 ml of sea water sample was weighted into a 60 ml Teflon vial, especially designed for distillation, acidified with 1 mL 8 M $H_2SO_4$ and 200 μl KCl. The quantities of added $H_2SO_4$ and KCl were later verified and optimized, particularly in case of pre-acidified sea water sample with HCl, in which the addition of reagents was not necessary.

Step 2: Horvat et al [1] reported that the distillation should be performed at such a heating block temperature to achieve distillation rate of about 6 to 8 mL per hour, and purging with nitrogen gas. In order to achieve appropriate distillation rate, the temperature of the new heating block (Tekran, Canada) was adjusted to 122 ºC. With increasing the temperature the distillation rate increased and consequently recoveries of MeHg decreased. In addition, we removed the purging step to simplify and decrease costs of the procedure. The distillates were collected into a glass flask, which was also used in the measurement step described below.

Step 3: After the distillation, samples were buffered with 300 μL of acetate buffer (2 M) to the final pH between 4.5 and 5 and 50 μL of ethylation reagent ($NaBEt_4$) was added to all samples. The reaction was allowed to proceed for at least 15 min without bubbling at 25 °C. This was followed by purging the volatile ethylated Hg species from the sample to Tenax trap for 5 min and for vapour removal dry nitrogen was purged over the Tenax trap for 3 min. The Hg species on the Tenax trap were released onto gas chromatography column by thermal desorption. The eluted Hg species were afterwards under the flow of argon converted to $Hg^0$ by thermal decomposition in pirolytic cell and detected by CV AFS, Brooks Rand Model III. This step was fully automated, using a Brooks Rand MERX analyzer (Seatle, USA). The sensitivity of the instrument is very good as it allows precise detection of 0.03 pg of MeHg. The overall LOD of the procedure using optimized conditions for distillation was found to be 0.42 pg/L.

As certified reference material (CRM) for MeHg in marine water does not exist the results from distillation were compared with an independent method based on extraction into methylene chloride and back extraction into water [1] followed by Step 3 described above.

The recovery for both procedures was checked by spiking the water samples with 100 μL of 0.1 ng MeHg in aqueous solution per mL prior separation techniques. Reagent and distillation blanks were also carefully evaluated in each set of measurement. At least three blanks were measured. The LOD was calculated on the basis of the three standard deviations of the values for the blanks. As this values were critically important to achieve good LODs special care was dedicated to the cleaning procedure and the use of very clean reagents [1].

## 3 Results and Discussion

In order to achieve appropriate distillation rate (6.3 to 6.7 mL/h) the temperature of the new distillation unit (Tekran, Canada) was optimized at 122 °C. The recoveries at this condition varied from 80 to 85 %, at the volume of collected distillate of about 40 ml, (80 % of water taken for analysis). At higher distillation rates recoveries were lower. This is in agreement with previous work [1].

An important improvement in this work compared to previous work was that purging with nitrogen gas was omitted. This reduces the costs of the distillation procedure. Comparison of the distillation with and without purging with nitrogen gas showed recoveries of 81 ± 3 % and 79 ± 1% (based on 12 independent analysis), respectively. It has been noted that the distillations were initially performed on the old distillation unit with limited temperature control. The distillation recoveries without purging with nitrogen gas using new distillation unit obtained by Tekran were between 80 to 85 %. The recovery curve for MeHg from a 50 ml water sample without purging with nitrogen gas is shown in Figure 1 and confirms that the collection of 40 ml of water sample results in recoveries above 80%.

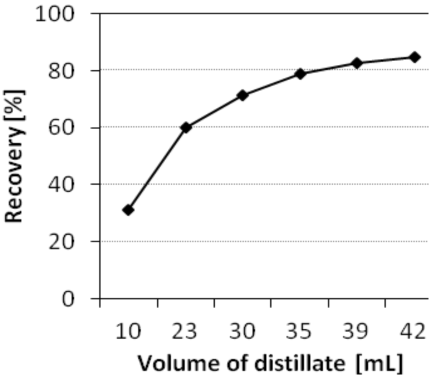

**Figure 1:** Distillation recovery curve for MeHg from 50 ml of sea water

As the pH of the distillate is critically dependent on the reagents added to the sample prior distillation, the addition of acids was also re-checked. It was found that the quantity of $H_2SO_4$ needs to be lowered as compared to previous protocol (1 mL of 8 M $H_2SO_4$). The optimal recovery (above 80 %) was obtained by the addition of 0.2 ml 4M $H_2SO_4$. In case of the seawater samples that are acidified by HCl (1% v/v) in the field, it was found that no additional reagents were needed prior distillation to obtain recoveries above 80%.

Comparison of the results obtained by distillation and extraction is shown in Table 1. Each measurement was done in duplicates. Overall the comparison is good. However, the precision and sensitivity of the distillation is far better than the solvent extraction technique. The LOD of the extraction procedure was 1.5 pg/L and for the distillation 0.42 pg/L.

**Table 1:** Comparison of the results for MeHg obtained by distillation and solvent extraction

| | **Extraction [pg/L]** | | **Distillation [pg/L]** | |
|---|---|---|---|---|
| **Sample** | | Average | | Average |
| 1 | 18,8 | 17,8 | 13,6 | 16,7 |
| | 16,9 | | 19,7 | |
| 2 | 41,3 | 28,5 | 15,6 | 15,6 |
| | 15,6 | | 15,6 | |
| 3 | 3,87 | 7,20 | 9,40 | 12,5 |
| | 10,5 | | 15,7 | |
| 4 | 16,1 | 17,2 | 21,3 | 21,0 |
| | 18,4 | | 20,7 | |
| 5 | 58,7 | 39,5 | 17,3 | 16,9 |
| | 20,3 | | 16,4 | |
| 6 | 28,5 | 23,0 | 26,8 | 25,6 |
| | 17,5 | | 24,5 | |

The distillation was also used in real samples from the Mediterranean Sea where expected low concentrations of MeHg were. Results show that concentrations of MeHg in sea water are very low and increase with the depth (1.4 to 72.5 pg/L).

## References

[1]M. Horvat, L. Liang, N.S. Bloom. Comparison of distillation with other current isolation methods for the determination of methyl mercury compounds in low level environmental samples: Part II. Water. *Analytical Chemical Acta*, 282: 153-168, 1993.

[2]J. Kotnik, M. Horvat, E. Tessier, N. Ogrinc, M. Monperrus, D. Amouroux, V. Fajon, D. Gibičar, S. Žižek, F. Sprovieri, N. Pirrone. Mercury speciation in surface and deep waters of the Mediterranean Sea. *Marine Chemistry*,107: 13-30, 2007

[3]UNEP Chemicals, Global mercury Assessment, Geneva, Switzerland, 2002.

## For wider interest

The aim of the research is to understand better the chemistry of mercury in aqueous media. Speciation of chemical species of mercury in water is of ultimate importance to understand its distribution, partitioning and fate in the environment.

The work presented is focused on the accurate determination of very low concentrations of a chemical form of mercury – monomethylmercury (MeHg), which is one of the most toxic compound that accumulates and biomagnifies in biosphere. Due to very low concentrations found in the environment, especially in water, the first step was to optimize the procedure and to improve the limit of detection, so that environmentally consistent data can be obtained. The method optimized has shown to be fit for purpose as demonstrated on real samples taken from the Mediterranean Sea. Concentrations in sea water are very low and are increasing with depth (from 1.4 to 72.5 pg/L). Because of low concentrations it is necessary to take all the precautions not to contaminate the samples and to use methods which are the most reliable. That is why the distillation is our method of choice.

Next steps will include further refinement of the distillation procedure form solid samples, such as sediments, where the proportion of inorganic mercury can interfere the analysis by artificial formation of MeHg.

# Photodegradation of Benzophenones

**Kristina Pestotnik**[1,2], **Tina Kosjek**[1], **Uroš Krajnc**[3], **Ester Heath**[1,2]

[1] Department of Environmental Sciences, Jožef Stefan Institute, Ljubljana, Slovenia

[2] Jožef Stefan International Postgraduate School, Ljubljana, Slovenia

[3] Ecological Engineering Institute Ltd, Maribor, Slovenia

kristina.pestotnik@ijs.si

**Abstract.** Over the last decade there has been increasing concern regarding the presence and possible toxic effects of pharmaceuticals and personal care products (PPCPs) in the environment. The studied benzophenones include UV filters, a pharmaceutical, its phototransformation products and others. The aim of this work was to gain a better understanding of the fate of the selected benzophenones in the aquatic environment under the influence of ultraviolet irradiation. Compounds were exposed to UV irradiation using low pressure (LP) monochromatic mercury lamp with a peak emission at 254 nm and medium pressure (MP) mercury lamp with a pyrex glass filter. Whereas ketoprofen was prone to UV irradiation (it was completely degraded after 15 minutes of irradiation with MP lamp), other compounds were found to be highly resistant. Therefore the efficiency of the UV treatment was increased by combining UV irradiation (LP lamp) and hydrogen peroxide. As a result of adding 0.1 % hydrogen peroxide, improved removal of 2-hydroxy-4-methoxybenzophenone (77 %) and 3-i-propylbenzophenone (92 %) was achieved.

**Keywords**: Benzophenones, UV irradiation, photodegradation, UV/$H_2O_2$

## 1 Introduction

An increasing amount of pharmaceuticals and personal care products (PPCPs) enter the environment globally. In the last decade the problem of the potential adverse effects on human health and environmental organisms has been found to be an important aspect of public health. Compounds that include benzophenone structure (Figure 1) are widely used in various fields. The studied benzophenones include UV filters (benzophenone, 4-hydroxybenzophenone, 2-hydroxy-4-

methoxybenzophenone 2,4-dihydroxybenzophenone, 2,2'-dihydroxy-4-methoxybenzophenone), a pharmaceutical (ketoprofen), its phototransformation products (3-ethylbenzophenone, 3-acetylbenzophenone) [1] and others (3-i-propylbenzophenone). Ketoprofen is a commonly used nonsteroidal anti-inflammatory drug with analgesic, antipyretic and anti-inflammatory activity [1]. UV filters have the ability to absorb ultraviolet light and are therefore used in many cosmetic products such as sunscreens, moisturizers, hair sprays, shampoos and lipsticks [2].

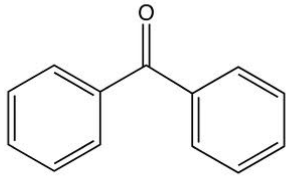

**Figure 1** : Chemical structure of benzophenone

To date, only a few studies have been reported regarding the presence of UV filters in the environment, most of them in bathing waters. The compounds were detected in ng $L^{-1}$ levels in seawaters [2], [3], lakes [4], [5] and rivers [4]. They were also reported in ng to µg $L^{-1}$ levels in swimming pools [3], [4], industrial and municipal wastewaters [2]. Their concentrations vary depending on the sample location and the intensity of recreational activities, reaching the highest concentrations during summer months. Studies also report the presence of ketoprofen in wastewaters and surface waters [6], [7].

The aim of this work was to gain greater knowledge of the fate of selected benzophenones in the aquatic environment. As photodegradation of PPCPs caused by sunlight irradiation may be of great significance in the natural elimination process, we evaluated their photodegradation.

## 2 Methods and materials

Due to low environmental concentrations of benzophenones, the first step was to develop an analytical method that would allow trace level determination. The process included optimization of solid phase extraction (SPE) in order to achieve best method performance. Further, optimal derivatization time, temperature and choice of derivatizing agent were determined for the detection of benzophenones using gas chromatography-mass spectrometry in ng to μg $L^{-1}$ concentration range.

UV irradiation of benzophenones was investigated in lab-scale experiments (Figure 2). Spiked deionized water samples with initial concentration of 1 μg $L^{-1}$ were exposed to UV irradiation using low pressure (LP) monochromatic mercury UV lamp (6 W) with a peak emission at 254 nm and medium pressure (MP) mercury lamp fitted with a pyrex glass filter (125 W). To determine the degradation kinetics of benzophenones, different times (0-420 min) were used. Due to the high resistance of most benzophenones to UV irradiation, the efficiency of the UV treatment was increased by adding different concentrations (0.01-1 %) of hydrogen peroxide prior to UV exposure (9 min).

**Figure 2 :** UV reactor

## 3 Results and discussion

The best performance of SPE was achieved using Oasis$^{TM}$ Hydrophilic-Lipophylic Balance (HLB) reversed-phase sorbent with extraction efficiency of the studied benzophenones higher than 87 %. Due to differences in the structure of the benzophenones, the optimal conditions for derivatization varied (Table 1).

**Table 1 :** Optimal conditions for derivatization of the selected benzophenones

| derivatizing agent | temperature | time | compounds |
|---|---|---|---|
| MSTFA* | 60°C | 1 h | 4-hydroxybenzophenone<br>2,4-dihydroxybenzophenone<br>2-hydroxy-4-methoxybenzophenone<br>2,2'-dihydroxy-4-methoxybenzophenone |
| PFBHA** | 60°C | 1 h | 3-acetylbenzophenone |
| PFBHA** | 60°C | 15 h | benzophenone<br>3-ethylbenzophenone<br>3-i-propylbenzophenone |

*MSTFA: N-methy-N-(trimethylsilyl) trifluoroacetamide

**PFBHA: O-(2,3,4,5,6-pentafluorobenzyl)hydroxylamine hydrochloride

All of the studied benzophenones, with the exception of ketoprofen, were proved to be highly resistant to irradiation with the MP lamp with removal < 20 % after 420 min. Ketoprofen was almost completely degraded after 15 min of irradiation (Figure 3). Elimination followed first order kinetics with a degradation rate constant equal to 0.253 min$^{-1}$ and elimination half-time of 2.74 min.

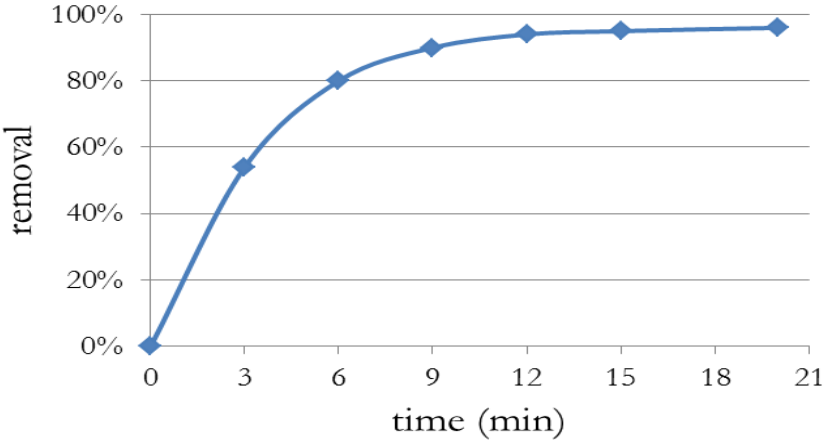

**Figure 3 :** UV-MP removal of ketoprofen

Since the majority of benzophenones proved resistant to UV irradiation, the efficiency of direct photolysis was enhanced by the addition of hydrogen peroxide. The combination of UV irradiation and the strong oxidant led to its photolytic dissociation and the further production of hydroxyl radicals, which facilitated the degradation process. As a result of adding 0.1 % $H_2O_2$, the removal of 2-hydroxy-4-methoxybenzophenone increased to 77 % and the removal of 3-i-propylbenzophenone reached 92 % (Figure 4).

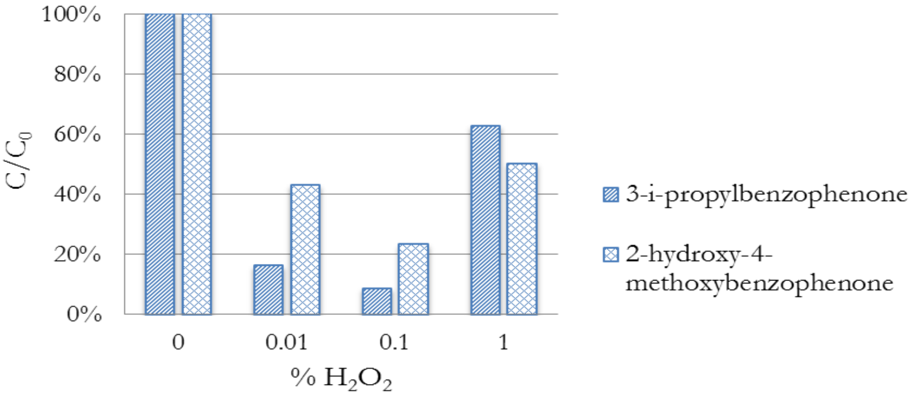

**Figure 4 :** UV/$H_2O_2$ degradation of the two selected benzophenones

## 4 Conclusion

The results of photodegradation treatment of the studied benzophenones will lead to a better understanding of the cycling and fate of these compounds in the environment. They will also provide information to whether or not UV irradiation has the potential for treating water, contaminated with benzophenones. In the future, our goal is to determine the photodegradation kinetics of other benzophenones and to evaluate their presence and fate in different environmental compartments (aqueous environment, soils and sediments).

## References:

[1]T. Kosjek, S. Perko, E. Heath, B. Kralj, D. Žigon. Application of complementary mass spectrometric techniques to the identification of ketoprofen phototransformation products. *Journal of Mass Spectrometry*, 46:391-401, 2011

[2]D.L. Giokas, A. Salvador, A. Chisvert. UV filters: From sunscreens to human body and the environment. *Trends in Analytical Chemistry*, 26(5):360-374, 2007

[3]D.A. Lambropoulou, D.L. Giokas, V.A. Sakkas, T.A. Albanis, M.I. Karayannis. Gas chromatographic determination of 2-hydroxy-4-methoxybenzophenone and octyldimethyl-*p*-aminobenzoic acid sunscreen agents in swimming pool and bathing waters by solid-phase microextraction. *Journal of Chromatography A*, 967:243–253, 2002

[4]P. Cuderman, E. Heath. Determination of UV filters and antimicrobial agents in environmental water samples. *Analytical and Bioanalytical Chemistry*, 387:1343-1350, 2007

[5]T. Poiger, H.R. Buser, M.E. Balmer, P.A. Bergqvist, M.D. Müller. Occurrence of UV filter compounds from sunscreens in surface waters: regional mass balance in two Swiss lakes. *Chemosphere*, 55:951-963, 2004

[6]T. Kosjek, E. Heath, A. Krbavčič. Determination of non-steroidal anti-inflammatory drug (NSAIDs) residues in water samples. *Environment International,* 31:679–685, 2005

[7]C. Tixier, H.P. Singer, S. Oellers, S.R. Müller. Occurrence and fate of carbamazepine, clofibric acid, diclofenac, ibuprofen, ketoprofen, and naproxen in surface waters. *Environmental science & technology*, 37(6):1061-1067, 2003

## For wider interest

The occurrence and fate of pharmaceuticals and personal care products (PPCPs) in the environment has become one of the emerging issues in environmental chemistry. This research was conducted to provide a better understanding of the fate of selected benzophenones in the aquatic environment under the influence of ultraviolet irradiation. The studied benzophenones include UV filters, a pharmaceutical (ketoprofen), its phototransformation products and others. Ketoprofen is a commonly used nonsteroidal anti-inflammatory drug with analgesic, antipyretic and anti-inflammatory activity. UV filters have the ability to absorb ultraviolet light and are therefore used in many cosmetic products such as sunscreen, moisturizer, hair spray, shampoo and lipstick.

As photodegradation of PPCPs caused by sunlight irradiation may be very important in the natural elimination process, we evaluated the photodegradation of the selected benzophenones. UV degradation was investigated in lab-scale experiments using mercury UV lamps. Whereas ketoprofen was prone to UV irradiation (it was completely degraded after 15 minutes of irradiation), other compounds were found highly resistant. Therefore the efficiency of the UV treatment was increased by combining UV irradiation and strong oxidant (hydrogen peroxide). As a result, the removal of benzophenones increased to up to 92 %.

The results of photodegradation treatment of the studied benzophenones will help us to get a better understanding of the cycling and fate of these compounds in the environment. They will also provide information whether UV irradiation has a potential for treatment of water, contaminated with benzophenones. In the future, our goal is to evaluate the presence and fate of benzophenones in different environmental compartments (aqueous environment, soils and sediments).

# Poly[perfluorotitanate(IV)] Compounds of Alkali Metals, Unexpectedly Complicated Species in the Solid State

**Igor Shlyapnikov**[1,2], **Evgeny Goreshnik**[1], **Zoran Mazej**[1],

[1] Department of Inorganic Chemistry and Technology (K1), Jožef Stefan Institute, Ljubljana, Slovenia

[2] Jožef Stefan International Postgraduate School, Ljubljana, Slovenia

igor.shlyapnikov@ijs.si

**Abstract.** Experiments carried out between $TiF_4$ and AF (A stands for alkali metals: Li, Na, K, Rb, Cs) in anhydrous HF (aHF) with different starting molar ratios AF : $TiF_4$, lead to different compounds. In the case of lithium only one product has been observed, i.e. $Li_2TiF_6$. Reactions between AF (A equals Na, K, Rb) and $TiF_4$ with starting molar ratios AF : $TiF_4$ = 2 : 1 and 1 : 1 lead to previously known $A_2TiF_6$ and novel $ATiF_5{\cdot}HF$ salts with infinite polymeric chains $([TiF_5]^-)_n$ in the crystal structures. Starting molar ratios AF : $TiF_4$ = 1 : 2 yields novel $NaTi_2F_9{\cdot}HF$ salt with NaF, meanwhile $K_4Ti_8F_{36}{\cdot}8HF$ and $Rb_4Ti_8F_{36}{\cdot}6HF$, with previously unknown octameric anions, have been isolated after reaction with KF and RbF.

**Keywords**: poly[perfluorotitanate(IV)] compounds, crystal structure, vibrational spectroscopy

## 1 Poly[perfluorotitanate(IV)] compounds

A great variety of poly[perfluorotitanate(IV)] compounds with octahedral coordination of titanium atom can theoretically exist. In all perfluorotitanates $Ti^{4+}$ ions are in an octahedral coordination of six F atoms, and polymeric ions are formed by sharing one or two fluorine atoms between two octahedra (shared apexes or edges – one or two bridging fluorine atoms, respectively). Theoretically, sharing three fluorine atoms is also possible (two octahedra share face – three bridging fluorine atoms), but crystal structures of those anions haven't been reported yet.

In the solid state polyanions are found as discrete species, chains, double chains, columns or layers [1,2]. Structures of known poly[perfluorotitanate(IV)] anions are presented in Figure 1.

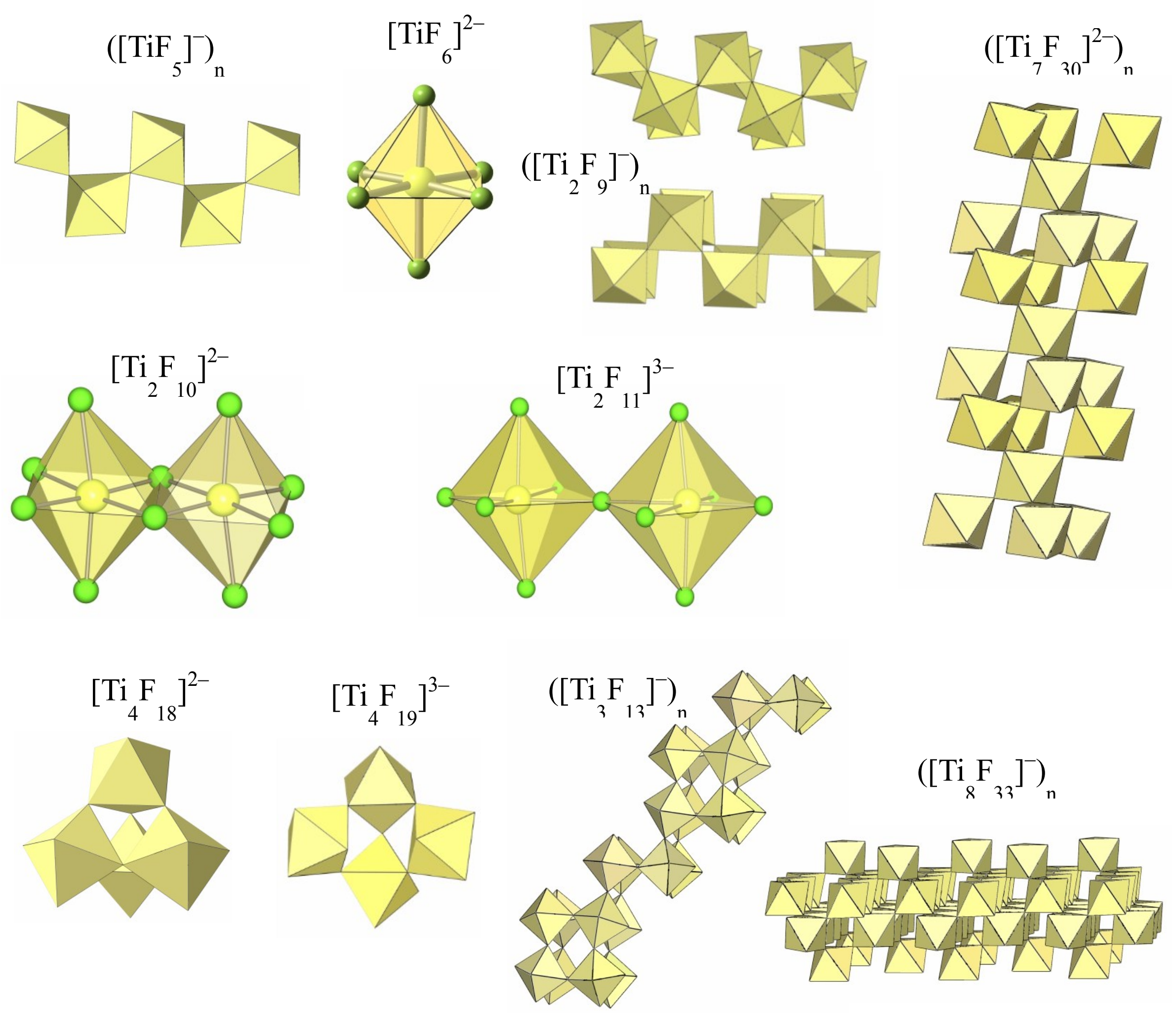

**Figure 1**: The known poly[perfluorotitanate(IV)] anions

The question, what influences the formation of different anions, is still opened. Among such factors are the size and the charge of cations. Declen et al [1], applied "volume-based" thermodynamic approach (VBT) and proposed, that the increase in the size of spherically symmetrical monocations favours the formation of $[Ti_2F_9]^-$ against $[Ti_4F_{18}]^{2-}$ ions, whereas small monocations with volume less than 0,019 nm$^3$ (volume of $Cs^+$) favour $[Ti_4F_{18}]^{2-}$ ions. This was later shown to be wrong [2].

In our study reactions between $TiF_4$ and AF compounds (where A stands for Li, Na, K, Rb, Cs) with different molar ratios in anhydrous HF were examined and crystal structures of obtained phases were determined. Reactions between LiF and $TiF_4$ lead only to the known phase $Li_2TiF_6$. In the system NaF-$TiF_4$-HF three different compounds were obtained. The reaction with molar ratio $n(NaF) : n(TiF_4) = 2 : 1$ yields the known $Na_2TiF_6$, whereas reactions with ratios 1 : 1 and 1 : 2 lead to previously unknown compounds $NaTiF_5{\cdot}HF$ and

$NaTi_2F_9·HF$, respectively. Anions appear as infinite monomeric or dimeric chains. Notably, in $NaTiF_5·HF$ salt there are two crystallographically independent Na atoms, which are coordinated with 6 or 7 fluorine atoms, meanwhile in $NaTi_2F_9·HF$ all Na atoms are coordinated with seven fluorine atoms.

In case of the largest $Cs^+$ cation, phases corresponding to formulas $Cs_2TiF_6$, $CsTiF_5$ and $CsTi_2F_9$ were obtained after reactions between CsF and $TiF_4$ with starting molar ratios 2 : 1, 1 : 1 and 1 : 2, respectively.

Completely unexpected results were achieved in the case of reactions with KF and RbF. Starting molar ratio $n(AF)/n(TiF_4) = 2 : 1$ (A = K, Rb) leads to well-known $K_2TiF_6$ and $Rb_2TiF_6$ phases. The reactions with 1 : 1 starting molar ratio yielded $KTiF_5·HF$ and $RbTiF_5·HF$, meanwhile, 1 : 2 molar starting ratios lead to compounds, which are formulated as $K_4Ti_8F_{36}·8HF$ and $Rb_4Ti_8F_{36}·6HF$. Their crystal structures consist from cubic poly[perfluorotitanate] anions (Figure 2) which haven't been observed before.

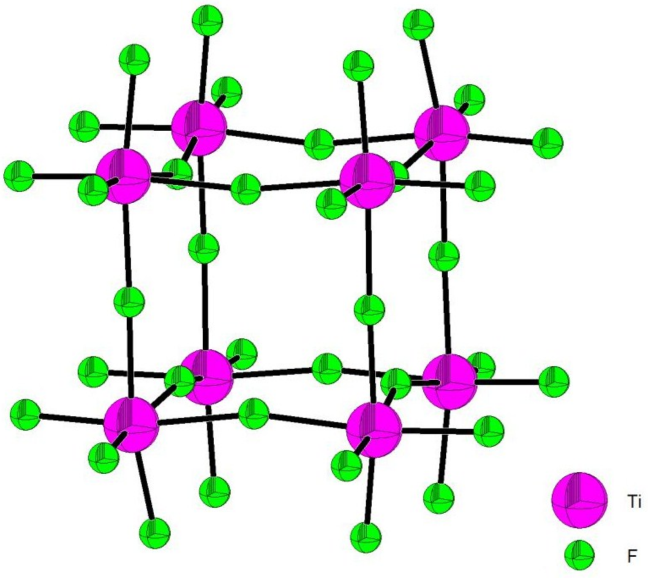

**Figure 2**: The structure of the novel $[Ti_8F_{36}]^{4-}$ anion

Monomeric chains (i.e. infinite $([TiF_5]^-)_n$ anions) observed in $ATiF_5$ compounds of Na, K, Rb and Cs are not completely identical. All of them are constructed according to zig-zag motif so, that each $TiF_6$ octahedron shares two equatorial fluorine atoms in *cis*- position with two neighbouring $TiF_6$ octahedra. In the $CsTiF_5$ salt, all Ti atoms belonging to the same chain, lie in the same plane. Octahedra completely overlap each other viewing along *a*-axe. In $NaTiF_5·HF$ the small tilting of octahedra is presented (torsion angle 15.32°). The largest tilting is observed in

$KTiF_5{\cdot}HF$ and $RbTiF_5{\cdot}HF$ salts. Pairs of octahedral $TiF_6$ species are rotated relative to each other by 67.84° and 66.22°, respectively. Parts of crystal structures of $ATiF_5({\cdot}HF)$ compounds are presented in Figure 3 (Na – grey, K – yellow, Rb – red, Cs – blue).

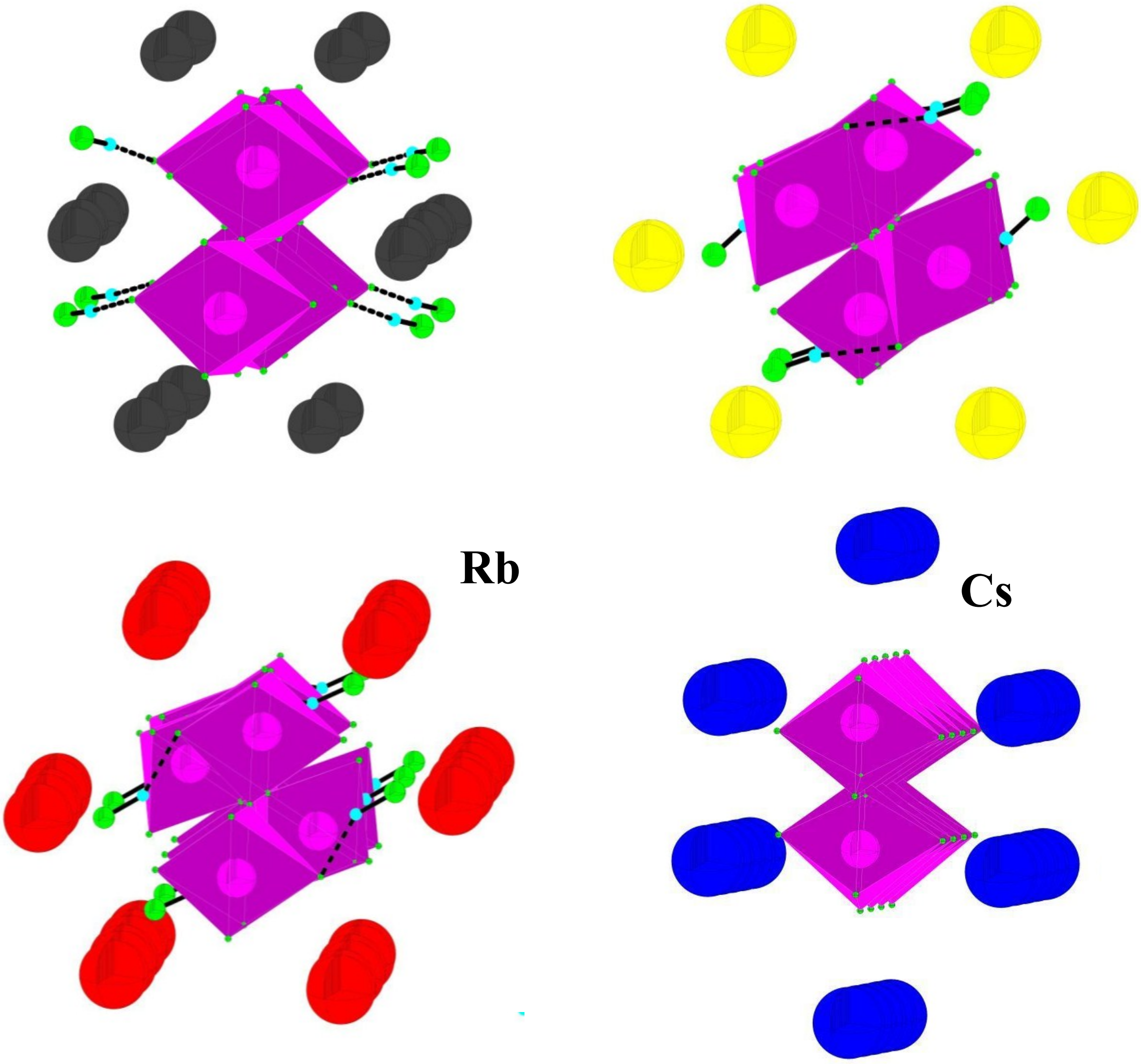

**Figure 3**: Parts of the crystal structures of $ATiF_5{\cdot}HF$ (A = Na, K, Rb) and $CsTiF_5$ compounds

## 2 Synthesis of poly[perfluorotitanate(IV)] compounds

A main synthetic method for the preparation of alkali poly[perfluorotitanate(IV)] compounds is carrying out reactions between titanium tetrafluoride $TiF_4$ and alkali metals fluorides AF (A = Li, Na, K, Rb, Cs) in anhydrous HF. Reactions were done in T-shaped vessels made from tetrafluoroethylen-hexafluoropropylen (FEP; Polytetra GmbH, Mönchengladbach, Germany) tubes (19 mm o.d. and 6 mm o.d.).

The wider tube is sealed from the bottom side and equipped with Teflon T-shaped cross and Teflon valve from the other side. The narrower tube is connected to the Teflon T-cross. All manipulations with volatile materials, such as aHF and $F_2$, are carried out in nickel-Teflon vacuum line and with non-volatile, such as $TiF_4$ – in a drybox (M. Braun) in an argon atmosphere.

The typical procedure consists from several steps. Firstly, calculated amounts of reactants ($TiF_4$ and AF, A = Li, Na, K, Rb, Cs) were loaded into the wider arm of a reaction vessel in the dry box. Argon was pumped away on nickel-Teflon vacuum line and aHF condensed into the reaction vessel at 77 K. Mixture was warmed to room temperature and constantly mixed. After one day a solution from the wide arm of the reactor was decanted into the narrower arm and a temperature gradient was maintained. When crystals, grown in narrower arm, were still covered with <1mm of aHF, perfluorinated oil (perfluorodecalin) was injected inside the narrower tube. The tube was cut and its content transferred to the cooled glass plate under the microscope. Single crystals were then selected from the crystallization products under the microscope and then transferred into the cold nitrogen stream of the diffractometer.

## 3 Characterisation of poly[perfluorotitanate(IV)] compounds

The synthesised compounds were structurally characterised by means of X-Ray single crystal structure analysis. Data were collected on a Rigaku AFC7 diffractometer equipped with a Mercury CCD area detector using graphite-monochromated Mo-$K_\alpha$ radiation ($\lambda$ = 0,71069 Å) at 200 K. The structures were solved by direct methods with the use of the SIR-92 program (program package TeXsan) and refined with the SHELXL-97 software implemented in the program package WinGX. The figures were prepared using the program DIAMOND 3.1.

## References:

[1]A. Decken, H. D. B. Jenkins, C. Knapp, G.B. Nikiforov, J. Passmore, J.M. Rautiainen. The autoionization of [$TiF_4$] by cation complexation with [15]crown-5 to give [$TiF_2$([15]crown-5)][$Ti_4F_{18}$] containing the tetrahedral [$Ti_4F_{18}$]$^{2-}$ ion. *Angew. Chem., Int. Ed.*, 44:7958-7961, 2005

[2]Z. Mazej, E. Goreshnik. Poly[perfluorotitanate(IV)] salts of [$H_3O$]$^+$, $Cs^+$, [$Me_4N$]$^+$ and [$Ph_4P$]$^+$ and about the existence of an isolated [$Ti_2F_9$]$^-$ anion in the solid state. *Inorg. Chem.*, 48:6918-6923, 2009

## For wider interest

Combining facts, that fluorine is the smallest and the most electronegative compound in the Periodic Table with the low bond energy in $F_2$ molecule, its compounds show quite specific properties, which could be very different between various fluorides (i.e. from great chemical stability to high reactivity, from resistance to high-temperatures to low temperature decomposition with release of fluorine). Two typical examples are highly chemically inert polytetrafluoroethylene (Teflon®) and highly reactive fluorinating agent $MnF_4$. Thus, fluorides could be successfully applied in various branches of science, technology and everyday life.

Much of the research is usually done due to economic benefits of industrial processes. But also contributions to fundamental science shouldn't be missed. They can't be precisely evaluated nowadays, but benefit in future. It's almost impossible to achieve highest possible results in any branch of human activities without strong theoretical explanations of processes. And that's what fundamental science does. Researches lead to various hypothesis and then to real operating theories and concepts. Also this work, which is devoted to poly[perfluorotitanate(IV)] compounds, mostly contributes to fundamental knowledge by collecting experimental material for understanding mechanisms of synthesis and opens new ways to selective synthesis of determined perfluorotitanates that then could be used as selective catalysts in different industrial productions.

# Vibrational spectra calculation of triphenylene: comparison of DFT and MP2 methods

**Gleb Veryasov**[1], **Dmitry Morozov**[2], **Gašper Tavčar**[1]

[1] Department of inorganic chemistry and technology, Jožef Stefan Institute, Ljubljana, Slovenia

[2] Lomonosov Moscow State University, Moscow, Russia

glebveryasov@gmail.com

**Abstract.** The infrared (IR) and Raman spectra of triphenylene with intensities were calculated using both density functional theory (DFT, B3LYP method) and Moller-Plesset perturbation method of second order (MP2) with cc-pVDZ basis set. Spectra were compared with experimentally measured; the agreement between the observed and calculated spectra is good in case of IR spectroscopy, MP2 simulated spectra were found have less vibrational band deviation from the real spectrum. In case of Raman spectroscopy, both methods gave good band position evaluation, however intensities are hardly correlated with experimental spectrum.

**Keywords**: Triphenylene, calculation, vibrational spectra.

## 1 Introduction

Vibrational spectra of aromatic hydrocarbons were intensively investigated for a significant period of time [1-7]. Such an investigation is important for developing trace analyses of these compounds by vibrational spectroscopic techniques, e.g. surface enchanted spectroscopy [8] and a very useful instrument for band assignment and detailed investigation of the vibrational spectra.

Detailed triphenylene crystal structure investigation was made by Ahmed and Trotter [9]. First calculation of vibrational spectra of triphenylene with detailed band assignments was made by Schettino [10]. Recent works reported were devoted to density functional theory (DFT) study of vibrational spectra of 1- and 2-nitrophenylene [8] and theoretical modeling of the influence of structural disorder on the charge carrier mobility was investigated by Mikolajczyk et. al. [11].

Current work provides comparison of applicability of methods – density functional theory, DFT and Moller-Plesset perturbation theory of the second order, MP2 for geometry optimization and vibrational spectra calculation of triphenylene by comparison of calculated spectra and bond distances to experimentally obtained.

# 2 Experimental part

## 2.1 Chemicals and instrumentation

Triphenylene was bought from Alfa Aesar.

Raman spectra was measured on triphenylene crystals on Horiba Jobin-Yvon LabRAM HR High Resolution Raman Spectrometer with internal laser 633 nm and power of 1,7 mW with total 100 scans.

IR spectrum was measured on PerkinElmer GX spectrometer in KBr cell using Nujol mull with resolution 1 $cm^{-1}$.

## 2.2 Computational details

All calculations were performed using DFT with B3LYP functionals [12-13] and MP2. All computations were performed carried out using GAMESS(US) program package [14]. We used cc-pVDZ basis set as well known for correlated methods. We also used $D_{3h}$ space symmetry group to reduce Hessian evaluation procedure time. First initial geometry of triphenylene was optimized with both methods, this gived us minimum energy points from which vibration spectra should be calculated. Then Forces Constants matrix (also known as Hessian matrix), which is matrix of the second derivatives of Energy by all coordinates, were calculated. Normal modes frequencies and corresponding IR intensities were evaluated by diagonalization of Force Constants matrix. For Raman spectra intensities polarizability tensor was calculated and then resulting Raman activities ($S_i$) were converted to Raman intensities ($I_i$) using following relationship from the intensity theory of Raman scattering [15-17]:

$$I_i = \frac{f(v_0 - v_i)^4 S_i}{v_i \left[1 - exp^{\left(-\frac{hcv_i}{kT}\right)}\right]} \qquad (1)$$

Where $\nu_0$ – is the exciting frequency ($cm^{-1}$) and $\nu_i$ – is the vibrational wave number of the i-th normal mode ($cm^{-1}$).

For the simulated spectra plots Doppler broadening was used with a bandwidth at half height of peak 30 cm$^{-1}$.

## 3 Results and discussion

Geometry of triphenylene (Fig. 1) was optimized within DFT and MP2 methods; detailed summary on optimization results in comparison with experimental data [9] is given in Table 1. Absence of symmetry in experimental data can be explained as crystal defects of single crystal used (reported R value was 9.6). Preparing a model for calculation we have taken into account $C_{3h}$ symmetry of the molecule, which resulted in decrease of the processor time required.

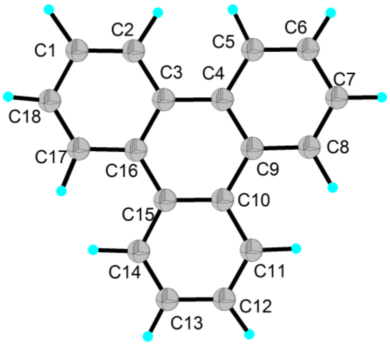

**Figure 1**: Triphenylene molecule (hydrogen atoms are not numbered)

**Table 1**. C-C bond lengths values in triphenylene molecule, shown in Fig. 1., experimental and calculated values (all values are given in Å)

| Bond | Experimental | DFT | MP2 |
|---|---|---|---|
| C1-C2 | 1,389 | 1,386 | 1,394 |
| C2-C3 | 1,408 | 1,416 | 1,421 |
| C3-C4 | 1,445 | 1,469 | 1,468 |
| C4-C5 | 1,434 | 1,416 | 1,421 |
| C5-C6 | 1,356 | 1,386 | 1,394 |
| C6-C7 | 1,386 | 1,404 | 1,410 |
| C7-C8 | 1,397 | 1,386 | 1,394 |
| C8-C9 | 1,402 | 1,416 | 1,421 |
| C9-C10 | 1,465 | 1,469 | 1,468 |
| C10-C11 | 1,427 | 1,416 | 1,421 |
| C11-C12 | 1,379 | 1,386 | 1,394 |
| C12-C13 | 1,405 | 1,404 | 1,410 |
| C13-C14 | 1,372 | 1,386 | 1,394 |
| C14-C15 | 1,418 | 1,416 | 1,421 |
| C15-C16 | 1,431 | 1,469 | 1,468 |
| C16-C17 | 1,405 | 1,416 | 1,421 |
| C17-C18 | 1,374 | 1,386 | 1,394 |
| C18-C1 | 1,411 | 1,404 | 1,410 |
| C16-C3 | 1,421 | 1,423 | 1,429 |
| C9-C4 | 1,411 | 1,423 | 1,429 |
| C15-C10 | 1,413 | 1,423 | 1,429 |

Both methods gave satisfactory results in bond lengths evaluation. Maximum deviation from the experimental data is 0,038 Å, observed for C5-C6 bond in MP2 method and C15-C16 bond in DFT.

## 3.1 Spectra discussion

Obtained and calculated spectra are represented in Fig. 2 and detailed band information is summarized in table 2. Most intensive band in Raman spectra, obtained experimentally (Exptl) was observed at 1339 cm$^{-1}$ occurred in calculated spectra at 1256 cm$^{-1}$ and 1468 cm$^{-1}$ in DFT and MP2 methods, respectively. It should be noted that both methods gave good band position evaluation, e.g. vibration appeared at 1299 cm$^{-1}$ (Exptl), 1300 cm$^{-1}$ (DFT) and 1298 cm$^{-1}$ (MP2);780 cm$^{-1}$ (Exptl), 787 cm$^{-1}$ (DFT) and 778 cm$^{-1}$ (MP2); 1457 cm$^{-1}$ (Exptl), 1461 cm$^{-1}$ (DFT) and 1468 cm$^{-1}$(MP2). However, relative intensities are hardly correlated with experimental spectrum, which can be explained by two factors: not taking into account the effect of surrounding in crystal and by inability to evaluate contribution of an alternating exciting electromagnetic field – calculation was made for a constant field.

Switching to infra-red spectra, it should be noted that calculated IR bands are in good correlation with experimental spectra, which can be observed even visually (Fig. 2, b). It was noted that MP2 method have lesser band wavenumber deviation: most intensive peak appeared at 740 cm$^{-1}$, 759 cm$^{-1}$ and 743 cm$^{-1}$ in measured spectrum, calculated by DFT and MP2, respectively. Bands devoted to the C-H (above 3000 cm$^{-1}$) vibrations in calculated spectra are shifted to higher wavenumber values in comparison with simulated spectra, which can be explained as influence of the surrounding in crystal in experimental spectrum.

Such a difference in spectra can be explained from the point of view of the nature of spectra in Raman and infra-red spectroscopy. In case of Raman spectroscopy spectra appears because of induced dipole moment which is caused by polarization of molecule and in IR spectra appear because of own dipole moment of molecule; so, spectra observed in Raman on morphology of the Raman tensor. Moreover, in calculation, as it was mentioned above, we consider a single molecule in vacuum, not taking into account surrounding, and, in case of Raman spectroscopy, we are not taking into account an alternating external filed.

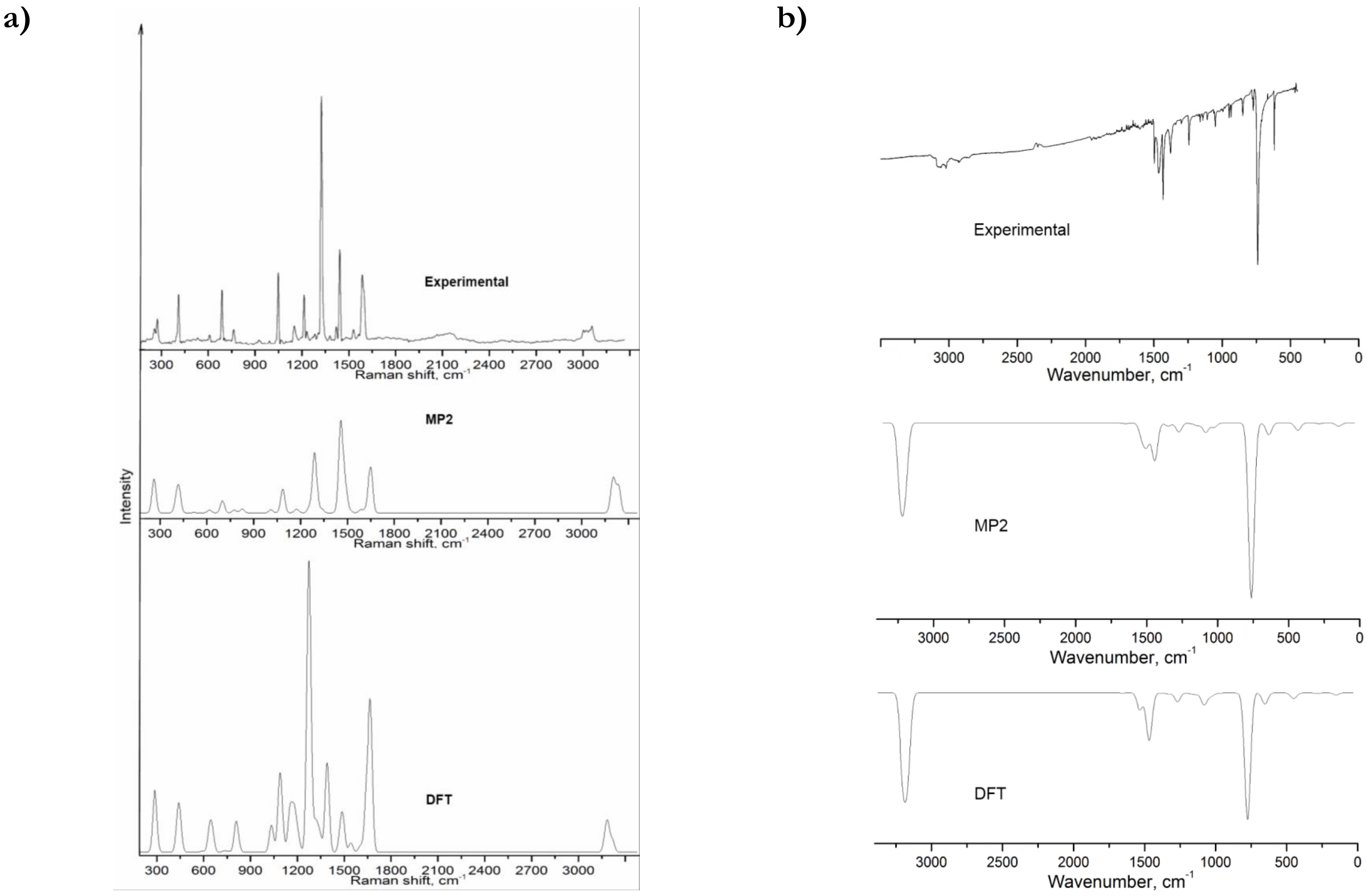

**Figure 2:** Calculated and experimental vibrational spectra of triphenylene, Raman (a) and IR (b)

**Table 2.** Calculated and experimental bands* and their intensities** (in brackets) in Raman and IR spectra of triphenylene

| DFT | | | MP2 | | | Experimental | |
|---|---|---|---|---|---|---|---|
| IR | Raman | | IR | Raman | | IR | Raman |
| 126 (0,02) | 260 (0,32) | 1379 (0,06) | 118 (0,02) | 257 (0,05) | 1597 (0,04) | 619 (0,33) | 261 (0,08) |
| 411 (0,01) | 277 (0,01) | 1461 (0,08) | 404 (0,01) | 260 (0,14) | 1626 (0,02) | 740 (1,00) | 280 (0,12) |
| 434 (0,04) | 411 (0,14) | 1476 (0,17) | 410 (0,03) | 393 (0,01) | 1659 (0,26) | 772 (0,11) | 416 (0,22) |
| 633 (0,04) | 422 (0,16) | 1528 (0,03) | 617 (0,03) | 404 (0,05) | 3217 (0,07) | 780 (0,04) | 616 (0,06) |
| 759 (1,00) | 617 (0,13) | 1590 (0,04) | 743 (1,00) | 420 (0,24) | 3230 (0,04) | 850 (0,10) | 697 (0,24) |
| 808 (0,01) | 633 (0,10) | 1629 (0,25) | 1013 (0,01) | 617 (0,02) | 3234 (0,22) | 936 (0,08) | 772 (0,08) |
| 1020 (0,01) | 711 (0,01) | 1654 (0,43) | 1073 (0,03) | 700 (0,13) | 3247 (0,02) | 951 (0,08) | 1060 (0,30) |
| 1069 (0,05) | 787 (0,17) | 1660 (0,28) | 1131 (0,01) | 708 (0,01) | 3264 (0,02) | 1051 (0,09) | 1164 (0,09) |
| 1135 (0,01) | 806 (0,01) | 3174 (0,02) | 1266 (0,03) | 778 (0,02) | 3266 (0,24) | 1109 (0,04) | 1227 (0,21) |
| 1259 (0,04) | 1014 (0,12) | 3175 (0,03) | 1342 (0,01) | 828 (0,02) | | 1142 (0,04) | 1244 (0,07) |
| 1461 (0,19) | 1020 (0,02) | 3189 (0,03) | 1439 (0,11) | 1013 (0,02) | | 1162 (0,04) | 1297 (0,06) |
| 1528 (0,07) | 1069 (0,31) | 3192 (0,12) | 1496 (0,06) | 1092 (0,26) | | 1244 (0,17) | 1339 (1,00) |
| 3175 (0,01) | 1087 (0,08) | 3204 (0,01) | 1530 (0,04) | 1177 (0,02) | | 1299 (0,03) | 1392 (0,05) |
| 3189 (0,29) | 1135 (0,16) | 3223 (0,05) | 3217 (0,01) | 1196 (0,01) | | 1340 (0,02) | 1434 (0,09) |
| 3207 (0,01) | 1159 (0,20) | 3225 (0,01) | 3230 (0,16) | 1266 (0,03) | | 1433 (0,44) | 1457 (0,39) |
| 3223 (0,30) | 1177 (0,08) | | 3247 (0,01) | 1298 (0,67) | | 1497 (0,23) | 1546 (0,08) |
| | 1192 (0,04) | | 3264 (0,19) | 1342 (0,02) | | 2856 (0,02) | 1580 (0,06) |
| | 1256 (1,00) | | | 1439 (0,01) | | 2926 (0,05) | 1603 (0,30) |
| | 1259 (0,39) | | | 1468 (1,00) | | 3021 (0,08) | 3031 (0,08) |
| | 1300 (0,17) | | | 1496 (0,12) | | 3057 (0,08) | 3051 (0,07) |
| | 1326 (0,11) | | | 1505 (0,02) | | 3077 (0,08) | 3070 (0,08) |
| | 1374 (0,24) | | | 1530 (0,01) | | 3107 (0,02) | 3086 (0,09) |

* - band positions are given in $cm^{-1}$. In table are given only bands with non-zero activity

** - intensities are given in relative units, normalized to the most intensive peak in spectrum

## 3 Conclusions

Geometry optimization and vibrational spectra calculation within density functional method, DFT and Moller-Plesset perturbation of second order, MP2 were made in GAMESS(US) program package. Comparison of data obtained with experimentally measured spectra and bond distances, available in literature showed that both method give good evaluation of the atom bond distances and normal frequencies for the IR spectra, except C-H vibrations region, which appear at lower wavenumber values in experimentally obtained spectrum, what can be explained as influence of the surrounding in solid phase. For Raman spectroscopy both methods gave good evaluation of band positions, however intensities are hardly correlated to the real spectrum because of absence of opportunity to take into account effect of the surrounding and of an alternating exciting electromagnetic field. It shows that IR spectra calculation for the moment is more promising for qualitative correlation of calculated and experimental spectra.

To summarize, both methods are suitable for spectra calculation; MP2 method showed lesser band position deviation from the both experimentally obtained spectra – Raman and IR.

## References:

[1]V. Schettino, N. Neto, and S. Califano, *J. Chem. Phys.* 44, 2724, 1966

[2]V. Schettino, *J. Chem. Phys.* 46, 302, 1967

[3]R. Mecke and K. Witt, Z. *Naturforsch.* A 21, 1899, 1966

[4]R. Mecke and K. Witt, Z. *Naturforsch.* A 21, 1247, 1967

[5]J. Semmler, P. W. Yang, G. E. Crawford, *Vibr. Spectrosc.* 2, 189, 1991

[6]K. Meerkel, A. Kocot, R. Wrzalik, B. Orgasinsak, *Acta. Phys. Pol.* A 98, 525, 2000

[7]D. M. Hugins, S. A. Sandford, *J. Phys. Chem.* A 102, 329, 1198

[8]K. K. Onchoke, M. E. Parks, A. H. Nolan, *Spectrochim. Acta* A 74, 579, 2009

[9]F. R. Ahmed and J. Trotter, *Acta. Cryst.* 16, 503, 1963

[10]V. Schettino, *J. Mol. Spectrosc.*24, 78, 1970

[11]M. M Mikolajczyk, P. Toman, W. Bartkowiak, *Chem. Phys. Lett.* 485, 253, 2010

[12]A. D. Becke, *J. Chem. Phys.*98, 5648, 1993

[13]C. Lee, W. Yang, R. G. Parr, *Phys. Rew.* B 37, 785, 1998

[14] M. W. Schmidt, K. K. Baldridge, J. A. Boatz, S. T. Elbert, M. S. Gordon, J. J. Jensen, S. Koseki, N. Matsunaga, K. A. Nguyen, S. Su, T. L. Windus, M. Dupuis, J. A. Montgomery*, J. Comput. Chem.* 14, 1347, 1993

[15] P. L. Polavarapu, *J. Phys. Chem.* 94, 8106, 1990 (RAMAN)

[16]G. Keresztury, Raman spectroscopy: theory, in: J. M. Chalmers, P. R. Griffiths (Eds.), Handbook of Vibrational Spectroscopy, vol. 1., Wiley, 2002, 71-87

[17]G. Keresztury, S. Holly, J. Varga, G. Besenyei, A. Y. Wang, J. R. Durig, *Spectrochim. Acta* 49 A, 2007, 1993

## For wider interest

Computational methods in chemistry, or just “calculations” is a powerful instrument for revealing mechanisms of reactions, theoretical modeling of different processes and molecules. Modern supercomputers allow to model and even predict reactions even in such complicated tasks in biological systems as fermentative reactions, where geometry of an active center in molecule play fundamental role. This research is devoted to spectroscopy of aromatic hydrocarbons; we focused on two vibrational spectroscopy methods – Raman spectroscopy and infra-red spectroscopy (IR). Current work provides investigation of applicability of two calculation methods – density functional theory (DFT) and Moller-Plesset perturbation theory of second order (MP2). Applicability of methods was evaluated by comparison of calculated atomic coordinates and spectra with in literature available coordinates and experimentally obtained spectra. This investigation contributes to the building of the model for further calculations of more complicated structures, containing polycyclic aromatic hydrocarbons (PAH), e.g. complex compounds, which can include PAH molecules as a $\pi$- donor ligands or different PAH nitro- derivatives, which were proved to be mutagenic . Opportunity to predict and calculate spectra can help in understanding and detailed investigation of spectra of these compounds and, moreover, help to invent more precise methods for trace analysis of pollutants by sensitive spectroscopic methods.

# Hydrodynamic cavitation: a technique for augmentation of removal of persistent pharmaceuticals?

**Mojca Zupanc**[1,2], Tina Kosjek[1], Boris Kompare[3], Željko Blažeka[4], Uroš Ješe[5], Matevž Dular[5], Brane Širok[5], Ester Heath[1,2]

[1] Department of Environmental Sciences, Jozef Stefan Institute, Ljubljana, Slovenia

[2] Jozef Stefan International Postgraduate School, Ljubljana, Slovenia

[3] Faculty of Civil and Geodetic Engineering, University of Ljubljana, Ljubljana, Slovenia

[4] Ecological Engineering Institute Ltd, Maribor, Slovenia

[5] Faculty of Mechanic Engineering, University of Ljubljana, Ljubljana, Slovenia

mojca.zupanc@ijs.si

**Abstract.** Pharmaceutical residues enter the environment mainly due to insufficient wastewater treatment. Many pharmaceuticals are not readily degraded during conventional wastewater treatment, therefore advanced technologies to remove them need to be investigated. In our study we examined the removal of six pharmaceuticals (clofibric acid, ibuprofen, naproxen, ketoprofen, carbamazepine and diclofenac) using a combination of hydrodynamic cavitation and hydrogen peroxide. We performed the experiments in distilled water under different operating conditions (initial pressures set at 6, 5, 4 bar). The results showed good removal of naproxen (up to 86%) and satisfactory removal of both carbamazepine (up to 72%) and diclofenac (up to 77%), which are only moderately removed during biological water treatment (21% and 48%, respectively). Removal of clofibric acid, ibuprofen and ketoprofen by cavitation was lower and inconsistent (45%±35%, 48%±31% and 52%±27%, respectively).

**Keywords**: pharmaceuticals, hydrodynamic cavitation, removal

## 1 Introduction

Awareness of the presence of pharmaceuticals in the environment began around 30 years ago [1]. Since then the scientific community has made a significant effort into understanding fate, behaviour and the risks posed by pharmaceuticals in the environment [2], [3], [4]. Pharmaceuticals are developed for human and veterinary use [5] and after their application they reach wastewater treatment plants mostly *via* the domestic sewage system [6]. Their concentrations detected in different environmental compartments are in the ng $L^{-1}$ to μg $L^{-1}$ range [1], [3]. Since many pharmaceuticals are not readily degradable by conventional treatment schemes [6], research into and development of alternative methods like advanced oxidation processes is important [7].

Cavitation is a physical phenomenon where the formation, growth and subsequent collapse of small bubbles and bubble clusters occurs simultaneously releasing high amounts of energy [7]. Cavitation belongs to a group of advanced oxidation processes (AOP), the basis of which is *in situ* formation of hydroxyl radicals that can oxidise recalcitrant organic compounds [7], [8]. In hydrodynamic cavitation, the inception and collapse of small bubbles and bubble clusters is the result of an increase of the fluid velocity and the decrease of static pressure, which occurs when the fluid passes through a constriction [7]. The destruction of organic compounds can occur *via* two pathways: free radical attack and pyrolysis, and which of the two predominates depend on the properties of the compound and on cavitation intensity [7]. The addition of hydrogen peroxide enhances the amount of free radicals.

The main objective of our study was to test a series of techniques that could be coupled to biological treatment to enhance overall removal efficiency. For this purpose we investigated the removal of six pharmaceuticals (clofibric acid: CLA, ibuprofen: IBP, naproxen: NP, ketoprofen: KTP, carbamazepine: CBZ and diclofenac: DF) with hydrodynamic cavitation under different operating conditions including the addition of hydrogen peroxide.

## 2 Experimental setup

The hydrodynamic cavitation reactor (HC-reactor) setup included two reservoirs connected by a symmetrical venturi pipe with a constriction of 1 mm height and 5 mm width. As the flow passes through the constriction, it accelerates, causing a drop in the static pressure resulting in cavitation. The sample is introduced into the left reservoir (Figure 1), while the right reservoir remains empty. The pressure in the left reservoir is then increased to the desired level, while the pressure in the right reservoir is kept at 1 bar. When the regulating valve is opened, the reactor contents are transferred from the left reservoir to the right one in about 10s. The process is then reversed (cycled) for a given number of times. Figure 1 shows a schematic of the reactor set up.

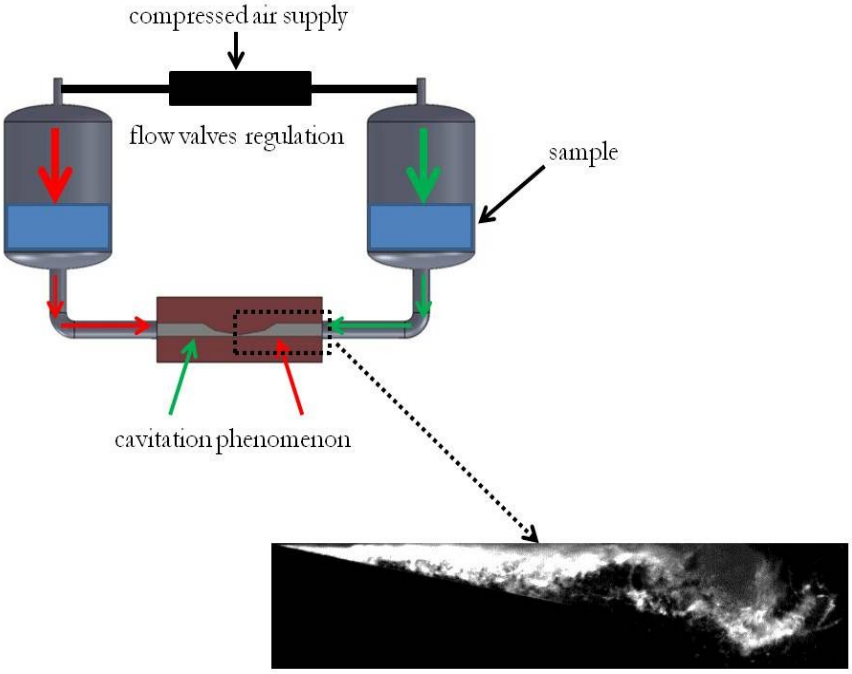

**Figure 1**: HC-reactor set up and cavitation phenomenon

In our experiments we observed the effects of cavitation in 1 L of distilled water spiked with a mixture of the model pharmaceuticals (clofibric acid, ibuprofen, naproxen, ketoprofen, carbamazepine and diclofenac) at environmentally relevant concentrations (1 µg $L^{-1}$). The operating conditions were selected in previous experiments (data not shown) and were as follows: cavitation time (30 minutes) and $H_2O_2$ addition (30%, 20 mL). As a variable, we selected initial pressure since this parameter defines flow velocity and the intensity of cavitation. Experiments were made at 4, 5, and 6 bar. In order to ascertain the repeatability of cavitation, we performed the experiments under optimum conditions (6 bar) in 10 parallels.

## 3 Results and discussion

The results show that highest removal of all six pharmaceuticals was achieved at 6 bar (Figure 2). This was in agreement with the presumption that a higher initial pressure results in an increase in cavitation intensity. The removal of pharmaceuticals at 5 bar was slightly better than at 4 bar.

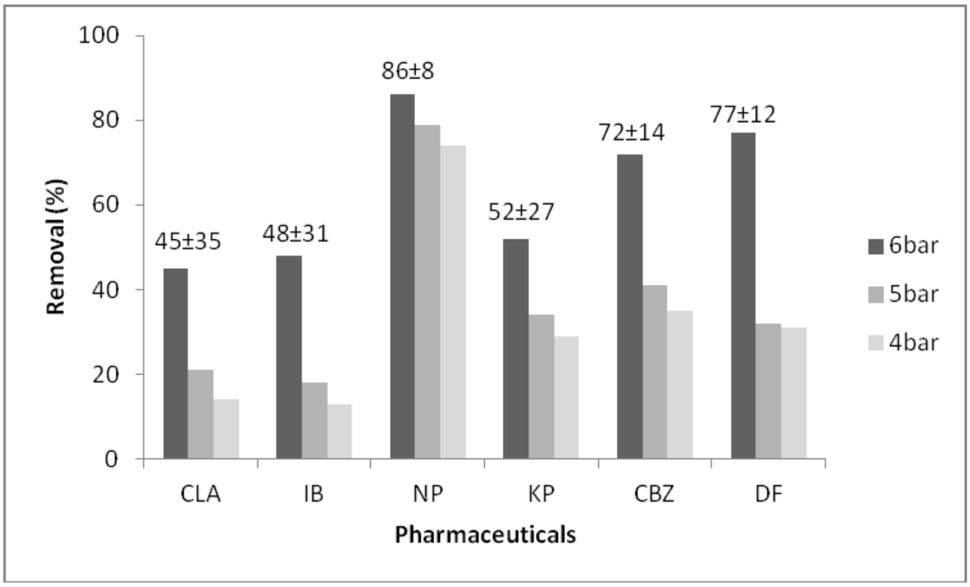

**Figure 2**: Removals (%) of pharmaceuticals with hydrodynamic cavitation under different initial pressures (6, 5 and 4 bars)

At 6 bar we achieved 86%±8% removal of naproxen and 72%±14% and 77%±12% of carbamazepine and diclofenac, respectively. The removal efficiencies of clofibric acid, ibuprofen and ketoprofen were lower and inconsistent compared to naproxen. As mentioned before the destruction of organic compounds with hydrodynamic cavitation is dependent on their structure and chemical properties and the different chemical structure of the selected pharmaceuticals may be the reason for different removal efficiencies.

Since carbamazepine and diclofenac are not readily and consistently removed during biological waste water treatment (21% and 48%, respectively), which we established in our previous work and is in accordance with the literature [8], [9], hydrodynamic cavitation could be a viable technique for augmenting their removal. To authors knowledge few data exist regarding the removal of pharmaceuticals using hydrodynamic cavitation. Since cavitation is a technique that is relatively easy to scale up [10], it should be given more attention.

In the future we will combine hydrodynamic cavitation and Fenton process to achieve better removal of recalcitrant pharmaceuticals (clofibric acid, ibuprofen and ketoprofen) and further augment the removal of naproxen, carbamazepine and diclofenac. After the determination of removal efficiencies and optimal operational conditions for this combination in distilled water, we will transfer the technology to more complex matrices (effluents of biological wastewater treatment plants). Last but not least, our aim is to determine the best combination of different processes considering removal of pharmaceuticals, feasibility and cost effectiveness, possibly coupling AOP sequentially to biological treatment.

## References:

[1]J. P. Bound, K. Kitsou, N. Voulvoulis. Household disposal of pharmaceuticals and perception of risk to the environment. *Environmental Toxicology and Pharmacology,* 21: 301–307, 2006

[2]Halling-Sørensen B., Nors Nielsen S., Lanzky P.F:, Ingerslev F., Holten Lützhøft, Jørgensen. Occurence, Fate and Effects of Pharmaceutical Substances in the Environment – A Review. *Chemosphere*, 36 : 357-393, 1998

[3]Ternes T.A., Giger W., Joss A. Introduction. *In: Human Pharmaceuticals, Hormones and Fragrances: The challenge of micropollutants in urban water management.* Ternes T.A., Joss A., 2006.

[4]Farre M., Perez S., Kantiani L., Barcelo D. Fate and toxicity of emerging pollutants, their metabolites and transformation products in the aquatic environment. *Trends in Analytical Chemistry*, 27 : 991-1007, 2008

[5]O.V. Enick, M.M. Moore. Assessing the assessments: Pharmaceuticals in the environment. *Environmental Impact Assessment Review* , 27: 707–729, 2007

[6] A. Joss, S. Zabczynski, A. Göbel, B. Hoffmann, D. Löffler, C. S. McArdell, T. A. Ternes, A. Thomsea, H. Siegrist. Biological degradation of pharmaceuticals in municipal wastewater treatment: Proposing a classification scheme. *Water Research*, 40: 1686 – 1696, 2006

[7]P.R. Gogate, A.B. Pandit. A review of imperative technologies for wastewater treatment I:oxidation technologies at ambient conditions. *Advances in Environmental Research,* 8: 501-551, 2004

[8]P. Braeutigam , M. Franke, R. J. Schneider , A. Lehmann , A. Stolle, B. Ondruschka. Degradation of carbamazepine in environmentally relevant concentrations in water by Hydrodynamic-Acoustic-Cavitation (HAC). *Water Research,* 46: 2469-2477, 2012

[9]M. Ravina, L. Campanella, J. Kiwi. Accelerated mineralization of the drug Diclofenac via Fenton reactions in a concentric photo-reactor. *Water research*, 36: 3553-3560, 2002

[10]A.G. Chakinala, P.R. Gogate, A.E. Burgess, D.H. Bremner. Treatment of industrial wastewater effluents using hydrodynamic cavitation and the advanced Fenton process. *Ultrasonics Sonochemistry*, 15: 49-54, 2008

Investing in your future
OPERATION PART FINANCED BY THE EUROPEAN UNION
European Social Fund

## For wider interest

To meet the ever growing demand for improved healthcare, pharmaceuticals are being produced in increasing amounts. As a consequence, pharmaceutical residues in the environment are becoming a concern. This is because many of these compounds have been proven to be resistant to conventional microbiological wastewater treatment. In response, new technologies are necessary to reach increasingly stringent regulation on water quality.

In this study we investigated hydrodynamic cavitation which is a potent advanced oxidation process (AOP) and is relatively cost-effective and easy for scale up. Caviation is the term given to the formation and subsequent implosion of bubbles that result when the partial local pressure in a fluid drops below vapour pressure. The collapse of the bubbles can generate a significant increase in local pressures and temperatures, called "hot spots". Such extreme conditions can result in the formation of free radicals, which are potent oxidising species capable of breaking down organic compounds. Our intention is to make use of these free radicals by deliberately cavitating the effluent flow from a wastewater plant. Additionally, our idea is to increase the amount of free radicals formed by adding hydrogen peroxide. Initial experiments have been carried out using a two reservoir system in which the fluid can be transferred from one to the other by varying the pressures in each. As the fluid passes from one reservoir to the other, it must pass through a constriction, which creates a pressure drop in the fluid resulting in cavitation. We tested the apparatus using six common pharmaceuticals: clofibric acid, ibuprofen, naproxen, ketoprofen, carbamazepine and diclofenac at various pressures 4, 5 and 6 bar. A pressure of six bars was optimum. In the case of carbamazepine and diclofenac, the results have been positive, improving the removal efficiency by 50% and 30 %, respectively, compared to conventional water treatment. In the case of clofibric acid, ibuprofen and ketoprofen the results are less conclusive. Further study will involve optimisation of cavitation process and its combination with biological water treatment in order to improve overall removal of resistant contaminants.

# Informacijske in komunikacijske tehnologije (Information and Communication Technologies)

# Reducing costs with computer power management

**Lucas Benedičič**[1], **Peter Korošec**[2]

[1] Jožef Stefan International Postgraduate School, Ljubljana, Slovenia

[2] Computer Systems Department, Jožef Stefan Institute, Ljubljana, Slovenia

lucas.benedicic@gmail.com

**Abstract.** In this work, we present a software-based solution to automate the power control of desktop computers. The deployment of the proposed software system is simply done over the existing infrastructure of the organization, thus minimizing the required investment. Our initial analysis shows a cost reduction of more than 52% by reducing the power consumption of computers and their monitors.

**Keywords:** energy, efficiency, automatic control, computer.

## 1 Introduction

Information technology (IT) has an enormous potential for implementing environmentally-friendly practices. As Sheehan explains in [1], IT is a major consumer of energy and a net contributor of greenhouse gas emissions and other forms of waste. In a report by Gartner Inc., cited in [1], it is estimated that the IT industry is responsible for 2% of global $CO_2$ emissions. This a priori relatively small percentage is actually equivalent to the impact the airline industry has in the environment [2].

Different works have been published confirming the ineffective use of energy in IT [3], [4], but only some of them implement solutions to tackle this problem [5]. Unfortunately, most of these systems impose significant obstacles to practical deployment, by either requiring modifications to network interface hardware or, in some cases, the host operating system software.

We propose a software-based solution to save power by automatically turning personal computers (PCs) off (without user's intervention) when they are not being used. Our system takes advantage of the existing server infrastructure within an organization.

## 2 System architecture

The architecture of the system is depicted in Figure 1. A Power Server (PS) controls the power state of $n$ hosts ($h_1$, $h_2$, …, $h_n$) by receiving events from $m$ personnel registration terminals ($r_1$, $r_2$, …, $r_m$). When a user arrives at her/his workplace in the morning, she/he identifies at one of the registration terminals, thus triggering the 'arrive' event. The registration terminal informs the Time Management System (TMS) that the user has arrived. The TMS, in turn, informs the PS. The PS reacts by sending a Wake on LAN (WOL) magic packet [6] to the user's computer, thus turning it on from its previous sleep, hibernate or off state. Similarly, when the user leaves her/his workplace by identifying at a terminal, the 'leave' event is generated. In this case, the PS changes the power state of the user's computer from active to sleep, hibernate or off, depending on the user's personal configuration.

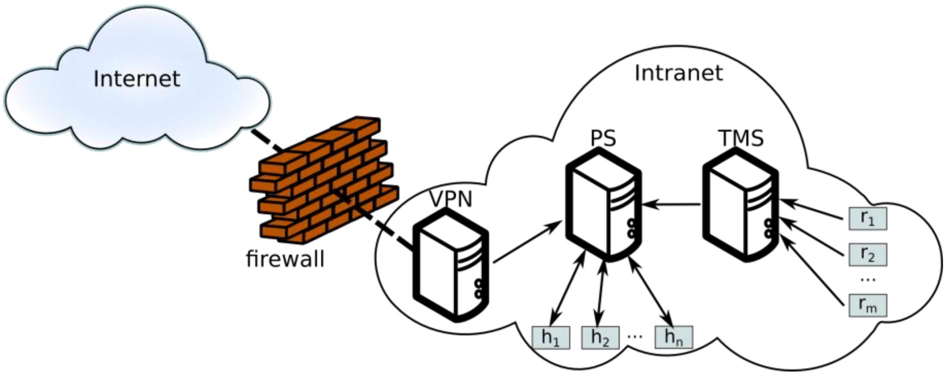

**Figure 1**: System architecture

The PS also receives events regarding remote Virtual Private Network (VPN) connections into the organization's intranet. These events, 'arrive' for authorized logins into the VPN and 'leave' when logging off, cause the same power state changes at the user's computer as the registration terminals do.

# 3 Implementation

## 3.1 Server side

The PS is entirely implemented as a web application. Hypertext transfer protocol secure (HTTPS) is used to transfer common HTML pages, which are used for the administration tasks and adjusting the users' configuration. Each of the 'arrive' and 'leave' events are accessed through their own uniform resource identifier (URI) over HTTPS, enforcing additional authentication to avoid misuse and emphasize the security aspect, e.g. https://ps.example.si/*usr_id*/wakeup, where *usr_id* is a key that uniquely identifies the user that generated the event, either by arriving at her/his workplace or by connecting to the organization's VPN. On the other hand, https://ps.example.si/*usr_id*/sleep, handles the event triggered by the user leaving office or disconnecting from the VPN.

## 3.2 Host side

A Service Application (SA) runs on every host ($h_1$, $h_2$, …, $h_n$ as marked in Figure 1) that is controlled by the PS. The main objective of the SA is to make sure that the centrally-controlled power schema, imposed by the PS, does not conflict with the user's activities. Such situations appear, for example, when the user starts a long-running process that finishes after the user has left, or when dealing with software updates, or even with long file transfers like backup operations. The SA makes sure that the host changes its power state only after the on-going execution has finished. To achieve this, it is constantly monitoring processor usage and network activity on the host after the 'sleep' message has been received from the PS. Once both monitored measures fall below the configured threshold for a given amount of time, the previously queued power-state change is executed.

# 4 Analysis

Power consumption measurements were taken using a Voltcraft Energy Check 3000 power meter. A total of 30 computers were measured, including different hardware, software and operating systems. The power consumption of each computer was continuously measured for 24 hours, separating between active (the user is operating the computer) and standby modes (the computer goes into sleep mode). During the active mode, ordinary operations were carried out by the users, e.g. web browsing, editing documents, receiving and sending mail, etc. The measurement results, expressed in watts/hour, are shown in Table 1.

**Table 1**: Power consumption measurements (W/h).

| Equipment | Mode | Minimum | Maximum | Average | Std. Dev. |
|---|---|---|---|---|---|
| Computer | Active | 35.73 | 127.91 | 78.39 | 31.27 |
| Computer | Standby | 1.32 | 2.63 | 1.69 | 0.74 |
| Monitor | Active | 16.10 | 128.22 | 42.48 | 25.45 |
| Monitor | Standby | 0.30 | 4.77 | 1.15 | 1.05 |

We have also calculated the potential savings, achievable by the PS after its deployment for similar conditions. For the environment without PS, we have assumed the PCs are in use during weekdays for 9 hours per day, spending the average consumption for active mode. For the remaining 15 hours, as well as during weekends and public holidays (i.e. no-activity periods), we have considered the minimum active-mode consumption. The other environment we have considered is PS-enabled. The only difference is the consumption over the no-activity periods, for which we have assumed the average consumption in standby mode. All consumption values are shown in Table 1. The estimation results, depicted in Table 2, were calculated for 249 working days during the year 2012, for complete PCs (computers and monitors). The average price of electricity for the industrial sector was provided by SURS [7].

**Table 2**: Cost-saving estimation for one year (in EUR).

| Equipment | Price (kWh) | Costs (no PS) | Costs (PS) | Savings |
|---|---|---|---|---|
| 100 PCs | 0.1109 | 6764.83 | 3210.02 | 3554.81 |
| 310 PCs | 0.1109 | 20970.96 | 9951.06 | 11019.90 |

## 5 Conclusion

We have presented an innovative solution for computer power management that automatically turns PCs off when they are not in use. The solution installation requires a minimal initial investment, since it is completely software-based and takes advantage of the existing infrastructure. The initial results of our analysis show a cost reduction of more than 52%, saving more than 10,000 EUR a year from of a group of 300 PCs.

## References

[1] M.C. Sheehan, S.D. Smith, and EDUCAUSE Centre for Applied Research. *Powering Down: Green IT in Higher Education*. EDUCAUSE, 2010.

[2] C. Pettey. *Gartner estimates ICT industry accounts for 2 percent of global* $CO_2$ *emissions.* http://www.gartner.com/it/page.jsp, 2007.

[3] M. Chetty, AJ Brush, B.R. Meyers, and P. Johns. It's not easy being green: understanding home computer power management. In *Proceedings of the 27th international conference on Human factors in computing systems*, pages 1033–1042. ACM, 2009.

[4] E. Reinhard, B. Champion, N.N. Schulz, R. Gould, E. Perez, and N. Brown. Computer power consumption and management: earth, wind, and fire: Sustainable energy for the 21st century. In *Power Systems Conference and Exposition (PSCE)*, 2011 IEEE/PES, pages 1–8. IEEE, 2011.

[5] Y. Agarwal, S. Hodges, R. Chandra, J. Scott, P. Bahl, and R. Gupta. Somniloquy: augmenting network interfaces to reduce PC energy usage. In *Proceedings of the 6th USENIX symposium on Networked systems design and implementation*, pages 365–380. USENIX Association, 2009.

[6] S.T. Bui. Wake on LAN power management, 2006, US Patent. 11/403, 452.

[7] M. Suvorov and J. Zalar. Statistični urad RS - Cene energentov, Slovenija, 1. polletje 2011, http://www.stat.si/novica_prikazi.aspx?id=4151, 2012.

## For wider interest

Many organizations are increasingly leaving their networked computers turned on 24 hours a day, 7 days a week, to allow for out-of-hours access by employees. Some administrators may say they want to do a backup, or the user may want to be able to remotely connect into her/his computer. But most of the time these personal computers (PCs) remain idle, wasting significant amounts of energy.

In this work, we present a software-based solution to automate the power control of desktop PCs. The deployment of the proposed system is simply done over the existing infrastructure (i.e. hardware) of the organization, thus minimizing the required investment. The controlling software, named Power Server, reads events from the personnel registration terminals. These events generate the power-state changes of the owner's PC, turning it on when arriving to office, and off when leaving home. Power Server also reacts to remote VPN connections in a similar way. The user may also modify the configuration and select, for example, to put the PC into a low-energy sleep or hibernation mode instead of turning it off.

The energy savings come from the fact that each PC is kept running strictly for the time it is being used, neither more nor less. Since even the latest low-power desktop PCs consume around 40 watts of power when idle, the potential savings of a Power Server installation are very promising: more than 52% of energy-consumption reduction, which means more than 10,000 EUR a year for an organization hosting just 300 desktop PCs.

There is other software that can be used to wake up sleeping PCs, such as Apple's Wake-on Demand and Microsoft's Sleep Proxy, but none of them provides the needed level of flexibility to maximize energy savings. Moreover, Power Server works without user's intervention, since the power-state changes are automatically performed, based on external events.

# Risk Assessment Using Local Outlier Factor Algorithm

**Božidara Cvetković**[1,2], **Mitja Luštrek**[1,2]

[1] Department of Intelligent Systems, Jožef Stefan Institute, Ljubljana, Slovenia

[2] Jožef Stefan International Postgraduate School, Ljubljana, Slovenia

boza.cvetkovic@ijs.si

**Abstract.** In this paper we introduce the unsupervised machine-learning algorithm named Local Outlier Factor (LOF), for health risk assessment. In general the LOF algorithm is used with numerical attributes and the outcome of the algorithm is parting the patterns into normal and abnormal events. In this paper we introduce the extended LOF algorithm with three experimental contributions: (i) utilization of complex nominal attributes, (ii) the developed methodology for detecting the level of event anomaly (low risk, medium risk and high risk) and (iii) providing the information about the risk status for each analysed parameter.

**Keywords**: anomaly detection, unsupervised machine-learning, LOF, nominal attributes, health risk assessment

## 1 Introduction

The purpose of the medical expert systems is to disburden the workload of physicians and ease the detection of abnormal events. Research in this field is quite mature. However, modules that assemble the expert system are based on predefined rules created by an expert or models trained on the labelled data. For example, when a patient's health is normal, the parameters characterizing it usually follow some recurrent patterns. When the patient's health is not normal certain parameters move from the normal state and influence others. The rules and models created to detect the risk are highly correlated with the disease they were created for. This means that in case we would like to analyse a different disease, new domain rules have to be created and models re-trained. For that we would need a relatively large amount of labelled data.

There are four problems we are focused on in this research (i) can we use unlabelled data, (ii) is it possible to consider the individuality of the patient regarding the pattern of vital signs and their influence to each other, (iii) can we detect the level of the abnormality and (iv) is it possible to detect how much do the analysed parameters contribute to the risk?

In this research we have adopted the Local Outlier Factor (LOF) algorithm, since it seems the most appropriate method to detect the abnormal events using unlabelled data and by that keep the individuality of the person. The algorithm was extended with the procedure for abnormality level detection per monitored parameter. The developed algorithm enables the doctor to see which of the monitored parameters contribute to the overall risk at most.

## 2 The Anomaly Detection for Risk Assessment

When a patient's health is normal, the parameters characterizing it usually follow some recurrent patterns. Such patterns can be learned and when a new pattern – an anomaly – is detected, the doctor is notified. If the doctor judges the new pattern to be normal, he can indicate this to the anomaly detection sub-component, and the sub-component will not consider such a pattern anomalous in the future.

### 2.1 Local Outlier Factor Algorithm

We use the Local Outlier Factor (LOF) algorithm [1] to detect anomalies. The algorithm compares the density of data instances around a given instance A with the density around A's neighbors. If the former is low compared to the latter, it means that A is relatively isolated – that it is an outlier. Such outliers are considered anomalous. The LOF algorithm computes the so-called LOF value for each instance, which is a measure of how anomalous the instance is.

To use the LOF algorithm for risk assessment, it must be trained on a number of instances consisting of the parameters of a patient when his/her risk is normal. For the purpose of the anomaly detection sub-component, such risk is considered low, even though it may be high in absolute terms. After the training data is processed, the parameters of the algorithm must be set: (1) the number of neighbors to consider, (2) the low threshold, which separates the LOF values corresponding to low risk (green) from those corresponding to medium risk (yellow), and (3) the high threshold, which separates the LOF values corresponding to medium risk from those corresponding to high risk (red). Finally, the algorithm can compute the LOF values of new instances and assess the risk.

### 2.2 The number of neighbours and thresholds

To evaluate the performance of the LOF algorithm, both normal (low risk) and anomalous (elevated risk) instances are needed. We use the concept of the receiver operating characteristic (ROC) curve. The ROC curve plots the true positive rate (TPR or sensitivity) vs. the false positive rate (FPR or 1 – specificity) at all possible thresholds. The TPR is the fraction of instances correctly classified as normal among all the truly normal ones. The FPR is the fraction of instances incorrectly classified as normal among all the truly anomalous ones. An example of the ROC curve can be seen in Fig. 1. Curves above the diagonal indicate a beneficial classifier, and curves below the diagonal a misleading one. The area under the ROC curve (AUC) is a threshold-independent measure of the performance of a classifier.

The selection of thresholds is also experimental. We want the low threshold to be such that few anomalous instances are below it. This means that the FPR must be below a maximum value. We want the high threshold to be such that few normal instances are above. This means that 1 – TPR must be below a maximum value. Finally, the instances between the thresholds (yellow) may be normal or abnormal.

### 2.3 Individual parameters

The LOF algorithm merely computes how anomalous an instance is, while we are also interested in the contribution of the individual parameters to its anomalousness. Therefore we compute per-parameter LOF values, which are done the same way as for the regular LOF values, except that the distances (d and k-distance) are computed only with respect to the parameter of interest.

## 3 Experiment and Results

The experiment was done on preliminary data. The data consists of the activity and energy expenditure computed by the CHIRON activity monitoring methods, heart rate, and body temperature of five persons during the following scenarios: lying still, sitting still and standing still, sitting doing light activities, walking and standing doing light chores, scrubbing the floor, sweeping, sit-ups and jumping jacks, walking normally, walking quickly, running slowly, running normally, stationary cycling normally, stationary cycling vigorously.

All the recorded data were considered normal. We split each scenario in four parts, using the first and third part for training, and the second and fourth for testing. We also needed anomalous test data, which we generated by replacing the values of a parameter at one time (for example the heart rate during lying) with the values at another time (the heart rate during walking briskly).

We had to devise a distance measure for the activity parameter, since it is nominal and has no "natural" distance. We represented each activity by the vector of attributes used for the activity recognition, averaged over all the instances of the activity in the training data. We then computed the Euclidean distances between each pair of activity vectors, yielding the activity-distance matrix.

Fig. 2 shows the prototype of the risk assessment for patients with cardiac disease. The first panel shows the overall deviation with the risk detected. The second panel represents the values of the instance. Other panels are per-parameter risks. We can observe that the parameter for energy expenditure is in the medium risk level, shown on the last panel. This indicates that the energy expenditure level is too low for the measured heart beat and the activity.

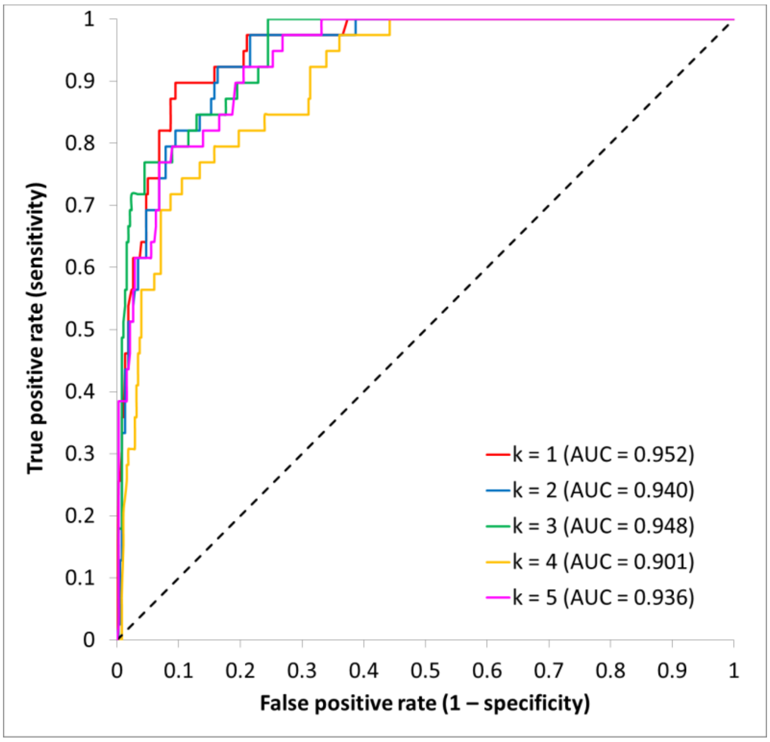

**Figure 1:** ROC curves for different number of neighbours k = 1, 2, 3, 4, 5.

## 4 Conclusion

In this paper we have shown that LOF can be used for health risk assessment. We have extended the general LOF to use nominal values in our case activity and to show the level of abnormality.

The disadvantage of LOF as a risk assessment method is that a new pattern is not necessarily a sign of increased risk. However, the advantage is that it can detect any kind of anomaly – there is no need for an expert to describe the possible anomalies and no need for examples of the anomalies (labelled data).

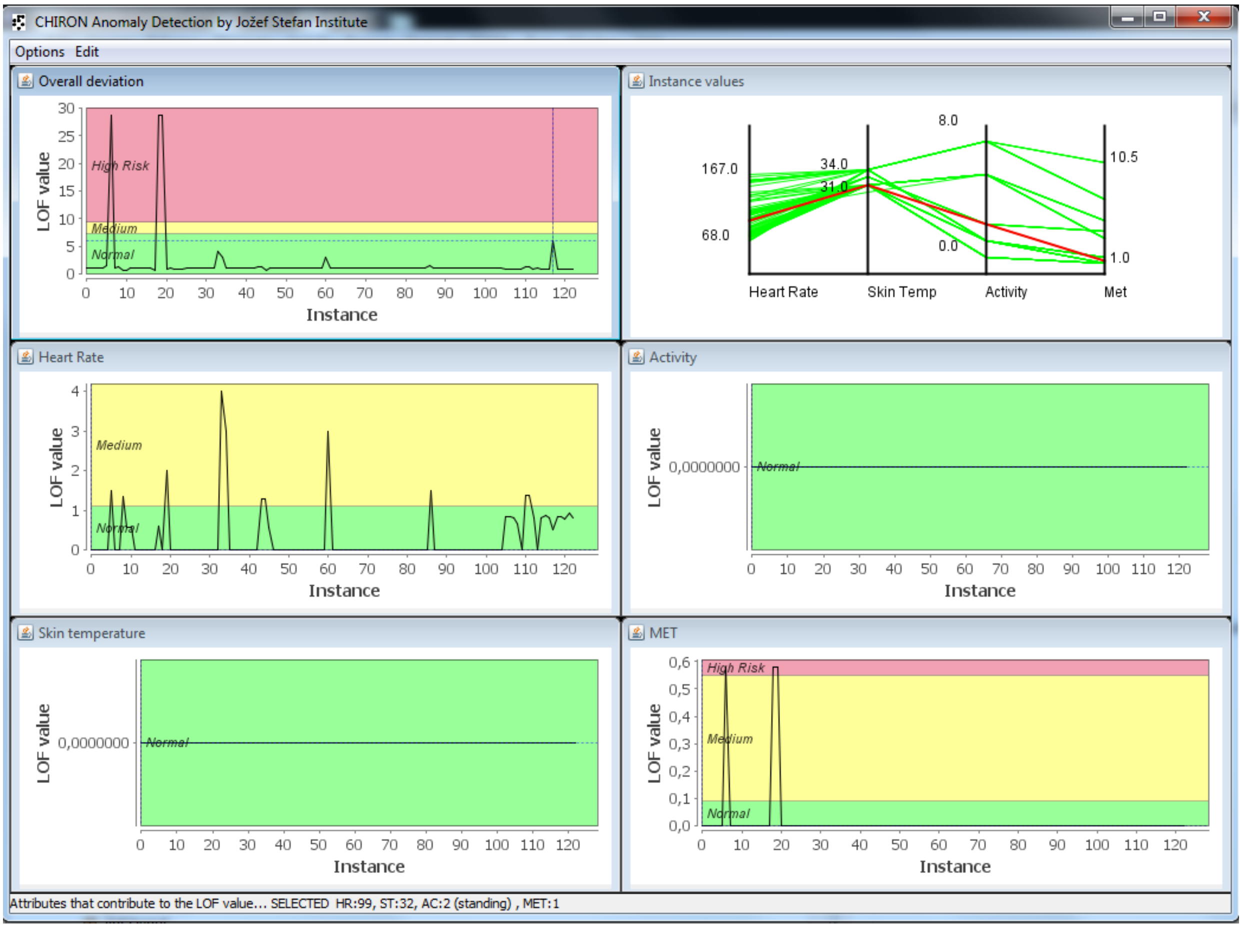

Attributes that contribute to the LOF value... SELECTED HR:99, ST:32, AC:2 (standing) , MET:1

**Figure 2:** The prototype showing the anomaly detection due to the MET value.

## References:

[1] M. M. Breunig,, H.-P. Kriegel, R. T. Ng & J. Sander. LOF: Identifying density-based local outliers. In *Proc. of ACM SIGMOD International Conference on Management of Data,* 2000.

## For wider interest

The purpose of the medical expert systems is to disburden the workload of physicians and ease the detection of abnormal events. Research in this field is quite mature. However, modules that assemble the expert system are based on predefined rules created by the expert or models trained on the labelled data. For example, when a patient's health is normal, the parameters characterizing it usually follow some recurrent patterns. When the patient's health is not normal certain parameters move from the normal state and influence others. The rules and models created to detect the risk are highly correlated with the disease they were created for. This means that in case we would like to analyse a different disease, domain new rules have to be created and models trained. For that we would need relatively large amount of relevant labelled data.

There are four problems we are focused on in this research (i) can we use unlabelled data, (ii) is it possible to consider individuality of the patient regarding the pattern of vital signs and their influence to each other, (iii) can we detect the level of the abnormality and (iv) is it possible to detect how much do the analysed parameters contribute to the risk?

In this research we have adopted the Local Outlier Factor (LOF) algorithm, since it seems the most appropriate method to detect the abnormal events using unlabelled data and by that keep the individuality of the person. The algorithm was extended with the procedure for abnormality level detection per monitored parameter. The developed algorithm enables the doctor to see which of the monitored parameters contribute to the overall risk at most.

The disadvantage of LOF as a risk assessment method is that a new pattern is not necessarily a sign of increased risk. However, the advantage is that it can detect any kind of anomaly – there is no need for an expert to describe the possible anomalies and no need for examples of the anomalies (labelled data).

# Diagnostika sistemov z gorivnimi celicami in izboljšanje njihovega delovanja

**Andrej Debenjak**[1,2]

[1] Odsek za sisteme in vodenje, Institut »Jožef Stefan«, Ljubljana, Slovenija

[2] Mednarodna podiplomska šola Jožefa Stefana, Ljubljana, Slovenija

andrej.debenjak@ijs.si

**Povzetek.** Dejavniki, kot so omejene zaloge fosilnih goriv, vse večja svetovna poraba energije in vse ostrejši okoljevarstveni predpisi, spodbujajo iskanje novih rešitev na področju okolju prijaznega pridobivanja energije. PEM gorivne celice so se izkazale za obetajočo tehnologijo, ki predstavlja alternativo današnjim virom energije tako v stacionarnih kot transportnih aplikacijah manjših moči. Največji potencial kažejo na področjih osebnega prevoza, logistične opreme za ravnanje s transportnim blagom, zasilnih in brezprekinitvenih napajalnih sistemih ter porazdeljene proizvodnje energije. Kljub vsemu je za uspešen prodor tehnologije na trg potrebno rešiti še nekatere težave, ki so povezane z zanesljivostjo delovanja PEM gorivnih celic. Največjo še ne rešeno težavo predstavljata poplavljanje celic in izsuševanje membran med delovanjem, ki negativno vplivajo na delovanje in v skrajnih primerih lahko vodijo v okvare. Te napake v delovanju je mogoče učinkovito odpravljati s pomočjo naprednih sistemov vodenja, pri čemer je odločilnega pomena diagnostika napak, saj tako poplavljanja kot tudi izsuševanja ni mogoče zaznati z neposrednimi meritvami.

**Ključne besede**: PEM gorivne celice, zanesljivost delovanja, diagnostika.

## 1 Uvod

Gorivne celice (GC) so elektrokemične naprave, ki kemično energijo vodika neposredno pretvarjajo v električno in toplotno energijo. Pri delovanju se porabljata vodik in kisik, kot edini stranski produkt pa nastaja voda, zato so GC popolnoma čist vir energije.

V transportnih in stacionarnih aplikacijah, kjer so potrebni viri električne energije moči do 100 kW, so se kot najprimernejše izkazale GC s protonsko prevodno membrano (ang. Proton Exchange Membrane – PEM) [1]. PEM GC poleg že opisanih lastnosti odlikujejo še nizka obratovalna temperatura, tiho delovanje in velika gostota moči. Področja, kjer so PEM GC primerne za vgradnjo, so: avtomobili in manjša prevozna sredstva za osebni prevoz, manjši delovni in transportni stroji, zasilni in brezprekinitveni napajalni sistemi, porazdeljeno sopridobivanje električne in toplotne energije ter vojaške aplikacije.

Trenutno največjo oviro masovni uporabi PEM GC predstavljajo težave povezane z zagotavljanjem zanesljivosti delovanja [2]. Nezanesljivost je večinoma posledica neželenih pojavov znotraj celic, ki se dogodijo med samim delovanjem. To sta poplavljanje celic in izsuševanje PEM membran. Ti dve napaki sta nemerljivi s standardnimi postopki, zato je za njihovo zaznavanje potrebno uporabiti diagnostične metode. Povečanje zanesljivosti delovanja pa se doseže tako, da se informacija, pridobljena z diagnostiko, uporabi v sklopu sistema vodenja, ki izvede ustrezno regulacijsko akcijo z namenom odpraviti napako.

V prispevku je predstavljena elektrokemična impedančna spektroskopija (EIS), ki je že dokazano učinkovita metoda za diagnosticiranje poplavljanja in izsuševanja samostojnih GC ob uporabi laboratorijske merilne opreme [3, 4]. Ker pa so realni sistemi sestavljeni iz več deset GC povezanih v serijo, ki tvorijo sklad GC, je potrebno metodo prilagoditi, saj v tem primeru posamezne GC niso neposredno dostopne in je potrebno metodo izvajati na celotnem skladu. Največjo s tem povezano težavo predstavlja izredno zakrita iskana informacija, saj se napake navadno dogodijo le znotraj nekaj celic sklada, diagnostika pa se opravlja nad celotnim skladom.

## 2 Predstavitev problema

PEM gorivna celica med delovanje proizvaja vodo, ki jo je potrebno odvajati, hkrati pa je nekaj vode potrebne za vzdrževanje ustrezne vlažnosti PEM membrane. Tako se celica tekom delovanja neprestano nahaja med preveč prisotne vode in pomanjkanjem vode, pri čemer je intenzivnost odvajanje vode regulirana s pomočjo temperature in pretoka zraka [1].

V primeru, ko je odvajanje vode nezadostno, se le-ta začne kondenzirati v zračnih kanalčkih in povzroči poplavljanje celice. Nastale kapljice vode v kanalčkih onemogočajo dostop zraka do mesta, kjer poteka kemijska reakcija, kar povzroči primanjkljaj reaktantov in posledično nezmožnost zagotavljanja zahtevane izhodne električne moči. Navzven je to vidno kot padec izhodne napetosti in izkoristka celice.

Protonska prevodnost PEM membrane je odvisna od vsebnosti vode v njej, zato je potrebno neprestano zagotavljati zadostno vsebnost le-te znotraj membrane. V primeru preobsežnega odvajanja nastale vode začne izhlapevati tudi voda iz membrane, kar vpliva na znižanje protonske prevodnosti. To pa hkrati pomeni, da se notranja upornost gorivne celice poveča in izhodna napetost pade. Ob tem lahko ob dolgotrajnem in močnem izsuševanju pride tudi do fizičnih okvar PEM membrane.

## 3 Uporaba EIS na sistemih s skladom gorivnih celic

EIS je elektrokemična diagnostična metoda, ki omogoča zaznavanje napak poplavljanja in izsuševanja PEM GC. Bistvo metode predstavlja ideja, da se posamezne napake različno manifestirajo v impedančni karakteristiki GC. To pomeni, da je potrebno GC med delovanjem vzbujati z vsiljenim tokovnim signalom, posneti njen napetostni odziv in izračunati njeno impedančno karakteristiko, na podlagi katere je nato mogoče določiti, kaj se znotraj celice dogaja.

Meritve po metodi EIS se izvedejo tako, da v določeni delovni točki (ki je določena z bremenskim tokom) enosmerni komponenti toka superponiramo sinusni vzbujalni signal manjše amplitude in znane frekvence [5]. Ob predpostavki, da je sistem gorivne celice v okolici delovne točke linearen, se le-ta na sinusno vzbujanje odzove s sinusnim napetostnim odzivom. Tokovni in napetostni signal lahko zapišemo s pomočjo kompleksorjev.

$$\begin{aligned} I &= I_0 e^{j\omega_0 t} \\ U &= U_0 e^{j(\omega_0 t+\varphi)} \end{aligned} \tag{1}$$

Kjer je $\omega_0$ krožna frekvenca signalov, $I_0$ in $U_0$ amplitudi signalov in $\varphi$ fazni zamik napetostnega odziva. Vrednost impedance $Z$ gorivne celice pri vzbujeni krožni frekvenci $\omega_0$ je po Ohmovem zakonu:

$$Z = \frac{U}{I} = \frac{U_0 e^{j(\omega_0 t+\varphi)}}{I_0 e^{j\omega_0 t}} = Z_0 e^{j\Phi}, \tag{2}$$

kjer je $Z_0$ amplituda impedance in $\Phi$ fazni kot impedance gorivne celice pri izbrani krožni frekvenci $\omega_0$.

Metoda EIS je že preverjeno učinkovita pri diagnosticiranju samostojnih PEM GC, njena uporaba pa še ni razširjena na diagnosticiranje večjih sistemov, ki so sestavljeni iz sklada več deset GC. Namen eksperimentalne študije, ki je bila izvedena, je bil raziskati možnosti, na kakšen način je mogoče EIS uporabiti kot diagnostično orodje na večjih realnih sistemih z GC, kjer je dostopna le meritev impedance celotnega sklada. Študija je bila izvedena na sistemu sestavljenem iz 80 GC izhodne električne moči 8 kW.

Pri študiji so bili izvedeni trije nizi meritev. Meritve impedance so bile izvedene pri normalno obratovalnih pogojih, kjer ni bilo prisotnih napak, pri prisotnem poplavljanju in pri prisotnem izsuševanju. Napake so bile spodbujene s pomočjo nastavljanja vlažnosti vhodnega zraka. Da so bile napake res prisotne, je dokazoval opazen padec izhodne napetosti sistema.

Slika 1 prikazuje rezultate študije. Predstavljeni so Nyquistovi diagrami izmerjenih impedanc sistema pri normalnem delovanju in pri prisotnem poplavljanju oziroma izsuševanju. Razvidno je, da je impedanca odvisna od prisotnih napak. Največje razlike se kažejo v frekvenčnem območju od 20 do 300 Hz. Slika 1 sicer nakazuje na to, da se impedance pri nižjih frekvencah izrazito razlikujejo, vendar je to zavajajoče, ker rezultati v tem frekvenčnem področju izkazujejo izredno veliko varianco, ki je predstavljena s črtkanim področjem (95 % pas zaupanja) in se zato rezultati dejansko prekrivajo. Na frekvenčnem področju nad 300 Hz se impedance normalno obratujočega in izsušenega sistema prekrivajo, medtem ko se impedanca poplavljenega še vedno loči od ostalih dveh.

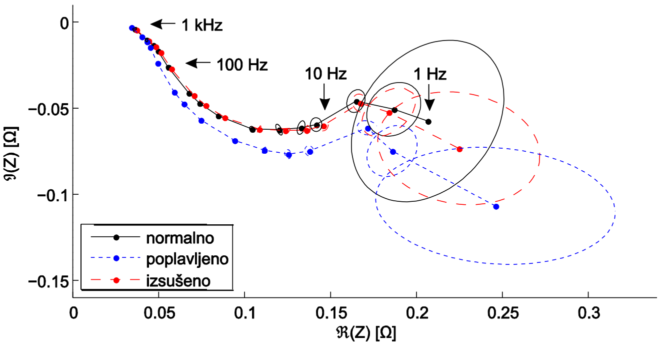

**Slika 1**: Nyquistov diagram impedančnih karakteristik sistema

Študija je pokazala, da je s pomočjo EIS mogoče odkrivati napake na večjih sistemih, in še pomembneje, da je hkrati mogoče določiti katera izmed napak je prisotna. Na podlagi spodbudnih rezultatov je smiselno zasnovati diagnostični sistem, ki ga bo mogoče vgraditi neposredno na sistem z gorivnimi celicami v realnih aplikacijah. Največjo oviro pri tem predstavlja izvedba vzbujanja sistema. V primeru eksperimentalne študije je vzbujanje gorivne celice zagotavljalo elektronsko breme, ki omogoča superponiranje sinusne komponente na bremenski tok. V primeru realnih aplikacij, ko je na izhodu priključeno navadno breme (npr. elektro motor), le-to tega ne omogoča, zato je potrebno zasnovati vzbujalni modul. Rešitev se ponuja v implementaciji vzbujalnega modula v sklopu DC/DC pretvornika, ki v osnovni funkciji skrbi za zahtevane napetostne oziroma tokovne nivoje, hkrati pa bi v tem primeru omogočal superponiranje vzbujalnega signala. Naslednji pomemben sklop so senzorji skupaj s procesno enoto, ki skrbijo za izvedbo meritev in zajemanje ter obdelavo podatkov. Na ta način zbrani in obdelani podatki se nato uporabijo v sklopu naprednega vodenja, ki poskrbi, da se odkrite napake odpravijo in s tem izboljša trenutno delovanje in zanesljivost sistema z GC. Shematično je predlagani koncept prikazan na sliki 2.

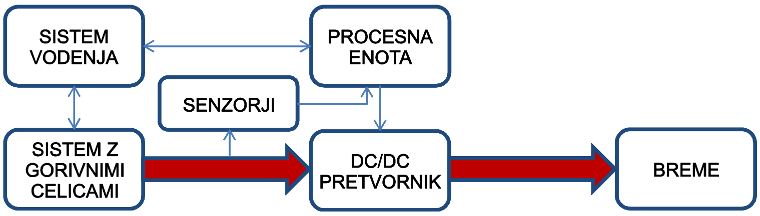

**Slika 2**: koncept diagnostičnega sistema

# 4 Zaključki

Eksperimentalna študija je pokazala, da je metoda EIS učinkovita diagnostična metoda tudi v primeru uporabe na večjih sistemih, kjer se meri samo impedanca celotnega sistema, ne pa posameznih celic. Nadaljnje delo bo težilo k temo, da se metodo najprej izpopolni, da bo dajala čim boljše rezultate. Nadalje pa bo potrebno razviti strojno opremo (senzorji, DC/DC pretvornik in procesna enota), ki bodo učinkoviti pri opravljanju diagnostike, hkrati pa bo tudi njihova cena primerna za vgradnjo v sisteme za širšo uporabo.

# Literatura:

[1] F. Barbir, PEM Fuel Cells: Theory and Prectice, Elsevier, 2005.

[2] D. P. Wilkinson and J. St-Pierre, "Durability," *Handbook of FCs*, John Wiley & Sons, 2005.

[3] X. Yuan, H. Wang, J. Sun and J. Zhang, "AC impedance technique in PEM fuel cell diagnosis – A review," *International Journal of Hydrogen Energy*, 32(17), str. 4365-4380, 2007.

[4] J.M. L.Canut, R. M. Abouatallah and D. A. Harrington, "Detection of Membrane Drying, Fuel Cell Flooding, and Anode Catalyst Poisoning on PEMFC Stacks by EIS," *Journal of The Electrochemical Society,* 153(5), str. A857-A864, 2006.

[5] X. Z. Yuan, C. Song, H. Wang and J. Zhang, Electrochemical Impedance Spectroscopy in PEM Fuel Cells, Fundamentals and Applications, Springer, London, 2010.

## Za širši interes

Gorivne celice so naprave, ki kemično energijo goriva (največkrat je to vodik) neposredno pretvarjajo v električno energijo. Energija se pretvarja s pomočjo elektrokemične reakcije, pri kateri se vodik spaja s kisikom, pri tem pa kot edini produkt nastaja voda. Zaradi tega so gorivne celice izredno čista tehnologija za pridobivanje električne energije.

Ob tem, da so gorivne celice okolju prijazne, jih odlikujejo tudi nekatere druge lastnosti: ne vsebujejo nobenih premičnih ali vrtečih se delov, tihost delovanja in visoki izkoristki. Te njihove dobre lastnosti jih delajo primerne za vgradnjo v raznorazne aplikacije, kjer lahko nadomestijo trenutne okolju neprijazne vire energije.

Pri aplikacijah, kjer so potrebni viri električne energije manjših moči, so se kot najprimernejše izkazale gorivne celice s protonsko prevodno membrano (ang. Proton Exchange Membrane – PEM). PEM gorivne celice, poleg že predstavljenih lastnosti, dodatno odlikujejo tudi nizka obratovalna temperatura in velika gostota moči. Področja, kjer so PEM gorivne celice primerne za uporabo, so: avtomobili in manjša prevozna sredstva za osebni prevoz, manjši delovni in transportni stroji, zasilni in brezprekinitveni napajalni sistemi, porazdeljeno sopridobivanje električne in toplotne energije ter vojaške aplikacije.

Še ne odpravljene težave, ki ovirajo prodor PEM gorivnih celic na širši trg, so povezane z zagotavljanjem zanesljivosti delovanja celic. Nezanesljivost je v največji meri posledica napak povezanih z nastalo vodo med delovanjem in njenim odvajanjem iz celic. Ti dve napaki sta tako imenovani poplavljanje celic in izsuševanje PEM membran. Napaki sta nemerljivi s standardnimi postopki, zato je za njihovo zaznavanje potrebno uporabiti diagnostične metode. Povečanje zanesljivosti delovanja pa se doseže tako, da se informacija, pridobljena z diagnostiko, uporabi v sklopu sistema vodenja, ki izvede ustrezno regulacijsko akcijo z namenom odpraviti napake.

V prispevku je predstavljena elektrokemična impedančna spektroskopija, ki je bila uporabljena za diagnosticiranje napak tekom delovanja. Hkrati pa je podan tudi koncept za implementacijo metode znotraj sistema vodenja gorivnih celic, ki poskrbi za odpravo napak in ustreznost delovanja.

# Risk Assessment Model for Congestive Heart Failure

**Hristijan Gjoreski**[1,2]

[1] Department of Intelligent Systems, Jožef Stefan Institute, Ljubljana, Slovenia
[2] Jožef Stefan International Postgraduate School, Ljubljana, Slovenia
hristijan.gjoreski@ijs.si

**Abstract.** Congestive heart failure is a common, chronic and debilitating condition with an extremely poor prognosis. This paper presents an approach to creation of risk assessment model for congestive heart failure. Two types of hierarchical multi-attribute models are developed and compared: qualitative and quantitative. The results for both models showed that the models can successfully assist and help the experts in their decision for estimation of the patient's risk. Also, the models analysis techniques can assist additionally by giving advices for future improvement of patient's health.

**Keywords**: Congestive heart failure, Risk assessment model, Decision support, Expert system.

## 1 Introduction

Congestive heart failure (CHF) is a common, chronic and debilitating condition. It is an issue when the heart cannot pump enough blood to the rest of the body. It is more common than most cancers, including breast, testicular, cervical and bowel cancers. Approximately 14 million people suffer from CHF in Europe [1].

The CHF issue is addressed in the CHIRON project [2]. The CHIRON is a European project whose final goal is the development of a reference architecture for personal elderly healthcare. One of the modules of the project is the creation of CHF **R**isk **A**ssessment **M**odel (RAM), which should assist the doctors in assessing the CHF risk of a patient. The aim of the RAM is to provide to the doctors the information needed to make clinical decisions regarding the patient's health.

In this paper we describe the development of a long-term RAM for CHF. Two approaches were used: qualitative and quantitative. Additionally, for both RAMs a hierarchical attributes structure is created. The results showed that it is possible to create an accurate long-term RAM, and also to provide an explanation mechanism which assists the experts in their decision regarding the CHF risk factor.

## 2 Attributes and Alternatives

Attributes are an essential component in the development of RAMs. They represent relevant features that are used to model the risk. In our research, we first studied the literature and made a list of 70 relevant attributes. However, in this paper we focused only on a long-term risk. The idea of the long-term RAM is the modeling of a static risk. Therefore, only the attributes that are the most relevant for the long-term risk were used. This resulted in using 15 basic-information attributes that can be collected upon the patient's enrolment to the medical institution.

The first steps in creation of the model were: attribute understanding and grouping. The final hierarchy resulted in 4 layers, 15 basic and 11 aggregate attributes (shown in Figure 1). The different colors in Figure 1 show the importance of the attributes. Each attribute is labeled with an importance factor assigned by the medical expert (*high importance* – red, *medium importance* – yellow and *low importance* – green).

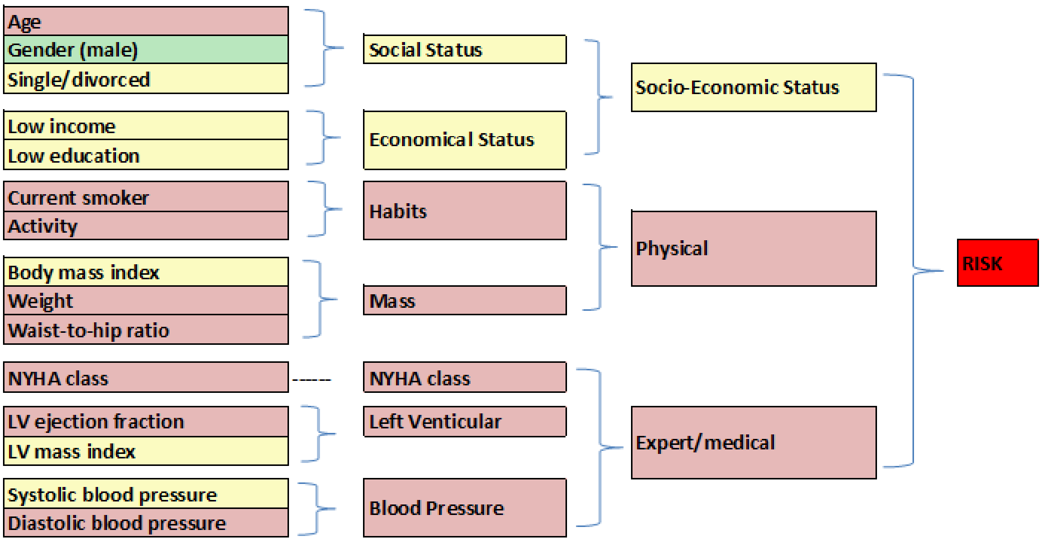

**Figure 1. Hierarchy of the attributes. Importance factor: high – red, medium – yellow and low– green.**

Alternatives are the options used for evaluation of the models. The alternatives analyzed by our models were: *low*, *medium* and *high-risk* patient. The data for these patients was provided by the medical expert in the CHIRON project. However, real-life data is expected in the later stage of the project.

## 3 Qualitative Hierarchical DEXi Model

The first model presented is the qualitative model. This model was developed using the DEXi software [3]. It is a hierarchical model that includes all of the previously described attributes and evaluates the data from the three alternatives.

One of the features in hierarchical modeling is the *utility function*. In qualitative models the utility function is a table of decision rules. This function maps all the combinations of the lower level attributes to the aggregate attribute. Furthermore, the importance of the attribute is encoded in the rules of the utility function.

Once the model was created, the next steps were the evaluation of the alternatives and model analysis. The model successfully evaluated each of the alternatives (Table 1). Further analysis was performed using two techniques: *Plus-minus-1* and *Selective explanation*. Some of the results are presented in the following paragraphs.

The *Plus-minus-1* analysis for the low-risk patient showed that, if the patient is less active in future, then s/he will be classified as a medium-risk patient. The same conclusion is for the smoking habit; if s/he decides to start smoking, the CHF risk increases significantly. The *Selective explanation* showed all the weak and strong attribute values that influence to a higher or lower risk. For the particular patient, the attribute values that influence towards a high risk are from the social-economic aspect: very old patient and low incomes; thus, they cannot be "improved".

The *Plus-minus-1* analysis for the medium-risk patient showed that, if s/he changes his activity level from medium to high, then s/he will be in the low-risk category. On contrary, if s/he starts smoking, then the CHF risk is significantly increased. The *Selective explanation* showed that it is important that s/he is not smoking and also the diastolic blood pressure is one of the strong points. On the other hand, the mass related attributes are in the high-risk zone and they should be "improved".

The analysis results showed that the qualitative model can definitely assist the experts in their risk decision, but also for future healthy advices for the patient. For instance, suggesting more activity, not smoking, losing weight are some of the advices that were revealed by this analysis. These advices overlap with the real-world advices which are usually given from a doctor to a patient.

## 4 Quantitative Hierarchical Model

The quantitative model was created by using the same attribute hierarchy. The differences with the qualitative model are in the *attribute values* and *utility functions*. In contrast to the quantitative symbolic values, the quantitative model uses numerical values. Additionally, the utility function for the quantitative model is a mathematical formula – weighted normalized sum of risks:

$$risk = \frac{1}{\sum_{i=1}^{N} w(p_i)} \sum_{i=1}^{N} w(p_i) risk(p_i) \tag{1}$$

$N$ is the number of attributes, and each attribute is associated with a weight, i.e. $w(p_i)$. The weights of the attributes were chosen with accordance to the importance of the attribute, i.e. low = 0.5, medium = 1, high = 1.5. The risk of each attribute, $risk(p_i)$, is the normalized risk value of the attribute (0 – low, 1 – very high risk).

The same alternatives were evaluated with this model, as well. The results showed that each patient is correctly evaluated (Table 1). For further analysis, the same Plus-minus-1 "advices" from the DEXi model were applied. Similar behavior for the quantitative model was noted, e.g. if the low-risk patient is less active, the risk factor is significantly increased (from 0.27 to 0.31). The changes in the other attribute values were not so significant. Therefore, one can conclude that both models have similar sensitivity to the changes of the important attributes values.

## 5 Qualitative vs. Quantitative models

Even though both models evaluated the alternatives correctly (Table 1), they differ on a very basic level. The qualitative model uses discrete values and the quantitative uses numerical values. Each of the models has its advantages and disadvantages.

**Table 1. Evaluation results for each of the models: qualitative and quantitative.**

| Alternatives | Low-risk Patient | Medium-risk Patient | High-risk Patient |
|---|---|---|---|
| DEXi model evaluation | **Low Risk** | **Medium Risk** | **High Risk** |
| Quantitative model evaluation (0 - low; 1 - high) | **0.27** | **0.44** | **0.69** |

In the qualitative model, the *utility function* is a table of decision rules. Most of these rules should be manually created and this can be exhaustive for the expert who is building the model. Therefore, qualitative models have a natural limitation in the number of attributes and their values. On the other hand, in the quantitative models the utility function is a mathematical function. Thus, there is no limitation with the number of attributes and their values. However, the definition of this function is a problem by itself.

The analysis techniques for the qualitative model are more informative and understandable. Usually users of such RAMs are people that do not want to look and play with numbers, but they want simple rules that explain the model.

Finally, the concept of *weights* in the quantitative model is straightforward; it is a number representing the importance of the attribute. On the other side, the qualitative functions have to encode the importance into the utility functions.

## 6 Conclusion

We presented an approach for creation of multi-attribute RAM for CHF. Two types of models were developed: qualitative and quantitative. The results for both models showed that it is possible to evaluate the patients with the correct long-term risk factor. Moreover, we showed that using a hierarchical structure of the attributes significantly improves the understandability and interpretation of the models. The results showed that the model can successfully assist and help the experts in their decision. Furthermore, the analysis techniques can assist with giving future advices for improving the life of the patients. For instance, suggesting to the patient to be more active, not to smoke or lose some weight, are only some of the healthy advices that were produced by these models.

## Acknowledgements

The author would like to thank dr. Matjaž Gams and dr. Marko Bohanec, whose guidance and expertise were of great assistance for this study. Also, the collaboration from the people involved in the CHIRON project was of great importance, i.e. dr. Mitja Luštrek, dr. Paolo Emilio Puddu and Simon Kozina.

## References:

[1] Stewart S et al. More 'malignant' than cancer? Five year survival following a first admission for heart failure. The European Journal of Heart Failure 2001; 3: 315-322

[2] CHIRON project JU ARTEMIS Grant Agreement # 2009-1-100228. http://www.chiron-project.eu/

[3] DEXi, A Program for Multi-Attribute Decision Making. http://kt.ijs.si/MarkoBohanec/dexi.html

## For wider interest

Congestive heart failure (CHF) is a common and chronic condition with an extremely poor prognosis. It is an issue when the heart cannot pump enough blood to the rest of the body. It is more common than most cancers, including breast, testicular, cervical and bowel cancers. Approximately 14 million people suffer from CHF in Europe.

In this paper we presented models that can predict the CHF risk of a patient. We were focused on predicting the long-term, static, risk that can be assessed upon patient's enrolment in the medical institution. The aim of the model was to predict the CHF risk, but also to provide additional explanation for the decision: the reason why the predicted risk is such as it is (low, medium or high).

To achieve this goal, we developed two types of hierarchical models: qualitative and quantitative. The first one is more user-friendly because it is using symbolic values for the data, e.g. low activity, high blood pressure, medium risk, etc. The other one is more mathematical and is using numbers instead of symbolic values.

We tested these models on a data created by a medical expert. First, the data is used as input to the models. Then, the models analyze the data and make the final decision (prognosis) for the risk. Additionally, both models have visualization mechanism, which shows the attributes that are extremes: the most and the least risky. Finally, the analysis techniques reveal healthy advices for the patient, such as: suggesting being more active, not to smoke and lose weight.

The results showed that the models successfully predict the correct risk factor, and also provide explanation mechanism which could assist the experts in their decision regarding the CHF risk factor.

# Prototip sistema za sprotni nadzor stanja industrijske opreme

**Matic Ivanovič**[1,2], **Đani Juričić**[1,2,3,4]

[1] Odsek za sisteme in vodenje, Institut "Jožef Stefan, Ljubljana", Slovenija

[2] Mednarodna podiplomska šola Jožefa Stefana, Ljubljana, Slovenija

[3] Univerza v Novi Gorici, Nova Gorica, Slovenija

[4] Univerza v Mariboru, Maribor, Slovenija

matic.ivanovic@ijs.si

**Povzetek.** V prispevku je predstavljen konceptualno nov sistem za sprotni nadzor stanja industrijske opreme, ki ga odlikujejo nizka cena, enostavna namestitev ter prilagodljivost različnim področjem uporabe. Ključna komponenta sistema je pametno senzorsko vozlišče, ki je sposobno zbirati signale iz lokalnih senzorjev, lokalno shranjevati poteke, le-te tudi lokalno obdelati s sodobnimi postopki ter rezultate brezžično poslati na oddaljen strežnik. Posebnost sistema je, da lahko lokalne postopke obdelave signalov poljubno spreminjamo kar na daljavo preko brezžičnega omrežja. Celotna aplikacija se razvije v Simulinku, ki predstavlja standardno orodje za načrtovanje, in se nato s posebno izdelanim programom avtomatsko prevede v obliko, primerno za ciljni procesor v vozlišču. Delovanje prototipa pametnega senzorskega vozlišča ter okolja za konfiguracijo smo preizkusili tudi na preprosti aplikaciji in pokazali, da je možno izdelati cenovno ugoden in zmogljiv sistem za sprotni nadzor stanja opreme.

**Ključne besede**: diagnostika, sprotni nadzor stanja, senzorsko vozlišče

## 1 Uvod

Sprotni avtomatiziran nadzor stanja opreme predstavlja pomemben trend v novih generacijah sistemov za avtomatsko vodenje procesov. Današnji postopki vzdrževanja procesne opreme so žal večinoma *reaktivni* (post-mortem), v najboljšem primeru pa *preventivni*. Napredno in ekonomsko bolj učinkovito *prediktivno* vzdrževanje pa se uporablja le v novejših in razmeroma kompleksnih aplikacijah. Prediktivno vzdrževanje temelji na naprednih postopkih diagnostike, prognostike in upravljanja vzdrževanja (angl. prognostics and health management, PHM), ki se nanašajo na napovedovanje preostale življenjske dobe komponent ter odločanje o vzdrževalnih posegih za zagotavljanje normalnega obratovanja naprav. Razlogi za majhno prisotnost prediktivnega vzdrževanja v industriji so predvsem visoka cena, zahtevna namestitev [1], pri tem pa so obstoječi nadzorni sistemi narejeni le za specifične aplikacije in jih ni možno enostavno prenesti na druge, podobne sisteme. Zato smo se odločili, da zgradimo dovolj splošno platformo s katero bi se izognili omenjenim slabostim.

Zgradbo nadzornega sistema lahko razdelimo na več nivojev. Na najnižjem nivoju so na posameznih mehanskih sklopih nameščeni različni senzorji. Povezani so na eno ali več manjših naprav, t. i. senzorska vozlišča, ki vršijo osnovno obdelavo izmerjenih podatkov in rezultate s pomočjo brezžičnih tehnologij pošiljajo na strežnik. Tu se vrši nadaljnja obdelava prejetih podatkov in shranjevanje v podatkovno bazo. Prav tako lahko preko strežnika razvijalec določa lastnosti senzorskega omrežja in nastavlja delovanje posameznih naprav v omrežju. Na najvišjem nivoju je zgrajen uporabniški vmesnik, ki upravljavcem omogoča vpogled v podatke o posameznih nadzorovanih napravah. Uporabniku je na voljo ocena trenutnega stanja naprave ter napoved preostale življenjske dobe naprave [2], [3]. Na podlagi teh podatkov se lahko upravljavci odločijo o morebitnih vzdrževalnih posegih.

V prispevku smo se omejili na predstavitev senzorskega vozlišča ter okolja za načrtovanje postopkov za obdelavo signalov na posameznih vozliščih. Opisan je tudi preizkus delovanja na preprostem eksperimentalnem sistemu.

## 2 Pametno senzorsko vozlišče

Pametno senzorsko vozlišče je osnovni gradnik nadzornega sistema. Gre za samostojno napravo, ki je sestavljena iz mikrokrmilnika, različnih senzorjev, komunikacijskega vmesnika ter napajalnega modula in po potrebi tudi dodatnega spomina. Slika 1 prikazuje blokovno shemo vozlišča z dejanskimi komponentami, ki smo jih uporabili pri izgradnji prototipa senzorskega vozlišča. Uporabili smo Atmelov mikrokrmilnik ATXMEGA32A4. Za analogno-digitalno pretvorbo signala iz senzorjev smo uporabili kar analogno-digitalni pretvornik (angl. analog-to-digital converter, ADC) mikrokrmilnika, ki je dovolj zmogljiv za potrebe naše aplikacije. Zaradi premajhnih spominskih kapacitet mikrokrmilnika smo uporabili dodatni zunanji spominski modul tipa SRAM, ki smo ga preko SPI (angl. Serial Peripheral Interface) vodila povezali z mikrokrmilnikom. Za brezžično komunikacijo smo uporabili ZigBee modul ETRX2 proizvajalca Telegesis. Na vozlišče je možno priklopiti do 4 senzorje vibracij, temperature in hitrosti vrtenja. Signale senzorjev vibracij je možno vzorčiti z frekvenco 10 kHz. Vozlišče ima baterijsko napajanje.

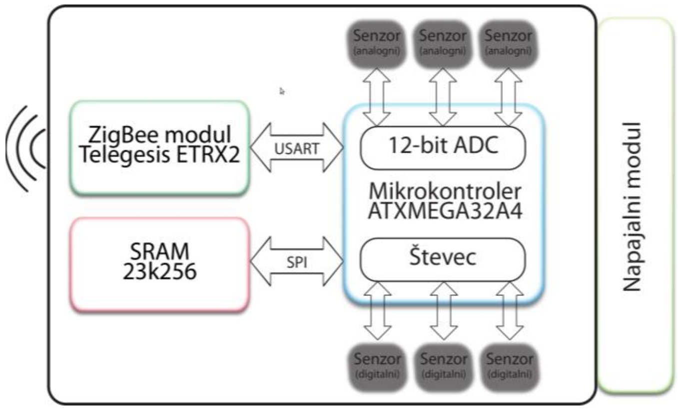

**Slika 1:** Blokovna shema vozlišča

Glavne naloge vozlišča so zajem podatkov iz senzorjev, matematična obdelava izmerjenih podatkov ter pošiljanje rezultatov obdelave podatkov na strežnik. Posebnost pa predstavlja možnost brezžične konfiguracije postopkov obdelave podatkov, ki potekajo na vozlišču. Več takšnih vozlišč je lahko povezano v brezžično senzorsko omrežje. ZigBee specifikacija ponuja izjemne možnosti za brezžično povezovanje, med katerimi je potrebno izpostaviti nizko ceno, majhno porabo energije, dolgo življenjsko dobo posameznih vozlišč ter fleksibilno vzpostavitev brezžičnega omrežja.

## 3 Okolje za načrtovanje

Zaradi lažjega in hitrejšega načrtovanja ter preizkušanja algoritmov obdelave signalov, smo se odločili, da bo le to potekalo v okolju Matlab/Simulink. Za programski paket Simulink smo izdelali posebno knjižnico, ki vsebuje bloke, iz katerih je možno zgraditi shemo za izračun potrebnih značilk za namene diagnostike. Knjižnica vsebuje vhodni in izhodni blok ter bloke, ki izvajajo osnovne računske postopke iz področja obdelave signalov. To so bloki za izračun korena srednje vrednosti kvadratov (angl. root mean square, RMS), variance, bloki za detekcijo ovojnice, za filtriranje ter za izračun hitre Fourierjeve transformacije signala.

Vsaka shema je lahko sestavljena iz vhodnih blokov, ki predstavljajo vhode za podatke iz senzorjev. Izhodni bloki predstavljajo značilke. Z vmesnimi bloki pa so definirani postopki za izračun želenih značilk. Skupno število vseh blokov je pogojeno s količino pomnilnika na mikrokrmilniku, ki pa ga je možno nadgraditi. Pri povezavi posameznih blokov v verigo je potrebno paziti na to, ali je vhod oziroma izhod bloka vektor ali skalar. Na sliki 2 je prikazana zelo preprosta shema.

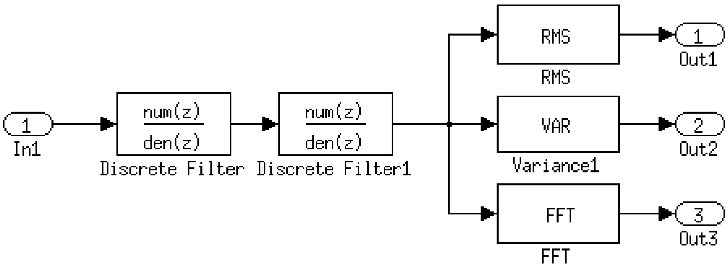

**Slika 2:** Primer sheme, zgrajene v programu Simulink

Funkcionalnost kakršnekoli delujoče sheme je potrebno prenesti na senzorsko vozlišče. Za ta namen smo v Matlabu napisali posebno funkcijo, ki vse potrebne podatke iz Simulink sheme zapiše v datoteko, katero lahko pošljemo na senzorsko vozlišče. Seveda smo morali temu primerno prilagoditi tudi program za senzorsko vozlišče, tako da podpira vse bloke iz Simulink knjižnice in omogoča izračun značilk, kot je definirano v izvorni Simulink shemi. Karakteristični podatki sheme so vrsta posameznih blokov, ki določa katero opravilo opravlja blok, in povezave med posameznimi bloki, ki določajo vrstni red izvajanja. Nekaterim blokom je potrebno definirati tudi parametre, ki narekujejo njihovo delovanje. Blokom za filtriranje je potrebno podati koeficiente prenosne funkcije izbranega filtra, blokom za izračun Fourierjeve transformacije pa število vzorcev za izračun. Ostali bloki za svoje delovanje ne potrebujejo posebnih parametrov.

## 4 Preizkus delovanja

Delovanje smo preizkusili na eksperimentalnem sistemu (Slika 3) in prikazali osnovni princip delovanja, na katerem lahko temelji nadzorni sistem za mehanske pogone. Na vozlišče smo priključili senzor vibracij, le-ta pa je bil fiksiran na izvor vibracij, kateremu je možno nastavljati frekvenco. V Simulinku smo izdelali shemo za izračun značilke, ki predstavlja prisotnost določene frekvence v signalu vibracij. Značilka je izračunana kot RMS vrednost signala vibracij, filtriranega s pasovno prepustnim filtrom pri izbrani centralni frekvenci, katera lahko predstavlja prisotnost napake na merjeni opremi. Ko na izvoru vibracij spreminjamo frekvenco vedno bližje izbrani frekvenci filtra, vrednost značilke narašča. To lahko uporabimo za zaznavanje prisotnosti določenih frekvenc v merjenem signalu vibracij npr. mehanskih pogonov, ki predstavljajo neželene spremembe pri obratovanju.

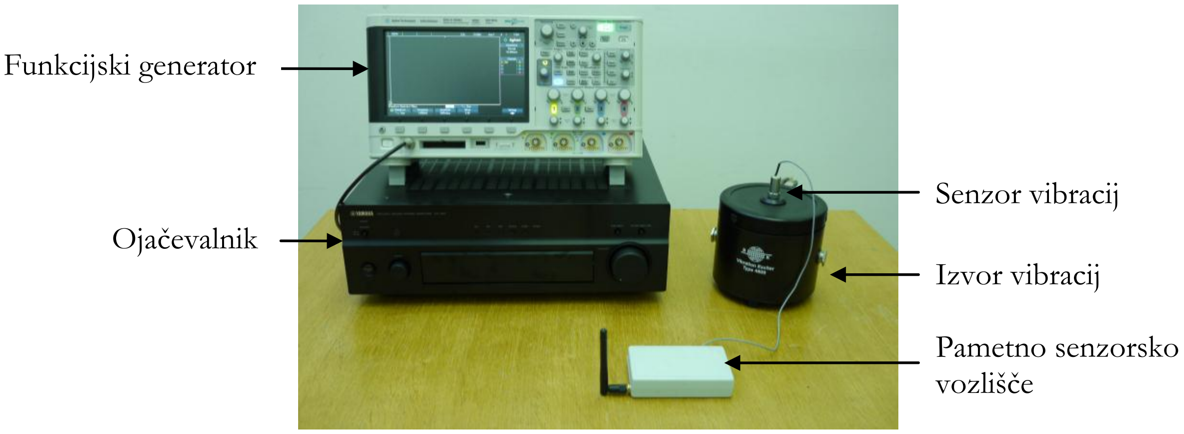

**Slika 3:** Postavitev eksperimentalnega sistema

## 5 Zaključek

Predstavili smo nov koncept nadzornega sistema. Novost predstavljata pametno senzorsko vozlišče ter okolje za hitro in enostavno načrtovanje postopkov obdelave signalov za pridobivanje značilk, iz katerih lahko razberemo stanje nadzorovanih naprav oziroma komponent. Postopke obdelave signalov pa je možno brezžično prenesti na poljubno senzorsko vozlišče, ki je del brezžičnega senzorskega omrežja. Ta lastnost predstavlja enega najbolj pomembnih in izvirnih doprinosov k izvedbi celotnega sistema.

## Literatura:

[1] N. Tandon, A. Parey. Condition monitoring of rotary machines. *Springer Series in Advanced Manufacturing: Condition Monitoring and Control for Intelligent Manufacturing*, 109–136, 2006.

[2] A. Heng, S. Zhang, A. Tan, J. Mathew. Rotating machinery prognostics: State of the art, challenges and opportunities. *Mechanical Systems and Signal Processing*, Vol. 23, No. 3, str. 724–739, 2009.

[3] M. Gašperin, Đ. Juričić, P. Boškoski, J. Vižintin. Model-based prognostics of gear health using stochastic dynamical models. *Mechanical Systems and Signal Processing*, Vol. 25, No. 2, str. 537–548, 2011.

## Za širši interes

Sprotni avtomatiziran nadzor stanja opreme predstavlja pomemben trend v novih generacijah sistemov za avtomatsko vodenje procesov. Današnji postopki vzdrževanja procesne opreme so žal večinoma *reaktivni* (post-mortem), v najboljšem primeru pa *preventivni*. Napredno in ekonomsko bolj učinkovito *prediktivno* vzdrževanje pa se uporablja le v novejših in razmeroma kompleksnih aplikacijah. Prediktivno vzdrževanje temelji na naprednih postopkih diagnostike, prognostike in upravljanja vzdrževanja (angl. prognostics and health management, PHM), ki se nanašajo na napovedovanje preostale življenjske dobe komponent ter odločanje o vzdrževalnih posegih za zagotavljanje normalnega obratovanja naprav. Razlogi za majhno prisotnost prediktivnega vzdrževanja v industriji so predvsem visoka cena, zahtevna namestitev, pri tem pa so obstoječi nadzorni sistemi narejeni le za specifične aplikacije in jih ni možno enostavno prenesti na druge, podobne sisteme. Naš cilj je izdelati dovolj splošno platformo za sprotni nadzor stanja opreme s katero bi se izognili omenjenim slabostim.

# IPSSC: Integration of structured expert knowledge

**Vladimir Kuzmanovski**[1, 2], **Sašo Džeroski**[1, 2], **Marko Debeljak**[1, 2]

[1] Department of Knowledge Technologies, Jožef Stefan Institute, Ljubljana, Slovenia

[2] Jožef Stefan International Postgraduate School, Ljubljana, Slovenia

vladimir.kuzmanovski@ijs.si

**Abstract.** This paper presents an effective implementation of data pre-processing methodology and data mining referring to integrate decision rules as part of manually written expert system (expert knowledge) with models inducted from data. The methods we have used are standard methods for data pre-processing, including techniques for handling missing data, feature construction, transformation and aggregation, and J48 machine learning algorithm, implemented in WEKA data mining tool set for the process of integration of the manually created expert rules given in decision tables.

**Keywords**: Data Pre-processing, Data mining, Decision trees, Expert systems

## 1 Background & Objectives

Decades ago, scientists started with some initial algorithms for knowledge discovery in market data that in the course of time were upgraded to satisfy new amount of data, new types of data and to be able to be implemented in various disciplines, such as environmental sciences, biology, medicine, etc. So, it was not enough only to find some kind of way to discover knowledge from data, but it is also important to update and upgrade the discipline for new type of problems. Having this in mind, we will integrate existing expert knowledge in a form of manually written rules which are given in decision tables with data mining. Such integrated models will present the base unites (modules) from which the decision support system will be structured.

The expert knowledge is already structured into manually built expert system owned by ARVALIS Institute. It is implemented to assess the risk of pesticide leaching from crop production. In fact, the expert system is a composition of modules covering different aspects of meteorological conditions, water flows in soil, agricultural interventions, and risk assessment and mitigation solutions to protect environment form phytochemical pollution (Figure 1).

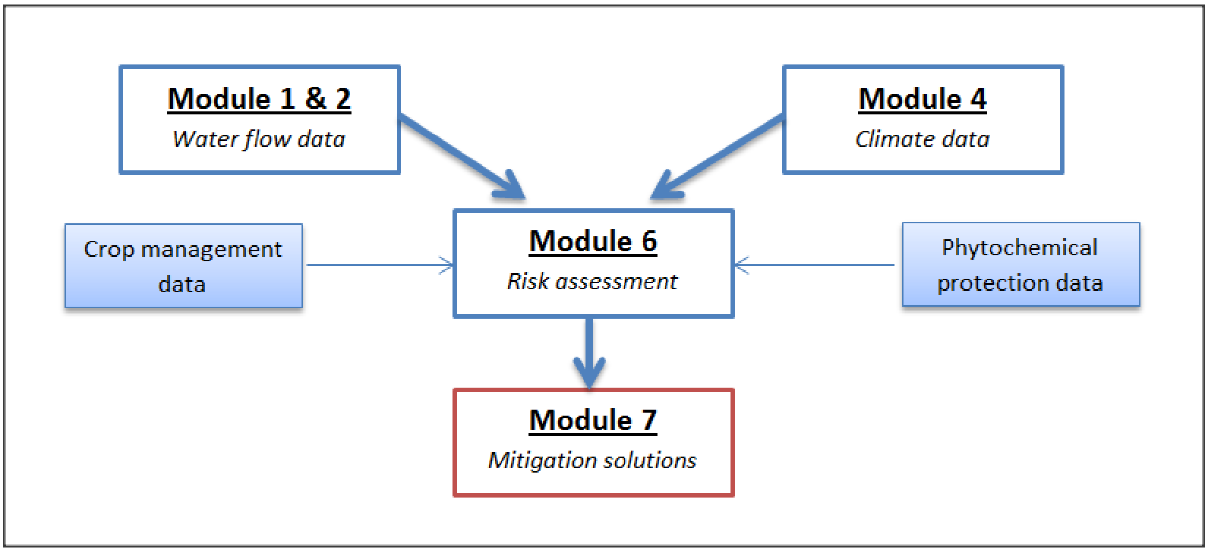

**Figure 1**: Expert system for assessing the risk of pesticide leaching in water

Since we know that our expert system is manually written in form of tables and complex documentation, the main problems are assessed. Firstly, the complexity of the documentation and whole expert system rise in a problem because the system is time-consuming for people who did not contribute in the creation process. Secondly, the expert system has not been validated with data but only reviewed by experts. One of the reason for not to be validated is the fact that the design of the expert system is complex and the data unstructured. Finally, our expert system has been developed for regional wide scale which is difficult to use for specific small unite of area or field-scale problems. So, the expert system can be upgraded with model inducted by data for better performance and accuracy in field and catchment scale risk assessments.

The main idea is that the expert system could be positioned as a baseline for the model that can be dynamically scale-adjusted using machine learning techniques and model inducted from data, and finally implemented in a decision support system. This approach can lead us to a solution of some complex problems like the absence of multi-scales usefulness (field-scale and catchment-scale), high-performance computing and inputs’ expensiveness.

## 2 Materials & Methods

The first step in the integration should be optimization of the expert system. The given expert system is in the form of decision rules written in tables. The optimization of the expert system includes reduction of the decision rules (where it is possible) and representation in the form of a decision tree.

Our expert system consists from decision rules written in tables. For the given task of expert system integration we will treat the rules in tables as a regular nominal data. The system contains 7 modules. In our work, we will use Module 1, Module 2, Module 4 and Module 6 (Figure 1). But, for this particular paper we will keep the attention to tables from Module 2 only, which are about the diagnosis of water flows from the fields.

Module 2 contains 34 raw tables, divided in 3 parts depending on the weather season: autumn-winter, spring and summer. Beside tables, Module 2 contains some additional information given in text documents and describing additional information that will be targeted as inputs attribute. For example, in tables' label can be found that these nominal values are valid for "impermeable substrate with no breaks (cracks) in permeability" or "permeable substrate with breaks in permeability". The dataset constructed from decision tables and additional information from text documents has 13 input attributes and 12 target independent attributes. All of the attributes have nominal values.

The quality of data mining models algorithms depends on the quality of the data. In order to keep data quality during the data extraction and pre-processing, we used methods for dealing with missing data, future construction, data transformation and data aggregation. To integrate pre-processed data extracted from expert decision tables, we used machine learning algorithm J48 for building classification decision trees which is implemented in WEKA data mining tool set [1].

### 2.1 Missing data

Incomplete data is an unavoidable problem in dealing with most of the empirical data sources. But in some situations in real world, under certain circumstances, it's natural some characteristics not to have any value. So the first step and the most important one is to define the source of unknowingness. Knowing the sources of unknowingness, the task can be completed by choosing one of the existing methods for handling missing data [2], [3]. We used the method for ignoring instances with unknown feature values because we need to build a model that will satisfy the threshold of 100% correctly classified instances over the training data. Our task is not to make a classification model for unknown cases, but to make a model which will cover all combinations of rules from the expert decision tables.

### 2.2 Feature construction, transformation and aggregation

Future subset selection, construction and transformation are the process of identifying and removing as much irrelevant and redundant information as possible. This may reduce the dimensionality of the data, but may allow learning algorithms to operate faster and more effectively. Furthermore, the problem of information mining among the data available can be addressed by constructing new attributes from the basic future set. Transformed attributes generated by attribute construction may provide a better discriminative ability than the best subset of given attributes [3]. In addition, the discovery of meaningful attributes may contribute in better understanding of the learned concept.

### 2.3 Classification decision trees

Decision trees are a classic way to represent information from a machine learning algorithm, and offer a fast and powerful way to express structures in data. According to the problem at hand and type of a given data, we used J48 algorithm for inducing classification decision trees. J48 is a version of an earlier algorithm developed by J. Ross Quinlan, the popular C4.5 [1].

## 3 Results & Discussion

In the process of integration, the total 12 classification decision trees were built, one for each target attribute. Here we will describe the decision tree model for “transfer by drainage” which refers to the water transfer in drainage pipes which are buried under the fields.

The top most attribute in the drainage model (Figure 2) is “season” which splits the model according its values “autumn and winter” and “spring and summer”. The followed attributes “the slope of the soil” and “the presence of shrinkage cracks in soil". The decision tree model's depth is 9 levels and has total 35 leaves. The full model is presented on the poster for this paper.

The model has been built over dataset with 6818 instances, but 2402 of them were ignored because of the target attribute's missing value, due to the chosen method for handling missing values, as mentioned before. On the other hand, the correctly classified instances over training dataset are 100%.

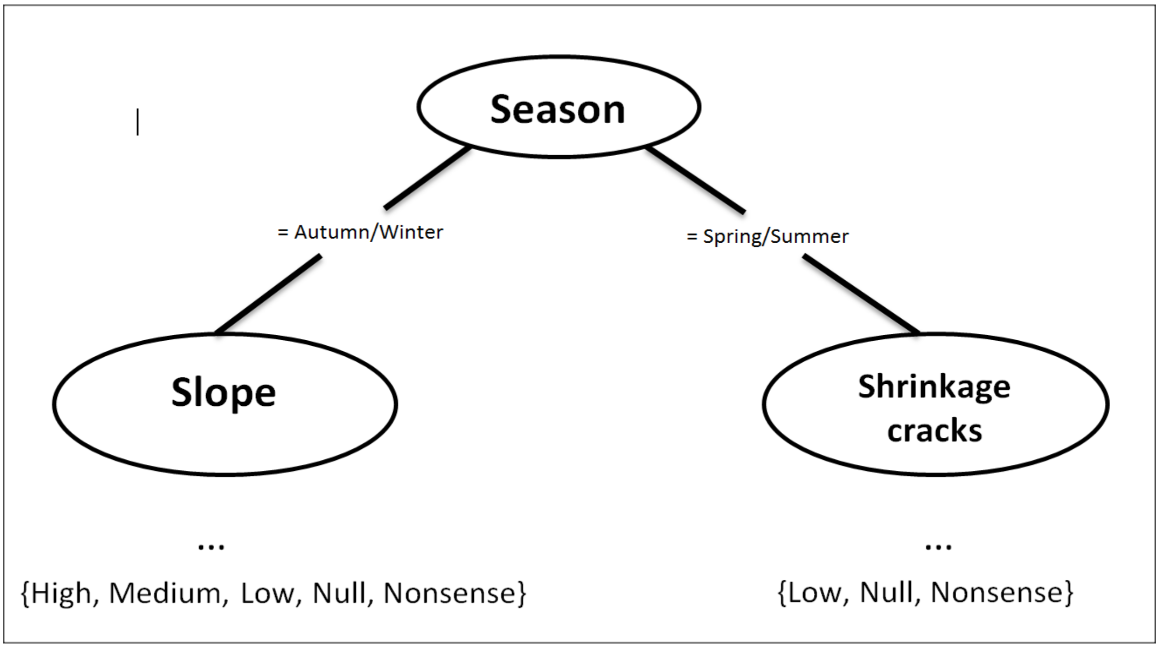

**Figure 2**: Top-most structure of "the drainage" classification model

The model that has been built can be used for validation of the expert system and discussion for the complexity of the existing expert knowledge. Furthermore, the described approach to integration of a given expert system and its further networking with the models induced from data collected during the regular data collection could result in a new generation of decision support systems which will significantly increase the reliability of decision maker.

## 4 Conclusion

In this paper we proposed the new approach of integration of expert knowledge that is written as rules in decision tables with models inducted from data. The outcome of the integration process could be a good base for building decision support system. Furthermore, the proposed approach will solve the main addressed problems. Firstly, the complexity of the expert system and the difficultness of the system's implementation are solved by compact structured model. Secondly, the validation of the expert knowledge with data is done by validating the built model. Finally, the adjustment to the field and catchment scale diagnosis has been addressed as further work on the decision support system.

## References:

[1] I. H. Witten and E. Frank. *Data Mining: Practical machine learning tools and techniques, 2nd Edition*. Morgan Kaufmann, 2005.

[2] Arnaud Ragel & Bruno Cremilleux. *Treatment of Missing Values for Association Rules,* p. 258.

[3] S. B. Kotsianitis, D. Kanellopoulos & P. E. Pintelas. *Data Pre-processing for Supervised Leaning,* 2006

## For wider interest

Discovering knowledge in data or data mining becomes a very important discipline as part of information technologies. It helps people, companies and even whole businesses to use their own data in very practical way by finding interesting and sometimes scientifically approved patterns and knowledge. Basically, the value of information is always proportional to the scale of the problem it addresses.

Learning from the data and especially combine the learned patterns and knowledge in decision support system will significantly increase the reliability of decision maker and will produce a better support in decision making process.

The next generation of improvements of decision support systems will cover the expert knowledge integration. We proposed an approach of integration of expert knowledge with models inducted from data into final decision support system by integration of expert knowledge (expert system) with data mining algorithms.

# VESNA based platform for spectrum sensing in ISM bands

**Zoltan Padrah**[1,2], **Tomaž Šolc**[1], **Mihael Mohorčič**[1,2]

[1] Department of Communication Systems, Jožef Stefan Institute, Ljubljana, Slovenia

[2] Jožef Stefan International Postgraduate School, Ljubljana, Slovenia

zoltan.padrah@ijs.si

**Abstract.** The radio spectrum used by wireless communication systems is becoming increasingly crowded. One approach to overcome this problem is to perform real-time dynamic spectrum assignment. To this end, it is necessary to collect information about the radio spectrum, also called spectrum sensing. In this paper a framework is presented which can be used for collecting information about radio spectrum usage. This framework is based on the low-cost and versatile VESNA sensor platform. A spectrum sensing experiment has been performed in the 2.4 GHz to demonstrate the capabilities of the framework.

**Keywords**: spectrum sensing, wireless sensor platform

## 1 Introduction

All radio systems use the same shared resource for communication: the radio spectrum. This spectrum is managed by regulatory agencies, which allocate frequency bands to various systems. A notable category of allocated frequency bands are the Industrial, Scientific and Medical (ISM) bands, which can be used by any device for communication. In order to develop new technologies that operate in these frequency bands, or to optimise existing systems, it is necessary to observe the usage of the ISM bands. For new systems, one of the concepts being investigated is cognitive radio (CR) [1], in which devices optimize their communications based on the collected information about the radio spectrum. This information can be collected by each device independently or collaboratively by device-internal or external spectrum sensing capabilities. In this paper we present a low-cost device-external spectrum sensing solution, which can be used in experiments related to cognitive radio to independently or collaboratively monitor the activity in ISM bands.

The rest of the paper is organised as follows. Section 2 first introduces the overall spectrum sensing framework based on the VESNA wireless sensor node platform [2]. Section 3 presents the hardware part of the VESNA based spectrum sensing platform, while Section 4 presents the custom developed software support for spectrum sensing using this platform. The infrastructure software used for processing the measurement data is presented in Section 5. The experiment carried out by VESNA based spectrum sensing platform is presented in Section 6, while Section 7 concludes the paper.

## 2 Sensing system overview

The spectrum sensing framework is depicted in Figure 1. It consists of two parts: the sensing and infrastructure part. For the communication between the two parts of the framework an RS232 connection is used.

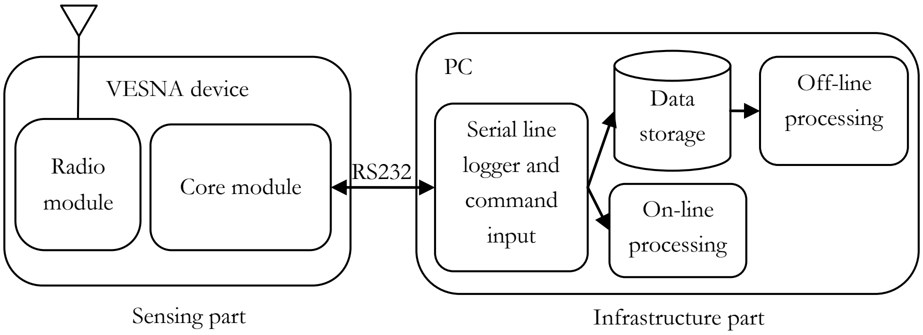

**Figure 1:** Overview of the VESNA based spectrum sensing framework

The sensing part performs the radio spectrum measurement, applies optional pre-processing of the collected data and sends the data to the infrastructure part of the framework. It is capable of changing the sensing parameters by applying different sensing profiles; switching between these profiles is triggered by commands received on its RS232 interface. The sensing part has been implemented on the VESNA wireless sensor node platform by developing special software application for the device. The software application running on VESNA is presented in detail in Section 4.

The infrastructure part performs the control of the sensing part and it stores and processes the measurement data. It is implemented by software modules running on a PC. These modules receive the collected data from the RS232 connection, process and display it, and also store it for later use. The real-time display of the data allows on-site inspection of measurements, while the stored data can be converted to formats that allow the importing of the measurement data into various data processing tools, for instance for building the Radio Environmental Maps (REMs) [3] or to support the spectrum sharing algorithms. The infrastructure part also provides the user interface for selecting the active sensing profile for the sensing part. This way, radio spectrum measurements with different parameters can be easily carried out.

## 3 VESNA based spectrum sensing hardware

The VESNA based spectrum sensing platform is a modular wireless sensor node platform consisting of three modules: Sensor Node Core (SNC), Sensor Node Radio (SNR) and Sensor Node Expansion (SNE). The SNC module contains a 32 bit ARM Cortex-M3 microcontroller with 96 kB of RAM and 1 MB of Flash memory, the standardized radio and expansion connectors, sensor connectors, RS232 interface, non-volatile memory, power regulators and battery charger. The standardized expansion connectors allow the connection of various radio (SNR) and expansion (SNE) modules to the SNC. The SNR module used for spectrum sensing experiments reported in this paper is built around the Texas Instruments' (TI) CC2500 radio, operating in the 2.4 GHZ ISM band. The list of available SNE modules includes the debugging and programming board, Ethernet to serial converter, Wi-Fi to serial converter, protoboarding modules and the additional power supply module. Several open source development tools are available for the VESNA platform, including OpenOCD, GNU compiler toolchain and Eclipse IDE.

## 4 Software support for VESNA based spectrum sensing

In order to use VESNA platform for spectrum sensing, an application has been developed, that sets up different sensing profiles for the radio located on the SNR module, collects the measurements from the radio, processes the raw measurement data and sends the measurement results to the infrastructure part of the framework.

Sensing profiles contain settings for the radio. The exact available settings depend on the capabilities of a given radio and typically include the frequency band in which the sensing should be performed, the channel bandwidth on which the radio should operate, the list of frequencies on which the sensing band should be applied and the number of samples that should be averaged in order to obtain one data point. By using different sensing profiles, trade-offs can be made between the parameters of the sensing, such as resolution, accuracy, bandwidth, speed of sensing and minimal signal level than can be detected. The selection of sensing profiles is controlled by the infrastructure part of the sensing framework, by sending commands to the sensing part. These commands are received on the RS232 interface on the SNC, and processed in software.

The data sent to the infrastructure is organized in lines; each line describes the power level detected at each of the frequencies specified in the active sensing profile. Besides measurement data, lines contain a timestamp of the measurement and markers for line start and line end used for corruption detection at the end of a sensing activity. If sensing is interrupted, the successfully transmitted lines can be easily recovered based on the line start and line end markers.

## 5 Infrastructure software

The infrastructure part of the framework (i) allows the user to select the active sensing profile, (ii) displays the spectrum measurement data in real time, in order to allow the monitoring of the measurements and (iii) stores the spectrum data on the PC, in order to allow off-line processing.

The selection of the current sensing profile is performed by manually typing the command that selects a given sensing profile. The list of available sensing profiles and a short description is provided by a “help” command. The real-time data monitoring interface is shown in Figure 3. It presents the received signal power versus time, in the frequency band defined by the active sensing profile. The same data is saved on the PC, in order to be processed offline. The format of the saved data is identical to the data transmitted on the RS232 connection; however, it is guaranteed that the saved data contains only valid lines. In order to import the data into MATLAB or Octave, scripts have been developed, which load the saved files and stores the available data in data structures specific to the programs mentioned. After this importing procedure, the data can be freely processed.

# 6 Experiments

The spectrum sensing framework presented in this paper has been used to analyse the radio spectrum usage in the 2.4 GHz ISM band. Figure 3 presents the measurement results obtained by the real-time data analyser. The frequency bands used by Wi-Fi (2400–2483 MHz) have been scanned for several minutes. The vertical lines on the plot are the result of a known limitation of the CC2500 radio. The patterns appearing on the left side of the plot indicate the Wi-Fi activity. Based on the plot, it can be concluded that the Wi-Fi devices have been transmitting on the center frequency of 2412 MHz, which corresponds to the Wi-Fi channel 1. Also, a weak signal can be observed around 2431 MHz.

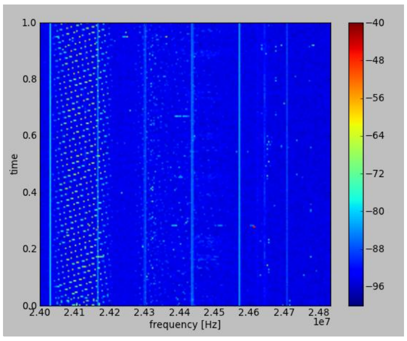

**Figure 2:** Real-time data monitoring interface for the system

# 7 Applications and future work

A VESNA platform based spectrum sensing framework has been presented which is capable of collecting information about radio spectrum usage. This information could be used in optimization of radio networks, implementation of dynamic spectrum access or as a sensing component for cognitive radio systems. The future direction of this work is to integrate multiple sensing devices into one network, and perform collaborative spectrum sensing and thus provide more comprehensive measurements.

## References:

[1] J. Mitola III and G. Q. Maguire, Jr., Cognitive radio: making software radios more personal, *IEEE Personal Communications Magazine*, vol. 6, nr. 4, pp. 13-18, Aug. 1999

[2] VESNA hardware platform. SensorLab. http://sensorlab.ijs.si/hardware.html

[3] Atanasovski, V., et. al.. Constructing radio environment maps with heterogeneous spectrum sensors. *2011 IEEE Symposium on New Frontiers in Dynamic Spectrum Access Networks (DySPAN)*, pp. 660-661, 3-6 May 2011

## For wider interest

All radio systems, including mobile phone network, Wi-Fi for computer networks, FM radio, satellite systems, use the same shared resource for communication: the radio spectrum. This spectrum is managed by regulatory agencies, which allocate frequency bands to various systems. A notable category of allocated frequency bands are the Industrial, Scientific and Medical (ISM) bands, which can be freely used for communication by any device. For example Wi-Fi and Bluetooth systems use this band. In order to develop new technologies that operate in different frequency bands, or to optimise existing systems, it is necessary to monitor the radio activity in a given band.

A low-cost spectrum sensing framework has been developed, which is able to monitor the signal power in the ISM frequency bands. This system is based on the VESNA wireless sensor platform. Wireless sensor networks are usually low-power networks of devices which collect information about their environment, such as temperature, humidity, pressure. In this case the wireless sensor node hardware has been used for collecting information about radio spectrum usage. This framework is being used for collecting experimental data about new, experimental radio systems, which will be more efficient. It is also planned to integrate the sensing capabilities of this framework with more advanced radio systems.

# Improving Performance of Wireless Mesh Networks with Network Coding

**Erik Pertovt**[1,2], **Kemal Alič**[1,2], **Aleš Švigelj**[1,2], **Mihael Mohorčič**[1,2]

[1] Department of Communication Systems, Jožef Stefan Institute, Ljubljana, Slovenia

[2] Jožef Stefan International Postgraduate School, Ljubljana, Slovenia

erik.pertovt@ijs.si

**Abstract.** In Wireless Mesh Networks, various mechanisms are used to enhance the performance of the network. Network Coding (NC) is a novel approach for enhancing the network performance as it can significantly increases the network capacity through broadcasting encoded packets while maintaining the desired Quality of Service. The effects of NC can be even better exploited with appropriate support of NC-aware routing algorithms. In this paper, we present implemented NC algorithms, routing supported algorithms for NC, and custom designed NC simulation model that allows in depth study of procedure effects, evaluation and comparison, eventually leading into better understanding of the problem challenges and its improvements. The results show that networks with NC included can handle up to two times more traffic than existing networks where NC is not used.

**Keywords**: Network coding, coding-aware routing, simulation model.

## 1 Introduction

Wireless Mesh Networks (WMNs) are typical representatives of wireless access networks, where nodes are connected to each other through multi-hop wireless links. In WMNs, several mechanisms can be used to improve the network performance, such as advanced physical layer techniques (e.g. multi-radio and multi-channel technology), multi-path routing for load balancing and fault tolerance, protocols for reliable data transport as for real-time delivery, protocols for network management (i. e. mobility and power management, and network monitoring), cross-layer design, scheduling algorithms, etc. The mechanism, which experiences an increasing attention in the past few years in both, wired and wireless networks, is network coding (NC), mainly due to promising results from the initial research and testbed deployments.

NC enables encoding multiple packets either from the same or from different traffic flows into one encoded packet for saving bandwidth and thus increasing the network capacity while maintaining the desired Quality of Service parameters. In wireless networks, NC exploits the broadcast nature of the wireless medium, where nodes can overhear packets which are not destined to them, resulting in new coding opportunities. These packets are later on needed for decoding process.

In our opinion, the true potential of NC in the network layer can only be used in strong collaboration with routing, which has to be adopted to fully exploit NC principles. By applying NC-aware routing [1], paths with more coding opportunities can be discovered resulting in modified paths where more packets are being coded together, thus using less bandwidth for transferring the same amount of traffic from source to destination.

In order to design NC-aware routing algorithms, the understanding of NC and its influences on other OSI layers has to be acquired, potentially allowing also cross layer optimization. In this respect, simulation models present an appealing solution for studying causes and consequences, as well as to evaluate and compare the performance of different approaches. We have developed a NC simulation model [2], using the OPNET Modeler [3] simulation tool. Several routing techniques, e.g. Dijkstra's, Bellman-Ford, and genetic ants-based routing algorithms and several routing metrics, such as number of hops, distance, expected transmission count (ETX), modified ETX, and coding enhanced ETX are being under investigation [4]. In addition, we are examining the possibilities to improve metrics based on the response of routing to the number of coding opportunities, packets queue lengths, etc. Moreover, we are also developing new NC algorithms and NC-aware routing procedures to better exploit NC principles.

NC simulation model currently supports our own routing-independent method BON - Bearing opportunistic network coding [5], and the well-known COPE [6] method. The results show that both BON and COPE significantly improve the network performance in terms of network capacity as compared to reference scenario (i.e. no-NC) cases where NC algorithms are not used.

In the rest of the paper, we describe the simulation model and present implemented NC and routing algorithms. Furthermore, we show results comparing COPE and BON methods, and the no-NC case.

## 2 Simulation Model

The architecture of the simulation model enables building networks with different topology and parameter scenarios with little manual work. In such networks, NC and NC-aware routing algorithms can be tested and evaluated.

### 2.1 Network Coding Simulation Model

The simulation model consists of several parts. The supporting network topology generator is developed in MATLAB and is able to generate random wireless topologies built around the arbitrary number of nodes that can communicate with arbitrary number of neighbours through wireless links (graphically presented with dashed lines in Figure 1) selected according to nodes positions and transmission "range" or other parameters of nodes. The network description program, also developed in MATLAB, prepares the information of desired topology, nodes, links and parameters for communication procedures (e.g. throughputs, number of packet retransmissions, loads, etc.) to import into the OPNET Modeler simulation model [3], where the main simulation takes place. The latter consists of five functional layers: (i) traffic generator is responsible for creating the network load, (ii) routing module takes care of routing the packets through the network, (iii) the wireless module takes care of successful packet distribution through the wireless channel to the right address taking into account links conditions, (iv) network topology module defines network architecture and links conditions, (v) network coding module enables coding.

### 2.2 Implemented NC and Routing Algorithms

Two NC algorithms have already been implemented in the model. The first one is an efficient and routing-independent method BON [5]. It is a novel method, which requires no traffic information on which packets can be coded together, but selects packets to be encoded together based solely on position of nodes thus bringing little additional overhead. The method was purposely designed to work in WMN. The second implemented NC method is the well-known COPE [6] which is more complex, introduces a lot of overhead as compared to BON and works only with ETX-based routing algorithms.

Three algorithms are implemented for routing table calculation, two shortest path algorithms, Dijsktra and Bellman-Ford, and ants-based routing algorithm which uses the probabilistic routing tables updated by ants traversing routes according to the conditions in the network. The currently supported metrics, which can be used to determine link cost(s) at routing calculation, are hop count, distance, delivery probability-based metrics, etc.

## 3 Simulation Parameters and Results

The simulation model was used to obtain numerous simulation results considering various topologies, traffic loads and distributions, combinations of simulation parameters and NC and routing algorithms. In this section, we present representative results from the user point of view acquired based on the comparison of BON, COPE and no-NC scenario (ref.sc.) for the two topologies shown in Figures 1 and 2.

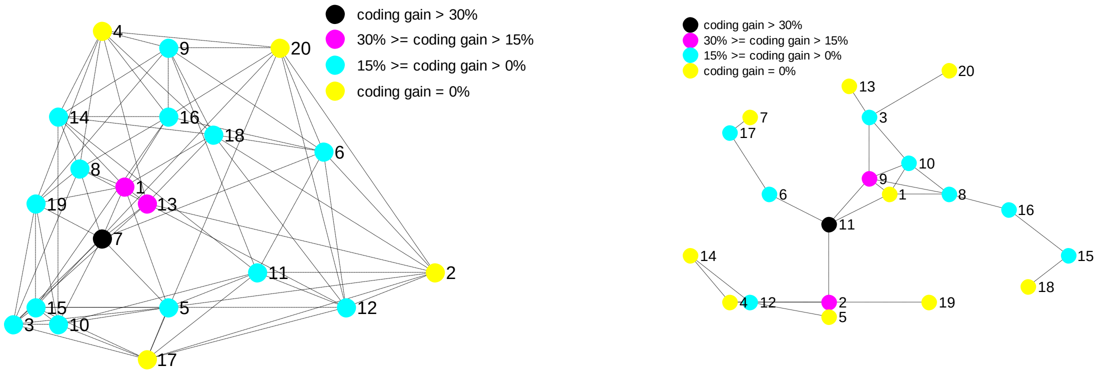

**(a)** **(b)**

**Figure 1**: Nodes coding gains: (a) COPE - nodes with 7 neighbours, (b) BON

Representative networks have 20 wireless nodes with ideal symmetric wireless links (1Mbit/1Mbit). Nodes are same configured as, e.g. in a homogeneous network.

Traffic load is generated on all nodes with the same intensity using exponential distribution of inter-arrival times and constant packet lengths (i.e. 10 kbit). The traffic load is increased through simulation runs until it can not be handled any more by neither of scenarios. All network nodes are source nodes generating traffic with the same probabilities and selects destination nodes using uniform probability distribution among all network nodes.

Figure 1 indicates with different colours the coding gain (G) [6] for each node, defined as the ratio between the number of source packets (without coding) $N_S$ and the number of packets required to send source packets with coding $N_C$:

$$G = \frac{N_S}{N_C}$$

Thresholds of coding gains have been set at 1.3, 1.15 and 1, representing 30, 15, and 0 percent of packets being coded on particular node. The cases are for COPE (Figure 1.a) and BON (Figure 1.b), however coding opportunities appear for both algorithms at the same locations.

In Figure 2.a, the delay between the source and destination nodes for the increasing network load and case scenarios is presented for the topology in Figure 1.b. For the same topology, we present the traffic throughputs in Figure 2.b.

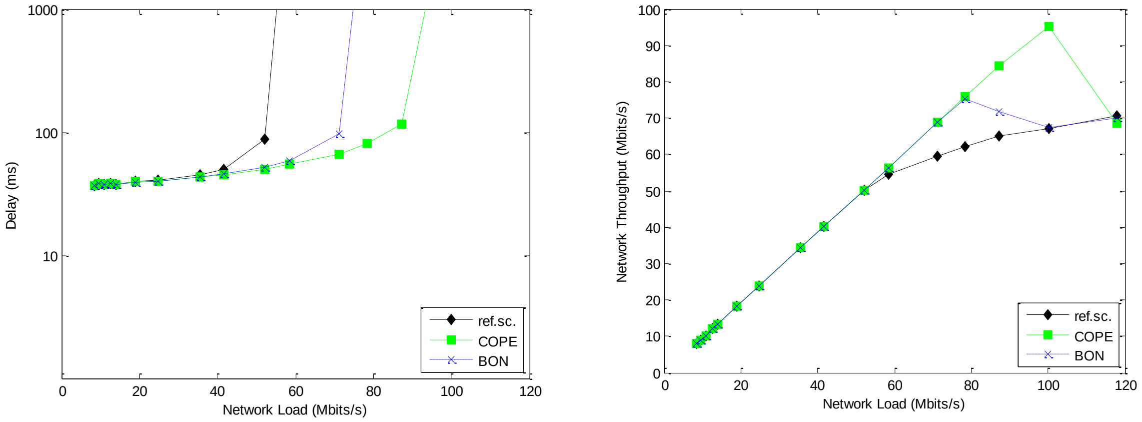

**(a)** **(b)**

**Figure 2**: Delay (a) and network throughput (b) in dependency of network load for BON, COPE and no-NC (ref.sc.) scenario for topology in Figure 1.b.

From the results, we can see that COPE can handle the highest given load, though the BON method is not far behind, while the no-NC scenario can handle the lowest load showing that BON and COPE significantly improve the network capacity.

COPE only works on networks that use routing based on delivery probability metric and is more demanding in terms of processing power and storage, since it needs the information on the packets held by the neighbouring nodes. Furthermore, it has high overhead, since nodes send out reports on the packets they have acquired, thus additionally loading the network in its normal operational conditions. BON, on the other hand, is an efficient method that is not related to any routing protocol. It needs less processing power and storage capacity than COPE and introduces less overhead.

## 4 Conclusion and Further Work

In this paper, we present an overview of our work in NC with representative results showing that NC supported WMN networks significantly improve the network capacity. The results were obtained through briefly presented custom-designed NC simulation model. Our future work is focusing on further investigation of new NC algorithms and NC-aware routing.

## References:

[1] M. A. Iqbal, B. Dai, B. Huang, A. Hassan, S. Yu, "Survey of network coding-aware routing protocols in wireless networks," in Journal of Network and Computer Applications, vol.34, no. 6, pp. 1956-1970, August 2011.

[2] K. Alič, E. Pertovt, A. Švigelj, "Simulation environment for network coding," in Mosharaka International Conference on Communications, Networking and Information Technology (MICCNIT 2011), Dubai, UAE, 2011.

[3] OPNET web page, available at http://www.opnet.com/, accessed May 2010.

[4] E. Pertovt, K. Alič, M. Mohorčič, A. Švigelj, "ETX-based Metrics and Adapted Routing Algorithms for Network Coding," in 20th Electrotechnical and Computer Science Conference (ERK 2011), Portorož, Slovenija, September 2011.

[5] K. Alič, E. Pertovt, A. Švigelj, 'unpublished' "Routing-Independent Practical Network Coding Algorithm," 2012 International Symposium on Network Coding (NetCod 2012), Boston, MA, USA, June 2012.

[6] S. Katti, H. Rahul, W. Hu, D. Katabi, M. Médard, and J. Crowcroft, "XORs in the Air: Practical Wireless Network Coding," IEEE/ACM Transactions on networking, vol. 16, June 2008.

## For wider interest

Wireless Mesh Networks (WMN):

- typical representatives of wireless access networks, where nodes, such as wireless routers, are highly connected to each other through multi-hop wireless links enabling various large-scale communications as e.g. Internet connection

Network Coding (NC):

- enables encoding multiple packets either from the same or from different traffic flows into one encoded packet for saving bandwidth and thus increasing the network throughput while maintaining the desired Quality of Service

Network simulation model for network coding:

- supports building WMN networks
- support for different NC and routing algorithms

Our work:

- studying, evaluating and comparing causes and consequences on the network performance of different NC approaches
- investigating several routing techniques for NC
- improving metrics based on the response of routing to the number of coding opportunities, packets queue lengths, etc.
- developing new NC and NC-aware routing algorithms and protocols for different environments

Results:

- NC significantly improves the performance of WMN; network throughput is increased and end-to-end packet delay is decreased

Our goal:

- further improvement of the capacity of WMN and similar networks through novel NC and routing techniques

# Mobile terminal as opportunistic sensor network device for research on cognitive radio networks

**Marko Pesko**[1,3], **Luka Vidmar**[1], **Mitja Štular**[1], **Mihael Mohorčič**[2,3]

[1] Telekom Slovenije, Cigaletova 15, 1000 Ljubljana, Slovenia

[2] Department of Communication Systems, Jožef Stefan Institute, Ljubljana, Slovenia

[3] Jožef Stefan International Postgraduate School, Ljubljana, Slovenia

marko.pesko@telekom.si

**Abstract.** The cognitive radio (CR) concept is promising to relax the pressure on the available radio resources and increase the efficiency of their use by dynamic spectrum allocation and spectrum sharing. Research focus related to CR networks is recently moving from simulation-based investigations to actual testbeds, many of them based on Wireless Sensor Networks (WSN), which support some CR research scenarios. Advanced mobile terminals can extend WSN features with mobility, sensing and measurements collection. This paper presents the concept of using a mobile terminal as an opportunistic sensor network device, capable of cooperation with dedicated sensor nodes to build Radio Environment Map to support the operation of CR networks.

**Keywords**: Mobile terminals, sensor nodes, Wireless Sensor Networks opportunistic, spectrum sensing, cognitive radio, hidden node.

## 1 Introduction

There are various wireless devices around us, which share the same frequency spectrum. In this respect, national and regional regulators recommend, set, and enforce output power and energy radiation rules for spectrum frequencies divided to the licenced and non-licenced bands. Due to such regulation, frequency bands are not fully exploited neither in time nor space. To solve this issue, the cognitive radio (CR) concept was introduced [1]. Its main advantage in comparison to traditional radios used today is a cognition cycle, which includes radio environment observation, learning from previous experiences and planning its own operation.

While majority of initial CR related research relied on computer simulations, more recent studies started to investigate spectrum sensing, opportunistic spectrum access and spectrum sharing procedures in real testbeds, many of them based on Wireless Sensor Networks (WSN). Practical experimentations in this field can be performed in ISM (Industrial Scientific Medical) frequency bands, in which expensive professional measurement equipment (e.g. spectrum analysers), medium-cost devices (e.g. USRPs) as well as low-cost devices, such as WSN nodes, can be used for testing. However, real sensing scenarios' goal is to have a maximum number of measuring devices available in order to acquire the most accurate results in the specific field of interest. To achieve this, sensor nodes seem a suitable choice, since they offer a good compromise between the price, the number of devices, and their computing, communication and sensing capabilities. As presented in [2], there are already several WSN testbeds, which use dedicated WSN gateway(s) to transfer the sensor measurements to the remote server locations for further analysis and processing. However, static deployment of dedicated sensor nodes and gateways is not always an optimal solution, resulting in many initiatives to use advanced mobile terminals equipped with different embedded sensors and communication interfaces as opportunistic sensors nodes and/or gateways [3]. In this respect, the aim of this paper is to present the mobile terminals' sensing capability and opportunistic sensor network role in CR research scenario. In the following, Section 2 presents mobile terminals' sensing and communication features. Section 3 presents difficulties and solutions of accessing sensors on the mobile terminals. Section 4 depicts our considered spectrum sensing scenario and in parallel presents a possible solution for the issues from Section 3. Finally, Section 5 concludes the paper.

## 2 Sensing and communication features of mobile terminals

Mobile terminals can be treated as a specific type of sensor nodes, however, their embedded higher processing, storing and communicating capabilities reflect in larger energy consumption, mostly due to the high resolution displays and relatively fast communication interfaces. It can be noticed that also low-power WSN adopted radios, in addition to Bluetooth technology, are slowly gaining the attention of the mobile terminals developers, whereas they already integrate many different types of sensors.

**Table 1** Android most common supported embedded and virtual sensors

| | | |
|---|---|---|
| Microphone | Magnetic field sensor | Pressure sensor |
| Camera | Gravity sensor | Proximity sensor |
| Touch screen display | Gyroscope sensor | Relative humidity sensor |
| Buttons | Light sensor | Rotation vector sensor |
| Global Positioning Sensor (GPS) | Ambient temperature sensor | Linear accelerometer sensor |
| Orientation sensor | Radio interfaces sensors for GSM, CDMA (logical level) | Radio interfaces sensors for Wi-Fi, Bluetooth (logical level) |

Several most common embedded and virtual sensors, supported by increasingly popular Android-based mobile terminals, are listed in Table 1, however, none of them is actually appropriate for spectrum sensing on the physical level. A solution could be implemented through the usage of additional external sensors. Wired connections with sensors can be established over the serial connectors, USB connectors or even SD and uSD card sockets, while wireless connections are mostly available over high-power consuming Wi-Fi, medium-power Bluetooth or low-power WSN communication interfaces, if available.

## 3 Challenges related to mobile terminals used as sensor nodes

To efficiently access and retrieve sensor measurements from dedicated sensor nodes and opportunistic sensor network devices (e.g. mobile terminals) in the public networks, both device types must communicate and cooperate. However, access to mobile terminals through the internet over the mobile network cannot be done in a straightforward manner. In principle, mobile terminals can only post sensor measurements over self-created data session called Packet Data Protocol (PDP) context in GSM/UMTS and EPS bearer in LTE to the servers in the public networks, as depicted in Figure 1. Namely, all measurement retrieval requests coming in the opposite direction, as depicted by the red line in Figure 1, are not possible, since the mobile operators normally block all communication session initiation attempts coming from the public networks.

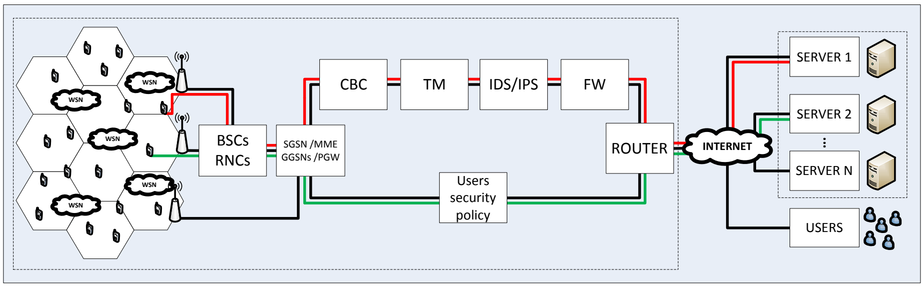

**Figure 1:** Typical sensor measurements transport routes over the mobile network

## 4 Spectrum sensing scenario with opportunistic sensor devices

Our considered sensing scenario for practical demonstration of Radio Environment Map (REM) [4] creation is depicted in the left side in Figure 2. It consists of the fixed sensor nodes (F) forming WSN and mobile opportunistic sensor network device(s) (M). This enables spectrum sensing over the specific area of interest to build an efficient REM needed for detection of the hidden node or primary user transmitter (H), as presented on the right side in Figure 2.

Such scenario can be realized with majority of the mobile terminals available despite the issues presented in Section 3. On the mobile network side a private access point name (APN) for a connection with its own security policy has to be prepared to allow the access to measurements from the external networks, as depicted in Figure 1 with the green line. To prove the concept for the mobile terminal, we took Android-based Samsung I9100 mobile terminal, which lacks WSN compatible radios and sensors being capable of spectrum sensing. We selected VESNA sensor node [5] capable of spectrum sensing to which we connected Roving Networks XBT RN-41 Bluetooth module. Thus, we enabled communication among mobile terminal and VESNA node together presenting an

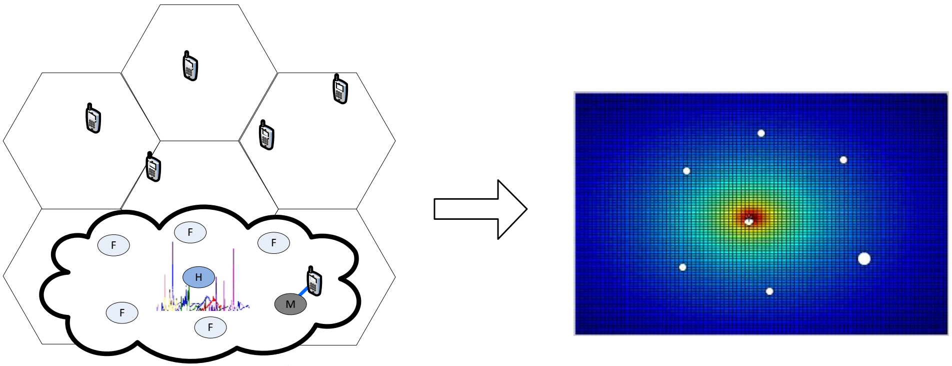

spectrum sensing

REM

**Figure 2:** Spectrum sensing scenario with sensor nodes and opportunistic sensor network device capable to cooperate and construct REM

opportunistic sensor network device. A test software for managing such a virtual sensor network device was written as a code in C programming language on the side of VESNA node and as Java-based Android application communicating with data frames, presented in [6].

## 5 Conclusion and future work

In this paper we outlined mobile terminals' sensing capabilities and their prospects to become opportunistic sensor network devices capable of cooperating with WSNs in spectrum sensing scenarios if complemented by appropriate sensors. Their sensor measurements can be accessed over the mobile network over private APNs. Our further work includes testing of opportunistic sensor network devices in real outdoor scenarios with the aim to support development of algorithms for hidden node detection.

## Acknowledgements

This work has been in part funded by the European Community from the European Social Fund under the Operational Programme Human Resources Development for the period 2007 – 2013.

## References

[1] J. Mitola III and G. Maguire, "Cognitive radio: making software radios more personal," *IEEE Personal Communications*, vol. 6, pp. 13-18, 1999.

[2] M. Vučnik, C. Fortuna, M. Porcius, and M. Mohorčič, "WSN Testbeds For Lighting Control And Environmental Monitoring," in *3rd Jožef Stefan International Postgraduate School Students Conference*, Ljubljana, Slovenia, 2011.

[3] M. Shin, C. Cornelius, D. Peebles, A. Kapadia, and D. Kotz, "AnonySense: A system for anonymous opportunistic sensing," *Pervasive and Mobile Computing*, vol. 7, 2011.

[4] V. Atanasovski, J. v. d. Beeky, A. Dejonghe, D. Denkovski, L. Gavrilovska, S. Grimoudyy, P. Mähönen, M. Pavloski, V. Rakovic, J. Riihijärvi, and B. Sayracyy, "Constructing Radio Environment Maps with Heterogeneous Spectrum Sensors," in *IEEE International Symposium on Dynamic Spectrum Access Networks*, Aachen, Germany, 2011.

[5] *VESNA hardware platform*. Available: SensorLab http://sensorlab.ijs.si/hardware.html

[6] M. Pesko, M. Štular, M. Vučnik, M. Smolnikar, and M. Mohorčič, "Bluetooth-based mobile gateway for wireless sensor network," in *The Second International Workshop on Sensing Technologies in Agriculture, Forestry and Environment*, Belgrade, Serbia 2011.

## For wider interest

Wireless Sensor Networks (WSN):
- are wireless networks build of spatially distributed small and low-power autonomous devices called sensor nodes, equipped with heterogeneous sensors to measure various physical phenomena over specific area of interest.

Opportunistic sensor network devices:
- are devices which can be used as sensor nodes,
- can be mobile terminals which can opportunistically cooperate with WSNs in various scenarios.

Cognitive radio principles:
- include methods for more efficient spectrum usage,
- enable multiple users sharing the same frequency spectrum in a cooperative or competitive way,
- enable non-licensed secondary users to communicate on the same frequencies as licenced primary users if and only if they do not cause any harmful interference.

Hidden node problem:
- is a problem in cognitive networks where secondary users in some situations are not aware of the primary user's presence in the vicinity.

Our work:
- outlining mobile terminals' features which enable them becoming opportunistic sensor network devices,
- pointing out mobile network issues related to sensor measurements access on mobile terminals and their lack of WSN compatible communication interfaces,
- presenting solutions for these issues.

Future work:
- to test mobile terminals as opportunistic sensor network devices in real testbeds meant for spectrum sensing and efficient Radio Environment Maps building to support multiple issues in cognitive networks.

# Inteligentni sistem za zaznavanje zdravstvenih težav pri starejših

**Bogdan Pogorelc**[1,2,3]

[1] Institut »Jožef Stefan«, Odsek za inteligentne sisteme, Ljubljana, Slovenija

[2] Špica International d.o.o., Ljubljana, Slovenija

[3] Mednarodna podiplomska šola Jožefa Stefana, Ljubljana, Slovenija

bogdan.pogorelc@ijs.si

**Povzetek.** Članek predlaga semantični in splošni pristop k prepoznavanju zdravstvenih težav starejših. Gibanje oseb je zajeto s sistemom za zajem gibanja in izhodne časovne vrste koordinat so modelirane z obema predlaganima pristopoma. Semantični pristop uporablja atribute na osnovi medicinskega znanja (semantične atribute) in klasifikacijsko metodo podpornih vektorjev. Splošni pristop ima za atribute vse izmerljive kote sklepov in klasificira s kombinacijo algoritma k-najbližjih sosedov in modifikacijo algoritma dinamičnega ukrivljanja časa (DTW). Kljub temu da je drugi pristop splošnejši in uporaben tudi za druge klasifikacijske metode, doseže primerljivo visoko klasifikacijsko točnost kot semantični pristop.

**Ključne besede** Zdravstvene težave, hoja, podatkovno rudarjenje, dinamično ukrivljanje časa.

## 1 Uvod

Razvite države se soočajo s hitro rastjo svojega prebivalstva. Napovedi kažejo, da naj bi se odstotek populacije nad 65 let v razvitih državah povečal iz 7,5 % v 2009 na 16 % v 2050 [1]. Starejši navadno živijo izolirani od potomcev, zato v primeru bolezni težko dobijo pravočasno pomoč. Namen te študije je razviti tehnologije, ki bi olajšale njihovo samostojno življenje.

Dva pristopa podatkovnega rudarjenja k inteligentnemu in vseprisotnemu sistemu nadzora zdravja z namenom razpoznati nekaj najpogostejših in najpomembnejših bolezni starejših, ki so lahko razpoznane preko opazovanja in analize karakteristik njihovega gibanja, sta predlagana v prispevku. Semantični pristop uporablja atribute na osnovi medicinskega znanja (semantične atribute) in metodo podpornih vektorjev. Splošni pristop ima za atribute vse izmerljive kote sklepov v kombinaciji z algoritmom k-najbližjih sosedov in dinamičnega ukrivljanja časa (DTW). Naloga je klasificirati vzorce hoje v pet različnih zdravstvenih stanj, eno zdravo in štiri bolezenska.

S sistemom za zajem gibanja, ki sestoji iz znač, pritrjenih na telo in senzorjev, nameščenih v stanovanju, je zajeto gibanje uporabnika. Izhodne časovne vrste koordinat so obdelane s predlaganima pristopoma, da bi razpoznali specifično zdravstveno težavo.

V literaturi je zajem gibanja navadno narejen z inercialnimi senzorji [2, 5], s strojnim vidom, s specifičnim senzorjem za merjenje kota upognjenosti sklepa [3] ali z elektromiografijo [4]. V naši študiji smo uporabili sistem (infrardečih) IR senzorjev z značkami pritrjenimi na telo. Ne naslavljamo samo razpoznave značilnih aktivnosti, kot je hoja, sedenje, ležanje, itd., kot je realizirano npr. v [6, 8], ampak razpoznavamo tudi zdravstvene težave. Z uporabo podobnega sistema za zajem podatkov so v [7] ločevali med hemiplegijo in diplegijo.

Pogostejši pristop iz sorodnega dela je zajem podatkov s sistemom za zajem gibanja in kasnejša ročna analiza podatkov [3, 4, 9]. Tak pristop ima pomanjkljivost v primerjavi z našim, da zahteva stalno pregledovanje strokovnjakov.

## 2 Materiali in metode

**Zdravstvene težave za detekcijo.** Vse zdravstvene težave, ki jih prepoznavamo, so bile predlagane s strani sodelujočega medicinskega strokovnjaka, na osnovi pogostosti nad 65 let starosti, medicinske pomembnosti in možnosti razpoznavanja iz gibanja. Sistem hojo klasificira kot: hemiplegijo (navadno po možganski kapi), Parkinsonovo bolezen, bolečino v nogi, bolečino v hrbtu in referenčno zdravo hojo.

**Atributi za podatkovno rudarjenje.** Meritve sestavljajo pozicije koordinat v $x,y,z$ za 12 znač nošenih na ramenih, komolcih, zapestjih, kolkih, kolenih in gležnjih, zajete s sistemom za zajem gibanja Smart z 10 Hz. Primeren prikaz uporabnikovega gibanja je bil pomemben del naše študije.

Semantični pristop smo zasnovali na osnovi dejstva, da zdravnik diagnosticira obravnavane zdravstvene probleme iz opazovanja hoje [10]. Ker so si vzorci podobni, mora biti pozoren na veliko detajlov, ki smo jih poskušali zapisati z merljivimi spremenljivkami. Za nalogo avtomatske prepoznave bolezni smo predlagali in testirali uporabo 13 značilk, kot npr. : povprečni kot komolcev, razlika med maksimalno in minimalno višino ramena, razlika hitrosti gležnjev.

Pri splošnem pristopu je gibanje predstavljeno z enostavnimi in splošnimi atributi, da bo klasifikator s temi atributi delal dobro tudi na drugačnih gibanjih, saj zajamemo le majhen del vseh možnih gibanj. Upoštevajoč našteto smo zasnovali atribute kot kote med sosednjimi deli telesa:

- kot levega in desnega ramena glede na zgornji del trupa v trenutku t:
- kot levega in desnega kolka glede na spodnji del trupa
- kot med spodnjim in zgornjim delom trupa:
- levi in desni komolčni ter levi in desni kolenski kot:

Koti med deli telesa, ki rotirajo v več kot eno smer, so izraženi s kvaternioni.

**DTW.** Dinamično ukrivljanje časa (DTW) poravna 2 časovni vrsti na način, da minimizira neko mero. Optimalna poravnava je dobljena s preslikavo več zaporednih vrednosti ene časovne vrste v eno vrednost druge časovne vrste in tako je lahko DTW računan tudi na časovnih vrstah različnih dolžin. V nasprotju z Evklidsko razdaljo, DTW lahko najde podobnosti med vzorcema dveh časovnih vrst, tudi če ta vzorca nista časovno poravnana ali pa sta vzorca različnih dolžin.

**Prispevek: multivariantno dinamično ukrivljanje časa.** DTW algoritem, ki je navadno opisan v literaturi, je uporabljen le za poravnavo univariantnih časovnih vrst. Splošni pristop te študije pa poravnava multivariantne časovne vrste. Najprej je vsaka točka zajete časovne vrste pretvorjena v prostor kotnih atributov, kjer bo izvedena klasifikacija.

Imamo testno meritev, ki jo želimo poravnati z učno meritvijo (kjer je bil klasifikator naučen) in najprej izračunamo matriko lokalnih razdalj $d(i,j)$, v kateri vsak element $(i,j)$ predstavlja lokalno razdaljo med $j$-to časovno točko učne in $i$-to časovno točko testne meritve. Naj bo $L_{jf}$ element generičnega atributnega vektorja glede na učno meritev in $T_{if}$ naj bo element atributnega vektorja, relativno na novo testno meritev za razpoznavo, kjer je $1<=f<=N$ upoštevani atribut. Za definicijo lokalne razdalje je bila uporabljena Evklidska razdalja

Na osnovi matrike lokalnih razdalj je zgrajena matrika globalnih razdalj $D$. Končni izhod algoritma je vrednost minimalne globalne razdalje za celotno poravnavo DTW in je najdena v zadnji vrstici in stolpcu, $D(R_I,C_J)$.

## 3 Eksperimenti in rezultati

Meritve so obsegale 256 posnetkov zdravih posameznikov in posameznikov z določenimi zdravstvenimi težavami, pri čemer je bil vsak posameznik 4-5 krat posnet z različnimi hitrostmi izvajanja aktivnosti.

Pri splošnem pristopu klasifikacijski proces upošteva eno vhodno testno časovno vrsto, ki jo primerja z vsemi ostalimi, da najde minimalno globalno razdaljo za vsako poravnavo in sklepa, da je vhodna meritev istega razreda kot učna meritev, ki ima najmanjšo razdaljo do te vhodne meritve.

Evaluacija "izpusti-enega" je rezultirala v klasifikacijski točnosti 97,9 % oz. 97,6 % za semantični oz. splošni pristop.

## 4 Zaključek

Prispevek predstavlja semantični in splošni pristop k detekciji zdravstvenih težav za namen podaljšanja samostojnega življenja starejših. Metoda "izpusti-enega" da klasifikacijski točnosti 97,9 % oz. 97,6 % za semantični oz. splošni pristop. Semantični pristop je zahtevnejši za izvedbo zaradi gradnje specifičnih semantičnih atributov, ki zahtevajo medicinsko znanje. Kljub temu, da je drugi pristop bolj splošen in lahko razpozna tudi nove vrste gibanj, dosega visoke klasifikacijske točnosti, podobne semantičnemu pristopu.

## Zahvala

Operacije, ki so pripeljale do tega članka, je delno sofinancirala Evropska Unija, Evropski socialni sklad. Avtor članka se zahvaljuje mentorju prof dr. Matjažu Gamsu za pomoč.

# Literatura:

[1] United Nations (2009) World Population Ageing. Report.

[2] Strle D., Kempe V., "MEMS-based inertial systems", MIDEM 37(2007)4, 199-209.

[3] Ribarič S., Rozman J., "Sensors for measurement of tremor type joint movements", MIDEM 37(2007)2, 98-104.

[4] Trontelj J., et al., "Safety margin at mammalian neuromuscular junction – an example of the significance of fine time measurements in neurobiology", MIDEM 38(2008)3, 155-160.

[5] Bourke A.K et al., An optimum accelerometer configuration and simple algorithm for accurately detecting falls. In Proc. BioMed 2006 (2006), 156–160.

[6] Confidence Project. http://www.confidence-eu.org.

[7] H. Lakany, Extracting a diagnostic gait signature. Patt. recognition 41(2008), 1627–1637.

[8] Luštrek, M., and Kaluža, B. Fall detection and activity recognition with machine learning. Informatica 33, 2 (2009).

[9] Moore ST, et al., Long-term monitoring of gait in Parkinson's disease, Gait Posture (2006).

[10] Pogorelc B, Bosnic Z, Gams M (2012) Automatic recognition of gait-related health problems in the elderly using machine learning. Multimed Tools Appl 58:333–354. doi:10.1007/s11042-011-0786-1.

## Za širši interes

V razvitem svetu je vedno večji delež starejšega prebivalstva. Starejši navadno živijo izolirani od otrok, zato v primeru bolezni ali poškodbe težko dobijo pravočasno pomoč. Namen te študije je razviti tehnologije, ki bi olajšale samostojno življenje starejših. Članek predstavlja dva pristopa k razvoju sistema za detekcijo zdravstvenih težav pri starejših z namenom podaljševanja njihovega samostojnega življenja. Če je zaznana zdravstvena težava, sistem avtomatsko obvesti medicinsko službo. Gibanje starejših je zajeto s sistemom za zajem gibanja in celoten sistem je naučen, da prepoznava specifične zdravstvene težave. Semantični pristop uporablja semantične atribute, ki jih uporablja zdravstvena stroka, splošni pa za atribute uporablja vse izmerljive kote sklepov namesto specifičnih atributov za posamezne bolezni. Kljub temu dobro prepoznava zdravstvene težave, podobno kot semantični in pristopi iz literature.

# Sentiment analysis on tweets in a financial domain

**Jasmina Smailović**[1,2], **Miha Grčar**[1], **Martin Žnidaršič**[1]

[1] Dept of Knowledge Technologies, Jožef Stefan Institute, Ljubljana, Slovenia
[2] Jožef Stefan International Postgraduate School, Ljubljana, Slovenia
jasmina.smailovic@ijs.si

**Abstract.** This paper investigates whether sentiment analysis of public mood derived from large-scale Twitter feeds can be used to identify important events and predict movements of stock prices. We used the volume and sentiment polarity of Apple financial tweets to identify important events and predict future movements of Apple stock prices. Statistical analysis using the Granger causality test showed that we were able to predict the rise or fall in closing price of Apple stocks two days before the change happens.

**Keywords**: sentiment analysis, classification, Twitter, stock price prediction.

## 1 Introduction

Sentiment analysis or opinion mining [1] is a research area aimed at detecting the authors' attitude, polarity (positive or negative) or opinion about a given topic expressed in a document collection. In this paper we investigate whether sentiment analysis of public mood, derived from large-scale collections of daily posts from online microblogging service Twitter can predict movements of stock prices. Specifically, we analyse Apple financial tweets to identify important events and predict the movement of Apple stock prices.

Trying to determine the future revenue or stock value has been attracting great attention of numerous researches. Early research on this topic claimed that stock price movements do not follow any patterns or trends and past price movements cannot be used to predict the future ones [2]. Later studies, however, show the opposite [3][4]. Recent research indicates that the analysis of online texts such as blogs, web pages and social networks can predict trends of various economic phenomena. It was shown [5] that blog posts can be used to predict spikes in actual consumer purchase decisions. Sentiment analysis of weblog data was used to predict movie success [6]. Twitter posts were also shown to be useful when predicting box-office revenues of movies in advance of their release [7]. Furthermore, it has been shown [8] that the stock market itself is a direct measure of social mood. So, it is reasonable to expect that the analysis of public mood can be used to predict movement of stock market values. Moreover, Bollen et al. [9] show that changes in a specific public mood state can predict daily changes in the closing values of the Dow Jones Industrial Average index.

The paper is structured as follows: selection of data preprocessing settings for the SVM classifier is explained in Section 2, followed by an example in Section 3. Conclusions are given in Section 4.

## 2 Selection of data preprocessing settings for the SVM classifier

Here we describe how the most appropriate classifier for sentiment analysis of financial tweets was chosen. Three common approaches to sentiment analysis are: machine learning, lexicon-based methods and linguistic analysis. In this work we use the machine learning approach. In this approach, classification refers to a procedure for assigning a given piece of input data (instance) into one of a given number of categories (classes). In our case, input data is a tweet and it can be classified into one of two categories: positive or negative, which represent attitude of the tweet`s author. An instance is described by a vector of features (in our case, words and word pairs), also called attributes, which constitute a description of all known characteristics of the instance. An algorithm that implements classification is known as a classifier. Classification usually refers to a supervised procedure, i.e., a procedure that learns to classify new instances based on a model learnt from a training set of instances that have been properly labelled. For our training set we used a collection of 1,600,000 (800,000 positive and 800,000 negative) tweets collected by the Stanford University [10], where positive and negative emoticons were used as labels. For testing we used a set of manually labelled 177 negative and 182 positive tweets from the same source [10]. The $SVM^{perf}$ classifier [11] was used for training and testing. It is an implementation of the *Support Vector Machine* machine learning algorithm. As attribute weights, we used TFIDF (term frequency–

inverse document frequency) which reflects how important a word is to a document in a collection or corpus. We explored the usage of unigrams, bigrams, replacement of usernames with a token, replacement of web links with a token, word appearance thresholds and removal of letter repetitions (e.g. 'looooove' is changed to 'love'). Table 1 summarizes the experimental results.

**Table 1:** Classifier performance evaluation for various preprocessing settings.

| Maximum N gram length | Minimum word frequency | Replace usernames with a token | Replace web links with a token | Remove letter repetition | Accuracy | Precision/Recall |
|---|---|---|---|---|---|---|
| 2 | 2 | No | Yes | Yes | 81.06% | 81.32%/81.32% |
| 2 | 2 | No | No | Yes | 78.83% | 77.60%/81.87% |
| 2 | 2 | Yes | No | Yes | 78.55% | 75.86%/84.62% |
| 2 | 2 | Yes | Yes | Yes | 78.27% | 76.53%/82.42% |
| 2 | 3 | No | No | Yes | 76.88% | 77.97%/75.82% |
| 1 | 2 | No | No | Yes | 76.32% | 72.99%/84.62% |

As it can be seen from the table, the best classifier is obtained by using both unigrams and bigrams, using words which appear at least two times in the corpus, with replacing links with a token and with removal of repeated letters.

## 3 Classifying financial tweets

Our main data resource for collecting financial Twitter posts is the Twitter API, i.e. Twitter Streaming and Search API. The Streaming API allows near-realtime access to various subsets of Twitter data while Search API returns tweets that match a specified query. By the informal Twitter conventions, the dollar-sign notation is used for discussing stock symbols. For example, $AAPL tag indicates that the user discusses Apple stocks. This convention simplifies the retrieval of financial tweets. We noticed that there are many tweets with similar content which are mainly a result of re-tweeting and spam. Twitter's re-tweet feature allows users to quickly post other users` messages. Spammers, on the other hand write nearly identical messages from different accounts. We employed the algorithm based on Jaccard similarity [12] to discard tweets that were detected as near duplicates. We analysed English posts that discussed Apple stocks in the period from March 11 to December 9, 2011. After pre-processing, 33,733 tweets were left and these were classified with the classifier described in Section 2. After classification, we count the number of positive and negative tweets for each day (Figure 1). Peaks show the days where people intensively talked about Apple. The analysis shows that these days correspond to important events.

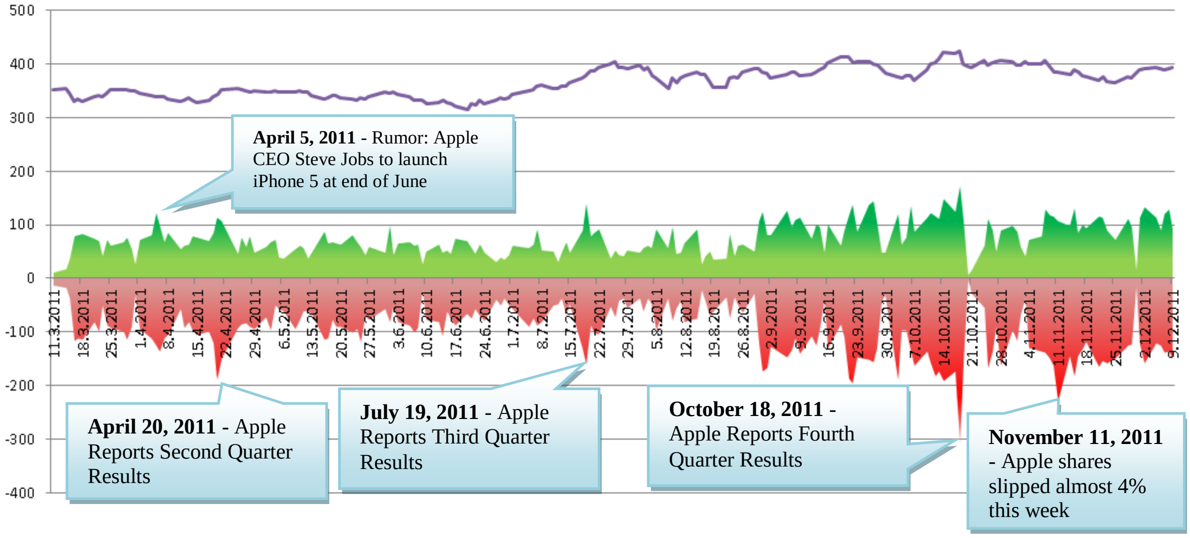

**April 5, 2011** - Rumor: Apple CEO Steve Jobs to launch iPhone 5 at end of June

**April 20, 2011** - Apple Reports Second Quarter Results

**July 19, 2011** - Apple Reports Third Quarter Results

**October 18, 2011** - Apple Reports Fourth Quarter Results

**November 11, 2011** - Apple shares slipped almost 4% this week

**Figure 1:** Number of positive (green), negative (red) tweet posts and closing price (violet) per day.

Next, we calculated the positive sentiment probability for each day. To enable the comparison of closing price and positive sentiment probability time series, we normalize them to z-scores. The z-score of time series *Xt*, is defined as:

$$Z_{Xt} = \frac{X_t - \bar{x}(X_{t\pm1})}{\sigma(X_{t\pm1})} \tag{1}$$

where $\bar{x}(X_{t\pm1})$ and $\sigma(X_{t\pm1})$ represent the mean and standard deviation of the time series within the period [t-1; t+1]. Next, we applied a statistical hypothesis test for determining whether positive sentiment probability time series is useful in forecasting the closing price. More specifically, we performed the Granger causality analysis [13] for the period between September 1 and December 8, 2011 as we notice that this is the period of big changes in the stock price when people also posted a large amount of messages. The Granger causality test (results shown in Table 2) indicates that positive sentiment probability could predict stock price movements, as we got a significant result (p-value < 0.1) in our dataset for a two day lag. This means that changes in values of positive sentiment probability could predict a similar rise or fall in closing price two days in advance.

**Table 2:** Statistical significance (p-values) of Granger causality correlation between positive sentiment probability and closing stock price.

| Lag (days) | p-value |
|---|---|
| 1 | 0.4855 |
| 2 | **0.0565** |
| 3 | 0.0872 |

## 4 Conclusions

Predicting future values of stock prices has always been an interesting task, commonly connected to the analysis of public mood. Various studies indicate that these kinds of analyses can be automated and can produce useful results as more and more personal opinions are made available online. In this paper, we investigated whether sentiment analysis of public mood derived from large-scale Twitter feeds can be used to identify important events and predict movements of stock prices. More specifically, Apple financial tweets were analysed, where our experiments showed that changes in values of positive sentiment probability with a delay of two days can predict a similar movement in the stock closing price. In the future, we plan to experiment with different datasets for training classifiers, analyse other companies‘ stocks and employ part of speech tagging in order to improve the classifier performance.

## Acknowledgements

The work presented in this paper has received funding from the European Community's Seventh Framework Programme (FP7/2007-2013) within the context of the Project FIRST, Large scale information extraction and integration infrastructure for supporting financial decision making, under grant agreement n. 257928 and by the Slovenian Research Agency through the research program Knowledge Technologies under grant P2-0103.

# References:

[1] P. Turney. Thumbs Up or Thumbs Down? Semantic Orientation Applied to Unsupervised Classification of Reviews. In *Proceedings of the Association for Computational Linguistics*, p. 417–424, 2002.

[2] E. Fama. Random Walks in Stock Market Prices. *Financial Analysts Journal*, 21(5): 55–59, 1965.

[3] K. C. Butler, S.J. Malaikah. Efficiency and inefficiency in thinly traded stock markets: Kuwait and Saudi Arabia. *Journal of Banking and Finance* 16, 197–210, 1992.

[4] M. Kavussanos, E. Dockery. A Multivariate test for stock market efficiency: The case of ASE. *Applied Financial Economics*, 11(5): 573-579, 2001.

[5] D. Gruhl, R. Guha, R. Kumar, J. Novak and A. Tomkins. The predictive power of online chatter. In *Proceedings of the eleventh ACM SIGKDD international conference on Knowledge discovery in data mining*, p. 78-87, New York, USA, 2005.

[6] G. Mishne and N. Glance. Predicting Movie Sales from Blogger Sentiment. In *AAAI Symposium on Computational Approaches to Analysing Weblogs AAAI-CAAW*, p. 155-158, 2006.

[7] S. Asur and B. A. Huberman. Predicting the Future with Social Media. In *Proceedings of the ACM International Conference on Web Intelligence*, arXiv:1003.5699v1, 2010.

[8] J. R. Nofsinger. Social Mood and Financial Economics. *Journal of Behavioral Finance*, 6(3): 144-160, 2005.

[9] J. Bollen, H. Mao, X. Zeng. Twitter mood predicts the stock market. *Journal of Computational Science*, 2(1): 1-8, 2011.

[10] A. Go, R. Bhayani, L. Huang. Twitter Sentiment Classification using Distant Supervision. *Association for Computational Linguistics*, p.30-38, 2009.

[11] T. Joachims. Training Linear SVMs in Linear Time. In *Proceedings of the ACM Conference on Knowledge Discovery and Data Mining (KDD),* 2006.

[12] A. Broder, S. Glassman, M. Manasse and G. Zweig. Syntactic Clustering of the Web. In *Proceedings of WWW6 and Computer Networks* 29:8-13, 1997.

[13] P. Wessa. Bivariate Granger Causality (v1.0.0) in Free Statistics Software (v1.1.23-r7), Office for Research Development and Education, http://www.wessa.net/rwasp_grangercausality.wasp/

## For wider interest

From psychological research it is known that emotions are essential to rational thinking. Also, it has been shown that the stock market is a direct reflection of the social mood. On the other hand, more and more people make their opinions available publicly online, making it available for analysis. Can we expect that the analysis of public mood can identify important events and predict the movement of stock market values? Our preliminary studies indicate that the answer is – yes. We analysed the Apple financial Twitter posts that were collected in a 10 months period. We identified days when people intensively talked about Apple and consequently identified important events for this company. Next, we performed statistical analysis for the period of specific 3 months, which is the period of the main changes in the stock price, to determine whether we can predict future movement of Apple`s closing price. The test showed that we are able to predict the rise or fall in closing price two days before it occurs. This kind of analysis can also be applied to other domains. For example, it can be used for the assessment of products, prediction of purchase decisions, earnings and other similar phenomena.

# Cross-lingual named entity extraction and disambiguation

**Tadej Štajner**[1,2], **Dunja Mladenić**[1,2]

[1] Artificial Intelligence Laboratory, Jožef Stefan Institute, Ljubljana, Slovenia
[2] Jožef Stefan International Postgraduate School, Ljubljana, Slovenia

tadej.stajner@ijs.si

**Abstract.** We propose a method for the task of identifying and disambiguation of named entities in a scenario where the language of the input text differs from the language of the knowledge base. We demonstrate this functionality on English and Slovene named entity disambiguation

**Keywords**: Natural language processing, knowledge management, multilingual information management, cross-lingual information retrieval

## 1 Introduction

Since a lot of our world's knowledge is present in textual format in multiple languages rather than a more explicit or language-neutral format, an interesting challenge is automatically integrating texts with structured and semi-structured resources, such as knowledge bases, collections of entities having various properties, such as labels and textual descriptions. Recent work focuses on the fact that all of this knowledge can be spread over many languages [6]. While Wikipedia, the free encyclopaedia, is a famous example, the same problem is applicable on many domains where text is present in multiple languages. In the domain of cross-lingual text annotation, we focus on the tasks of entity extraction and disambiguation (NED). We demonstrate a multilingual named entity extraction and disambiguation pipeline, operating for English and Slovene in order to demonstrate the capability of re-using language resources across languages within the Enrycher system [8].

## 1 Motivation

Many machine translation systems are not aware of named entities and special handling that is often required for them, and instead simply attempt to literally translate them. This often results in errors, for instance in Google Translate changing the name of the music band “Foo Fighters” into “Sigur Ros”, an Icelandic music band, when translating from English to Icelandic. This illustrates the need for special handling of proper names when doing machine translation. By performing named entity extraction and disambiguation before translation, we are able to use a knowledge base to find a correct translation for that named entity.

The second problem comes up in performing NED in a language that has poor domain coverage in the knowledge base. Consequently, entities that are extracted are not correctly disambiguated, since they don’t exist in that particular language. However, the entity that we are looking for can exist in the knowledge base in a different language. However, directly using that language introduces new problems, since many of the components assume that the language of the input text corresponds to the language of the knowledge base labels and descriptions.

## 2 Related work

The simplest solution for cross-lingual entity disambiguation is the one that simply disregards the language mismatch and tries to use the full textual content to perform the context similarity without any additional processing [1]. The authors have shown that using a merged bilingual knowledge base performed significantly better than using just the document language knowledge base, mainly due to better domain coverage, but it performed much worse than a monolingual scenario. Another simple baseline uses the equivalent of just using the context-independent ‘mention popularity’ measure, backed by a dictionary [2]. The dictionary can be constructed from looking at anchor texts from non-English to English Wikipedia pages. An ideal system would be the one that would simply translate the document in the desired language and do the disambiguation on the translation. While doing so manually is not feasible for our task, one may use machine translation to do this [6]. While they achieve up to 94% performance of a monolingual baseline, machine translation greatly complicates and slows down the processing, opening an window for more efficient approaches.

## 3 Problem description

We state the problem as identifying and disambiguating concepts that appear as mentions within a fragment of text. Disambiguation is important because phrases may have many distinct meanings. While human readers are able to infer the meaning from context, this task is difficult for computers. For instance, the phrase "Washington" can be either a person, location or an organization, and even constraining its type to a location yields over sixty possible different location that are named that way.

### 3.1 Named entity extraction

Named entity extraction is the task of using the surrounding context to isolate the part of text which represents an entity, referred to by a proper name. It is often coupled with entity classification, determining to what class it belongs to, for instance a person or an organization. In general, these are implemented as supervised sequence classifiers.

### 3.2 Named entity disambiguation

Ambiguities, which are inherently present in natural languages represent a challenge of determining the actual identities of entities mentioned in a document (e.g., Paris can refer to a city in France but it can also refer to a small city in Texas, USA or to a 1984 film directed by Wim Wenders having title Paris, Texas).

Well-defined entities and relationships are a property of the knowledge model which asserts that a single term has only a single meaning. In that case, we refer to terms as entities. We achieve this property by performing entity resolution. In general, state of the art entity disambiguation systems use three main heuristics:

- **Mention popularity** captures the overall most likely meanings of entity phrases. It is typically modelled by the conditional probability of the named entity given a mention.
- **Context similarity**: This heuristic captures the entity that best fits the topical context around the mention. It is modelled by the similarity of the mention's context and the entity's context, using a similarity measure operating on a bag-of-words model. The mention's context is a window of words around the mention in the input text, and the entity's context is its description.
- **Coherence**: This heuristic collectively captures the entities that make sense appearing together because they are somehow related to one another. While context similarity operates on a single mention-entity pair, the coherence heuristic is collective, operating on the whole input document. It is typically solved by a greedy graph pruning algorithm.

### 3.3 Cross-lingual named entity disambiguation

When extending this pipeline into a scenario where the input and the knowledge base are represented in multiple languages, the biggest impact of this change is on the context similarity heuristic. Because it operates on the level of lexical similarity, its output has little meaning when the assumption of a single language is removed.

## 4 Proposed method

We propose a method that incorporates a cross-lingual similarity measure into the framework. Instead of just computing literal context similarity between two contexts of different languages, we use an additional linear mapping that is able to map one vector of bag-of-words features into another such vector in another language. This enables us to perform meaningful similarity computation on the same vector space.

The method used in this approach is Regression Canonical Correlation Analysis (rCCA), a dimensionality reduction technique operation on two views that finds a linear combination of vectors from both views (languages) that are maximally correlated. The first vector corresponds to the input document, while the second one corresponds to the optimal mapping of it. However, instead of calculating this mapping in advance, we solve the optimization problem for each input document separately around the input document as the initial projection vector.

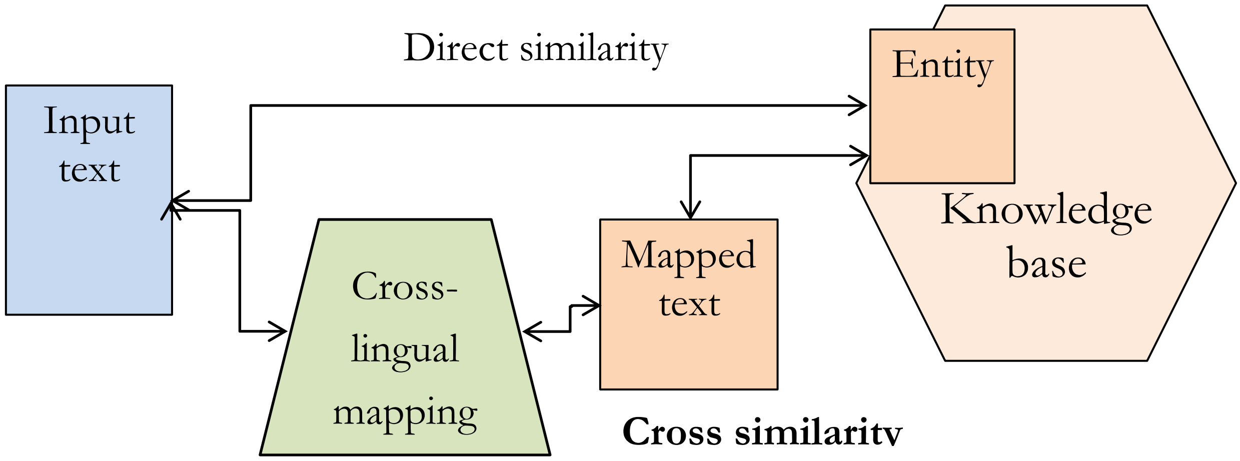

**Figure 1**: The setup of obtaining similarity in cross-lingual NED

Figure 1 represents the two ways of obtaining a context similarity measure between an input document and one of the candidate entities. When the languages of the input and the knowledge base are the same, we use direct similarity. When they differ, we first try to map the cross-lingual mapping (green triangle) into a vector space, compatible with the knowledge base. However, using a cross-lingual mapping exposes us to the risk of poor domain coverage. Initial experiments show that because the cross-lingual mapping was not able to map some of the words from the input document, it will have poor performance. Therefore, we interpolate the cross-similarity with the direct similarity with the proportion of the words that the cross-lingual mapping was able to recognize. In pre-processing, we use the Stanford Named Entity Recognizer [9] for English named entity recognition. For Slovene, we have developed a Slovene named entity recognizer using a CRF (Conditional random fields) model trained on the SSJ-500k corpus [9].

## 5 Discussion and conclusions

Current preliminary experiments show that obtaining a cross-lingual mapping does improve on the context-similarity based NED when the training corpus and the input text share a common topic. However, it is not yet certain whether it compares favourably to a machine translation based system. Current work demonstrates that the interpolation between direct and cross-lingual similarity help the robustness of the systems. Future work will involve evaluating different cross-lingual similarity models, as well as transliteration models and data integration issues that arise when dealing with multilingual knowledge bases.

## References:

[1] A. Lommatzsch et al, Named Entity Disambiguation for German News Articles*, WIR 2010*

[2] Spitkovsky, V.I. and Chang, A.X., Strong baselines for cross-lingual entity linking, *TAC 2011*

[3] T. Štajner and D. Mladenić: Entity resolution in texts using statistical learning and ontologies, *ASWC 2009*

[4] J. Rupnik, B. Fortuna. Regression Canonical Correlation Analysis. *Learning from Multiple Sources, NIPS Workshop, 2008*

[5] Hoffart, J., Yosef, M.A., Bordino, I., Fürstenau, H, Pinkal, M., Spaniol, M., Taneva, B., Thater, S., Weikum, G. (2011). Robust Disambiguation of Named Entities in Text. *Proceedings of the 2011 Conference on Empirical Methods in Natural Language Processing, 782-792.*

[6] McNamee, P., Mayfield, J., Oard, D. W., Lawrie, D., & Doermann, D. (2011). Cross-Language Entity Linking. *IJCNLP 2001, 255-263.*

[7] Učni korpus "Sporazumevanje v Slovenskem Jeziku", *http://www.xn--slovenina-gfb73g.eu/Vsebine/Sl/Aktivnosti/UcniKorpus.aspx, April 2012*

[8] Štajner, T., Rusu, D., Dali, L., Fortuna, B., Mladenić, D., Grobelnik, M. *A service oriented framework for natural language text enrichment. Informatica (Ljublj.), 2010, vol. 34, no. 3, 307-313. http://enrycher.ijs.si*

[9] Jenny Rose Finkel, Trond Grenager, and Christopher Manning. 2005. Incorporating Non-local Information into Information Extraction Systems by Gibbs Sampling. *Proceedings of the 43nd Annual Meeting of the ACL (ACL 2005), pp. 363-370.*

## For wider interest

When attempting to understand text, one of the tasks that need to be solved is named entity disambiguation: for instance, Paris can refer to a city in France but it can also refer to a small city in Texas, USA or to a 1984 film directed by Wim Wenders having title Paris, Texas. Knowing the correct answer to that depends on the context. However, context is difficult to interpret if the input text is expressed in a different language than the knowledge base that these entities belong to.

This is a very common scenario in processing Slovene text. While using the Slovene Wikipedia for this purpose is easy, it does not contain many entities that we may be interested in. While the English one is over thirty times bigger, it introduces a language barrier. We overcome this by applying techniques from cross-lingual information retrieval to the problem of identifying proper names in text and linking them to concrete knowledge base concepts.

Another goal was to re-use language resources from languages with more resource in languages with less available resources. The work presented has resulted in a usable named entity extraction and disambiguation service that is able to work on Slovene text even while having a knowledge base in English.

The demonstration is available at http://enrycher.ijs.si

# Extending the Multi-Criteria Decision Making Method DEX

**Nejc Trdin** [1,2], **Marko Bohanec** [1]

[1] Jožef Stefan Institute, Department of Knowledge Technologies, Ljubljana, Slovenia

[2] Jožef Stefan International Postgraduate School, Ljubljana, Slovenia

`{nejc.trdin, marko.bohanec}@ijs.si`

**Abstract.** The purpose of this work is to propose a plan for future research and development of the qualitative decision support method DEX. DEX is a qualitative multi-attribute modelling method used to evaluate and analyse multiple decision alternatives in order to select the best alternative. We propose six extensions to DEX: supporting full hierarchies, using numeric attributes, probabilistic and fuzzy evaluations, general aggregation functions, modularization and using relational models. These will be implemented in a new decision support platform.

**Keywords**: Decision making, decision support, DEX, probability, fuzzy logic, aggregation functions, modularization, relational models.

## 1 Introduction

People are able to make simple decisions very quickly, but are prone to making sub-optimal decisions when facing a complex decision. *Decision making* can be supported by appropriate techniques [1, 2]. One of such techniques is DEX [3, 4], a *qualitative decision modelling method*. DEX was successfully used in many applications such as ecology, industry and health care [5, 6, 7].

The motivation for this work follows from the observed needs for new functionalities in practical applications. We propose six possible extensions of DEX that will be further investigated and implemented in the future. In the following, we first describe the DEX methodology (section 2) and then propose the extensions (section 3). Section 4 concludes the work.

## 2 The DEX methodology

Decision making is a process which involves *evaluating* multiple *alternatives*, in order to select the best alternative. The selected alternative should satisfy the *goals* of the decision maker [1, 2, 4].

DEX is a representative of *qualitative multi-attribute decision support methods* [2, 3, 4]. Its main property is that the observed attributes are represented with *qualitative attributes*. The model developed using DEX methodology is described as a *hierarchy* of attributes. The input attributes are at the lowest level, all other (aggregated) attributes are concepts that logically depend on lower level attributes. Each hierarchy has one or more special nodes, the *root node(s),* that have no parents. The value given to the root nodes represent the final evaluations of the alternative. The main difference between DEX and other multi-attribute methods is in the *aggregation functions*, which are rules evaluating alternatives - each aggregated attribute has one function. Aggregation functions in DEX are represented as tables.

A model developed according to these rules can be used to evaluate alternatives. Alternatives' values are assigned to the lowest attributes of the hierarchy. The evaluation is done in a bottom-up fashion, using aggregation functions. The model is also typically used for the analysis of decision alternatives, such as *what-if analysis*.

DEX is implemented in the software named DEXi [4, 8]. Also, there are some other programs that implement extensions to the basic methodology:

- proDEX [9]: Motivated by demands in ecological modelling [10], proDEX implements *probabilistic* evaluation of alternatives. The final result of evaluation is a probability distribution over the values of the root attribute.
- Model revision [11]: This is a process of creating a new model from an existing model and newly acquired data. The methodology revises the model by modifying probabilities of rules in the model, without affecting the structure of the model.
- HINT [12]: This is a method for constructing DEX models from data. The approach is based on *function decomposition*. HINT is a representative of concept machine learning methods.

# 3 Proposed extensions to DEX methodology

DEX methodology is evidently very understandable, easy to use and yet strong enough to assess complex decisions. However, further improvements are needed due to practical requirements. In the following, we propose six possible extensions to DEX methodology.

*Supporting full hierarchies.* In principle, the structure of the DEX model is a hierarchy, i.e., directed acyclic graph. So far, hierarchies were only indirectly supported in DEX [3] and DEXi software [8], using the concepts called "chaining" and "linking" of nodes. In the extension we wish to fully support hierarchies by representing them using the *native graph form*. Hierarchies also natively support multiple root attributes.

*Numeric attributes.* Currently, DEX models employ only qualitative (symbolic) attributes. The goal is to facilitate models that could simultaneously include both qualitative and *quantitative attributes*. This means that we have to design principles of including numeric attributes into DEX models. This extension is useful in situations where attributes are better described with numeric values, rather than symbolic; for example experts' preference, salary, etc. Numeric values should be used both to describe the properties of decision alternatives and decision makers' preferences according to those properties. Some advances on introducing numeric attributes into DEX are considered in [10, 13]. The main problem here is to introduce mechanisms for conversion and mapping of both types of attributes.

*Probabilistic and fuzzy evaluations.* The notion of probabilistic computation is needed for *uncertain* problem definitions. Actually, we would like to support both probabilistic and fuzzy computations. Another generalization would be that alternative input attributes would not only support crisp values, but also distributions of values. The problem with supporting both probability and fuzzy logic is combining both in the model, because computations are done differently.

*General aggregation functions.* With the introduction of numeric attributes, probabilities and fuzziness, we will also have to adapt aggregation functions. Functions will have to be able to compute with combinations of probabilities, fuzzy, symbolic and numeric values. Adding numeric attributes will require adding a whole new set of numeric aggregation functions. One of the main features of the aggregation function is the ability to extract information from the end-user with as low effort as possible. Furthermore, representations of aggregation functions must be comprehensible to the user. Another extension is the capability for functions to receive arbitrary number of inputs – functions such as *sum*, *min*, *max*, etc. The next way to generalize functions is using the current tables, by constructing similar tables with outputs dependant on the non-qualitative attributes. The main problem with this generalization is that the function must be able to adapt when adding or removing direct descendant attributes. The implementation must preserve as much information as possible when doing operations on the model structure.

*Modularization.* Modularization means to merge a part of the model into one *module*, which looks like an aggregated attribute. The newly created attribute would have the same inputs and outputs as the part of the model before merging. Grouping can be done in more levels, which leads to a tree-like structure of modules and attributes. This means that, in addition to the hierarchical model structure, we need to deal with another structure describing the grouping of attributes and modules. The modularization technique is useful in managing big models, which are hard to deal with. When a user completes a big part of some sub hierarchy, he would create a module from this sub hierarchy and use it in other decision models; this improves the *reusability* of developed components.

*Relational models.* Currently, DEX is capable of evaluating "flat" alternatives, that is, alternatives described by a vector of values. In reality, however, alternatives may be more complex. For example, we can have a company that is composed of departments; in order to assess the company, we have to evaluate each department separately and the company as a whole. We say that such an alternative is *relational.* We also encounter relational alternatives in group decision making, where all the decision makers have different preferences on the same matter - the matter can be treated as some part of the sub hierarchy. The top aggregation function, where the combination of all sub-model evaluations are combined, is the most important - the aggregation is not constrained just to calculating to simple functions, but it can have more complex structure. Similar technique was already implemented in DEX software as "groups", but in a limited fashion.

## 4 Conclusion

The primary contribution of this work was to propose possible extensions and generalization of the DEX methodology. Six extensions were proposed, which will considerably extend the functionality of the approach and facilitate addressing the most complex decision problems encountered to date in practice. These extensions will be further developed and implemented in a new software package with large capabilities.

## References:

[1] S. French. *Decision Theory: An introduction to the Mathematics of Rationality.* Halsted Press, 1986.

[2] D. Bouyssou, T. Marchant, M. Pirlot, A. Tsoukias and P. Vincke. *Evaluation and Decision Models with Multiple Criteria.* Springer, 2006.

[3] M. Bohanec and V. Rajkovič. DEX: An expert system shell for decision support. *Sistemica*, 1(1):145-157, 1990.

[4] M. Bohanec. *Odločanje in Modeli.* DMFA, 2006.

[5] M. Bohanec and V. Rajkovič. Multi-attribute decision modeling: Industrial applications of DEX. *Informatica*, 23(4):487-491, 1999.

[6] M. Bohanec, B. Zupan and V. Rajkovič. Applications of qualitative multi-attribute decision models in health care. *International Journal of Medical Informatics*, 58-59:191-205, 2000.

[7] M. Bohanec, S. Džeroski, M. Žnidaršič, A. Messeean, S. Scatasta and J. Wesseler. Multi-attribute modelling of economic and ecological impacts of cropping systems. *Informatica*, 28(4):387-392, 2004.

[8] DEXi: A program for multi-attribute decision making. http://kt.ijs.si/MarkoBohanec/dexi.html, 2012.

[9] M. Žnidaršič, M. Bohanec. Handling uncertainty in DEX methodology. In *URPDM 2010: Proceedings of the 25th Mini-EURO Conference*, Coimbra, Portugal, 2010.

[10] M. Žnidaršič, M. Bohanec and B. Zupan. Modelling impacts of cropping systems: Demands and solutions for DEX methodology. *European Journal of Operational Research*, 189(3):594-608, 2008.

[11] M. Žnidaršič and M. Bohanec. Data-based revision of probability distributions in qualitative multi-attribute decision models. *Intelligent Data Analysis*, 9(2):159-174, 2005.

[12] B. Zupan, M. Bohanec, J. Demšar and I. Bratko. Learning by discovering concept hierarchies. *Articial Intelligence*, 109(1-2):211-242, 1999.

[13] M. Žnidaršič, M. Bohanec and I. Bratko. Categorization of numerical values for DEX hierarchical models. *Informatica*, 27(4):405-409, 2003.

## For wider interest

The main purpose of this paper is to propose six new extensions to the DEX methodology. The methodology is a member of multi-attribute decision support techniques, which are used for supporting people at making better decisions. Usually such decisions are made in business environments, ecology, industry and also in personal decisions, e. g., choosing a family vehicle.

A DEX decision model is constructed as a hierarchy of attributes, which are connected in a logical sense. For example, when choosing a car, one would logically construct "maintenance price" from "buying price" and "consumption". The attributes used in the hierarchy are presented as qualitative (symbolic) values. The values are not presented as numerical (-1, 0.12, 18, …), but rather as "good", "medium" and "bad". This is particularly useful in decision situations where judgement prevails over exact formal treatment of criteria.

As written in the paper, the methodology was successfully used in many different applications, but still lacks some functionality for the decision maker. Three useful extensions were developed before, but there are still more functionalities needed from the system.

Our goal is to successfully design, investigate and finally implement six additional extensions to the DEX methodology in a new powerful decision support system. The presented extensions are related to the model structure (supporting full hierarchies), attribute representation (facilitating probabilistic and fuzzy computations, and numeric attributes), model representation (introducing modularization), aggregation functions (supporting general aggregation functions) and support for relational models.

# Development of Discovery and Identification Protocol for Sensor Networks

**Matevž Vučnik**[1,2], **Zoltan Padrah**[1,2], **Carolina Fortuna**[1,2], **Mihael Mohorčič**[1,2]

[1] Department of Communication Systems, Jožef Stefan Institute, Ljubljana, Slovenia

[2] Jožef Stefan International Postgraduate School, Ljubljana, Slovenia

`{matevz.vucnik, zoltan.padrah, carolina.fortuna, miha.mohorcic}@ijs.si`

**Abstract.** This paper describes a new application layer communication protocol Discovery and Identification Protocol (DIP). The DIP protocol is designed to be used in low power wireless sensor networks (WSN) for discovery of the sensor nodes and sensor data collection. We first describe the design of the protocol and then the implementation of the protocol in the event based operating system Contiki, which targets extremely low power devices such as sensor nodes. In the conclusion we give a comparison of DIP and Constrained Application Protocol (CoAP) which is an application communication protocol with a more general design enabling the evolution of the current Web to the "Web of Things".

**Keywords**: WSN, communication, discovery, web, measurements, metadata.

## 1 Introduction

Sensor data collection is one of the most important components in Wireless Sensor Networks (WSN). With sensor data we refer to (1) sensor measurements which are typically represented with a simple float number with a changing value, with exceptions such as cameras, where the output is an image or a video, and (2) the metadata, which gives the meaning to the measurement and normally does not change over time. The metadata consists of all the information about the measurement starting with measurement unit, accuracy, calibration parameters, etc. to contextual description of environment where the measurements were collected (e.g. environment characteristics, etc.). The measurements are normally significantly smaller than the metadata, but they change over time and need to be retrieved more frequently.

For retrieving the data and for automatic discovery of sensor nodes we implemented a protocol named Discovery and Identification Protocol (DIP). The DIP protocol was developed to simplify the management of actually deployed sensor networks. In our testbed and application deployments the WSNs are based on VESNA[1] sensor nodes and can be interacted with over the Web[2] [1].

DIP is an application layer protocol. It introduces a sensor network coordinator which on one side communicates with sensor nodes and on the other with the infrastructure. As infrastructure we refer to a remote server for interacting with sensor network which will store the sensor data to the databases or another kind of storage, e.g. more expressive triplestores and make them accessible on the Web. The infrastructure is included in the protocol to minimize the traffic in the sensor network by separating measurements and metadata.

## 2 DIP Protocol design

The DIP protocol consists of three separate cycles indicated in protocol sequence diagram in Fig. 1; node discovery, measurements collection and node identification. Node discovery begins by the coordinator broadcasting "Hello" message, which the nodes receive and respond to. The coordinator receives responses from the nodes and stores the nodes' addresses in the table of known nodes, which is used in the measurements collection cycle. In this cycle the coordinator goes through the table and requests the measurements from each node. The table also implements "Time To Live" (TTL) parameter for each node. Every time the coordinator receives the node response on broadcasted "Hello" message the TTL for that particular node is set to maximum whereas TTL for nodes that did not send the response is decreased. When TTL is elapsed the node is discarded from the coordinator table. This is efficient way of keeping the coordinator table clean of the nodes that do not respond for whatever reason. There also exists a limit in size of the table to avoid the coordinator crashes due to exceeding the memory for the table in the case of large sensor network. This effectively limits the network size per one coordinator.

---

[1] sensorlab.ijs.si/hardware.html

[2] gsn.ijs.si, sensors.ijs.si

Our measurements collection protocol running on the coordinator node pulls the measurements from the nodes found in the table and pushes them towards the infrastructure, unaware if the server knows the measuring nodes. The coordinator waits for the infrastructure response and in case the infrastructure does not know a given node it sends a request for identification of that node to the coordinator. Upon request the coordinator demands the metadata from the node and forwards it to the infrastructure (see Fig. 1). Metadata gives meaning to the measurements so they can be used in various applications.

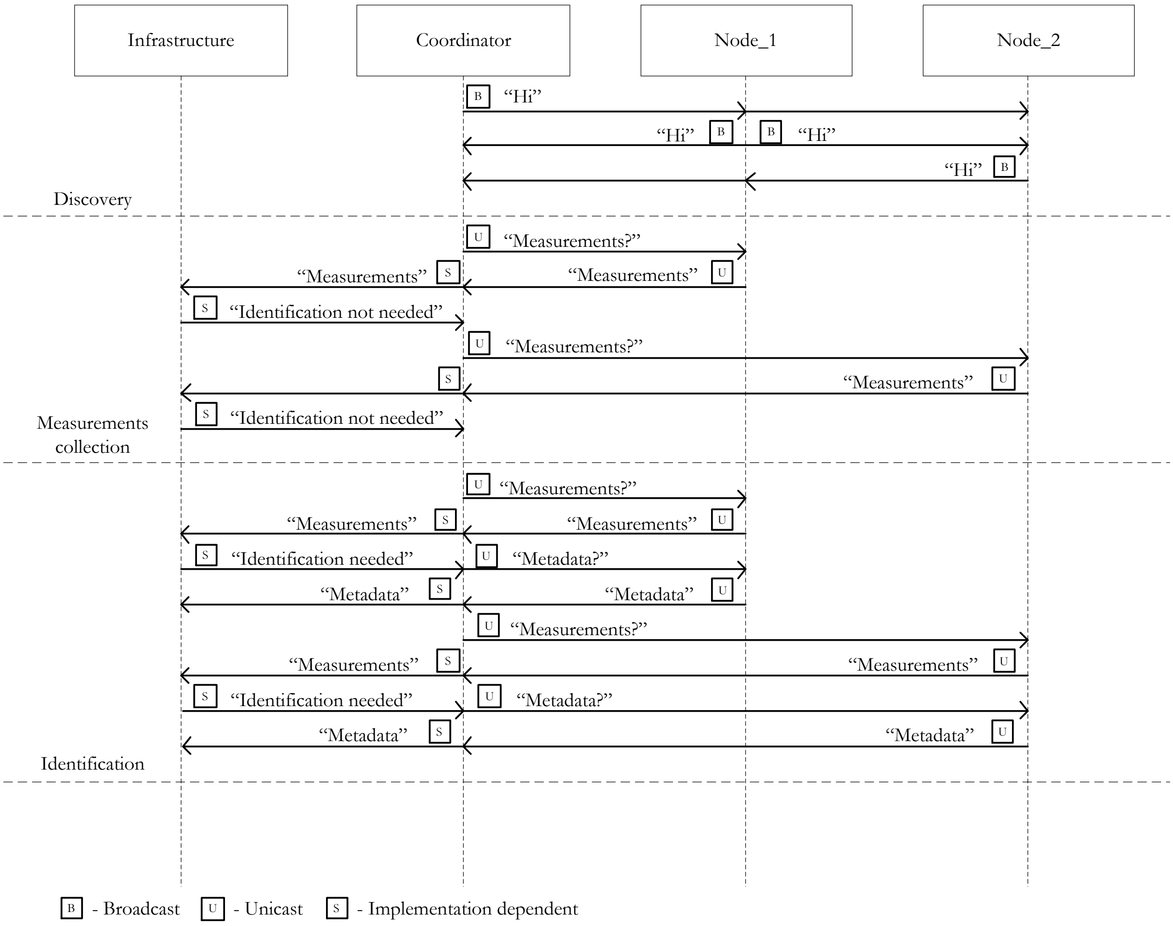

**Figure 1**: The DIP sequence diagram

## 3 Implementation of DIP in Contiki operating system

For the implementation of DIP we used a VESNA sensor node platform running the Contiki[3] operating system. Contiki has a communication stack called RIME which offers features like addressing, broadcast, reliable unicast and reliable bulk

---

[3] www.contiki-os.org/

unicast for transferring large amounts of data etc. All mentioned features are needed for the implementation of DIP.

Implementation starts with addressing of nodes which has to be automatic. Each node should have a unique address therefore we use microcontrollers' unique 96-bit serial number as the basis. RIME has adjustable address space, so considering the size of the test network we addressed the nodes with 16-bit addresses. The address used was obtained by calculating 16-bit CRC on microcontroller's serial number to preserve the uniqueness of the 16 bits.

Next we implemented the node protocol which is a simple request response protocol. This means that nodes wait until they receive a predefined message, i.e. "Hi", "Measurement request" or "Metadata request". Upon receiving one of these messages the node answers with the appropriate response.

The central part of DIP is the coordinators protocol which ensures the communication between the infrastructure and sensor network. As mentioned above it is responsible for discovery, measurements collection and identification of the nodes in the sensor network. The main part of coordinators protocol is its table depicted in Fig. 2. We implemented in Contiki a custom data structure called sensornode_t which contains RIME address (node_address) and the TTL parameter. Consequently the coordinator table is an array of sensor nodes and the size is defined by MAX_KNOWN_NODES. The size can be adjusted as needed for every application.

```
+-+-+-+-+-+-+-+-+-+-+-+-+-+-+-+-+-+
|       coordinator table         |
+-+-+-+-+-+-+-+-+-+-+-+-+-+-+-+-+-+
| index | node_address   |  TTL   |
+-+-+-+-+-+-+-+-+-+-+-+-+-+-+-+-+-+
|   0   |    141.155     |  10    |
+-+-+-+-+-+-+-+-+-+-+-+-+-+-+-+-+-+
|   1   |    146.132     |  10    |
+-+-+-+-+-+-+-+-+-+-+-+-+-+-+-+-+-+
```

**Figure 2**: The coordinator table

The discovered nodes are added to the table. The coordinator iterates over the nodes and pulls the sensor measurements from them, as well as metadata, if needed. The latter is encoded in JSON format, for the purpose of easier parsing, and stored on every node. Metadata is sent using RIME's reliable unicast bulk transfer. DIP sends requests through the opened RIME connection and expects the response in a callback function which is called directly from the radio driver, whereas the RIME stack introduces a more cross layer approach for communication.

## 4 Conclusion and Future Work

In this paper we described the DIP protocol custom designed for discovery of the sensor nodes and sensor data collection. The DIP protocol is suitable for narrow field, special purpose applications requiring light-weight protocol stack implementation. As an alternative to DIP, and more generally suitable for various applications, a layered approach can be used assuming implementation of the whole internet protocol suite from physical layer to application layer on the sensor node. This includes IEEE 802.15.4 compliant radios used along with the multitasking operating system Contiki, which implements protocols such as 6LoWPAN, IPv6, UDP and CoAP, enabling the evolution of the current Web to the "Web of Things" [2]. The Contiki OS implements all the necessary communication layers and corresponding protocols to have CoAP working on top of it. The MAC layer is already implemented inside the IEEE 802.15.4 compliant radio.

The IP protocol stack enables new applications similar to the ones in the current Web, only running on small low power devices and forming the "Web of Things". With the newly developed CoAP framework in Java language called Californium (Cf)[4] new cloud services based on "Things" are possible [3].

## References:

[1] M. Vučnik, C. Fortuna, M. Porcius, M. Mohorčič. WSN Testbeds For Lighting Control And Environmental Monitoring. In *Proceedings of the 3rd Jožef Stefan International Postgraduate School Student's Conference*. Ljubljana, Slovenia, 2011

[2] M. Kovatsch. Demo abstract: Human-CoAP interaction with Copper. In *Distributed Computing in Sensor Systems and Workshops (DCOSS)*, Barcelona, Spain, 2011.

[3] M. Kovatsch, S. Mayer, B. Ostermaier. Moving Application Logic from the Firmware to the Cloud: Towards the Thin Server Architecture for the Internet of Things. In *Proceedings of the 6th International Conference on Innovative Mobile and Internet Services in Ubiquitous Computing (IMIS 2012)*, Palermo, Italy, 2012.

---

[4] https://github.com/mkovatsc/Californium

## For wider interest

This paper describes a new protocol which is useful for collecting sensor measurements and metadata from sensor networks. The protocol is called Discovery and Identification Protocol (DIP).

Sensor networks are increasingly used to deliver sensor data from the world or real things and processes. Sensor data includes sensor measurements, which are samples typically in the form of a number (e.g. temperature), and the metadata, which is typically static information that gives meaning to the measurements (e.g. accuracy, calibration parameters, sensor settings etc.).

The DIP protocol was designed as a light-weight protocol to be used on sensor nodes which consume very little energy and can run on batteries. Sensor nodes are connected to the network through a wireless interface.

The paper is divided into two parts where the first part describes the design of the protocol and the second part describes the implementation of the protocol. In the conclusion we give a comparison of DIP and another more general protocol called Constrained Application Protocol (CoAP).

The protocols described enable the evolution of the current Web so as to include also the "Web of Things".

# Nanoznanosti in nanotehnologije (Nanosciences and Nanotechnologies)

# Spectroscopic THz imaging using organic DSTMS (4-N,N-dimethylamino-4'-N'-methyl-stilbazolium 2,4,6-trimethylbenzenesulfonate) crystals

**Andreja Abina**[1], **Uroš Puc**[1], **David Heath**[1], **Aleksander Zidanšek**[1,2]

[1] Jožef Stefan International Postgraduate School, Ljubljana, Slovenia

[2] Department of Condensed Matter Physics, Jožef Stefan Institute, Ljubljana, Slovenia

andreja.abina@mps.si

**Abstract.** Application of terahertz (THz) electromagnetic waves offers several opportunities for quality inspection in various industries. The THz waves penetrate many kinds of materials such as pharmaceutical coating, paper, plastic, ceramic, cardboard, wood, clothing, etc. We investigated possibilities of applying a THz imaging system in transmission geometry using the organic DSTMS crystals as a THz generator and detector. We applied different methods to construct an image from the array of THz pulses. Time-domain THz imaging has the advantage of the fast sample scanning. It is however appropriate only for detection of imperfections or impurities inside the material as well as for the thickness distribution measurement. For identification of the observed substance multispectral imaging is necessary.

**Keywords**: Material characterization, Organic DSTMS crystals, THz spectroscopy, THz imaging.

## 1 Introduction

Terahertz (THz) region of the electromagnetic spectrum was not well explored until recently. This THz gap is located between infrared waves and microwaves with corresponding wavelengths between 3 mm and 30 micro meters [1] as depicted in Fig. 1. One of the most promising aspects of this new technology is its high sensitivity to interactions between molecules and THz responses which exhibit some interesting characteristics. The THz sensor is able to probe not only rotations as in case of microwaves, but also the various intermolecular bonds such as hydrogen bonds and van der Waals forces [2], lattice vibrations, isomeric and polymorphic configurations [3], stretching modes and twisting around hydrogen bonds [2]. High sensitivity of THz waves to interactions between molecules allows differentiating between different substances. THz waves penetrate barriers made of dielectric or non-conducting materials such as plastic, ceramic, paper, cardboard, wood, natural and synthetic fabrics [4]. The main benefit compared to alternative methods like X-ray or gamma ray imaging is non-ionizing nature of THz waves. This allows non-invasive high-resolution imaging and material identification through spectroscopy. The development and the commercialization of the THz pulsed spectroscopy (TPS) and the terahertz pulsed imaging (TPI) systems in the last ten years stimulated several ideas to use THz systems for the various industrial purposes [5-7]. In this paper we present two concepts of THz imaging in transmission geometry using the organic DSTMS (4-N,N-dimethylamino-4’-N’-methyl-stilbazolium 2,4,6-trimethylbenzenesulfonate) crystals as a THz generator and detector. We demonstrate that time-domain imaging (TDI) is suitable for the detection of imperfectness or impurity inside the materials and thickness distribution measurement, whereas for identification purposes a multispectral imaging is necessary. Some results obtained in our laboratory with the THz imaging system in transmission geometry based on the DSTMS organic crystals are also presented and discussed.

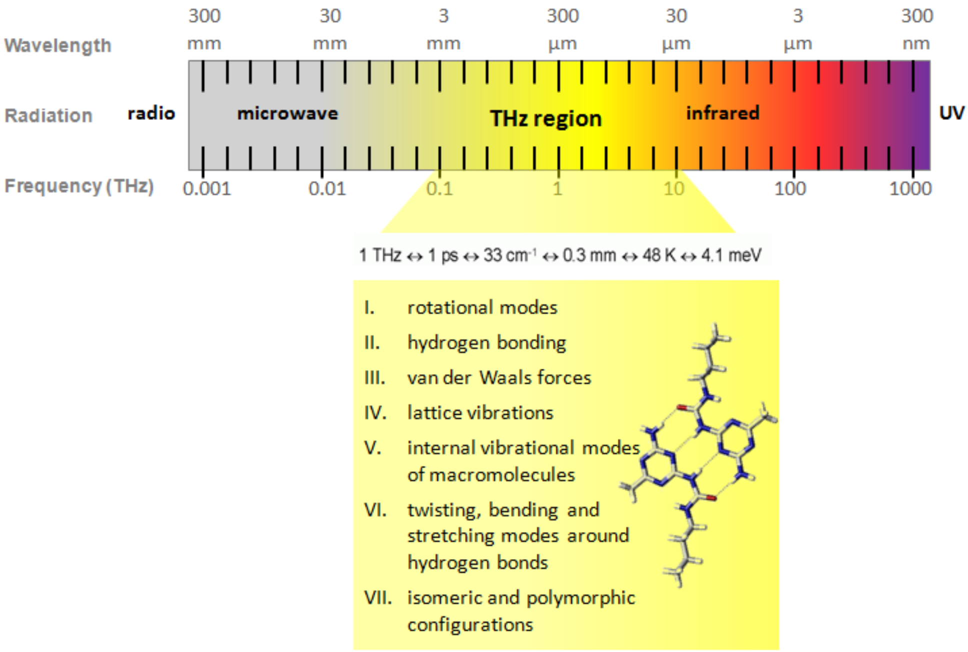

**Figure 1**: Spectrum of electromagnetic waves in THz region and interactions between molecules which THz technology is able to probe.

# 2 Methodology and imaging methods

## 1.1 THz imaging system

The selected THz imaging system offers two operational geometries in transmission and reflection mode. In this paper the focus is on a transmission geometry system which includes optical, mechanical and electronic components for the generation and detection of THz waves. The most important THz system parts are the delay line, THz generator, THz detector, optics (lens, mirrors), electronics and appropriate software for data acquisition and analysis. For THz generation and detection we use the organic crystal DSTMS with the spectral range of 0.3–11 THz. The system is used with a femtosecond laser source with wavelengths of 1560 nm. The operation principles involve generation and then detection of terahertz electro-magnetic transients that are produced in a crystal by intense femtosecond optical laser pulses. At the optical splitter lens the incident beam is divided into two beams: a pump and a probe beam. The pump beam is delayed for a few ps and reflected to the THz generator crystal, where THz waves are generated. Furthermore, THz waves are reflected from elliptic mirror through the sample and focused by another elliptic mirror to the THz detector crystal. The signal is finally detected by a photodiode detector and transferred to the computer for further signal processing and data analysis.

## 1.2 THz imaging methods

In this experiment we used two different imaging techniques suitable for various purposes. In general, we could divide these techniques into time-domain and frequency domain imaging methods. Frequency domain imaging could be further divided into multispectral imaging and a spatial distribution map. In both, the time and frequency domain, the THz images are obtained by raster scanning the terahertz beam across the sample. The obtained time-domain image does not contain any spectral information, so this type of imaging could be used only for detection purposes whereas imaging in the frequency domain contains important information about each individual substance. As such, this technique could be used for identification as well as classification purposes.

# 3 Results and discussion

Time-domain imaging is used for the fast imaging without the need for spectroscopic information. The image is constructed on the basis of key parameters, which are obtained from the THz time-domain waveform. We could extract information about the maximum amplitude, minimum amplitude, peak to peak value, or time of the peak value. In our case we chose the maximum amplitude option (Fig. 2). At each point on the sample the time-domain waveform is recorded, than the amplitude peak value is extracted and the time-domain THz image produced by using the peak intensity at each pixel. By combining the acquired signals in a 2D matrix we get a raster scanned THz image of a sample as shown in Fig. 3 right. The main pulse of the THz waveform represents the terahertz interaction with the substance at the sample surface, and the peak amplitude is determined by the change in the refractive index at the air/sample interface. The change of a refractive index between different layers produces multiple reflection peaks in the THz waveforms. The peak positions and the magnitude of each pulse represent different material characteristics. Consequently, the amplitude, position and shape of the signal are material dependent. Thus, THz imaging permits the detection and location of hidden objects as well as analysis and visualisation of various layers.

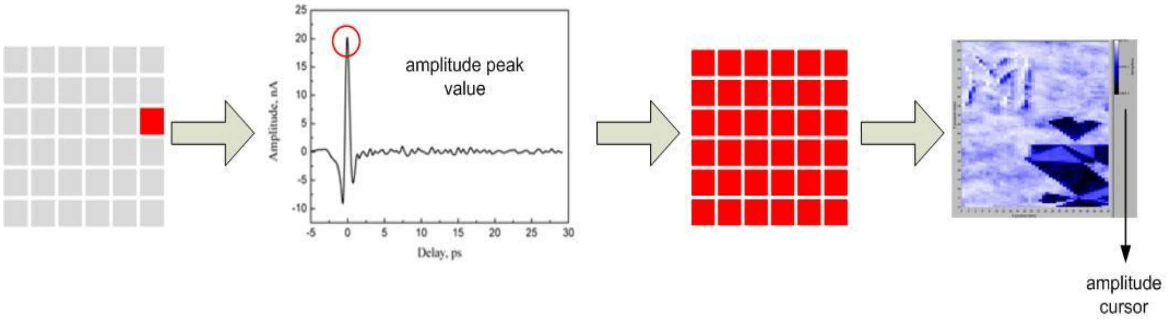

**Figure 2**: Schematic illustration of THz time-domain imaging.

In our experiment we used three different materials placed on a paper sheet: black permanent marker, double sided adhesive foam tape with thickness of 2 mm, and isolation tape with thickness below 0.5 mm. As depicted with a red eclipse in the time-domain THz image in the right part of Fig. 3, one can distinguish between regions with one layer or more layers of the isolation tape. The thinner regions of the isolation tape are dark blue coloured and the thicker regions of the foam tape are designated with a light blue colour. Here we prove that our system based on the organic crystals is capable of determining the sample thickness.

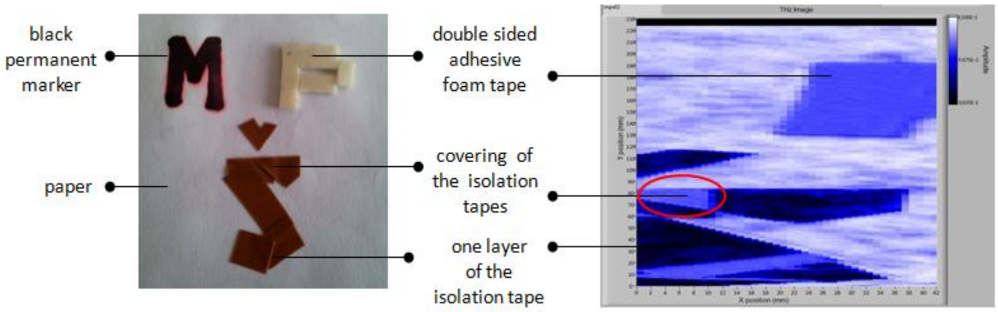

**Figure 3**: Discrimination between different material samples of various thicknesses.

Multispectral imaging is performed by using the Fourier transform of the time-domain waveform which gives a spectral response of the investigated material. In this case, in every single point the entire frequency spectrum is recorded. With this method we obtain a three-dimensional data set where two axes describe vertical and horizontal spatial dimensions and the third axis represents the spectral frequency dimension. This method allows imaging at different frequencies as shown in Fig. 4. Multispectral THz images in Fig. 4 are captured at frequencies of 1 THz, 2 THz and 3 THz. The Slovenian letter Š made from the isolation tape is the best visible at the frequency of 2 THz, whereas the letter P made from the foam tape is visible at all three frequencies. This imaging technique captures image data at specific frequencies across the THz range. Thus, it is possible to extract the spatial pattern of each component at different frequencies.

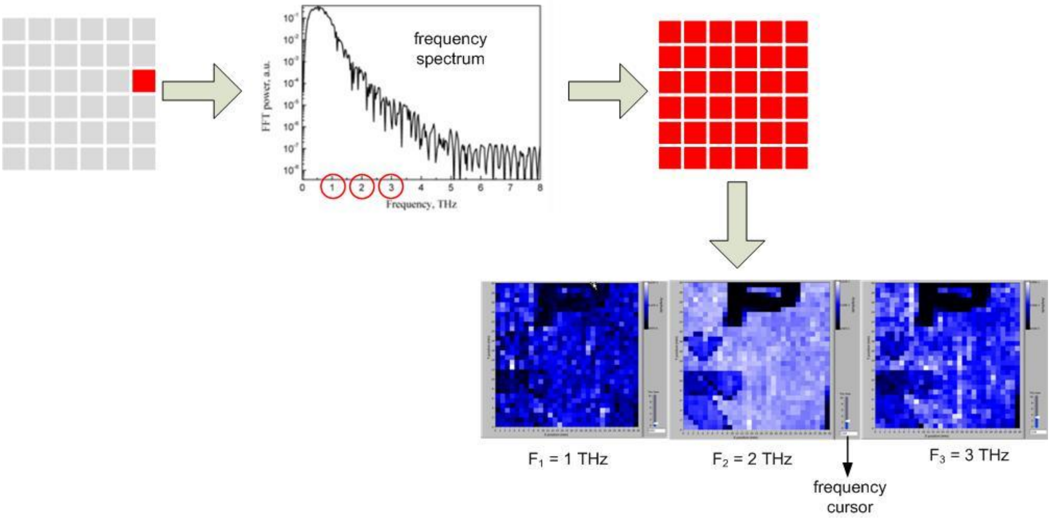

**Figure 4**: Schematic illustration of the THz frequency-domain imaging.

## 4 Conclusions

Capability of spectroscopic discrimination is one of the most promising features of the THz imaging system. On the one hand the acquired THz data contain rich information about the structure and composition of a given sample. On the other hand, the characteristic spectral signatures of each individual substance can also be extracted from the THz data, and this can be used for substance identification. We applied different methods to construct an image from the array of THz pulses. Time-domain THz imaging has the advantage of a fast sample scanning at the expense of lower resolution. Therefore, it is appropriate only for the detection of some imperfections or impurities inside the investigated material and for the thickness measurements, whereas for identification purposes the multispectral imaging method is necessary. The Fourier transform of the measured THz signal provides additional information about the investigated sample. Therefore, the frequency characteristics of each point can be viewed and the material properties, such as distribution of chemical compounds within the material, can be determined.

## References:

[1] Y.-C. Shen, P. F. Taday, D. A. Newnham, M. C. Kemp, and M. Pepper. 3D chemical mapping using terahertz pulsed imaging, In *Proceedings of the SPIE 5727*, 2005 .

[2] M. Walther, B. Fischer, A. Ortner, A. Bitzer, A. Thoman, and H. Helm. Chemical sensing and imaging with pulsed terahertz radiation, *Analytical and Bioanalytical Chemistry,* 397(3): 1009–1017, 2010.

[3] J. A. Zeitler, P. F. Taday, D. A. Newnham, M. Pepper, K. C. Gordon, and T. Rades. Terahertz pulsed spectroscopy and imaging in the pharmaceutical setting - a review, *Journal of Pharmacy and Pharmacology,* 59(2): 209–223, 2007.

[4] M. C. Kemp. Millimetre wave and terahertz technology for the detection of concealed threats: a review, In *Proccedings of Joint 32nd International Conference on Infrared and Millimeter Waves, 2007 and the 2007 15th International Conference on Terahertz Electronics. IRMMW-THz,* Cardiff, 2006.

[5] S. Yao-Chun and P. F. Taday. Development and Application of Terahertz Pulsed Imaging for Nondestructive Inspection of Pharmaceutical Tablet, *IEEE Journal of Selected Topics in Quantum Electronics,* 14(2): 407–415, 2008.

[6] E. Brundermann, U. Heugen, R. Schiwon, B. Born, G. W. Schwaab, S. Ebbinghaus, K. Schrock, D. R. Chamberlin, E. E. Haller, and M. Havenith. Terahertz imaging applications in spectroscopy of biomolecules, In *IEEE MTT-S International Microwave Symposium Digest 2005*, Long Beach, CA, 2005.

[7] C. Jansen, S. Wietzke, O. Peters, M. Scheller, N. Vieweg, M. Salhi, N. Krumbholz, C. Jördens, T. Hochrein, and M. Koch. Terahertz imaging: applications and perspectives, *Applied Optics,* 49(19): E48-E57, 2010.

## For wider interest

Terahertz (THz) region of the electromagnetic spectrum was not well explored until recently. This THz gap is located between infrared waves and microwaves at corresponding wavelengths between 3 mm and 30 micro meters. One of the most promising aspects of this new technology is its high sensitivity to interactions between molecules and some interesting characteristics in THz spectrum. Since THz waves are very sensitive to interactions between molecules this allows discrimination between different substances. Moreover, the THz waves penetrate barriers made of dielectric or non-conducting materials such as plastic, ceramic, paper, cardboard, wood, natural and synthetic fabrics. Thus, the THz technology presents an alternative method to X-ray or gamma ray imaging. The development and commercialization of the terahertz pulsed spectroscopy (TPS) and terahertz pulsed imaging (TPI) systems during the last decade put forward several ideas to use the THz systems for various industrial purposes.

One of the most promising features of a THz imaging system is its capability for spectroscopic discrimination. The acquired THz data contain rich information about the structure and composition of a sample. On the other hand, the characteristic spectral signatures of each individual substance can also be extracted from the THz data, and this can be used for substance identification. In this work we applied two concepts of the THz imaging in transmission geometry using organic DSTMS crystals as a THz generator and detector. We demonstrate that the time-domain THz imaging has the advantage of fast sample scanning at the expense of lower resolution. Therefore, it is appropriate only for the detection of some imperfections or impurities inside the investigated material and for thickness measurements, whereas for substance identification the multispectral imaging method is necessary. Fourier transform of the THz signal provides additional information about the investigated sample. Therefore, the frequency characteristics of each point can be viewed and the material properties, such as distribution of chemical compounds within the material, can be determined.

# Influence of different stress concentration factors in mono-leaf spring on its final fatigue life

**Predrag Borković, Borivoj Šuštaršič, Vojteh Leskovšek, Borut Žužek**

Institute of Metals and Technology, Ljubljana, Slovenia

`predrag.borkovic@imt.si`

**Abstract.** Fatigue life of a component is a very important information regarding safety and stability of any dynamically loaded systems. Since the failure under such loaded parts can occur even at lower stress than static tensile strength, the fatigue life has to be assessed by simulations or by performing tests on real components. Among many influencing factors on the fatigue life, the influence of irregular stress flow expressed by the stress concentration factor within the component is presented in this paper. Finite Element Method (FEM) based simulations have showed a clear difference in the fatigue life results by changing the transition radius of the mono-leaf spring following the change of a stress concentration factor as well. These FEM simulations are performed taking into account dynamic properties of the spring steel obtained by tests on specimens.

**Keywords**: fatigue life, stress concentration factor, mono-leaf spring, FEM simulation

## 1 Introduction

The estimation of the fatigue life by calculation is based on the global loading of the components, the knowledge about the stresses in the component and the behaviour of the material under dynamic loading [1]. For the stress determination, numerical methods are used, e.g. the finite element method, while load spectra are established by tests. The information about the strength behaviour of the material is the third group of input data for the calculation of the fatigue life. Also, influences of a different segregation orientation of alloying elements, a different tempering temperature and a notch effect on fatigue life were examined. The input data of the FEM based simulations are S/N curves, obtained by the fatigue tests on specimens made of the same material as a mono leaf spring.

## 2 Experimental work

The fatigue tests are performed by using a servo-hydraulic testing rig ± 250kN Instron 8802 at frequency of 30 Hz. Also, some additional tests were carried out on the high frequency pulsator known as a fast and reliable method of steel assessment [2]. The material of the tested specimens is the spring steel 51 CrV4 produced by Štore Steel, Slovenia. The chemical composition of the investigated spring steel is given in Table 1.

**Table 1**. Chemical composition of spring steel 51CrV4.

| Chemical element | ***C*** | ***Si*** | ***Mn*** | ***P*** | ***S*** | ***Cr*** | ***Mo*** | ***Ni*** | ***V*** |
|---|---|---|---|---|---|---|---|---|---|
| Composition wt. % | 0.52 | 0.35 | 0.96 | 0.011 | 0.004 | 0.94 | 0.05 | 0.13 | 0.12 |

Two types of specimens were prepared and tested: the longitudinal and the perpendicular relative to the rolling direction – segregation orientation, Figure 1.

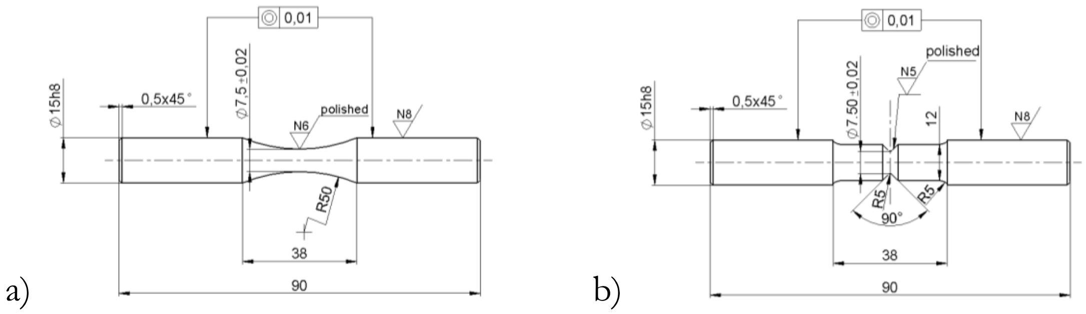

**Figure 1**: Standard cylindrical specimens: a) smooth and b) notched.

In addition to the fatigue tests, static tensile tests are performed as well. All specimens, both for the static tensile test and for the fatigue test, are cut off from the base spring steel material in the as-delivered condition (flat profile of dimensions 90x28 mm). After cutting and machining, the specimens were heat-treated, quenched in nitrogen at 5 bars overpressure and then tempered at two different temperatures. Both, perpendicular and longitudinal specimens are divided into two groups of tempering temperature, first of 425°C (HT1) and second of 475°C (HT2).

At the end of the experiment, a FEM simulation of the dynamic loading of the mono-leaf spring with the selected geometry is carried out using the experimental fatigue testing results obtained on specimens. Among many accessible computer codes based on the stress or strain life approach [3-6] and cumulative damage analysis [7] for the fatigue life assessment of the mono-leaf spring, ANSYS computer software has been used.

# 3 Results and discussion

## 3.1 Static test

Static tensile tests are performed using a 500kN Instron testing rig. Depending on the different specimen orientation and different tempering temperature, the following tensile properties of spring steel material were obtained, given in Table 2.

**Table 2**: Tensile test results.

| Orientation | Tempering temperature | Yield strength [MPa] | Tensile strength [MPa] | Fracture elongation [%] | Fracture contraction [%] |
|---|---|---|---|---|---|
| Perpendicular (λ=90°) | 475°C/1h | 1373 | 1448 | 7.04 | 24.6 |
|  | 425°C/1h | 1502 | 1591 | 5.16 | 15.8 |
| Longitudinal (λ=0°) | 475°C/1h | 1366 | 1442 | 10.6 | 41 |
|  | 425°C/1h | 1502 | 1606 | 9.9 | 42 |

## 3.2 Dynamic test

Influences of the heat-treatment and segregation orientation under the compression-tension dynamic loading were investigated. The S/N curves obtained by the compression-tension fatigue tests on the notched, as well as on the unnotched (smooth) specimens are presented in Figure 2 with the graphs a) and b) respectively. All specimens were mechanically polished (fine metallographic grinding; final paper 800) after heat-treatment in order to achieve required surface roughness.

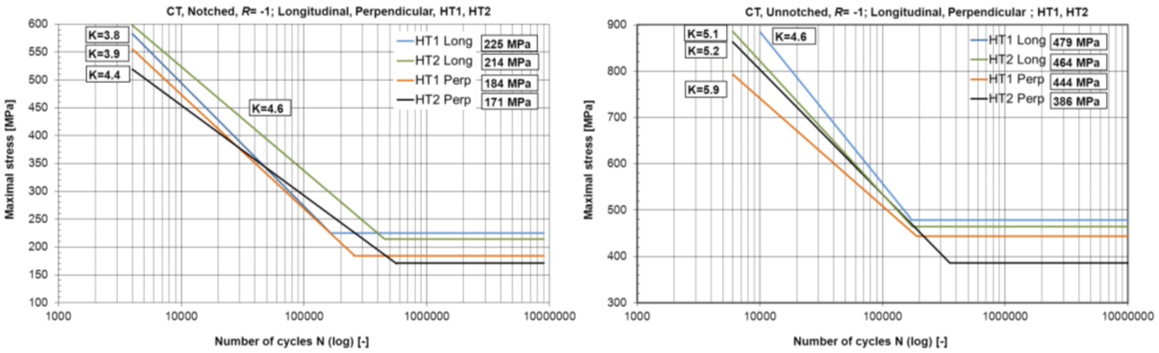

a) b)

**Figure2**: S/N curves of both segregation orientation for: a) notched and b) unnotched specimens.

### 3.3 Simulation of mono-leaf spring using the FEM –based software

The evaluation of the geometric influence, expressed by a different stress concentration factors on the final fatigue life of the mono-leaf spring is examined by the ANSYS computer program. It is well known that sharp notches resulting from stress gradients, act as stress raisers and present critical spots within the component. One way of improving the durability and safety of the mono-leaf spring is avoiding all sharp edge transitions at critical spots and replacing them with transition radii if structural and functional conditions allow such changes. Figure 3a shows the basic dimensions of the mono-leaf spring while 3b displays a detail of the critical spot with the highest stress. The edge at this spot is replaced by several different transition radii to evaluate the influence of a stress concentration factor on fatigue life of the mono-leaf spring.

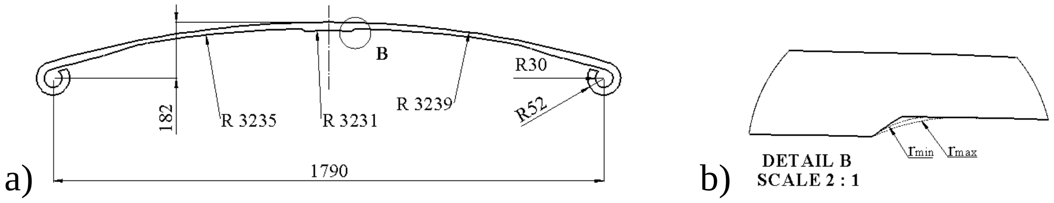

**Figure 3**: Mono-leaf spring: a) basic dimensions and b) transition radii.

The mono-leaf spring was first modelled by Solid Works and then exported to ANSYS where it was further upgraded (meshed, constrained, loaded) and finally simulated to the fatigue, Figure 4. By changing the radius ($r_{min}$ - $r_{max}$) during the simulation, fatigue life of mono-leaf spring varies according to Table 3.

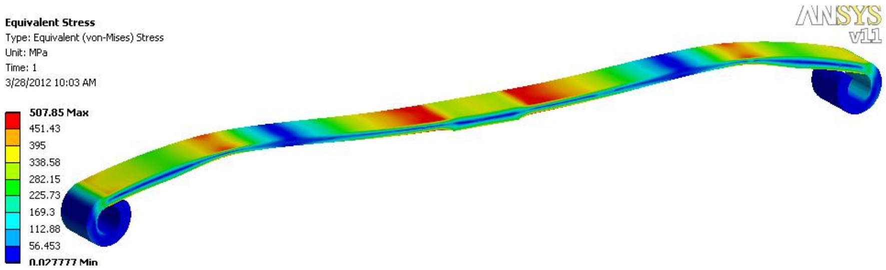

**Figure 4**: Fatigue simulation of mono-leaf spring using ANSYS software.

**Table 3**: Fatigue life of mono-leaf spring in dependence of different radii.

| r, Radius [mm] | F, Force [N] | Stress von-Misses [MPa] | N, Fatigue life [-] |
|---|---|---|---|
| 15 | 1690 | 539.65 | 71609 |
| 35 | 1690 | 503.32 | 80979 |
| 75 | 1690 | 489.57 | 84837 |
| 115 | 1690 | 476.82 | 5*10^7 |

## 4 Conclusion

On the base of the fatigue simulations it is clear that the longest fatigue life of the mono-leaf spring is obtained by using the largest transition radius of 115 mm. With this transition radius, the mono-leaf spring may be able to endure at least 50 Million cycles, according to the S/N curve of the unnotched longitudinal oriented specimens. Also, by using other S/N curves for the perpendicular specimen orientation as well as for the notched specimens, the fatigue life is longer too. Regarding the dynamic properties of selected spring steel, it is evident that the fatigue strength of perpendicular oriented specimens decreases for about 25% compared to the longitudinal oriented specimens accompanied with lower tensile and yield strength. Regarding the different stress concentration factors of the notched and smooth specimens, it is shown that the fatigue strength of the notched specimens is effectively lower than the stress concentration factor indicates.

## References:

[1]W. Eichlseder and H. Leitner, Influence of stress gradient on S/N – curve, *Fatigue 2002 Conference, Stockholm*,2783-2790, 2002.

[2]B. Šuštaršič, B. Senčič, V. Leskovšek: *Fatigue strength of spring steels and life-time prediction of leaf springs*, Assessment of reliability of materials and structures (RELMAS'2008), St. Petersburg, Russia, June 17-20, 2008; problems and solutions; international conference, Volume 1, St. Petersburg, Polytechnic Publishing House, pp. 361-366, 2008.

[3]S. Tavakkoli, F. Aslani et al: *Analytical Prediction of Leaf Spring Bushing Loads Using MSC/NASTRAN and MDI/ADAMS*, http://www.mscsoftware.com/support/library/conf/wuc96-/11b_asla.pdf.

[4]S. Kumar, S. Vijayarangan: Static analysis and fatigue life prediction of steel and composite leaf spring for light passenger vehicles, Journal of Scientific and Industrial Research, 662, pp.128-134, 2007.

[5]F. N. A. Refngah, S. Abdullah, A. Jalar, L. B. Chua: *Fatigue life evaluation of two types of steel leaf springs*, International Journal of Mechanical and Materials Engineering (IJMME), 42, pp. 136-140, 2009.

[6]G. S. S. Shankar, S. Vijayarangan: *Mono Composite Leaf Spring for Light Weight Vehicle – Design, End Joint Analysis and Testing*, ISSN 1392–1320 Materials Science (Medžiagotyra). 123, pp. 220-225, 2006.

[7]W. Eichlseder: Enhanced Fatigue Analysis – Incorporating Downstream Manufacturing Processes, Materials and Technology, 444, 185-192, 2010.

## For wider interest

One of the largest European producers of the spring steel material is Štore Steel Plant, which produces material for truck springs and the other springs for automotive applications.  Generally, spring manufacturers produce springs from steel in the as-delivered condition. The springs are then heat-treated and tested. However, the fatigue testing of springs after manufacturing is a time-consuming and an expensive task. It is also too late to provide information to the steel producer, who needs in-time and appropriate information about the quality of the steel in the production from batch to batch. The aim of this research work is to develop a model which will enable the assessment of the fatigue life of mono and double leaf-spring based on information of material properties in the as-delivered condition. The idea is to model both mono and double-leaf spring and then run the simulations and determine the lifetime of the leaf springs. For our project, we use their spring steel in the as-delivered condition to perform dynamic tests on specimens, in order to obtain the material properties, which are the base for the leaf spring simulation. Since the spring steel manufacturer, as well as the spring producer, need fast data about the quality of their products, the idea is to use a faster testing machine for evaluating base material properties.

# Tailoring electrically-induced properties by stretching relaxor polymer films

**G. Casar[1,2], A. Eršte[1,2], S. Glinšek[1,2], X. Li[3], X. Qian[3], Q. M. Zhang[3] and V. Bobnar[1,2]**

[1] Jožef Stefan Institute, Ljubljana, Slovenia

[2] Jožef Stefan International Postgraduate School, Ljubljana, Slovenia

[3] Department of Electrical Engineering and Materials Research Institute, The Pennsylvania State University, University Park, Pennsylvania 16802, USA
goran.casar@ijs.si

**Abstract.** Electrically-induced behaviuor was compared in the non-stretched and uniaxially stretched poly(vinylidene fluoride-trifluoroethylene-chlorofluoroethylene) terpolymer - a member of the relaxor polymer family that exhibits fast response speeds, a giant electrostriction, high electric energy density and a large electrocaloric effect. Although the temperature dependence of the low-field dielectric constant is almost identical, the dc bias electric field via a higher nonlinear contribution more heavily alters the dielectric response of the less-oriented non-stretched samples. Substantial differences in the polarization, electrocaloric response and induced electrostrictive strain of the non-stretched and stretched terpolymer suggest that electrically-induced properties of relaxor polymer films can be tailored by controlling the preparation conditions.

**Keywords**: relaxor, polymer, dielectric spectroscopy

Relaxor polymers are of great interest for various advanced applications because of their giant dielectric, electromechanical and electrocaloric response. We have investigated and compared these electrically-induced responses in the non-stretched and uniaxially stretched poly(vinylidene fluoride-trifluoroethylene-chlorofluoroethylene), P(VDF-TrFE-CFE), relaxor terpolymer. It is namely known that stretching of polymer films strongly affects their microstructure, i.e., the conformation of polymer chains – for example, a ferroelectric poly(vinylidene fluoride) spontaneously crystallizes into a nonpolar trans-gauche chain conformation, which is transformed into a ferroelectric all-trans conformation only after uniaxial stretching at least 3 times the original length [1]. On the other hand, P(VDF-TrFE) spontaneously crystallizes into the all-trans polar structure (the overall microstructure of ferroelectric and relaxor polymers consists of the crystallites embedded in the amorphous matrix), however, stretching still might affect its properties. This is even more likely in relaxor P(VDF-TrFE)-based polymers, where the all-trans chain conformation in the crystallites is randomly interrupted by the gauche conformation, introduced by irradiation or chlorine atoms [2].

Since electromechanical and electrocaloric investigations require applications of high dc bias electric fields, we have examined the dielectric response of both, stretched and non-stretched samples, in different dc bias electric fields. The real, ε', and imaginary, ε", parts of the complex dielectric constant have thus been measured between 360 K and 200 K by using a HP4284 Precision LCR Meter, with dc bias field applied after the sample has been heated to 360 K.

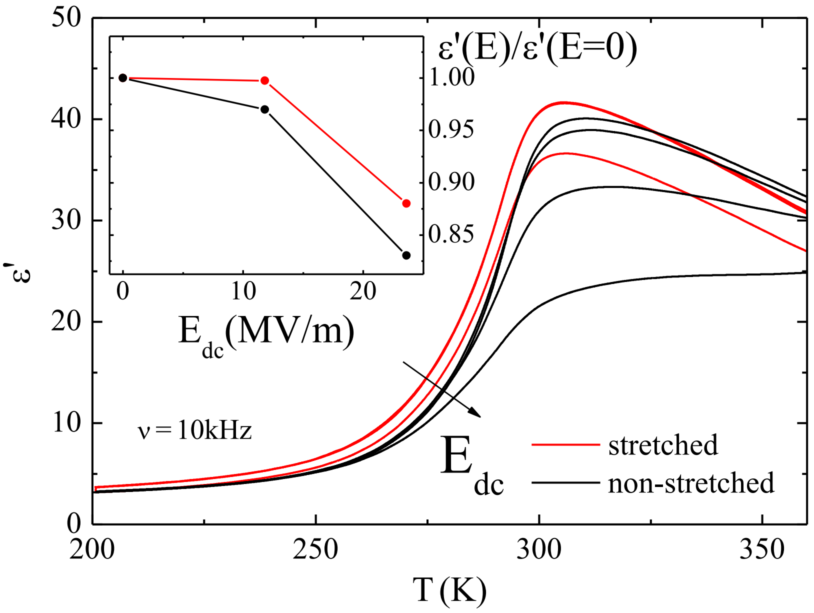

**Figure 1:** Temperature dependence of ε' at 10 kHz of stretched and non-stretched P(VDF-TrFE-CFE) samples in different dc bias electric fields (0, 11.8, 23.6, 47.2 MV/m). The arrow points in the direction of increasing electric field. The inset shows normalized ε' peak values as a function of the dc bias electric field in both samples.

Influence of the dc bias electric field on ε' is shown in Figure 1. We see that decreasing of ε' with increasing dc bias is higher in the non-stretched samples (in the stretched terpolymer the first two curves almost coincide). This is emphasized in the inset, which shows normalized ε' peak values as a function of the dc bias electric field in both samples. It has been shown recently that this difference in values of the dielectric constant in relaxors is due to the nonlinear dielectric susceptibility contribution. This can be positive as in some inorganic relaxors or negative as in relaxor polymers [3]. In accordance with this fact, Figure 2 reveals that dc bias electric field has higher impact on the characteristic relaxation frequency (determined from peaks in ε"(T) [3]) of the non-stretched sample.

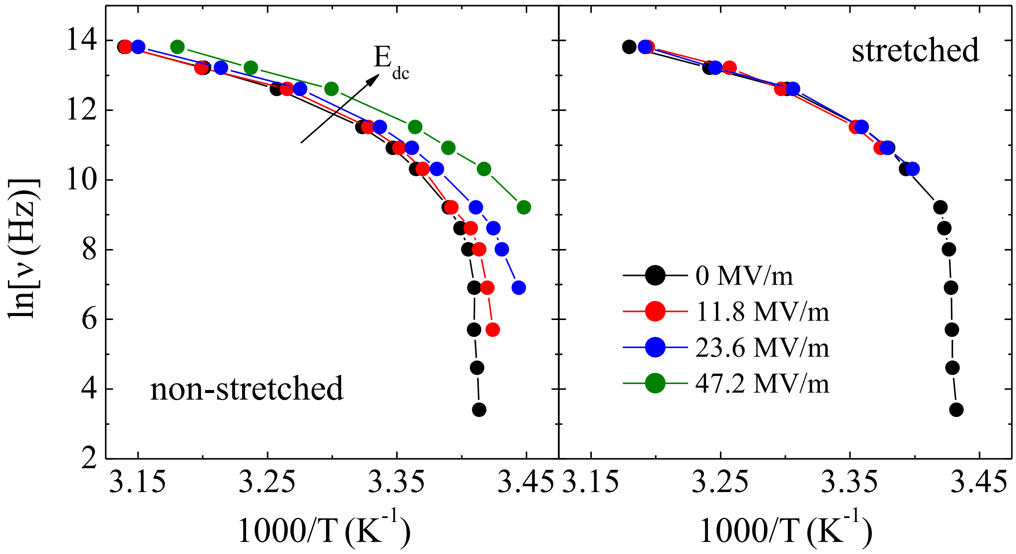

**Figure 2**: Temperature evolution of the characteristic relaxation frequencies for stretched and non-stretched P(VDF-TrFE-CFE) samples in different dc bias electric fields.

Since uniaxial stretching orders polymer chains in the amorphous matrix and changes the non-polar trans-gauche conformation into polar all-trans conformation in crystallites, electric polarization is higher in the stretched sample, as can be seen in Figure 3(a). Furthermore, a high electromechanical response, which is in relaxor polymers of an electrostrictive origin (which means that the induced strain is proportional to the square of the induced electric polarization, contrary to the piezoelectric effect, where the strain is linearly dependent on the external electric field), is consequently much higher in the more oriented stretched samples, as can be seen in Figure 3(b), which shows the induced strain in both types of the P(VDF-TrFE-CFE) terpolymer.[2] Both, the electric polarization and induced strain have been measured by using the commercial AixPES setup (Aixacct Systems, Aachen, Germany).

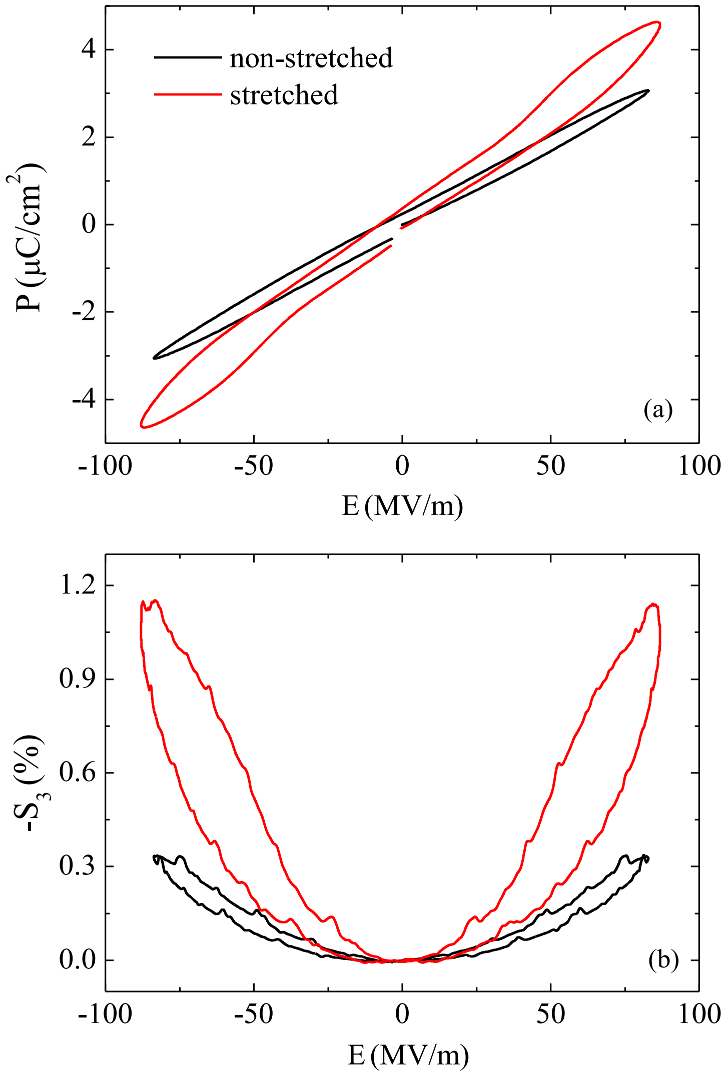

**Figure 3:** (a) Polarization hysteresis loops and (b) induced electrostrictive strain at 100 Hz in the stretched and non-stretched P(VDF-TrFE-CFE) samples.

Electrocaloric response (the change in temperature and/or entropy of a dielectric material due to the electric field induced change in dipolar states) of stretched and non-stretched samples at different temperatures (below, near and above the dispersive dielectric maximum) is shown in Figure 4*. The response is almost

---

* Details on the electrocaloric effect and measurement procedure can be found in Ref. 4.

identical in both types of the terpolymer only near the dielectric maximum, while at higher and lower temperatures the adiabatic temperature change is higher in the non-stretched terpolymer.

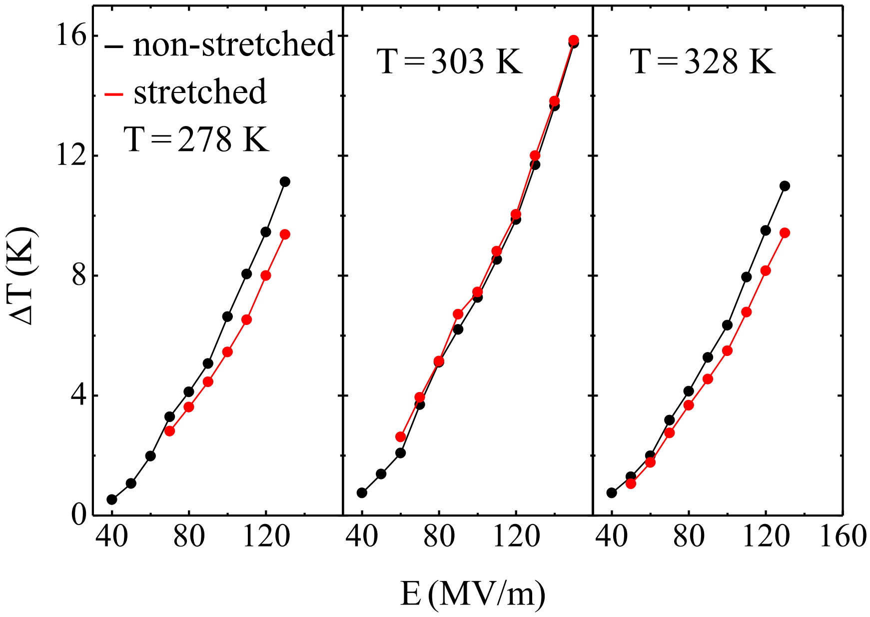

**Figure 4:** Comparison of the electrocaloric response as a function of the applied electric field, measured at three different temperatures: below, near and above dispersive dielectric maximum.

Obviously the stretching decreases the number of possible polar states and thus the electrocaloric response. Having in mind also the differences in the detected dielectric, polarization and electromechanical response of the stretched and non-stretched samples, we can conclude that electrically-induced properties of relaxor polymer films can be tailored by controlling the preparation conditions.

## References:

[1]A. J. Lovinger. Ferroelectric Polymers. *Science*, 220(4602): 1115-1121, 1983.

[2]Q. M. Zhang, V. Bharti, and X. Zhao. Giant Electrostriction and Relaxor Ferroelectric Behavior in Electron-Irradiated Poly(vinylidene fluoride-trifluoroethylene) Copolymer. *Science*, 280(5372): 2101-2104, 1998.

[3]V. Bobnar, A. Eršte, X.-Z. Chen, C.-L. Jia, Q.-D. Shen. Influence of dc bias electric field on Vogel-Fulcher dynamics in relaxor ferroelectrics. *Physical Review B*, 83(13): 132105, 2011.

[4]X. Li, X.-S. Qian, S. G. Lu, J. Cheng, Z. Fang and Q. M. Zhang. Tunable temperatue dependence of electrocaloric effect in ferroelectric relaxor poly(vinylidene fluoride-trifluoroethylene-chlorofluoroethylene terpolymer. *Appl. Phys. Lett.* 99, 052907, 2011.

## For wider interest

Dielectric spectroscopy investigates electrically-induced properties of a material as a function of frequency and/or temperature. Dielectric properties are related to polarizability and thus depend on the structure and molecular properties of a material. That is why dielectric spectroscopy is a useful tool for material characterization and it is used in pharmacy, biotechnology and material science.

The basic quantity in dielectric spectroscopy is complex dielectric constant ε*, which consists of the real, ε', and imaginary, ε'', part. The real part is related to the stored energy within the medium, whereas the imaginary part describes the losses. That is why the dielectric constant is very important in devices for storing electrical energy (capacitors).

Besides storing electrical energy, there are also materials that are able to convert it into mechanical work (electromechanical effect) or into heat (electrocaloric effect) – note that electrical energy converted into heat in electrocalorics is not due to the electrical current running through them. Such properties of a material can be utilized in many devices such as actuators, sonars, integrated microelectromechanical systems or artificial muscles, which use the electromechanical effect, or in heating/cooling devices of new generation, which use the electrocaloric effect.

Example of materials that possess giant electromechanical and electrocaloric effect are relaxors and ferroelectrics. Our subject of study was special class of relaxors – relaxor polymers. Relaxor polymers in comparison to the other inorganic relaxors have some advantages: they have greater electromechanical response, exhibit fast response speeds and can also be prepared in a variety of shapes. Their disadvantage would be that they are stable only at relatively low temperatures (below 100 °C).

Dielectric constant is important for the electromechanical application of relaxor polymers, since the input electrical energy that can be converted into the strain energy, is directly proportional to the values of the dielectric constant of the material. Thus, in order to achieve better efficiency, systems with high values of the dielectric constant must be developed.

# Terpolymer/copolymer blends on aluminum surface: Structural, caloric, and dielectric properties

**Andreja Eršte**[1,2], **Vid Bobnar**[1,2], **Xian-Zhong Chen**[3], **Cheng-Liang Jia**[3], **Qun-Dong Shen**[3]

[1] Condensed Matter Physics Department, Jožef Stefan Institute, Ljubljana, Slovenia

[2] Jožef Stefan International Postgraduate School, Ljubljana, Slovenia

[3] Department of Polymer Science and Engineering and Key Laboratory of Mesoscopic Chemistry of MOE, School of Chemistry and Chemical Engineering, Nanjing University, Nanjing, China

`andreja.erste@ijs.si` (email of corresponding author)

**Abstract.** We report structural, caloric, and dielectric properties of polymer blends of poly(vinylidenefluoride–trifluoroethylene–chlorofluoroethylene) terpolymer (a member of the relaxor polymers family that exhibits fast response speeds, giant electrostriction, high electric energy density, and large electrocaloric effect) and poly(vinylidenefluoride–chlorotrifluoroethylene) copolymer, developed on aluminium surface. Terpolymer films exhibit for a relaxor polymer very high values of the dielectric constant of ≈80 around room temperature, which decreases in terpolymer/copolymer blends to ≈60. This arises not only from the interference effect but also from the fact that copolymer additive disturbs the crystallizing process, as being revealed by X–ray diffraction and differential scanning calorimetry experiments. We show that addition of the copolymer enables us to govern the value of the dielectric constant of the films without influencing the relaxor dielectric dynamics.

**Keywords**: relaxor, polymer, blend, film on surface, dielectric spectroscopy

Relaxor polymers are very promising for a broad range of energy storage capacitor applications due to their unique physical properties. One of the advantages for use of polymers in such applications arises from the possibility of polymer film formation directly on a surface. Active metals such as aluminum can be used for substrates, as they are less expensive than noble metals and mechanically more stable than glassy carbon.

Investigations of relaxor poly(vinylidene fluoride–trifluoroethylene–chlorofluoroethylene) [P(VDF–TrFE–CFE)] terpolymer have revealed high values of dielectric constant at room temperature, fast response speeds, high strain levels and energy density, and large electrocaloric effect. Polymer blends exploit merits of both, base and additive polymer – due to the interference effect, properties of base polymer can be tailored and improved. Recent studies show that polymer blends composed of P(VDF–TrFE–CFE) terpolymer as a base with a small amount of poly(vinylidene fluoride–chlorotrifluoroethylene) P(VDF–CTFE) copolymer as an additive have even higher polarization response, energy density, elastic module, and breakdown field than pure relaxor P(VDF–TrFE–CFE) system [1,2]. We have thus decided to develop and investigate such polymer blend films on a metal surface: We have studied structural, caloric and dielectric properties of relaxor polymer blend films composed of P(VDF–TrFE–CFE) (66.3/26.4/7.3 mol %) terpolymer and P(VDF–CTFE) (91/9 mol %) copolymer on aluminum foil in terms of X-ray studies, differential scanning calorimetry, and detailed dielectric response analysis.

**Table 1**: (a) Total enthalpy change and DSC peak temperatures and the crystallinity of the terpolymer and blend films. For comparison, data of pure copolymer are included. (b) X–ray diffraction angle, lattice spacing, and the coherence length data of the terpolymer and blend films.

|  | (a) DSC |  |  |  |  | (b) XRD |  |  |
|---|---|---|---|---|---|---|---|---|
| sample | $\Delta H$ (J/g) | $T_1$ (K) | $T_2$ (K) | $T_3$ (K) | $X_C$ (%) | $\theta$ (°C) | $d$ (Å) | $L$ (nm) |
| terpolymer | 19.0 | 389.5 | 411.6 | – | 45.6 | 18.27 | 4.85 | 21.2 |
| 5 %–blend | 17.1 | 389.2 | 408.8 | – | 41.0 | 18.23 | 4.86 | 23.2 |
| 10 %–blend | 14.9 | 385.6 | 406.8 | 422.5 | 35.7 | 18.24 | 4.86 | 23.3 |
| copolymer | 31.5 | 417.7 | 437.8 | – | 75.5 |  |  |  |

Fig. 1a shows DSC traces of terpolymer samples blended with a different amount of copolymer. Each trace has two or more melting endothermal peaks. For pure terpolymer, the two endothermal peaks are caused by the melting of crystallites with different inclusion degree of CFE units – the peak at lower temperature indicates more CFE units are included in the crystallites and these defects can reduce the lattice positional ordering and result in the decrease of the melting temperature [3]. As the copolymer content increases, two apparent changes occur.

First, both endothermal peaks of the terpolymer shift towards lower temperature. This indicates that the copolymer disturbs the crystallizing process of the terpolymer. The CTFE units may be included in the terpolymer crystallites thus introducing more defects into the crystallites, which can be corroborated by the XRD data. Another proof that the crystallizing process is disturbed is the decreased crystallinity (for binary blends being calculated through the total enthalpy method) listed in Table 1a. Second, a new endothermal peak appears around 150°C, which can be attributed to the melting of copolymer crystallites. This indicates that the copolymer cannot totally co–crystallize with the terpolymer but is only partially embedded during crystallization of the terpolymer.

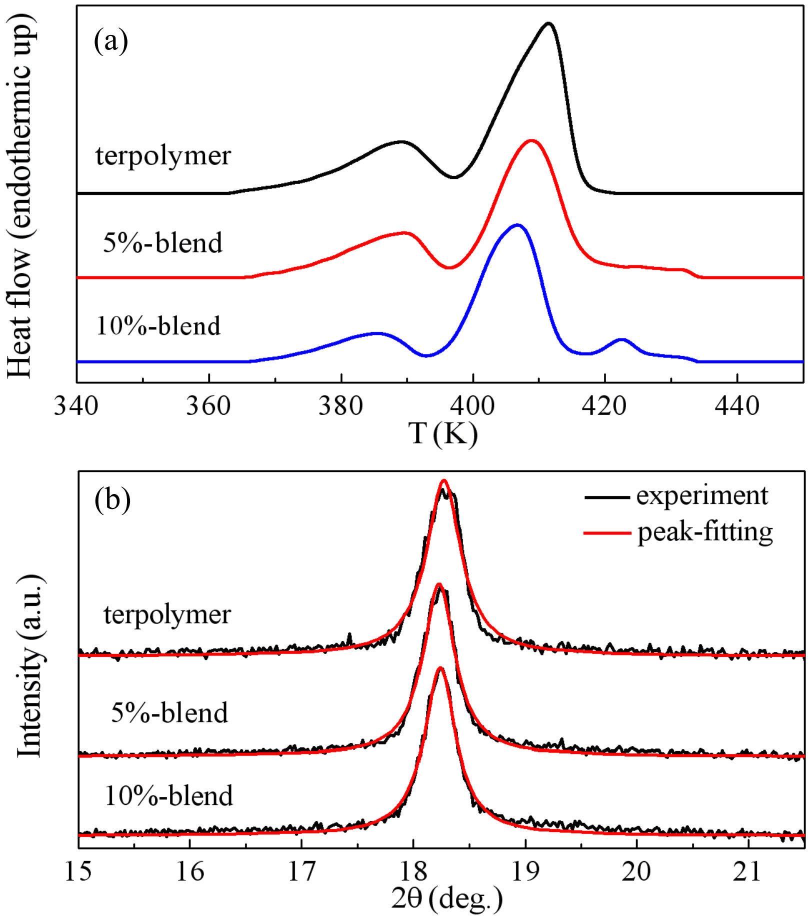

**Figure 1**: DSC traces (a) and XRD patterns (b) of the P(VDF–TrFE–CFE) terpolymer film and its blends with the P(VDF–CTFE) copolymer.

The XRD patterns are shown in Fig. 1b. Each sample exhibits only one peak, referent to the diffraction in planes (110,200). The detailed lattice parameters are listed in Table 1b. With the increase content of copolymer, the lattice spacing is expanded from 4.85 Å to 4.86 Å, which is due to incorporation of the CTFE units in the crystallites. The coherence lengths $L$ perpendicular to the (110,200) planes, representing the sizes of crystallites in the terpolymer, were estimated using Scherrer equation $L=K\lambda/B\cos(\theta)$, where $K$=0.9 is the shape factor, $\lambda$ is X–ray wavelength, and $B$ and $\theta$ are full width at half–maximum and angular position of the diffraction peaks, respectively. The coherence length increases from 21.2 nm for pure terpolymer to at least 23.2 nm for polymer blends. Enlarged coherence length and expanded lattice spacing both corroborate the DSC results that the addition of copolymer introduces more defects and distorts the crystalline ordering.

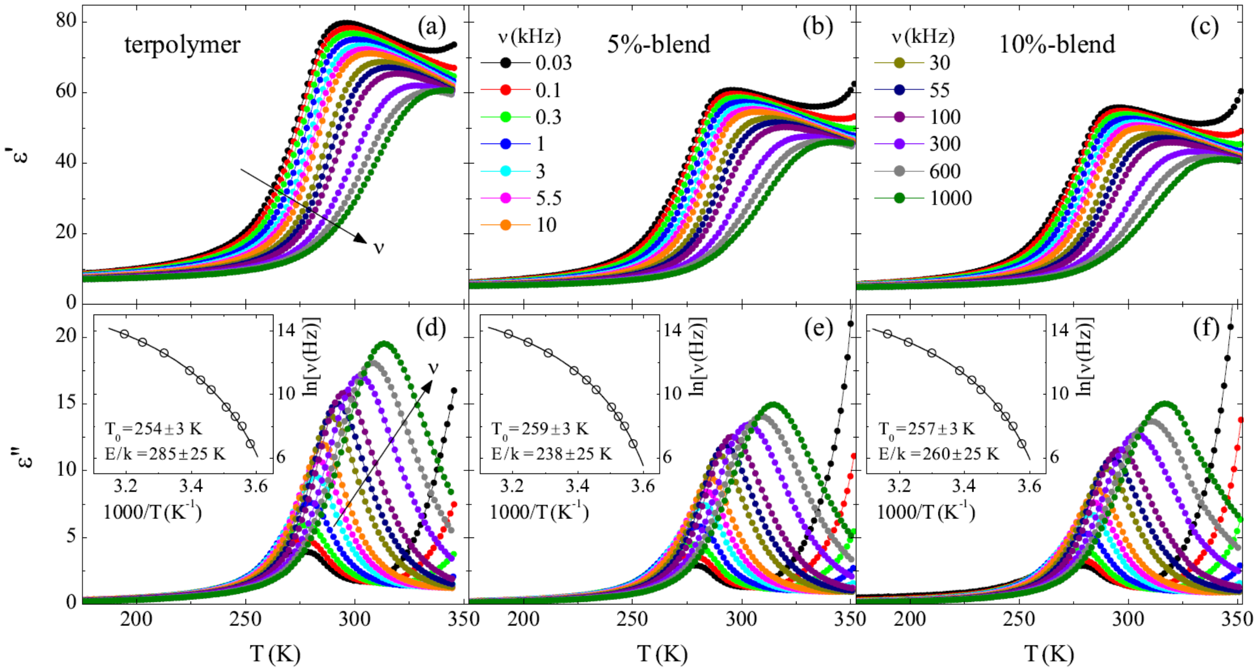

**Figure 2**: Temperature dependences of the real, $\varepsilon'$ (a–c), and imaginary, $\varepsilon''$ (d–f), parts of the complex linear dielectric constant, detected at various frequencies in the terpolymer and blend films. Insets show the Vogel–Fulcher temperature dependence of the characteristic relaxation time.

Fig. 2 depicts the dielectric constant data as a function of the temperature, obtained at several measuring frequencies between 30 Hz and 1 MHz, in terpolymer samples blended with a different amount of copolymer. A typical dispersive relaxor dielectric behavior with relatively high maximum value of ≈80 in the low–frequency range around room temperature has been detected in the P(VDF–TrFE–CFE) terpolymer film. Upon increasing mol % of P(VDF–CTFE) copolymer, values of both, $\varepsilon'$ and $\varepsilon''$, decrease. This is in concurrence with interference effect because the values of dielectric constant are lower in copolymer with respect to terpolymer [1]. Insets to Figs. 2d–f show that characteristic relaxation frequencies, determined from peaks in $\varepsilon''(T)$, follow the Vogel–Fulcher law (as being typical for relaxor systems [4]) $\nu = \nu_0 \exp[-E/k(T-T_0)]$, where $\nu_0$ is the inverse attempt frequency, $E/k$ is the activation energy (in which $k$ is the Boltzmann constant), and $T_0$ is the Vogel–Fulcher freezing temperature. No notable differences within statistical error in Vogel–Fulcher temperature and activation energy between terpolymer and terpolymer/copolymer blends have been detected, indicating that the level of crystallization has no influence on the relaxor dielectric dynamics of the terpolymer film.

In summary, we have investigated structural, caloric, and dielectric properties of relaxor polymer blend films composed of P(VDF–TrFE–CFE) (66.3/26.4/7.3 mol %) terpolymer and P(VDF–CTFE) (91/9 mol %) copolymer on aluminum foil. DSC and XRD results indicate that in this system, the copolymer additive disturbs the crystallizing process of the terpolymer. Measurements of temperature–dependent dielectric response revealed that upon increasing mol % of the copolymer, values of both, $\varepsilon'$ and $\varepsilon''$, decrease in comparison to pure terpolymer, which is in concurrence with interference effect (as values of dielectric constant are lower in pure copolymer). Analysis of temperature–dependent dielectric response has revealed that the addition of the copolymer does not influence the relaxor dynamics of the system: There are no notable differences within statistical error between Vogel–Fulcher temperatures and activation energies of terpolymer and blends with 5 or 10 mol % of copolymer.

## References:

[1]B. Chu, B, Neese, M, Lin, S-G Lu, and Q. M. Zhang. Enhancement of dielectric energy density in the poly(vinylidene fluoride)-based terpolymer/copolymer blends. *Applied Physics Letters*, 93(15): 152903, 2008.

[2]B. Neese, B. Chu, S-G Lu, Y. Wang, E. Furman, and Q. M. Zhang. Large electrocaloric effect in ferroelectric polymers near room temperature. *Science*, 321(5890): 821-823, 2008.

[3]R. J. Klein, J. Runt, and Q. M. Zhang. Influence of crystallization conditions on the microstructure and electromechanical properties of poly(vinylidene fluoride-trifluoroethylene-chlorofluoroethylene) terpolymers. *Macromolecules*, 36(19): 7220-7226, 2003.

[4]V. Bobnar, B. Vodopivec, A. Levstik, M. Kosec, B. Hilczer, and Q. M. Zhang. Dielectric properties of relaxor-like vinylidene fluorideâˆ'trifluoroethylene-based electroactive polymers. *Macromolecules*, 36(12): 4436-4442, 2003.

## For wider interest

Relaxor polymers are very promising for a broad range of energy storage capacitor applications due to their unique physical properties. One of the advantages for use of polymers in such applications arises from the possibility of polymer film formation directly on a surface. Active metals such as aluminum can be used for substrates, as they are less expensive than noble metals and mechanically more stable than glassy carbon.

Investigations of relaxor poly(vinylidene fluoride–trifluoroethylene–chlorofluoroethylene) [P(VDF–TrFE–CFE)] terpolymer have revealed high values of dielectric constant at room temperature, fast response speeds, high strain levels and energy density, and large electrocaloric effect. Polymer blends exploit merits of both, base and additive polymer – due to interference effect, properties of base polymer can be tailored and improved. Recent studies show that polymer blends composed of P(VDF–TrFE–CFE) terpolymer as a base with a small amount of poly(vinylidene fluoride–chlorotrifluoroethylene) P(VDF–CTFE) copolymer (e.g. 5 or 10 mol %) as an additive have even higher polarization response, energy density, elastic module, and breakdown field than pure relaxor P(VDF–TrFE–CFE) system. We have thus decided to develop and investigate such polymer blend films on a metal surface.

We report structural, caloric, and dielectric properties of polymer blends of poly(vinylidenefluoride–trifluoroethylene–chlorofluoroethylene) terpolymer (a member of the relaxor polymers family that exhibits fast response speeds, giant electrostriction, high electric energy density, and large electrocaloric effect) and poly(vinylidenefluoride–chlorotrifluoroethylene) copolymer, developed on aluminum surface. Terpolymer films exhibit for a relaxor polymer material very high values of the dielectric constant of ≈80 around room temperature, which decreases in terpolymer/copolymer blends to ≈60. We show that addition of the copolymer enables us to govern the dielectric constant of the films without influencing the relaxor dielectric dynamics.

# The adhesion of bacteria to austenitic stainless steel (AISI 316L) with different surface finishes

**Matej Hočevar[1,2], Monika Jenko[1], Damjana Drobne[3], Sara Novak[3]**

[1] Institute of Metals and Technology, Ljubljana, Slovenia

[2] Jožef Stefan International Postgraduate School, Ljubljana, Slovenia

[3] Department of Biology, Biotechnical Faculty, University of Ljubljana, Ljubljana, Slovenia

matej.hocevar@imt.si

**Abstract.** Adhesion of bacteria and a biofilm formation on stainless steel is enhancing the material corrosion and presents a chronic source of the microbial contamination in food and medical industries. The aim of our research is to examine the effect of the surface roughness and topography of austenitic stainless steel (AISI 316L) on the adhesion of bacteria. The surface morphology of the samples was analysed by the atomic force microscope (AFM), the contact profilometer, the scanning electron microscope (SEM) and the contact angle goniometer. Different surface finishes of stainless steel correspond to different roughness ($R_a$) values. *Escherichia coli* (Exb-V1) was exposed to different surfaces. Based on the literature data, we hypothesized that the surface roughness and furrows of the similar size as bacteria or smaller, will affect the bacterial adhesion. So far, it was shown that the bacteria, for their attachment, prefer cracks and scratches over smooth surfaces.

**Keywords**: surface roughness, adhesion, bacteria, stainless steel

## 1 Introduction

In nature on exposed surfaces microorganisms usually adhere, grow and form aggregations known as biofilms [1]. The adhesion of bacteria to stainless steel presents a chronic source of the microbial contamination in food and medical industries [2], [3]. It also enhances the material corrosion, as well as decreases the performance of plants, heat exchangers and cooling towers [4], [5], [6].

The adhesion of bacteria to surfaces is an important biological process governed by the physicochemical parameters such as surface chemistry, composition, topography, roughness, bacterial hydrophobicity, surface charge, cell size and also the properties of the environment [7], [8]. The roughness of the surface plays a role in the attachment process, particularly when the surface irregularities are comparable to the size of the bacteria and can provide shelter from unfavourable environmental factors [9].

# 2 Materials and Methods

## 2.1 Material

Austenitic stainless steel (SS) disks, 15 mm in diameter and 1.5 mm thick, were made of 316L stainless steel sheets with the 2B surface finish. Different surface treatments (SiC grinding papers with granulation from 100 to 1200) were used to obtain different surface finishes and degrees of the surface roughness: Aizv (as delivered), A100, A320, A800, A1200 and Apol (polished samples).

## 2.2 Solid surface characterization

The SS disks surface characterization was made using the AFM (surface topography and surface roughness measurements), the contact profilometer (surface roughness measurements) and the contact angle goniometer (contact angle and surface free energy measurements).

## 2.3 Bacterial preparation

The bacterial strain *Escherichia coli* ExB-V1 was grown overnight in the Lauria-Bertani broth (LB) with shaking at 37 °C. The cells were harvested by centrifugation at 10000 g for 5 min at 20 °C and were washed once in sterile Phosphate buffered saline (PBS). After second centrifugation the final pellet was resuspended in sterile PBS to a concentration of approx. $10^9$ CFU/ml.

## 2.4 Adhesion experiments

Prior to any testing, the surfaces were first degreased by an alkaline detergent and ultrasonic bath in ethanol, followed by their sterilization. The SS discs were immersed horizontally in the bacterial suspension in static conditions at 37 °C for 2

h. The non-adhering bacteria were removed by rinsing the substrate three times with 10 ml of sterile PBS (Fig. 1). Samples were then prepared for SEM observations.

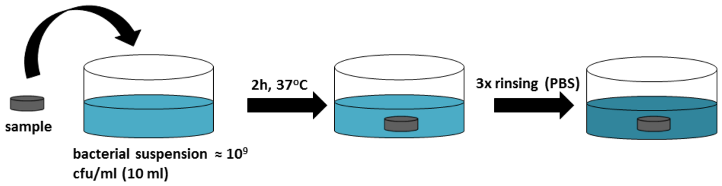

**Figure 1**: Schematic of the adhesion experiment.

## 3 Results

The topography of SS disks with different surface finishes clearly differs, as can be seen on AFM three-dimensional surface plots (Fig. 2). Sample Aizv has a network of subsurface crevices between grain boundaries due to the pickling treatment following the cold-rolling stage during the steel production (Fig. 2a). Finishes on the samples A100-A1200 have long linear grooves whereas the Apol sample has the smoothest surface (Fig. 2b-2f).

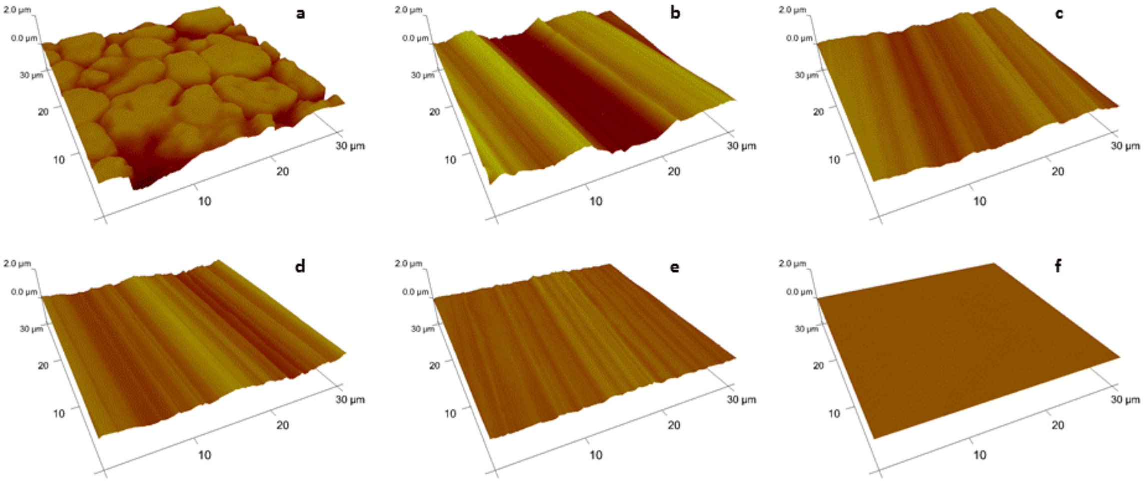

**Figure 2**: AFM three-dimensional surface plots of different stainless steel surface finishes: a) Aizv, b) A100, c) A320, d) A800, e) A1200 and f) Apol.

Surface roughness measurements show significant differences, the roughest sample is A100 and the smoothest sample is Apol (Fig. 3a and 3b). All samples had similar contact angles and consequently a similar surface free energy (Fig. 3c and 3d).

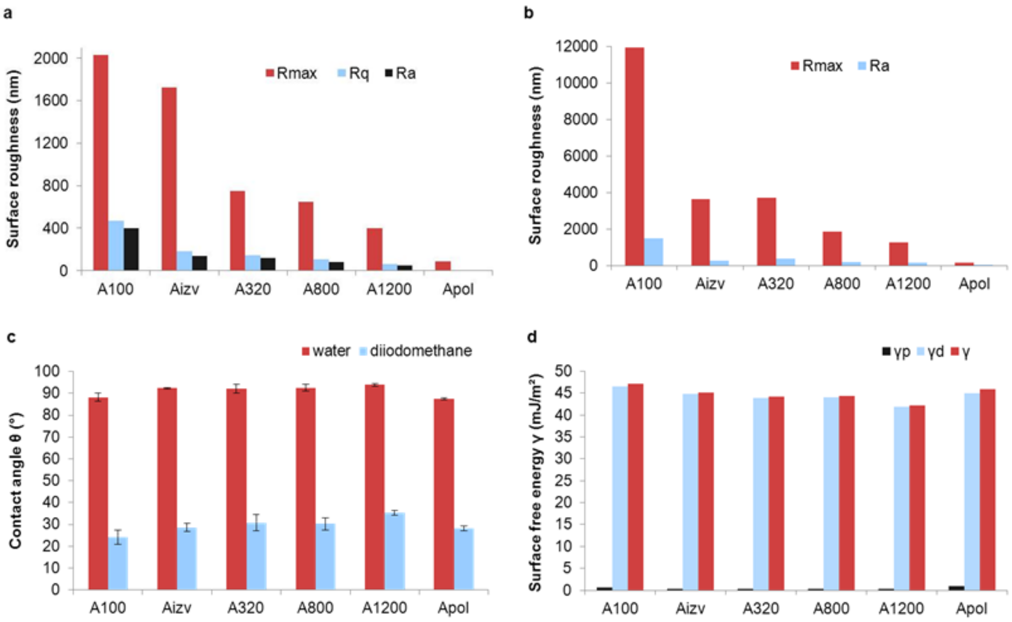

**Figure 3**: a) AFM surface roughness, b) profilometer surface roughness, c) contact angle and d) surface free energy.

The number and distribution of the attached bacteria on all investigated Aizv samples were similar. The bacteria usually attach to the immediate vicinity of the already attached bacteria, so that they form clusters. The bacteria prefer cracks, scratches and surface irregularities over the smoother surface. Individually attached bacteria are seen very rarely (Fig 4).

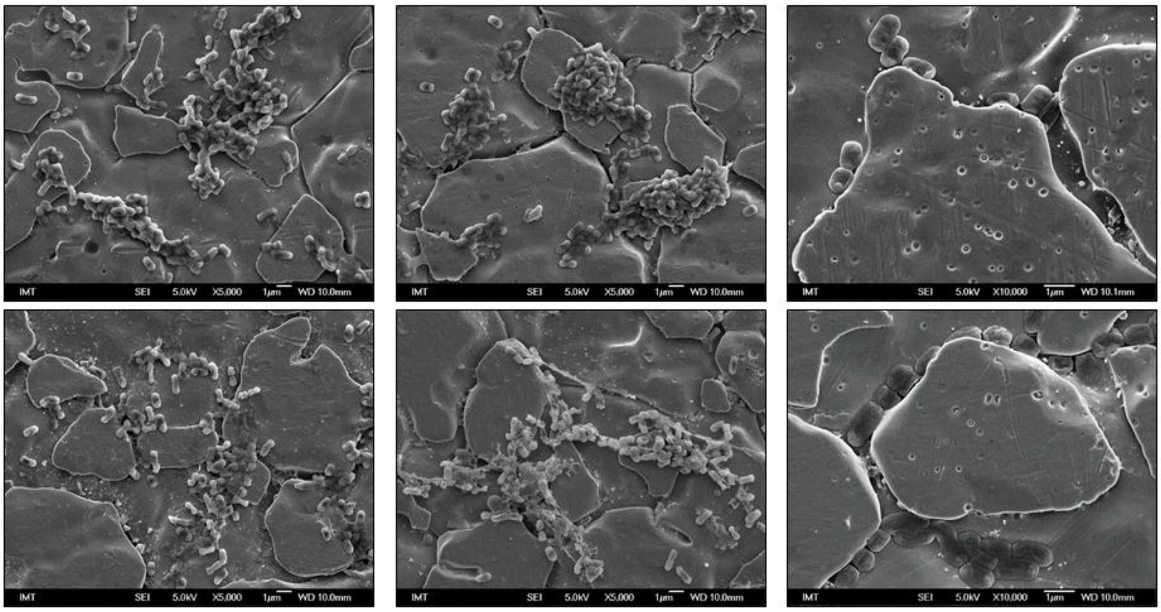

**Figure 4**: SEM images of attached *E. coli* to the sample Aizv: 5000x and 10000x magnification.

## 4 Conclusions

The topography and surface roughness measurements of the SS disks with different surface finishes show significant differences. Contact angle and surface free energy measurements show that the surface roughness of stainless steel in our case has a small effect on the surface energy. So far only the experiments on the Aizv samples were made. The number and distribution of the bacteria were similar on all Aizv samples. The bacteria prefer surface irregularities over the smooth surface, as they provide shelter from unfavourable environmental factors. Further work will be required to obtain the answer how different surface finishes affect the attachment and retention of the bacteria. In addition, different thin coatings will be applied on the surfaces.

## References:

[1]R. M. Donlan. Biofilms: Microbial Life on Surfaces. *Emerging infectious disease*, 8(9): 881–890, 2002.

[2]J. W. Arnold and G. W. Bailey. Surface Finishes on Stainless Steel reduce Bacterial attachment and Early Biofilm Formation: Scanning Electron and Atomic Force Microscopy Study. *Poultry Science*, 79:1839–1845, 2000.

[3]E. Medilanski, K. Kaufmann, L. Y. Wick, O. Wanner and H Harms. Influence of the Surface Topography of Stainless Steel on Bacterial Adhesion. *Biofouling: The Journal of Bioadhesion and Biofilm Research*, 18(3):193–203, 2002.

[4]H. A. Videla and L. K. Herrera. Microbiologically influenced corrosion: looking to the future. *International Microbiology*, 8:169-180, 2005.

[5]Q. Zhao. Effect of surface free energy of graded NI – P – PTFE coatings on bacterial adhesion. *Surface and Coatings Technology*, 185(2-3):199-204, 2004.

[6]J. P. Maréchal and C. Hellio. Challenges for the Development of New Non-Toxic Antifouling Solutions. *International Journa of Molecular Science*, 10(11):4623-4637, 2009.

[7]M. Katsikogianni and Y.F. Missirlis. Concise review of mechanisms of bacterial adhesion to biomaterials and of techniques used in estimating bacteria-material interactions. *European Cells and Materials*, 8:37-57, 2004.

[8]N. Kouider, F. Hamadi, B. Mallouki, J. Bengourram, M. Mabrouki, M. Zekraoui, M. Ellouali and H. Latrache. Effect of stainless steel surface roughness on *Staphylococcus aureus* adhesion. *International Journal of Pure and Applied Science*, 4(1):1-7, 2010.

[9]A. Allion, J. P. Baron and L. Boulange-Petermann. Impact of surface energy and roughness on cell distribution and viability. *Biofouling: The Journal of Bioadhesion and Biofilm Research*, 22(5):269-278, 2006.

## Za širši interes

V naravi mikroorganizmi na izpostavljenih površinah pogosto tvorijo skupke, ki jih imenujemo biofilmi. Adhezija bakterij na površino in tvorba biofilmov na nerjavnem jeklu predstavlja kronično vir kontaminacije z mikrobi v medicini in živilski industriji. Prisotnost bakterij povzroča tudi korozijo materiala ter zmanjšuje učinkovitost naprav, kot so toplotni izmenjevalci, hladilni stolpi in filtri. Adhezija bakterij na površino je kompleksen proces na katerega vplivajo lastnosti površine materiala (hrapavost, topografija, kemija), lastnosti bakterije in okoljski dejavniki.

Namen naše raziskave je preučiti vpliv hrapavosti in topografije nerjavnega jekla na adhezijo bakterij s pomočjo vrstičnega elektronskega mikroskopa (SEM) in mikroskopa na atomsko silo (AFM). Za namen naše raziskave smo iz nerjavnega jekla izdelali vzorce v obliki diskov s premerom 15 mm in debeline 1,5 mm. Površine vzorcev smo obdelali s pomočjo brusnega papirja različne granulacije (100-1200), da smo dobili različno topografijo in hrapavost naših vzorcev.

V raziskavi smo uporabili bakterijo *Escherichia coli*, ki smo jo čez noč gojili v Lauria-Bertani gojišču s stresanjem pri 37 $^{o}$C. Nato smo bakterije centrifugirali 5 minut pri 10000 g in dobljeno bakterijsko usedlino resuspendirali v pufru (PBS). Pred pričetkom adhezijskih poskusov smo vzorce očistili z detergentom, ultrazvočno kopeljo v absolutnem etanolu in sterilizacijo. Vzorce smo vodoravno potopili v 10 ml bakterijske suspenzije v statičnih pogojih pri 37 °C za 2 h. Nepritrjene oziroma slabo pritrjene bakterije smo odstranili s tremi zaporednimi spiranji s PBS. Po adhezijskih poskusih smo vzorce z bakterijami pripravili za mikroskopiranje s SEM.

Do sedaj so bili narejeni poskusi le na vzorcih Aizv. Število in razporeditev bakterij je pri vseh vzorcih podobna. Bakterije se pritrjajo v neposredno bližino že pritrjenih bakterij in tvorijo skupke, redkeje je opaziti posamezne bakterije. Bakterije se pogosteje pritrjujejo v razpoke, praske in druge nepravilnosti na površini, saj jih ščitijo pred neugodnimi dejavniki okolja. V nadaljevanju naše raziskave bomo poleg hrapavosti preučevali tudi vpliv tankih plasti na nerjavnem jeklu na adhezijo bakterij.

# Influence of the suspension stability on the deposition of cobalt ferrite particles under an applied magnetic field

**Petra Jenuš**[1,2] , Darja Lisjak[1] , Darko Makovec[1], Miha Drofenik[1,3]

[1] Department for Materials Synthesis, Jožef Stefan Institute, Ljubljana, Slovenia

[2] Jozef Stefan International Postgraduate School, Ljubljana, Slovenia

[3] Faculty for Chemistry and Chemical Engineering, Maribor, Slovenia

petra.jenus@ijs.si

**Abstract.** Cobalt ferrite nanoparticles were synthesized with coprecipitation or with the hydrothermal method. Stable water suspensions were prepared from the as-synthesized nanoparticles, with the addition of citric acid as a surfactant, and then used for the preparation of deposits under an applied magnetic field. The morphology of the cobalt ferrite nanoparticles was investigated with a transmission electron microscope, and their magnetic properties were measured with a vibrating-sample magnetometer. The particle sizes and their magnetic properties influenced the stability of the suspensions, which were evaluated in terms of their zeta-potentials and the sedimentation time. Furthermore, the same parameters significantly influenced the morphology of the deposits, which were observed with a scanning electron microscope.

**Keywords**: cobalt ferrite, coprecipitation, hydrothermal method, magneto(di)electric composites

## 1 Introduction

Cobalt ferrite (CoF), with the chemical formula $CoFe_2O_4$, is a spinel ferrite. In comparison with the other spinel ferrites, CoF has a high cubic magnetocrystalline anisotropy, a high coercivity and a moderate saturation magnetization [1]. These interesting magnetic properties, along with a good mechanical hardness, make cobalt ferrite a promising material for a large number of applications. In addition to this, CoF is also a magnetostrictive material suitable for magneto(di)electric (ME) composites [2, 3]. These ME composites are interesting for a variety of applications, such as tunable microwave devices based on the electric control of the spin-wave propagation, or new magnetic memories, in which the magnetic response is controlled by an electric field. The magnetostrictive phase in ME composites can be distributed in a ferroelectric matrix in the form of particles, as alternating layers or as vertical columnar structures. The latter is denoted as a 1-3 type structure (see also Figure 1d in the following) [4]. It has been shown that the largest magnetoelectric (ME) effect (the appearance of polarization/magnetization upon applying a magnetic/electric field) can be produced in the ME composites with 1-3 structure [5].

Columnar structures can be prepared using a variety of techniques, such as a pulsed-laser deposition - PLD [6] or a rf sputtering [7]. All these techniques are quite expensive and complicated. In the search for a simple and inexpensive method for the preparation of columnar structures, we decided to use the deposition of CoF nanoparticles under an applied magnetic field. In this work we investigated how the suspension stability influences the formation of columnar structures of CoF under an applied magnetic field.

## 2 Experimental work

Cobalt ferrite nanoparticles were prepared from aqueous solutions of $Fe^{3+}$ and $Co^{2+}$ ions by the coprecipitation (CC) method, where tetramethyl ammonium hydroxide (TMAH) was used as the precipitating agent and the temperature of the synthesis was 70°C. CoF nanoparticles were also synthesized by the hydrothermal (HT) method, where the precipitating agent was sodium hydroxide (NaOH), and different synthesis temperatures were applied (120°C, 150°C or 200°C). The CoF nanoparticles were stabilized with citric acid in water, at a pH of approximately 10. Ten drops of suspension were deposited on an $Al_2O_3$ substrate under an applied magnetic field (B = 0, 5 T) and then dried in the air at room temperature. The organic phase was removed by heating at 460°C for 2h. The deposition and the heating procedure were repeated three times.

The CoF nanoparticles were investigated with transmission electron microscopy (TEM) and with energy-dispersive X-ray spectroscopy (EDXS). The stability of the suspensions was evaluated from their zeta (ζ) potential and the sedimentation time. This time was determined as the time, before the first sediment of particles was observed in the suspension. The magnetic properties of the CoF nanopowders were measured with a vibrating-sample magnetometer (VSM). The morphology of the deposits was investigated by using scanning electron microscopy (SEM).

## 3 Results and Discussion

Suspension A was prepared from the CoF nanoparticles synthesized with the coprecipitation method. TEM studies showed that the particle size varies between 5 and 20 nm (Table 1). The particles were crystalline, but they were of irregular shape. The EDXS analysis revealed that the atomic ratio between Co and Fe was 1:2. The TEM studies of the particles prepared by the hydrothermal method (samples B, C and D) showed that the particle size increases with the increasing temperature of the synthesis (Table 1). It was also clear that with higher synthesis temperatures the fraction of larger particles increases. At the same time the shape of the particles becomes more defined, with a typical octahedral shape. In all three samples the EDXS analysis confirmed the atomic ratio of the Co:Fe ~ 1:2, as in $CoFe_2O_4$. With the increasing particle size the saturation magnetization (Ms) increased. The highest Ms (68 $Am^2/kg$) was obtained in a sample D and this Ms value can be compared to the Ms of the CoF bulk material.

**Table 1:** Properties of the suspensions

| Sample | Synth. method | $T_{synthesis}$ | Particle size (nm) | Ms of CoF powder ($Am^2/kg$) | c(g/L) | ζ-potential (mV) | $t_{sedimentation}$ (days) |
|---|---|---|---|---|---|---|---|
| **Susp.A** | CC | 70°C | 5-20 | 31 | 2 | -58 | > 200 |
| **Susp.B** | HT | 120°C | 10-30 | 55 | 2 | -47 | >21 |
| **Susp.C** | HT | 150°C | 15-40 | 61 | 10 | -45 | 21 |
| **Susp.D** | HT | 200°C | 15-50 | 68 | 10 | -45 | 21 |

As mentioned earlier, stable aqueous suspensions of CoF nanoparticles were prepared with the addition of citric acid as a surfactant. The stability of the prepared suspensions varied with the particle size and the magnetic properties (Table 1). We can see that the HT suspensions had lower $\zeta -$potentials and that the sedimentation occurred more quickly than in the CC suspension. With the increasing particle size and, consequently, with the increasing Ms of the as-synthesized CoF nanoparticles, the stability of the suspension decreases.

The SEM studies showed that the deposits prepared from the suspension A were relatively homogeneous and that columnar structures were not present (Figure 1a). In contrast to this in the deposits prepared from suspensions B, C and D columnar structures of CoF were formed. The morphology of the prepared columnar structures differed from sample to sample (Figure 1b and c). The vertical structures made from sample B were quite dense, but their shape was irregular and some cracks could be observed in the columns. In the deposits prepared from the suspensions C and D the distribution of columnar structures was more uniform and with fewer cracks. The difference between the two was in the density (the number of columns per area unit), which was higher for deposit D.

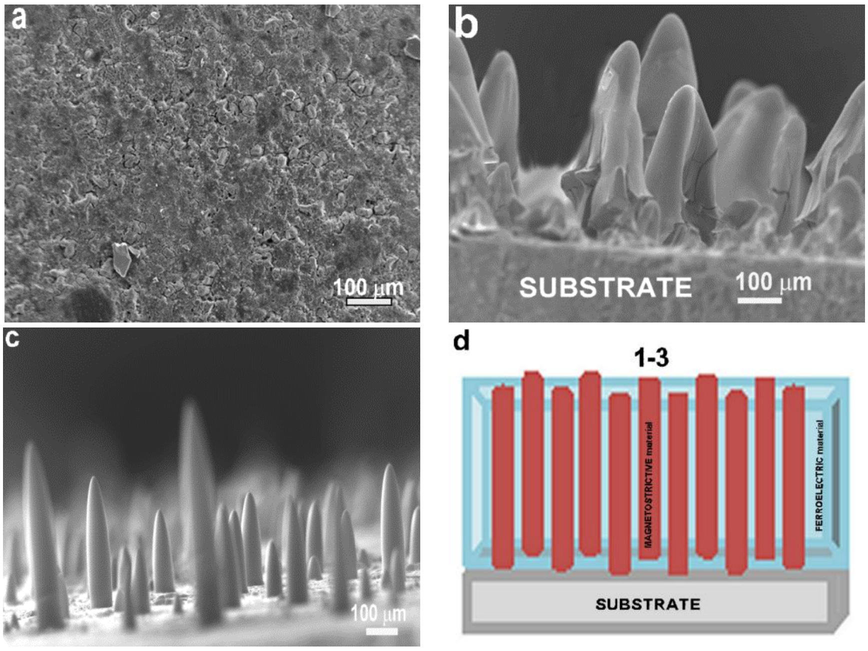

**Figure 1**: SEM images of the CoF deposits prepared under an applied magnetic field. a.) sample A (top view), b.) sample B (side view), c.) sample D (side view) and d.) ME composite with 1-3 structure type, where columns of magnetostrictive material are evenly distributed in a ferroelectric matrix.

The Ms (31 Am$^2$/kg) of the CoF nanoparticles in sample A is relatively small in comparison to those of the other samples (Table 1), and the value of the $\zeta$-potential (-58 mV) of this suspension was the highest among all the studied suspensions (Table 1). This low Ms value suggests weak magnetic dipole-dipole attractive forces, which together with the high absolute value of the $\zeta$-potential resulted in a very stable suspension. The high degree of stability could also be seen from the time of the onset of sedimentation, which was longer than 6 months in case of sample A (Table 1). The CoF nanopowders prepared by the hydrothermal method had higher values of Ms and, therefore, the attractive magnetic forces between these CoF particles in the suspension were stronger than in suspension A. The increasing attractive energy between the particles coincides with the smaller absolute value of the ζ-potential and, consequently, with the less stable suspension (see also the sedimentation time in Table 1). All this suggest the suspension stability affected the deposits' morphology and that the destabilization of a suspension was crucial for the formation of the columns.

## 4 Conclusions

In this work we investigated the influence of the suspension stability on the deposition of CoF particles under an applied magnetic field. It was shown that the deposits prepared from a stable suspension were relatively homogenous. From the suspensions with the lower zeta potential and shorter sedimentation time the deposits with columnar structures were formed. The columns were distributed uniformly on a substrate and had smooth surfaces when the deposits were prepared from the least stable suspensions.

## References:

[1] J. Smit, H. P. J. Wijn, Smit, J., Wijn, H. P. J., *Ferrites.* Eindhoven; Philips' Technical Library, 1959.

[2] H. Zheng, J. Wang, S. E. Lofland, Z. Ma, L. Mohaddes-Ardabili, T. Zhao, L. Salamanca-Riba, S. R. Shinde, S. B. Ogale, F. Bai, D. Viehland, Y. Jia, D. G. Schlom, M. Wuttig, A. Rotyburd, R. Ramesh, Multiferroic $BaTiO_3$ - $CoFe_2O_4$ Nanostructures, *Science*, 303, 661-663, 2004.

[3] J. X. Zhang, J. Y. Dai, W. Lu, H. L. W. Chan, Room Temperature Magnetic Exchange Coupling in Multiferroic $BaTiO_3$ /$CoFe_2O_4$ Magnetoelectric Superlattice, *J. Mater.Sci*, **44**, 5142-5148, 2009.

[4]Y. Wang, J. Hu, Y. Lin, C.-W. Nan, Multiferroic Magnetoelectric Composite Nanostructures, *NGP Asia Mater.*, **2**(2), 61-68, 2010.

[5] C.-W. Nan, G. Liu, Y. Lin, H. Chen, Magnetic-Field-Induced Electric Polarization in Multiferroic Nanostructures, *Phys. Rew. Lett*, 94, 197203, 2005.

[6]H. Zheng, J. Wang, L. Mohaddes-Ardabili, M. Wuttig, L. Salamanca-Riba, D. G. Schlom, R. Ramesh, Three-Dimensional Heteroepitaxy in Self-Assembled $BaTiO_3$–$CoFe_2O_4$ Nanostructures, *Appl. Phys. Lett.*, 85, 2035-2037, 2004.

[7] I. Fina, N.Dix, V.Laukhin , L.Fabrega , F.Sanchez, J.Fontcuberta, Dielectric Properties of $BaTiO_3$–$CoFe_2O_4$ Nanocomposite Thin Films*, J. Magn. Magn. Mater.*, 321, 1795-1798, 2009.

## For wider interest

*Magnetic nanoparticles (magnetic fluids, nanocomposites)*

New methods for the controlled synthesis of iron oxide based nanoparticles are being developed. Additionally, we are focused on the functionalization of magnetic nanoparticles, primarily for biomedical applications. The surface properties of nanopowders, which determine their applicability, are tuned with inorganic coatings (i.e., a thin film of amorphous silica), with polymer coatings or with single-molecule layers. The coating prevents the agglomeration of nanoparticles, which further enables their dispersion in various liquids, i.e., magnetic fluids or the homogeneous incorporation of nanoparticles in various matrices.

*Multifunctional materials*

Nanocomposites combining the various properties of the constituent materials can be prepared by mastering the surface properties of nanoparticles. Examples of our studies include combinations of ferrimagnetics and dielectrics (magnetodielectrics) and ferrimagnetic and ferroelectric (composite multiferroics) materials. Current studies are also related to the development of new, magneto-optic materials for sensors and magneto-catalytic materials for environmental applications.

*Magnetic materials for micro- and mm-waves*

Magnetic materials suitable for the absorbers of electromagnetic waves and for the non-reciprocal ferrite devices are being developed. Ceramics and composites based on ferrites are studied for the microwave applications, and a new method for the preparation of magnetically oriented thick hexaferrite films for self-biased mm-wave applications has been developed.

# Synthesis of cobalt ferrite nanoparticles using a combination of the co-precipitation and hydrothermal methods

**Sonja Jovanović**[1,2], Matjaž Spreitzer[1], Mojca Otoničar[1,2], Danilo Suvorov[1,2]

[1] Department of Advanced Materials, Jožef Stefan Institute, Ljubljana, Slovenia

[2] Jožef Stefan International Postgraduate School, Ljubljana, Slovenia

sonja.jovanovic@ijs.si

**Abstract.** In this work we have examined the influence of the pH on the structural and magnetic properties of cobalt ferrite ($CoFe_2O_4$) nanoparticles obtained by a combination of the co-precipitation and hydrothermal methods. The crystal structures and the particle sizes of the prepared powders were analyzed by the X-ray diffraction and transmission electron microscopy, while the magnetic properties of the cobalt ferrite nanoparticles were measured at room temperature using a vibrating-sample magnetometer. The results showed that an increase of the pH improves both the crystallinity of the $CoFe_2O_4$ nanoparticles and their average size. At the same time the pH affects the magnetic properties of the nanoparticles, since the saturation magnetization ($M_S$), remanent magnetization ($M_r$) and coercivity ($H_C$) increase with the increase of the pH.

**Keywords**: Cobalt ferrite; Nanoparticles; Hydrothermal synthesis; Magnetic properties

## 1 Introduction

The spinel ferrites are a large group of oxides that were first studied by Nishikawa (1915) and Bragg (1915); they have the structure of the natural spinel $MgAl_2O_4$ [1].In recent years, spinel ferrite nanoparticles have been actively investigated because of their magnetic and electrical properties. The general formula of spinel ferrites is $MFe_2O_4$, where M is a divalent ion such as $Co^{2+}$, $Ni^{2+}$, $Zn^{2+}$, $Mn^{2+}$, etc. Cobalt ferrite is a material that possesses an inverse spinel structure. It has a moderate saturation magnetization, a large magnetic anisotropy, a remarkable chemical stability and a mechanical hardness, and because of these properties it can be used for recording media, spintronics, magnetic refrigeration, ferrofluids, magnetic resonance imaging, the delivery of drugs to specific areas of the body, etc. [2-5].

In order to obtain $CoFe_2O_4$ with the appropriate physical and chemical properties, its synthesis via different methods has become an important area of research and development. Several methods for the preparation of cobalt ferrite nanoparticles have been reported, such as the ball milling, co-precipitation, hydrothermal synthesis, sol-gel, and reaction in a micro-emulsion [6-10]. A hydrothermal synthesis offers several advantages over other conventional processes, like the simplicity, cost effectiveness, higher dispersion, higher rate of reaction, better shape control, and lower temperature of operation in the presence of an appropriate solvent, etc [11]. In a recent study, Liu et al. examined the influence of the synthesis time and the concentration of metallic ions on the synthesis of $CoFe_2O_4$ nanoparticles [8]. They used sodium dodecyl sulfate (NaDS) during the synthesis, which enabled them to control the morphology of the particles to a certain extent. However, they did not investigate the influence of pH on the morphology and magnetic properties, which is the main purpose of our work.

## 2 Experimental

As in a typical synthesis, sodium dodecyl sulfate (8.5 mmol) was added to 25 ml of deionized water and stirred for a few minutes at 50°C, and 4.25 mmol of $CoCl_2 \cdot 6H_2O$ was added under stirring to ensure the complete dissolution. Then, 8.5 mmol of $FeCl_3 \cdot 6H_2O$ was added into this solution and stirred until its dissolution. Finally, 25 ml of 2,5 M aqueous solution of NaOH was added and stirred for several minutes. A black precipitate formed in the solution with pH=13.1. A similar sample was treated with 37 % HCl and its pH was adjusted to 8.0. The mixture was transferred into a Teflon-lined, stainless-steel autoclave with a capacity of 75 ml, closed, and kept at 120°C for 8h. The product was sonicated for 30-45 min, and then washed several times with distilled water, ethanol and then centrifuged. The product was dried at 70°C in air over night.

The crystal structure of the obtained powders was analyzed by the X-ray diffraction (XRD, Siemens D5000) with the Cu $K_\alpha$ ($\lambda$=1.5406 Å) radiation at room temperature for the $2\theta$ range from 20° to 80° ($2\theta$ step=0.04° with a counting time of 1s per step). The structural characteristics and the particle sizes were examined using a transmission electron microscope (TEM, JEM-2100, JEOL Ltd., Tokyo, Japan) operated at 200 kV. The magnetic properties of the cobalt ferrite nanoparticles were measured at room temperature using a vibrating-sample magnetometer (VSM, 7307 Lake Shore).

## 3 Results and Discussion

The XRD patterns of the as-prepared $CoFe_2O_4$ nanoparticles are shown in Figure 1. The results show that as the pH increases the diffraction maxima become sharper and more pronounced. This indicates that the crystallinity and the average particle size are increased as the pH increases. The crystal structure of the $CoFe_2O_4$ prepared at pH=13.1 has a cubic symmetry and is in accordance with JCPDS card No. 22-1086. The average crystallite size of the cobalt ferrite prepared at pH=13.1, based on the Scherrer formula [12], was estimated to be 15 nm.

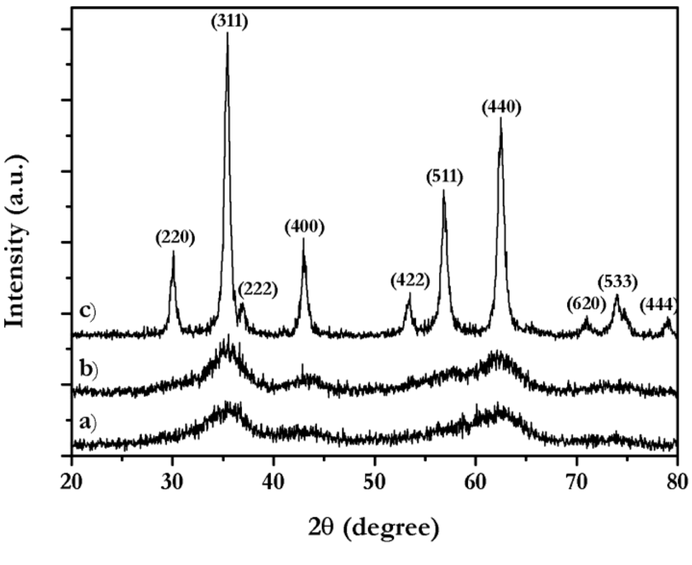

**Figure 1:** XRD patterns of the as-prepared $CoFe_2O_4$ nanoparticles: a) co-precipitation, b) pH=8.0 and c) pH=13.1.

Figure 2 presents TEM images of the as-prepared cobalt ferrite nanoparticles. The samples prepared at pH=8.0 and by co-precipitation are mainly amorphous, as corroborated by the XRD patterns (Figure 1). The crystallinity and the particle size of the samples increases with the pH. In the case of the highest pH the particles are of a cube-like shape and have a broad size distribution.

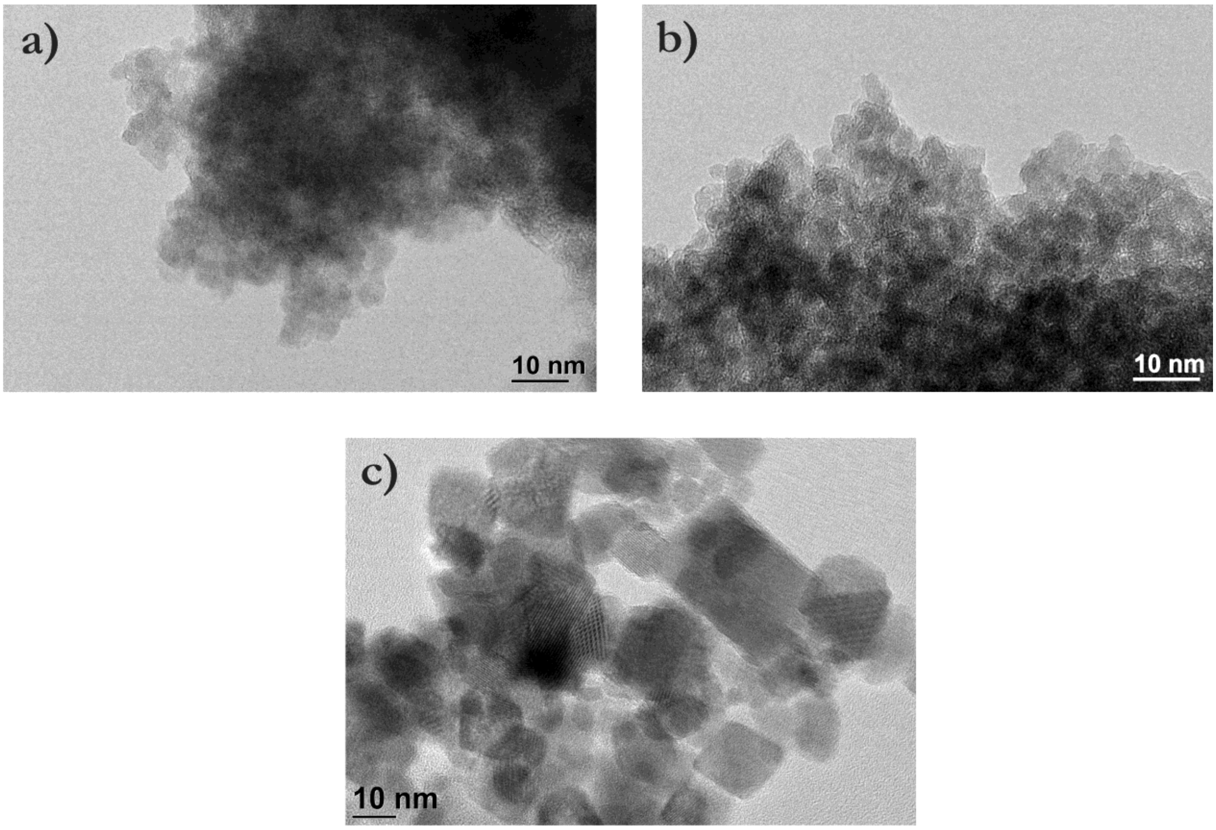

**Figure 2:** TEM images of the $CoFe_2O_4$ nanoparticles a) co-precipitation, b) pH=8.0 and c) pH=13.1.

The magnetic properties of the $CoFe_2O_4$ nanoparticles were investigated using a vibrating-sample magnetometer (VSM). Figure 3 shows the hysteresis loops that were measured at room temperature in a magnetic field of 15 kOe. The values for the saturation magnetization ($M_S$), remanent magnetization ($M_r$), and the coercivity ($H_C$) are shown in Table 1.

**Table 1:** Magnetic properties of the $CoFe_2O_4$ nanoparticles prepared at T=120 °C and pH = 8.0 and 13.1 and by co-precipitation

| **pH** | **$M_S$, emu/g** | **$M_r$, emu/g** | **$H_C$, Oe** |
|---|---|---|---|
| **Co-precipitation** | 3.2 | 0.00 | 3.9 |
| **8.0** | 10.9 | 0.01 | 5.7 |
| **13.1** | 65.4 | 19.95 | 775.8 |

The $M_S$, $M_r$ and $H_C$ values increase with increasing pH and for the sample synthesysed at pH=13.1 these values are 65.4 emu/g, 19.95 emu/g and 775.8 Oe, respectively. As is clear from Figure 3, with the increase of the pH the samples change their magnetic behaviour: they go from paramagnetic to ferromagnetic. We anticipated that an increase in the magnetic properties is related to the higher crystallinity of the sample obtained at pH=13.1. Furthermore, we observed that the values of $M_S$, $M_r$ and $H_C$ obtained here (Table 1) are higher than the corresponding values (60.27 emu/g, 15.63 emu/g and 465 Oe, respectively) reported by Liu at al. [8].

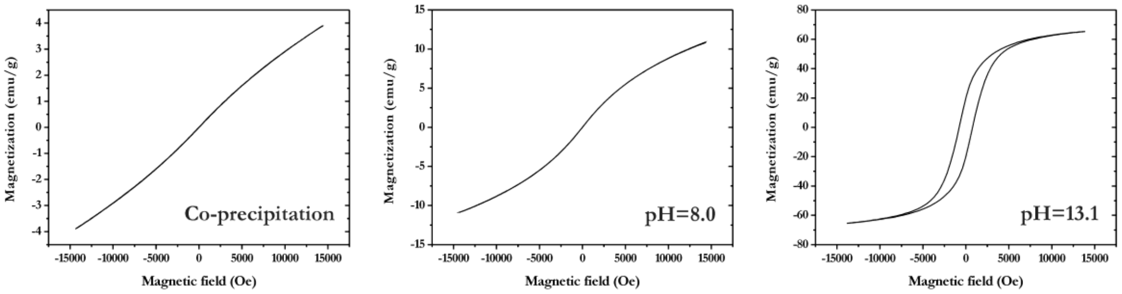

**Figure 3:** Hysteresis loops of the $CoFe_2O_4$ nanoparticles

## 4 Conclusion

The effect of pH on the structural and magnetic properties of the $CoFe_2O_4$ nanoparticles prepared by a combination of the co-precipitation and hydrothermal methods was investigated. The results show that the crystallinity and average particle size increase with the increase of the pH. Also, the values of $M_S$, $M_r$ and $H_C$ follow this trend. The sample prepared at pH=13.1 has the highest values of $M_S$, $M_r$ and $H_C$ (65.4 emu/g, 19.95 emu/g and 775.8 Oe, respectively) and, according to Scherrer's equation, the average crystallite size for the sample with pH=13.1 was estimated to be 15 nm.

## References:

[1]Raul Valenzuela. *Magnetnic ceramics*. Cambridge University Press, 1994.

[2]E. S. Murdock, R. F. Simmons, R. Davidson. Roadmap for 10 Gbit/in$^2$ Media: Challenges. *IEEE Transactions on Magnetics*, 28 (5): 3078-3083, 1992.

[3]S. N. Okuno, S. Hashimoto, K. lnomata. Preferred crystal orientation of cobalt ferrite thin films induced by ion bombardment during deposition. *Journal of Applied Physics*, 71 (12): 5926-5929, 1992.

[4]P. C. Rajath Varma, R. S. Manna, D. Banerjee, M. Raama Varma, K. G. Suresh, A. K. Nigam. Magnetic properties of $CoFe_2O_4$ synthesized by solid state, citrate precursor and polymerized complex methods: A comparative study. *Journal of Alloys and Compounds*, 453(1-2): 298-303, 2008.

[5]M. Kishimoto, Y. Sakurai, T. Ajima. Magneto-optical properties of Ba-ferrite particulate media. *Journal of Applied Physics*, 76 (11): 7506-7509, 1994.

[6]E. Manova, D. Paneva, B. Kunev, Cl. Estournès, E. Rivière, K. Tenchev, A. Léaustic, I. Mitov. Mechanochemical synthesis and characterization of nanodimnsional iron-cobalt spinel oxides. *Journal of Alloys and Compounds*, 485 (1-2): 356-361, 2009.

[7]I. Sharifi, H. Shokrollahi, M. M. Doroodmand, R. Safi, Magnetic and structural studies on CoFe2O4 nanoparticles synthesized by co-precipitation, normal micelles and reverse micelles methods, *Journal of Magnetism and Magnetic Materials*, 324 (10): 1854-1861, 2012.

[8]Q. Liu, J. Sun, H. Long, X. Sun, X. Zhong, Z. Xu. Hydrothermal synthesis of $CoFe_2O_4$ nanoplatelets and nanoparticles. *Materials Chemistry and Physics*, 108 (2-3): 269-273, 2008.

[9] I. H. Gul, A.Maqsood. Structural, magnetic and electrical properties of cobalt ferrites prepared by the sol-gel route. *Journal of Alloys and Compounds*, 465 (1-2): 227-231, 2008.

[10] V. Pillai, D. O. Shah. Synthesis of high-coercivity cobalt ferrite particles using water-in-oil microemulsions. *Journal of Magnetism and Magnetic Materials*, 163 (1-2): 243-248, 1996.

[11] M. Yoshimura, K. Burappa. Hydrothermal processing of materials: past, present and future. *Journal of Materials Science*, 43 (7): 2085-2103, 2008.

[12] Z. Zi, Y. Sun, X. Zhu, Z. Yang, J. Dai, W. Song. Synthesis and magnetic properties of $CoFe_2O_4$ ferrite nanoparticles. *Journal of Magnetism and Magnetic Materials,* 321 (9): 1251-1255, 2009.

## For wider interest

Because of its magnetic and electrical properties, cobalt ferrite is an interesting material. It has a moderate saturation magnetization, a large magnetic anisotropy, a remarkable chemical stability and a mechanical hardness. Because of these properties it can be used for recording media, spintronics, magnetic refrigeration, ferrofluids, magnetic resonance imaging, the delivery of drugs to specific areas of the body, etc. The presented results are part of the project aimed to improve the magnetic properties of cobalt ferrite particles along with the control of particle sizes and their stability, which would enhance the applicability of cobalt ferrite.

# Tempering Effects on the Microstructure, Mechanical Properties and Creep Rate of X20CrMoV121 and P91 Steels

**Fevzi Kafexhiu**[1,2], Franc Vodopivec[1], Jelena Vojvodič – Tuma[2]

[1] Department of Surface Engineering and Applied Surface Science, Institute of Metals and Technology, Ljubljana, Slovenia

[2] Jožef Stefan International Postgraduate School, Ljubljana, Slovenia

fevzi.kafexhiu@imt.si

**Abstract.** The effect of tempering on the microstructure and room-temperature yield stress of the two creep-resistant steels, X20CrMoV121 and P91, was investigated. The samples were tempered for 17520 h at 650 °C and 8760 h at 750 °C. After tempering, the room-temperature yield stress was determined. In addition, the SEM (Scanning Electron Microscopy) imaging on the tempered samples was carried out.

It was found that the effect of tempering at 750 °C on the microstructure and room-temperature yield stress was greater for both steels than the effect of tempering at 650 °C. Changes of yield stress for both steels were found to be mutually very similar; hence a general mathematical expression with specific parameters for both steels and tempering temperatures was deduced. For the samples tempered at 750 °C only, a fairly good correlation between the inter-particle spacing, yield stress and creep rate was observed.

**Keywords**: tempering, microstructure, yield stress, creep rate.

## 1 Introduction

In recent years there has been an increased demand to raise the efficiency of steam power plants for economic and environmental reasons. A straight-forward way to achieve it is to raise the inlet temperature and pressure of the steam that passes the turbines. This directly saves fuel and reduces $CO_2$ emissions [1].

Issues that arise with higher steam temperatures and pressures are largely material related, because at such conditions the microstructure changes with time, and as a result, materials properties change as well. Materials usually employed for power plants with enhanced steam parameters are the 9-12 % Cr steels [2].

A routine checking of materials properties in terms of the residual lifetime after certain periods of operation in power plants is always necessary. A creep test, as one of these routine methods, is expensive and time consuming, so it does not represent a suitable method for the lifetime prediction. Among faster and less expensive methods are room-temperature tensile tests, hardness measurements and microstructure examinations after certain tempering time, simulating changes of microstructure and properties in power plant conditions [3].

## 2 Experimental

Two martensitic creep-resistant 9-12 % Cr steels, X20CrMoV121 and P91, were used in this investigation. The samples were extracted from steam pipelines in the power plant Šoštanj. The samples' chemical composition is given in **Table 1**.

**Table 1:** Chemical composition of the X20 and P91 steels

| Chemical composition, wt % | | | | | | | | | | | | | |
|---|---|---|---|---|---|---|---|---|---|---|---|---|---|
| **Elements** | **C** | **Si** | **Mn** | **P** | **S** | **Cr** | **Ni** | **Mo** | **V** | **Cu** | **Nb** | **Al** | **N** |
| **X20CrMoV121** | 0.2 | 0.29 | 0.52 | 0.019 | 0.011 | 11 | 0.64 | 0.94 | 0.31 | 0.059 | 0.024 | 0.032 | 0.017 |
| **P91** | 0.1 | 0.38 | 0.48 | 0.012 | 0.002 | 7.9 | 0.26 | 0.98 | 0.23 | 0.14 | 0.11 | 0.016 | 0.064 |

The samples of both steels were tempered for 2 h, 4320 h, 8760 h and 17520 h (2 years) at 650 °C and up to 8760 h (one year) at 750 °C.

Static tensile tests at room temperature were performed on specimens extracted from the initial (as-delivered) and tempered material samples.

With the aim to assess the microstructure changes as a function of tempering time and temperature, the SEM specimens were prepared by standard metallographic techniques. The JEOL JSM-6500F Field Emission SEM was used to acquire five images on each specimen at a magnification of 5000×. Images were acquired from the specimens at initial (as-delivered) state and from those tempered up to 8760 h at both 650 °C and 750 °C.

## 3 Results and Discussion

The decrease of the yield stress $\sigma_y$ at both tempering temperatures is very similar for both steels. From the diagrams in Fig. 1 it is obvious that the decrease is more pronounced due to the tempering at 750 °C, where the yield stress $\sigma_y$ drops for 163 N/mm$^2$ and 216 N/mm$^2$ for the X20CrMoV121 and P91 steels, respectively.

In order to express the yield stress decrease analytically, a mathematical expression (Eq. 1) was appropriated. The parameter $k_1$ (Table 2) stands for the yield stress of as-delivered material, whereas using the R-software [4], we estimated the parameter $k_2$ such that, for both steels and tempering temperatures, Eq. 1 provides the closest fit to the experimental data (see Fig. 1).

$$\sigma_y(t) = k_1 - k_2 t^{1/3} \tag{1}$$

**Table 2**: Values of the parameters $k_1$ and $k_2$

| **Parameters** | **X20CrMoV121** | | **P91** | |
|---|---|---|---|---|
| | 650 °C | 750 °C | 650 °C | 750 °C |
| $k_1$ | 527 | | 546 | |
| $k_2$ | 1.44 | 7.68 | 1.2 | 10.23 |

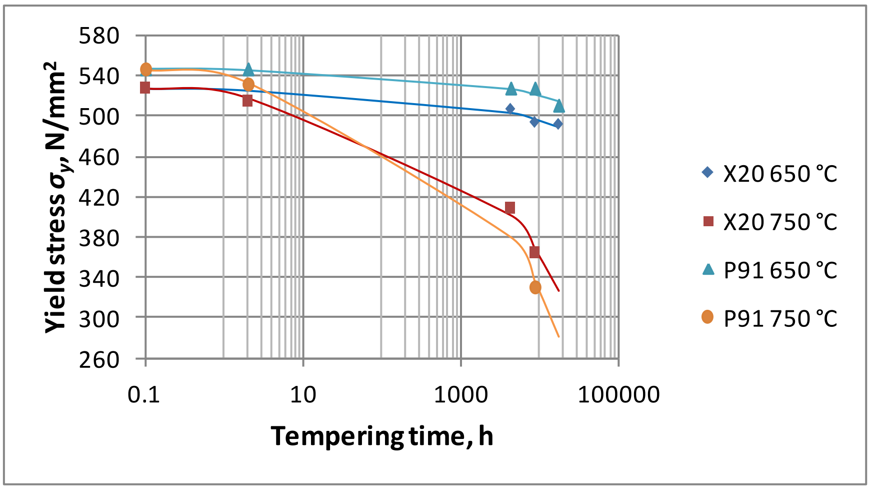

**Fig. 1**: Yield stress of the X20 and P91 steels as a function of tempering.

The SEM images in Fig. 2 indicate the effect of tempering on the size and distribution of carbide particles. Similar to the yield stress, the effect of tempering at 750 °C on the carbide particles is greater compared to the effect of tempering at 650 °C. This is due to the fact that at higher temperatures, the diffusion of alloying elements is faster, accelerating diffusion-related processes in the materials microstructure.

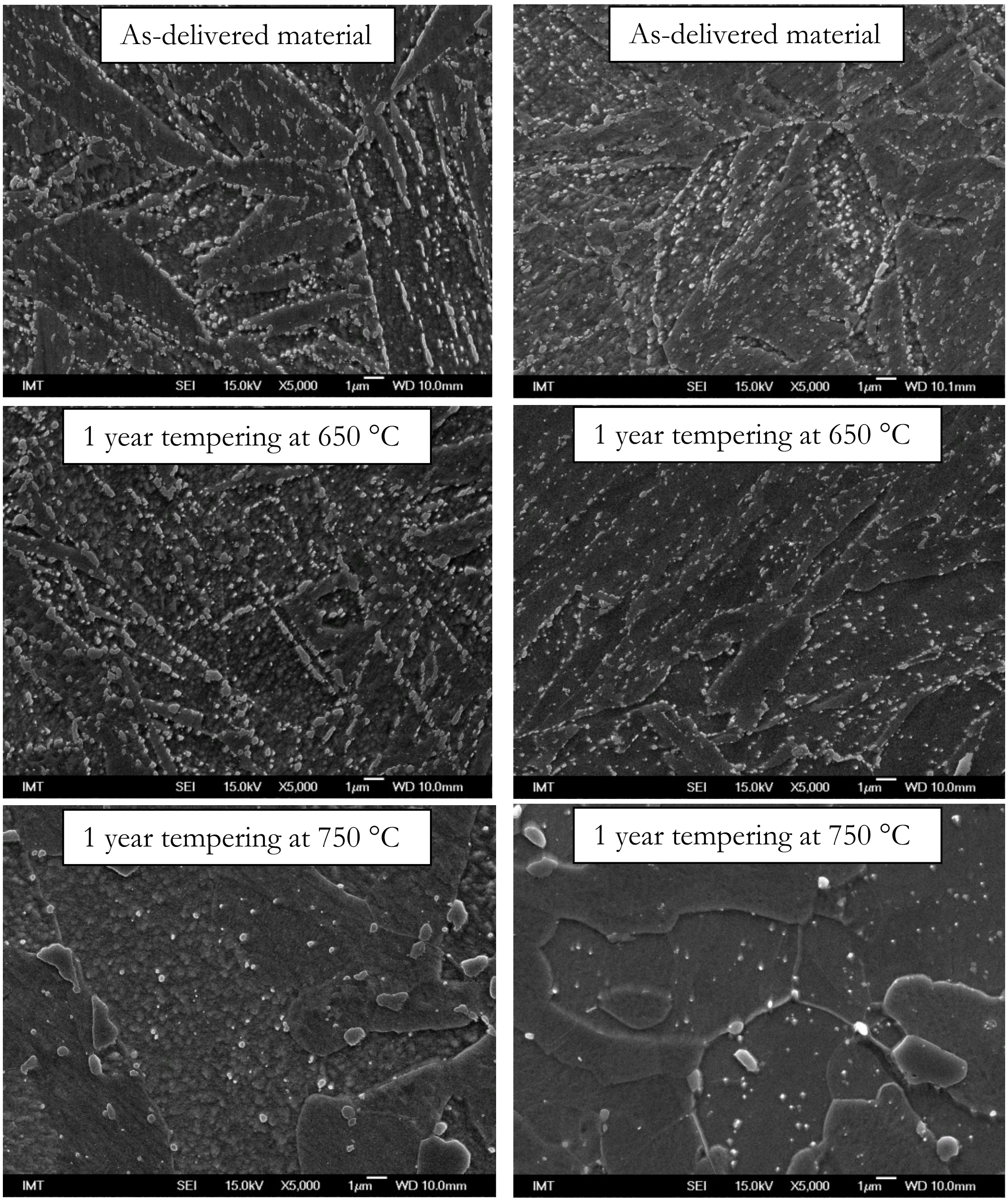

**Fig. 2**: Changes of the microstructure as a function of tempering time and temperature for the steels X20 – left and P91 – right.

The creep rate $\varepsilon'(\lambda)$ given by Eq. 2 [5], is graphically shown in Fig. 4 as a function of yield stress. The inter-particle spacing $\lambda$ is given by Eq. 3 [6] and graphically presented in Fig. 3.

$$\varepsilon'(\lambda) = \frac{b^2 \cdot \lambda \cdot \rho \cdot \sigma^2 \cdot D}{k \cdot T \cdot G_{cT}} \approx 3.69 \cdot 10^{-5} \cdot \lambda \tag{2}$$

$$\lambda = \frac{4d}{\pi \sqrt[3]{f}} \tag{3}$$

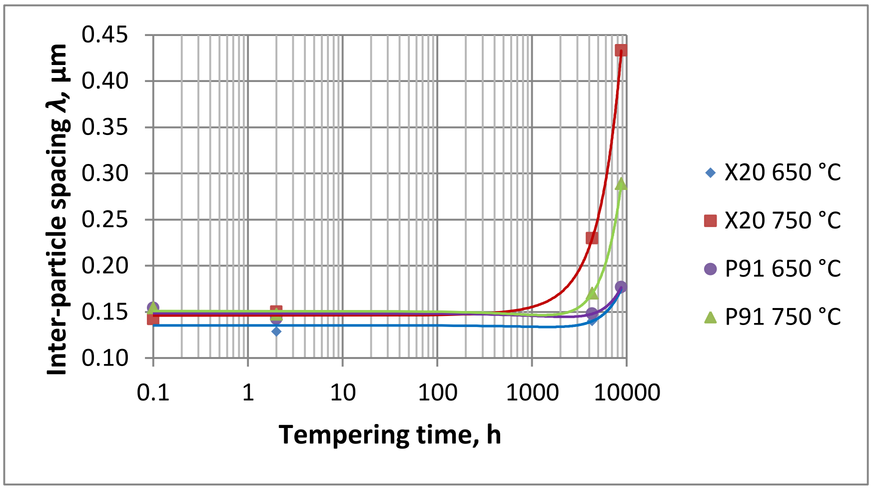

**Fig. 3**: Inter-particle spacing of the X20 and P91 steels as a function of tempering.

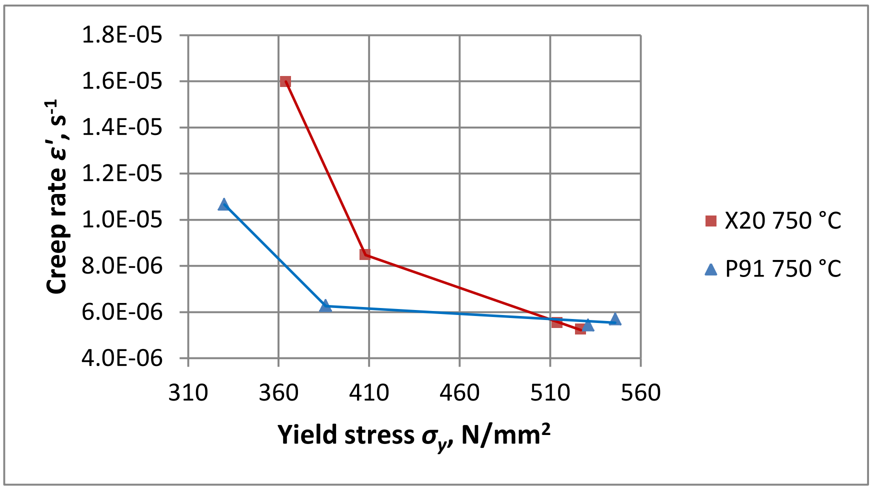

**Fig. 4**: Creep rate of the X20 and P91 steels as a function of measured yield stress.

## References:

[1]J. Hald. Microstructure and long-term creep properties of 9-12% Cr steels. *International Journal of Pressure Vessels and Piping*, 85:30-37, 2008.

[2]F. Abe, T. U. Kern and R. Viswanathan. *Creep Resistant Steels*. CRC Press, Cambridge, 2008.

[3]F. Masuyama, T. Tokumaga, N. Shimahata, T. Yamamoto and M. Hirano. Comprehensive approach to creep life assessment of martensitic heat resistant steels. In *Crceep and Fracture in High Temperature Components*, DEStech Publ. Inc: 19-30, 2009.

[4]The R Project for Statistical Computing. http://www.r-project.org, 2012.

[5]F. Vodopivec, J. V. Tuma, M. Jenko, R. Celin and B. Šuštaršič. Dependence of accelerated creep rate at 580 °C and room temperature yield stress for two creep resistant steels. *Steel Research*, 81(7): 576-580, 2010.

[6]F. Vodopivec, D. Kmetič, J. V. Tuma, D. A. Skobir. Effect of operating temperature on microstructure and creep resistance of X20CrMoV121 steel. *Materiali in Tehnologije*, 38: 233-239, 2004.

## For wider interest

An increased efficiency of the fossil-fired power plants is obtained with higher operating temperatures and pressures of the steam that enters the turbine. The standard operating temperatures are 540-565 °C, but during the last 20 years large efforts have been made to reach the so-called ultra-supercritical (USC) conditions with the steam parameters up to 300 bars and 620 °C. These conditions require materials with the high creep-resistance, i.e., the ability to withstand a long-term loading at high temperatures. This requires a careful material selection and a periodical checking of its properties and remaining residual lifetime after the determined period of operation in power plants. The checking of the creep rate and creep strength is expensive and time-consuming. For this reason, simpler methods are being developed, which use less expensive and faster tests that enable the establishment of the state of the built-in steel. One among these methods is to check the room-temperature mechanical properties and microstructure after tempering, which simulates the changes in the microstructure and properties that occur after a longer operation in the power plant (in real conditions) by correlating the measured properties with the creep rate. The latter is measured using the standard creep test.

# Phase transitions of the $NaNbO_3$ submicron-sized powder between room temperature and 700 °C

**Jurij Koruza**[1,2], **Jenny Tellier**[1,3], **Barbara Malič**[1,2], **Marija Kosec**[1,2]

[1] Electronic Ceramics Department, Jožef Stefan Institute, Ljubljana, Slovenia

[2] Jožef Stefan International Postgraduate School, Ljubljana, Slovenia

[3] SPCTS-UMR CNRS 6638, Centre Européen de la Céramique, Limoges, France

`jurij.koruza@ijs.si` (email of corresponding author)

**Abstract.** Phase transition behaviour of the *Q* polymorph, which was found in the submicron-sized $NaNbO_3$ powder, was investigated in the temperature range between room temperature and 700°C. The differential scanning calorimetry revealed three phase transitions upon heating: *Q*→*R* (326.5°C), *T(1)*→*T(2)* (571°C), and *T(2)*→*U* (636.8°C). A detailed X-Ray diffraction measurement combined with the Rietveld analysis was used to determine the structural changes during the *Q*→*R* phase transition. The observed symmetrisation of the unit cell was related to the increased regularity of the cuboctahedral cavities and the position of the Na cation.

**Keywords**: sodium niobate, antiferroelectrics, phase transition, polymorphism.

## 1 Introduction

Antiferroelectric ceramics have gained increased attention due to their large energy storage capacity, required for high-performance capacitors [1], and a large volume change accompanying the field-induced phase transition, which may be used in high-strain actuator and transducer applications [2]. Sodium niobate ($NaNbO_3$) is a prototype antiferroelectric. Furthermore, $NaNbO_3$ also exhibits the largest number of polymorphs[*] among all oxygen perovskites (Figure 1). The phase transitions in

---

[*] The term polymorphism describes the relations among different crystalline modifications (polymorphs) of the same chemical substance, which typically possess different physical properties. This phenomenon was observed in many technologically important ceramic materials, such as $ZrO_2$, $Al_2O_3$, $SiO_2$.

$NaNbO_3$ can be induced by the temperature [3], by the electric field [4], and, as indicated recently, also by the particle size [5, 6]. It is important to note that both room temperature (RT) polymorphs exhibit different electrical states: the *P* polymorph is antiferroelectric, while the *Q* polymorph is ferroelectric. The phase transition temperatures, reported in the literature, range from 270°C [7] up to 333°C [8], and almost no structural data about his phase transitions exist. Since the electrical characteristics of $NaNbO_3$, which are of interest for potential applications, vary between different polymorphs, further knowledge of the polymorphism is required. The aim of the present work was therefore to study the phase transition behaviour of the *Q* polymorph upon heating.

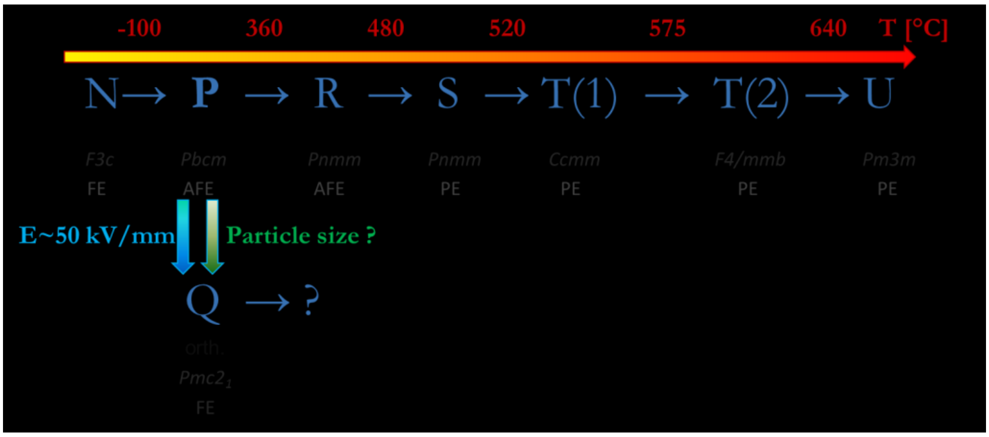

**Figure 1**: Phase transitions of $NaNbO_3$ after ref. [3, 4]. The blue letters denote the known polymorphs; the crystal system, space group, and electrical state are listed below (FE-ferroelectric, AFE-antiferroelectric, PE-paraelectric).

## 2 Experimental work

A single phase $NaNbO_3$ powder was prepared using the conventional solid state synthesis with double calcination at 700°C, 4 h. The details of the synthesis can be found elsewhere [6]. The obtained median particle size was 0.34 μm, as determined from the area distribution measured by a laser granulometer (Microtrac S3500). The X-ray diffraction (XRD) patterns were recorded with the angular 2θ range of 10°-90°, using a 0.026° step and 100 s/step, on a X'Pert PRO diffractometer (PANalytical). The crystal structure analysis was performed by the Rietveld method, using the JANA2006 software [9]. The differential scanning calorimetry (DSC) curves of the powder sample were recorded with a temperature ramp of 2 K/min using a Pt crucible and a DSC 204 F1 calorimeter (Netzsch).

## 3 Results and discussion

Using the crystallographic card 01-082-0606, the peaks of the RT XRD pattern of the as-synthesized $NaNbO_3$ powder were fitted with the space group $P2_1ma$ [10], which indicates the presence of the *Q* polymorph (Figure 2). This result is in agreement with that of Shiratori *et al.*, who reported the same space group for the submicron-sized $NaNbO_3$ powder [5].

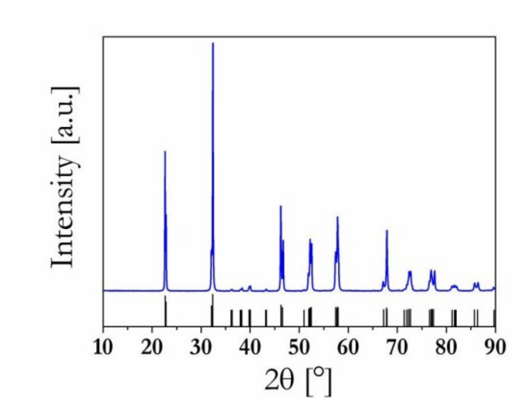

**Figure 2**: The XRD pattern of the $NaNbO_3$ submicron-sized powder at RT. The set of black tick marks corresponds to the reflections of the *Q* polymorph [10].

As indicated in the introduction section, little is known about the behaviour of the *Q* polymorph at temperatures above RT. In order to determine the phase transition temperatures we first performed a DSC analysis of the $NaNbO_3$ powder and the result is presented in Figure 3. Three anomalies were observed in the heating curve. The upper two were connected to the well-known phase transitions *T(1)→T(2)* at 571°C and *T(2)→U* at 636.8°C. Another anomaly was detected at 326.5°C. This temperature is close to the transition temperature of the *Q* polymorph reported by Shiratori *et al.* [8]. However, the DSC method does not give any information regarding the structure changes of the *Q* polymorph upon heating.

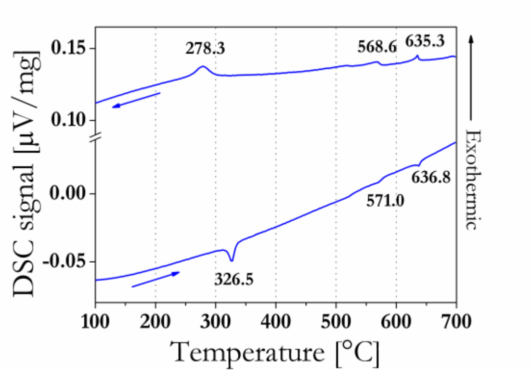

**Figure 3**: The DSC curve of the $NaNbO_3$ submicron-sized powder upon heating and cooling. The numbers indicate the phase transition temperatures.

In order to investigate the structural behaviour of the *Q* polymorph upon heating, we performed a detailed high-temperature XRD analysis between RT and 350°C with a step of 15°C. As an example, the evolution of the (202) and (040) diffraction peaks upon heating is presented in Figure 4a. These results were used to calculate the unit cell parameters and volumes for each temperature (Figure 4b). The unit cell parameters increase with a constant rate up to 265°C due to the thermal expansion. Above this temperature the values of the cell parameters *b* and *c* start to decrease, and consequently the cell volume decreases. Another change in the slope of the cell volume curve was observed at 325°C. This temperature is in a good agreement with the transition temperature, observed in the DSC curve (326.5°C).

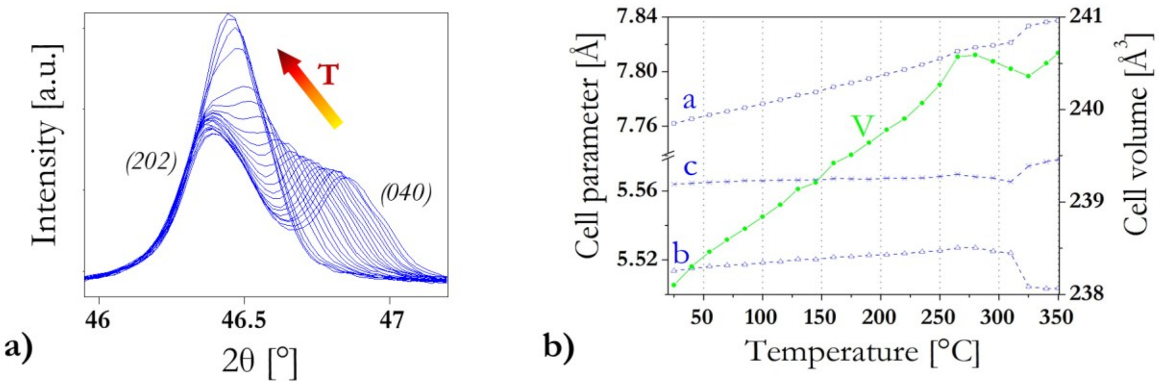

**Figure 4**: Evolution of the (202) and (040) XRD peaks (a), and the changes of the unit cell parameters and cell volume (b) upon heating from RT to 350°C.

In order to reveal the high temperature structure of the investigated $NaNbO_3$ powder, we used the Rietveld refinement method to calculate the structure parameters. We were able to refine the RT structure with the $Pmc2_1$ and the 420°C structure with the *Pmmn* space group. The calculated structures are presented in Figure 5. At RT the distortion of the structure is high: the oxygen octahedra are tilted in three directions and the Na cation is displaced in the *y-z* plane. Upon heating the symmetry of the structure increases; the Na cation is placed in the center of the *x-y* plane and only a slight displacement in the *z* direction is observed. The cuboctahedral cavities are more regular, which is the main reason for the observed symmetrisation of the unit cell.

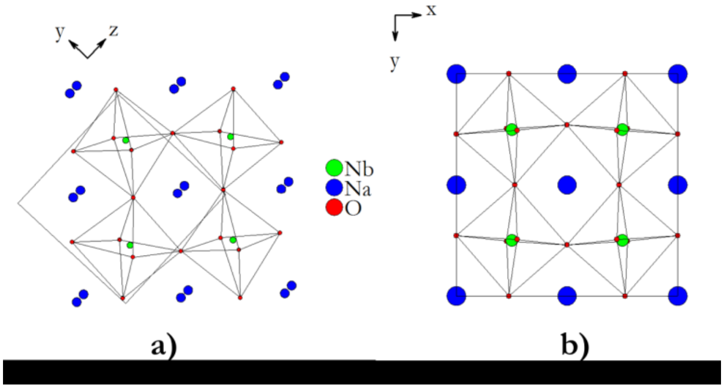

**Figure 5**: The calculated structures of the $NaNbO_3$ submicron-sized powder at room temperature (a) and 420 °C (b). Note that due to the difference in space groups different views were chosen for the sake of comparison.

## 4 Conclusion

Phase transition behaviour of submicron-sized $NaNbO_3$ powder was investigated using the DSC and XRD. Three anomalies were found in the DSC curve upon heating: *Q→R* (326.5°C), *T(1)→T(2)* (571°C), and *T(2)→U* (636.8°C). The structural changes during the *Q→R* transition were investigated using the XRD, and the increased symmetrisation of the structure was related to the increased regularity of the cuboctahedral cavities and displacement of the Na cation.

## Acknowledgments

This work was supported by the Slovenian Research Agency (contr. nr. 1000-08-310121; P2-0105). The authors would like to thank to Jena Cilenšek (DSC), Edi Kranjc (XRD), and Dr. Tadej Rojac.

# References

[1] N. H. Fletcher, A. D. Hilton, and B. W. Ricketts. Optimization of energy storage density in ceramic capacitors. *Journal of Physics D-Applied Physics*, 29(1): 253-258, 1996.

[2] W. Y. Pan, C. Q. Dam, Q. M. Zhang, and L. E. Cross. Large Displacement Transducers Based on Electric-Field Forced Phase-Transitions in the Tetragonal $(Pb_{0.97}La_{0.02})(Ti,Zr,Sn)O_3$ Family of Ceramics. *Journal of Applied Physics*, 66(12): 6014-6023, 1989.

[3] H. D. Megaw. 7 Phases of Sodium Niobate. *Ferroelectrics*, 7(1-4): 87-89, 1974.

[4] L. E. Cross, and B. J. Nicholson. LV. The optical and electrical properties of single crystal of sodium niobate. *Philosophical Magazine*, 46(376): 453-466, 1955.

[5] Y. Shiratori, A. Magrez, J. Dornseiffer, F. H. Haegel, C. Pithan, and R. Waser. Polymorphism in micro-, submicro-, and nanocrystalline $NaNbO_3$. *Journal of Physical Chemistry B*, 109(43): 20122-20130, 2005.

[6] J. Koruza, J. Tellier, B. Malic, V. Bobnar, and M. Kosec. Phase transitions of sodium niobate powder and ceramics, prepared by solid state synthesis. *Journal of Applied Physics*, 108(11), 2010.

[7] R. H. Dungan, Golding, R. D. Metastable Ferroelectric Sodium Niobate. *Journal of the American Ceramic Society*, 47(2): 73-76, 1964.

[8] Y. Shiratori, A. Magrez, W. Fischer, C. Pithan, and R. Waser. Temperature-induced Phase Transitions in Micro-, Submicro-, and Nanocrystalline $NaNbO_3$. *The Journal of Physical Chemistry C*, 111(50): 18493-18502, 2007.

[9] V. Petricek, and M. Dusek, *The Crystallographic Computing System JANA2006*, 2006, Institute of Physics, Academy of Scienecs of the Czech Republic: Prague.

[10] V. A. Shuvaeva, M. Y. Antipin, R. S. V. Lindeman, O. E. Fesenko, V. G. Smotrakov, and Y. T. Struchkov. Crystal structure of the electric-field induced ferroelectric phase of $NaNbO_3$. *Ferroelectrics*, 141(1): 307-311, 1993.

## For wider interest

The functional properties of ceramic materials directly depend on their crystal structure, which changes upon changing the temperature. Therefore the understanding of the crystal structure and the phase transitions is of great importance when the materials are to be used in devices for various applications.

In the present work we demonstrate the implementation of the two complementary analytical techniques for investigation of phase transitions and crystal structure of materials: the differential scanning calorimetry (DSC) and the X-Ray diffraction (XRD) combined with the Rietveld analysis. The first one was used to determine the transition temperatures, while the second one enabled the insight into the crystal structure of the material.

# Environmental Friendly Potassium Sodium Niobate Based Thin Films from Solutions

**Alja Kupec**[1,2,3] **Barbara Malič**[1,3,4,5] **and Marija Kosec**[1,2,3]

[1] Electronic Ceramics Department, Jožef Stefan Institute, Ljubljana, Slovenia

[2] Centre of Excellence NAMASTE, Ljubljana, Slovenia

[3] Jožef Stefan International Postgraduate School, Ljubljana, Slovenia

[4] Centre of Excellence on Nanoscience and Nanotechnology, Ljubljana, Slovenia.

[5] Centre of Excellence SPACE-SI, Ljubljana, Slovenia.

alja.kupec@ijs.si

**Abstract.** We present the synthesis of ~250 nm thick $K_{0.5}Na_{0.5}NbO_3$ thin films on platinized silicon substrates from alkoxide-based solutions with the stoichiometric composition and with the 5 or 10 mole % potassium acetate excess. The films crystallized into a pure perovskite phase, but depending on the amount of the alkali excess in solutions, they consisted of ~50 nm or of ~200 nm large grains. The fine-grained film from the solution with the 5 mole % alkali excess had the dielectric permittivity and losses of 610 and 1.5 %, respectively, and exhibited a ferroelectric polarisation–electric field dependence at room temperature.

**Keywords**: Chemical Solution Deposition, Thin film, Lead-free, Ferroelectric

## 1 Introduction

In the field of piezoelectric materials, lead-based complex perovskite systems are widely used due to their good functional response. The main drawback of these materials is the toxicity of lead compounds and, as a consequence, the research of environmentally friendly ceramic materials has been intensified in the last years.

Potassium sodium niobate $(K_xNa_{1-x})NbO_3$ has been considered as one of the candidates that could replace lead based perovskites. It is a solid solution of ferroelectric $KNbO_3$ and antiferroelectric $NaNbO_3$ with the best dielectric and piezoelectric properties near x = 0.5 (KNN).[1] The major problems related to this material are the humidity, sensitivity and volatilization of alkali compounds, which hinder the control over the composition and may contribute to a major reduction of its functional properties.

In the Chemical Solution Deposition of thin films, the alkali losses can be compensated by adding the alkali excess to the starting solution. Based on the reports in the literature, the alkali excess may not be needed or it ranges from up to 10 % to as much as 20 %, depending on the synthesis, deposition and further heating conditions.

In order to study the influence of different amounts of the K- excess in solutions on the formation and functional response of the films, we deposited the KNN thin films from alkoxide based solutions with the 0.5/0.5/1, 0.5/0.55/1 and 0.5/0.6/1 Na/K/Nb ratios, respectively.

## 1 Experimental

High purity potassium acetate ($KO_2C_2H_3$, 99+%, Sigma Aldrich), sodium acetate ($NaO_2C_2H_3$, 99.5%, Fluka), and niobium pentaethoxide ($Nb(OCH_2CH_3)_5$, 99.99%, Starck) were weighted in a stoichiometric ratio and dissolved in 2-methoxyethanol. Upon a 4 h reflux and distillation, the solution concentration was adjusted to 0.4 M and 0, 5 or 10 mole % of the potassium-acetate excess was added to the solutions, further denoted as *Stoich, +5K* and *+10K*, respectively. Due to the sensitivity of the starting reagents to the moisture, the solution synthesis was performed in a dry nitrogen atmosphere. The ~240 nm thick films on a platinized silicon substrate (or Pt/Si) were processed by a repeated spin coating and pyrolysis at 300 °C, 2 min, followed by final annealing at 750 °C for 5 minutes, in synthetic air with the heating rate of 10 K/s. The crystalline structures of the films were investigated by the X-ray powder diffraction (PANalyticalX`Pert PRO MPD) and the microstructure was analysed by the scanning electron microscopy (FE-SEM: Supra 35 VP, Carl Zeiss). For the electric characterization of the thin films, Cr/Au top electrodes with the diameter of 0.4 mm were applied through a shadow mask by sputtering and post annealed at 400 °C, for 15 minutes. The room temperature dielectric properties (impedance analyzer HP 4192A) and the polarisation versus electric field dependence (AixACCT TF Analyzer 2000) were measured at 300 K. Further details on the processing and characterization methods can be found elsewhere.[2]

## 2 Results

Fig. 1 shows that upon heating to 750 °C all films crystallized in a pure perovskite phase, regardless the solution chemistry. The asymmetric shape of the peaks in the *Stoich* KNN film reveals a decreased symmetry of the unit cell. The ratio of relative intensities between {100} and {110} diffraction peaks is inversed in comparison to the XRD pattern of the randomly oriented powder [3], meaning that the film crystallized with the preferential {100} orientation. A similar XRD pattern was obtained for the *+5K* film. The *+10K* KNN film also crystallized with the preferential {100} orientation, but the splitting of the {h00} diffraction peaks at ~22° and ~45° 2Θ indicated a pronounced monoclinic distortion of the unit cell (characteristic of KNN) and increased crystallite sizes as compared to the *Stoich* and *+5K* KNN films.

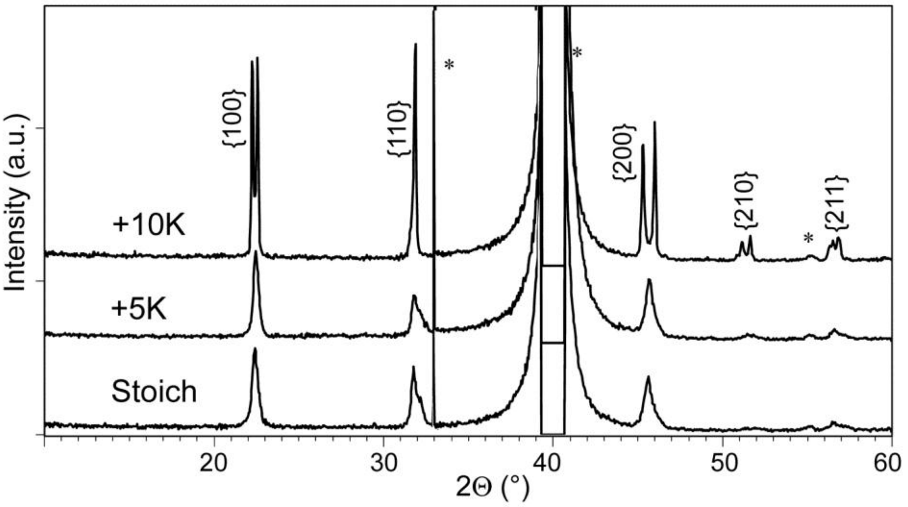

**Figure 1**: XRD diffraction patterns of the KNN films prepared from solutions with different amounts of potassium acetate excess.* Substrate.

The cross sectional and surface microstructures of the films obtained by FE-SEM are presented in Fig. 2. The microstructure of the ~250 nm thick *Stoich* film consisted of ~50 nm large equiaxed grains. The *+5K* film had a similar microstructure, but with a much more uniform grain size distribution. In contrast, the *+10K* film consisted of large grains of cuboidal shape with only one grain per thickness across.

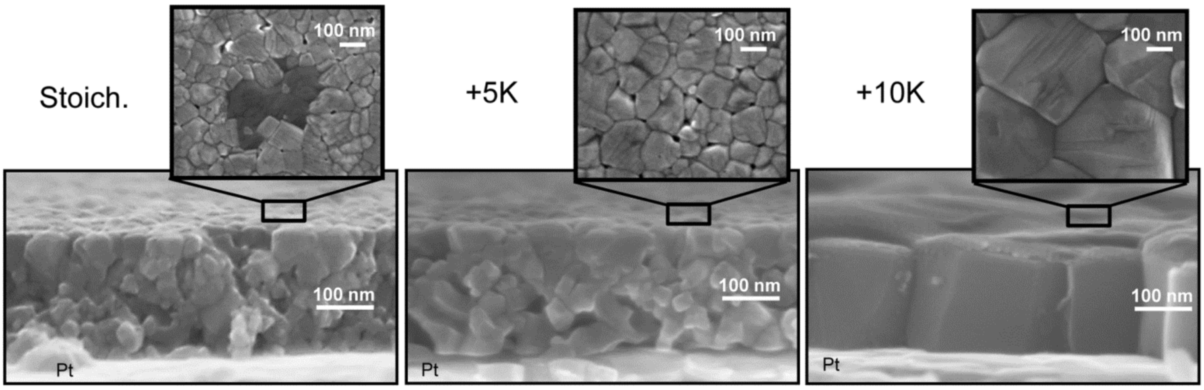

**Figure 2**: The cross-sectional and surface view of the Stoich., +5K and +10K KNN films.

Table 1 shows that the room temperature dielectric permittivity ε′ in *Stoich* and *+5K* films are 490 and 610, respectively, at 1 kHz, and this value slightly decreases with the increasing frequency. In both films, the losses are lower than 1.6 % in the measured frequency range. The dielectric properties values are in agreement with other reports on KNN thin films.[4] Only poor dielectric properties with high losses were measured in the *+10K* film, which could be related to the film microstructure. Namely, the grain boundaries, that could provide conduction pathways, are extending across the whole thickness of the film.

**Table 1**: Room temperature dielectric properties of the *Stoich* and *+5K* KNN films at 1, 10 and 100 kHz.

| Frequency (kHz) | S*toich.* | | +5K | |
|---|---|---|---|---|
| | $\varepsilon'$ | *tan* $\delta$ | $\varepsilon'$ | *tan* $\delta$ |
| 1 | 490 | 0.015 | 610 | 0.016 |
| 10 | 480 | 0.012 | 590 | 0.015 |
| 100 | 475 | 0.012 | 580 | 0.015 |

The Polarisation-electric field measurements (P-E) of the *Stoich*, *+5K* and *+10K* films at 300 K and 1 kHz are collected in Fig. 3. The remnant polarisation (Pr) and coercive field (Ec) of the *Stoich* KNN film are 5 μC/cm$^2$ and 100 kV/cm, respectively. The ferroelectric properties are slightly improved in the *+5K* film, reaching the values of the remnant polarisation and coercive field of 8 μC/cm$^2$ and 80 kV/cm, respectively. As expected from the low-field response, the *+10K* film exhibited a leaky P-E dependence. Wang et al. obtained the values of Pr = 16 μC/cm$^2$ and Ec = 42 kV/cm in about 3500 nm thick KNN films [5], what suggests that the thickness increasing of the *+5K* film could be advantageous.

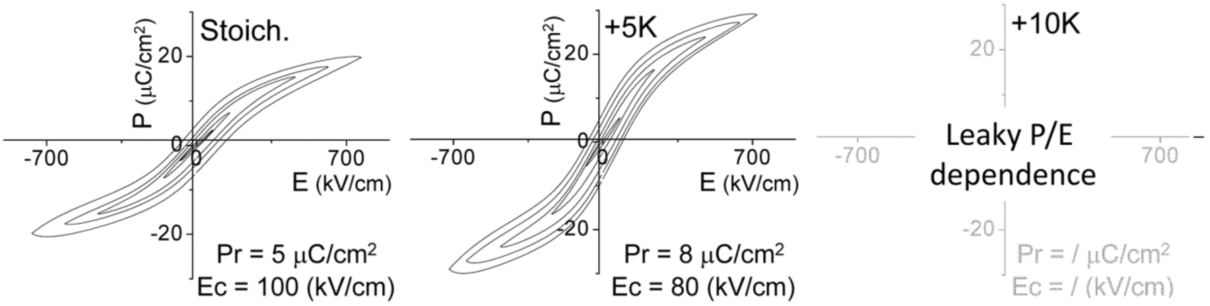

**Figure 3**: The polarization versus electric field dependence of the KNN films at 1 kHz and at 300 K.

## 3 Summary

Upon a rapid thermal annealing at 750 °C, single phase KNN thin films were prepared from the acetate-alkoxide based solutions with the stoichiometric composition and with the 5 or 10 mole % potassium acetate excess.

The amount of the potassium excess in solutions contributed to the final properties of the investigated films. The film from the solution with a larger amount of the alkali excess had a columnar microstructure, which consisted of about 200 nm large grains of a cuboidal shape. The grain boundaries extended across the whole thickness of the film and could therefore provide a conduction pathway and contribute to poor dielectric properties. In contrast, the films from the stoichiometric and from the 5 mole % potassium excess solutions, consisted of ~50 nm large equiaxed grains. The addition of a small amount of the potassium excess to the solution, contributed to a more homogeneous microstructure and to a slightly improved functional response. The ~250 nm thick film prepared from the 5 mole % potassium excess solution had the room temperature values of dielectric permittivity, dielectric losses, remnant polarization and coercive field at 1 kHz equal to 610, 0.015, 8 μC/cm$^2$ and 80 kV/cm, respectively.

## References:

[1] Y. Saito; H. Takao; T. Tani, et al. Lead-free Piezoceramics. *Nature,* 432: 84-87, 2004.

[2] A. Kupec; B. Malič; J. Tellier, et al. Lead-free Ferroelectric Potassium Sodium Niobate Thin Films from Solution: Composition and Structure. *Journal of the American Ceramic Society,* 95: 515-523, 2012.

[3] J. Tellier; B. Malič; B. Dkhil, et al. Crystal Structure and Phase Transitions of Sodium Potassium Niobate Perovskites. *Solid State Sciences,* 11: 320-324, 2009.

[4] K. Tanaka; H. Hayashi; K. I. Kakimoto, et al. Effect of (Na,K)-excess Precursor Solutions on Alkoxy-derived (Na,K)$NbO_3$ Powders and Thin Films. *Japanese Journal of Applied Physics,* 46: 6964-6970, 2007.

[5] L. Wang; K. Yao; P. C. Goh, et al. Volatilization of Alkali Ions and Effects of Molecular Weight of Polyvinylpyrrolidone Introduced in Solution-derived Ferroelectric $K_{0.5}Na_{0.5}NbO_3$ Films. *Journal of Materials Research,* 24: 3516-3522, 2009.

## For wider interest

Piezoelectric ceramic materials are used as sensors, actuators and micro-electro mechanical devices (MEMS). The continuous trend in miniaturization of micromechanic and microelectronic components has provided applications for thin films: the nanomaterials with thicknesses of less than 1 μm.

The properties of thin film-structures often differ from those of bulk ceramics and need to be understood in order to produce new devices. Thin films can be prepared by dry (physical) and wet (chemical) techniques. The former enable the preparation of high quality thin films but with an expensive equipment, while the latter are relatively quick, inexpensive and offer a good variety of possibilities for an easy modification of the composition for improvements in structure properties of functional thin films.

The basic steps of Chemical Solution Deposition (CSD) of thin films include the synthesis of the precursor solution, the deposition of the solution on the substrate, and the heat treatment of the deposited film. Among CSD, the alkoxide based sol-gel route enables the synthesis of different heterometallic solutions and gives the possibility to tailor the reactivity of the starting compounds. The detailed investigations of impacts of precursor solutions, nucleation and growth of the microstructure have led to increase the variety of materials systems that can be prepared and to tremendous improvements in the quality of the films.

The lead zirconate titanate based solid solutions ($Pb(Zr,Ti)O_3$, PZT) are among the most widely studied materials for piezoelectric thin films. However, in the past years the research of lead-free ceramic materials intensified as a consequence of the increased awareness of the society towards the protection of the environment and human health from a hazardous substance, lead.

# The Effect of the Firing Temperature on the Properties of LTCC

**Kostja Makarovič**[1,3,*], **Anton Meden**[2,3], **Marko Hrovat**[1,3], **Janez Holc**[1,3], **Andreja Benčan**[1,3], **Aleš Dakskobler**[1,3], **Darko Belavič**[1,3,4], **Marija Kosec**[1,3]

[1] Jožef Stefan Institute, Jamova 39, SI-1000 Ljubljana, Slovenia

[2] University of Ljubljana, Faculty of Chemistry and Chemical Technology, Aškerčeva cesta 5, SI-1000 Ljubljana, Slovenia

[3] CoE NAMASTE, Jamova 39, SI-1000 Ljubljana, Slovenia

[4] HIPOT-RR, Šentpeter 18, 8222 Otočec, Slovenia

*`kostja.makarovic@ijs.si`

**Abstract.** The influence of the firing temperature on the phase composition, microstructure and biaxial flexural strength of the DuPont 951 low temperature cofired ceramics (LTCC) material is presented. During the firing at temperatures around 700 °C, $Al_2O_3$ starts to partially dissolve in a low viscosity glass phase and the dissolution continues up to 800 °C. The anorthite phase starts to crystallize at 875 °C from the glass phase on the surface of the $Al_2O_3$ particles. The mass fraction of the anorthite increases with increasing temperature until it reaches a plateau value of around 22 w.% at 950 °C or higher temperatures. The biaxial flexural strength of the LTCC increases with increasing firing temperature from 135 MPa (at 800 °C) to around 214 MPa (at 850 °C). In this temperature range the major effect on the biaxial flexural strength of the LTCC is that of porosity. Further, increase of the biaxial flexural strength of the LTCC up to around 300 MPa is correlated with the crystallization of the anorthite.

**Keywords**: LTCC, firing temperatures, phase composition, biaxial flexural strength, anorthite.

## 1 Introduction

The low temperature cofired ceramics (LTCCs) technology is used for substrates in multilayer ceramic circuits, mainly for telecommunications, automotive, and medical applications. In recent times LTCCs were also recognized as useful materials for producing complex 3D structures with buried cavities and channels or so-called micro-electro-mechanical systems (MEMS).[1]

The majority of LTCCs are glass-ceramics composites. These glass-ceramic composites are usually designed to yield partial glass crystallization during the firing, which then minimizes the amount of glass the phase in the composite and influences the mechanical and electrical properties of the glass-ceramic material. Driven by the needs of the target application, the interactions of different glasses with ceramic fillers during firing as well as the phases, which crystallize from the glasses, were extensively studied.[1-3]

The main physical properties of commercially available LTCCs processed, using the parameters, which are specified by the producer, are available in datasheets and other open literature. However, the production of large or complex 3D LTCC structures requires a different, rather longer, firing procedure [4]. Unconventional firing processes affect the final functional properties of the LTCC material. To the best of our knowledge there is not much data available in the open literature about the influence of different firing conditions, such as a firing temperature, on the microstructure, phase composition, and, consequently, on the functional properties of the LTCC.

## 2 Experimental

For the investigation the mostly used commercial LTCC DuPont® Green Tape™ 951[5] was chosen. The green thickness of the used tape was 254 μm. Thicker samples were prepared by laminating the tapes at a pressure of 20 MPa at 80 °C for 15 minutes and cutting with a blade cutter.

The samples were heated at a heating rate of 7 K/minute to 450 °C and held there for 60 minutes at 450 °C to burn out the organic binder. Further, heating to the maximum temperature and cooling to room temperature was performed at a rate of 10 K/minute. The maximum temperatures were 600 °C, 700 °C, 750 °C, 800 °C, 850 °C, 875 °C, 900 °C, 950 °C and 1000 °C with a dwell time of 15 minutes.

To determine the phase composition, the fired samples were ground and analysed with a PANalytical X'Pert PRO MPD X-ray diffractometer (Almelo, Netherland). The XRD diffractometer was operated with a Cu $K_{\alpha 1}$ configuration using a wavelength of 1.54060 Å in the angle 2θ range between 10 ° and 70 °, a step of 0.034 ° and an integration time of 100 s. The ground samples were analyzed in a $\Phi$ = 27 mm holder with a powder depth of 2.5 mm. The analyses of the diffraction patterns and the search-match analyses were performed using a PANalytical X'pert HighScore version 2.1.2 software, PANalytical (Almelo, Netherland) using the PDF database 2004.

A quantitative phase analysis of the ground, fired samples was performed using a Rietveld refinement. The 30 w. % of ZnO (Alfa Aeser, Puratronic, 99.9995 %, Alfa Aeser, Karlsruhe, Germany) was added as an internal standard. The structural parameters used for the Rietveld refinement were obtained using the FindIt version 1.4.4 software, ICSD (Karlsruhe, Germany) and the database ICSD version 2010-1. The Rietveld refinements were performed on X-Ray diffraction patterns with the Bruker AXS Topas version 2.1 software, Bruker, (Karlsruhe, Germany). For the refinement the structures for $Al_2O_3$ (ICSD 73725), ZnO (ICSD 34477) and anorthite (ICSD 34667) were used.

The microstructures of the samples were characterized by using a Field-Emission Scanning Electron Microscope JSM-7600F (FEG-SEM).

The biaxial flexural strengths were measured on 10 replicas using a ball-on-three-balls (B3B) test with an Instron 1362 instrument equipped with a 5-kN load cell. The circular samples with a diameter of 17 mm were prepared by the lamination of three tapes and fired at temperatures above 750 °C.

## 3 Results and discussion

A quantitative phase analysis was performed on samples fired at different temperatures using a Rietveld refinement of the X-ray diffraction patterns. The results are shown in Figure 1. The samples fired at 600 °C and 700 °C consist only of $Al_2O_3$ (51 w.%) and the glass phase (49 %). After firing at 750 °C and 800 °C the amount of $Al_2O_3$ decreases and, consequently, the amount of the glass phase increases. At 800 °C, the amount of $Al_2O_3$ decreased to 41 w.% and the amount of glass phase increased by ~ 10 w.% to a 59 w.%, indicating that $Al_2O_3$ is partially dissolved into the glass phase. Above 800 °C, the $Al_2O_3$ mass fraction remains constant. The anorthite phase appears at 875 °C and its amount is increasing with increasing firing temperature at the expense of lowering the amount of the glass phase until it reaches the plateau value of 22 % at temperatures of 950 °C and 1000 °C. In the same temperature range the amount of glass phase decreases from 59 w.% at 875 °C to 38 w.% at 950 °C. The sintering curve of the investigated LTCC is also shown in Figure 1. From there we can see that the densification starts at ~650 °C and the final shrinkage of approximately 13 % is reached at ~850 °C. By comparing the sintering curve with the XRD results, the start of the partial dissolution of $Al_2O_3$ can be correlated with the occurrence of the “liquid glass” at 650 °C. As is known from the literature, the LTCC starts densifying at the temperature where the viscosity of the glass phase decreases sufficiently, i.e., at the temperature where the “liquid glass” is formed [6, 7]. Above this temperature the viscous flow assists the further sintering of the LTCC.

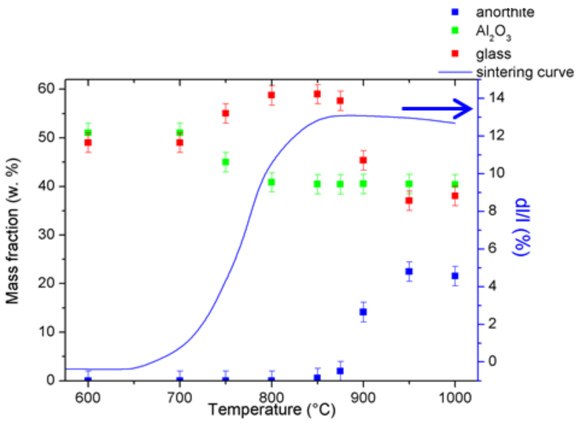

**Figure 1.** A quantitative phase analysis versus the firing temperature for the LTCC material, for the firing time of 15 minutes. The sintering curve presented as a blue line is added in the same graph.

The SEM analysis of the LTCC, using backscattered electrons (BE) was performed. In Figure 2 the SEM microstructures of the samples fired at 800, 875 and 1000 °C for 15 minutes are shown. The studied LTCC is composed of the $Al_2O_3$ phase (dark-grey particles) and the glass (bright matrix). The black round inclusions are pores. The brighter, small particles are $CoAl_2O_4$, which is added to the material for its characteristic blue colour.[8] In the sample fired at 875 °C a light-grey anorthite phase nucleates and crystallizes on the $Al_2O_3$ particles, and the amount of this phase increases, with the firing temperature (1000 °C). The results of the microstructure analysis are qualitatively consistent with the XRD results, showing an increased amount of anorthite with the increasing temperature.

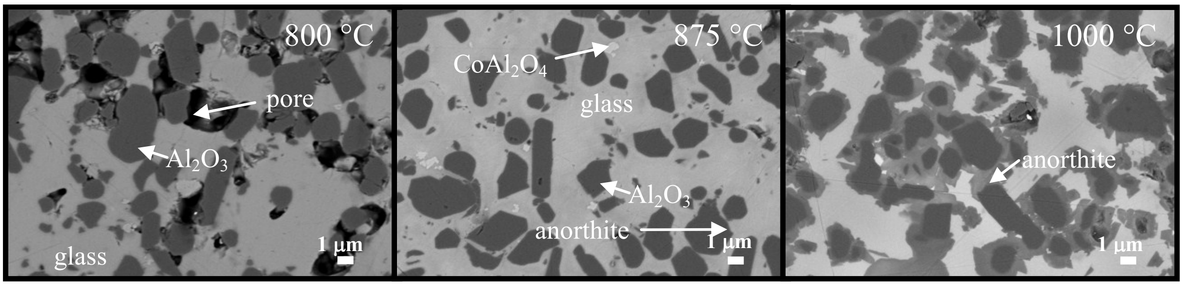

**Figure 2.** SEM microstructures of the samples fired at 800, 875 and 1000 °C for 15 minutes.

The influence of the firing temperature on the flexural strength was studied using the ball-on-three-balls method (Figure 3). The biaxial flexural strength presented in Figure 3 of the LTCC material fired at 800 °C is around 135 MPa and rises to ~ 220 MPa at 850 °C. In this temperature range the major effect on the biaxial flexural strength of the LTCC is that of porosity. The additional increase of the biaxial flexural strength up to ~300 MPa was obtained between 850 and 900 °C. In the material fired at higher temperatures only small, if any, improvement of biaxial flexural strength was observed.

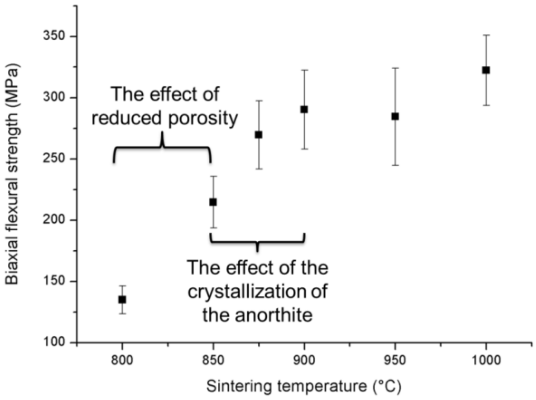

**Figure 3.** Biaxial flexural strengths of the LTCC material fired for 15 minutes at different temperatures, showing the region where strength is basically controlled by the porosity and anorthite, respectively.

## 4 Conclusions

Since the different firing procedures play a crucial part in the processing of large or complex 3D LTCC structures, the influence of firing temperatures on the phase composition, microstructure and biaxial flexural strength of the LTCC was investigated. The investigated DuPont 951 LTCC is composed of $Al_2O_3$ particles and glass. At 675 °C the LTCC starts to densify after the “liquid glass” is formed. Close to this temperature the particles of $Al_2O_3$ start to dissolve and the amount of glassy phase increases up to 800 °C. From 675 °C to ~875 °C the sintering of the LTCC takes place and the material is fully sintered at 875 °C. The anorthite crystallizes on the surface of the $Al_2O_3$ particles. The amount increases with the increasing firing temperature or time, until it reaches the plateau value at around 22 w.%. The amount of the glass is reduced accordingly. The biaxial flexural strength of the LTCC material fired at 800 °C is around 135 MPa and rises to ~ 220 MPa at 850 °C. The additional improvement of the biaxial flexural strength up to ~300 MPa was obtained between 850 and 900 °C when the anorthite crystallizes around the alumina particles. In the material fired at higher temperatures only small, if any, improvement of biaxial flexural strength can be observed.

## Acknowledgments

The Slovenian Research Agency is acknowledged for its financial support of the projects “Ceramic materials for 3D structures and study of functional properties” (L2-2343), the Young Researcher project 100-009-310145. The financial support of the CoE NAMASTE is gratefully acknowledged.

## References

[1] Imanaka, Y., *Multilayered low temperature cofired ceramics (LTCC) technology*, Springer: 2005.

[2] Müller, R., Meszaros, R., Peplinski, B., Reinsch, S., Eberstein, M., Schiller, W. A., Deubener, J., "Dissolution of Alumina, Sintering, and Crystallization in Glass Ceramic Composites for LTCC", *Journal of the American Ceramic Society*, 92 (8): 1703-1708, 2009.

[3] Imanaka, Y., Yamazaki, K., Aoki, S., Kamehara, N., Niwa, K., "Effects of alumina addition on crystallization of borosilicate glass", *Journal of the Ceramic Society of Japan*, 97 (3): 309-313, 1989.

[4] Khoong, L. E., Tan, Y. M., Lam, Y. C., "Overview on fabrication of three-dimensional structures in multi-layer ceramic substrate", *Journal of the European Ceramic Society*, 30 (10): 1973-1987, 2010

[5] DuPont® "951 Green Tape™" Datasheet, In DuPont Microcircuit Materials, 1-2, 2001.

[6] Kemethmüller, S., Hagymasi, M., Stiegelschmitt, A., Roosen, A., "Viscous Flow as the Driving Force for the Densification of Low-Temperature Co-Fired Ceramics", *Journal of the American Ceramic Society*, 90 (1): 64-70, 2007.

[7] Cole, S., Wellfair, G., High temperature viscosity control in multi-layer glasses - a new concept, Proceedings of the ISHM Symposium, Boston, Massachusetts: 25-34, 1974.

[8] Jones, W. K., Liu, Y., Larsen, B., Wang, P., Zampino, M., Chemical, Structural, and Mechanical Properties of the LTCC Tapes, Proceedings of the IMAPS International Symposium on Microelectronics, Boston, Massachusetts: 469-473, 2000.

## For wider interest

The low-temperature co-fired ceramic (LTCC) is an important composite glass-ceramic material in the production of ceramic multilayer structures mainly for the telecommunications, automotive, and medical applications. In recent times the LTCCs were also recognized as useful materials for producing complex 3D structures with buried cavities and channels or so-called micro-electro-mechanical systems (MEMS). For MEMS structures are very important their chemical, thermal and mechanical properties, while in electronic circuits of the main importance are electrical properties.

The characteristics of the commercially available LTCC tapes processed under prescribed procedures are available in the datasheets and other open literature; however, the large and complex multilayer structures are usually fired for longer firing times and/or, higher firing temperatures, than the relatively thin LTCC tapes. The firing procedures determine the phase composition and the microstructure, which both influence the physical properties, such as the mechanical and thermal properties of the material.

Our research is focused on the study of the effects of the firing temperature and firing time on the phase composition, microstructure, mechanical properties and coefficient of thermal expansion of the material in order to understand the processes during the firing and their effect on the final properties of the material. In order to reach the desired final properties of devices, the mechanisms of the sintering and the crystallization of glass material and their influences on the physical properties must be known. With this knowledge the new material with designed properties can be developed.

# Conformational preferences of alanine tripeptide in water, trifluoroethanol and dimethyl sulfoxide studied by vibrational spectroscopy

**Andreja Mirtič**[1], **Jože Grdadolnik**[1,2]

[1] National Institute of Chemistry, Ljubljana, Slovenia

[2] EN-FIST Centre of Excellence, Ljubljana, Slovenia

andreja.mirtic@ki.si

**Abstract.** Alanine tripeptide is a good model molecule to analyze a conformational distribution of an unstructured peptide backbone, to study a competition between the intra- and intermolecular hydrogen-bonding, as well as the favourable solvation conditions. In our work, we used three different spectroscopic techniques, the Raman and infrared (IR) spectroscopy, and the vibrational circular dichroism (VCD) that are conformation-sensitive and provide information about hydrogen bonded carbonyl groups (amide I region) and amino groups (amide II and III regions in the spectrum) of a peptide backbone. Alanine tripeptide in water exhibits low-frequency bands in the amide I region at 1618 cm$^{-1}$ and in the amide III region at 1260 cm$^{-1}$, suggesting a strong intramolecular hydrogen bond indicative of a $C_7$ conformation. This bond is disrupted in dimethyl sulfoxide (DMSO) where the solvent molecules interact with amino groups of alanine tripeptide forming intermolecular hydrogen bonds. A similar situation is found in trifluoroethanol (TFE) where alanine tripeptide forms mainly intermolecular hydrogen bonds with a hydrogen donor from solvent molecules.

**Keywords**: alanine tripeptide, Raman, infrared spectroscopy, vibrational circular dichroism, conformation, hydrogen bond, $C_7$ conformation

## Introduction

Each amino acid has its intrinsic backbone preferences ($\phi,\psi$) that determine the local structure in unfolded peptide chains and may guide the folding process at early stages of the folding. Alanine amino acid is a good model system due to its simpler vibrational spectra and thus an easier comparison of experimental data with the theory. A preliminary study of the amide III region in IR and Raman spectra of dipeptides showed that the population of alanine dipeptide in water is around 60% of polyproline II ($P_{II}$), 11% of the right handed helix ($\alpha_R$) and 29% of the beta ($\beta$) conformation [1]. The two main factors determine the conformational preferences of dipeptides: the competition between the intra- and intermolecular H-bonding, and the favourable solvation conditions [2]. In this work, we report the study of a conformational equilibrium of alanine tripeptide by characterizing the preferred conformations of the peptide backbone in water, proton donor solvent (TFE) and proton acceptor solvent (DMSO), respectively.

## Materials and Methods

We used alanine tripeptide with N-terminal blocking group acetyl (Ac) and C-terminal blocking group methylamine (NH-Me), at concentrations 0.2 M throughout. The Raman spectra were obtained with the 1064 nm excitation from a NdYAG Laser after 20000 scans. The infrared spectra were measured using the Bruker Vertex infrared spectrometer. For the IR and VCD spectroscopies the sample was placed into the $CaF_2$ cell with a path length of 25 μm. The spectral resolution was 4 $cm^{-1}$ for all measurements recorded in the range between 7000 and 450 $cm^{-1}$.

## Results and discussion

The analysis of the amide I and III bands of alanine tripeptide in water shows the presence of characteristic bands for conformations already found in alanine dipeptide. These band components belong to $P_{II}$ (1304 $cm^{-1}$), $\beta$ (1269 $cm^{-1}$) and $\alpha_R$ (1292 $cm^{-1}$) conformations, i.e., conformations that all form the intermolecular hydrogen bonding with solvent molecules. In contrast to alanine dipeptide several bands can be found in the amide I region of the Raman spectrum of alanine tripeptide in water. The band at 1680 $cm^{-1}$ was assigned to nearly free amide carbonyls, i.e., amide groups which are not involved with inter- or intramolecular hydrogen bonds. The two bands located at 1664 and 1648 cm$^{-1}$ belong to amide carbonyls which interact with the solvent. These two bands with similar frequencies can be found in the Raman spectra of alanine dipeptide in water. There are additional two low frequency amide I bands located at 1635 cm$^{-1}$ and 1618 cm$^{-1}$. These two low frequency bands indicate the presence of a stronger hydrogen bond between the carbonyl group and the proton donor group. The intermolecular hydrogen bonds with water protons, characterized with two bands at 1664 cm$^{-1}$ and 1648 cm$^{-1}$ are replaced with a stronger intramolecular hydrogen bond. The candidate for such hydrogen bond is the formation of the $C_7$ conformation [3]. In Figure 1 the spectrum of the amide III region shows an additional band at 1257 cm$^{-1}$ that is not present in the amide III region of alanine dipeptide in water. This component of amide III vibration is indicative also in the infrared spectra of alanine dipeptide in an argone matrix or in $CDCl_3$ where $C_7$ is the prevailing conformation. Measurement of alanine tripeptide in deuterium water indicates that bands at 1343 cm$^{-1}$ and 1283 cm$^{-1}$ correspond to $CH_2$ deformation modes.

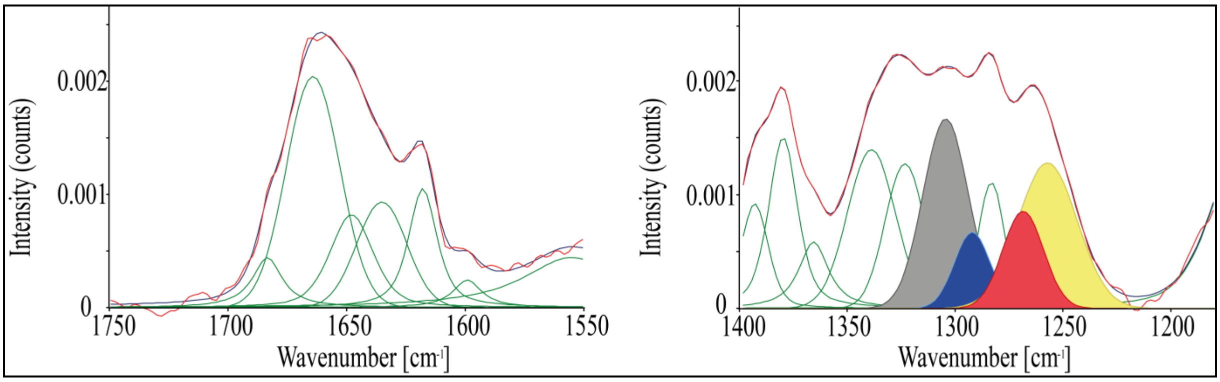

Figure 1. Fitted Raman spectrum in the amide I (left) and amide III (right) region of Ac-Ala$_2$-NHMe in water at a concentration of 0.2 M at room temperature. The band colour represents particular conformations: grey $P_{II}$, red $\beta$, blue $\alpha_R$, and yellow $C_7$.

DMSO is a strong proton acceptor that destroys or weakens intramolecular hydrogen bonds of β-turns [4]. However, it allows inverse bifurcated hydrogen bonds (two acceptors and one donor), causing a shift of the amide I band to higher wavenumbers [5]. In the infrared spectrum the amide I frequency of alanine tripeptide shifts from 1645 cm$^{-1}$ in water to 1664 cm$^{-1}$ in DMSO. It is known that alanine dipeptide in DMSO occupies mainly the β conformation with the intramolecular hydrogen bond [6]. A decomposition of the amide I region of alanine tripeptide in DMSO revealed three bands at 1682 cm$^{-1}$, 1669 cm$^{-1}$, and 1658 cm$^{-1}$ (Figure 2). Frequencies of those band components suggest nearly free or weak interacting carbonyl groups. However, low-frequencies of the amide II and III components (1503 cm$^{-1}$ and 1236 cm$^{-1}$) suggest that the solvent molecules are coordinated around the NH amide groups of alanine tripeptide forming strong intermolecular hydrogen bonds.

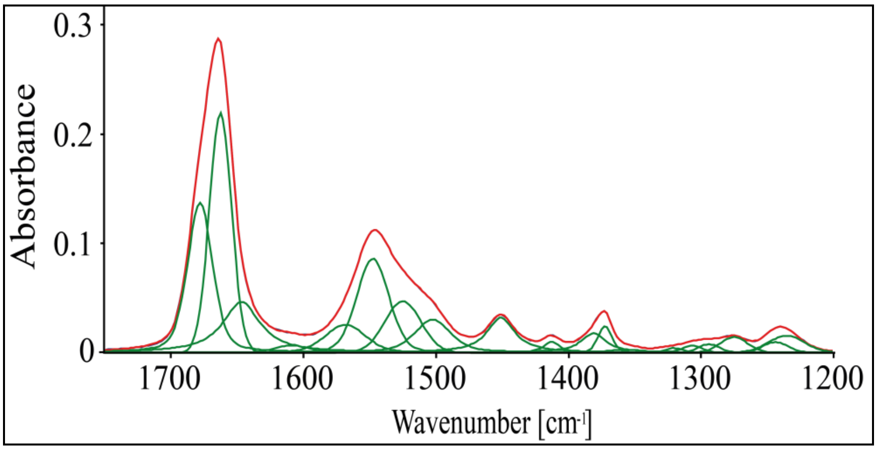

Figure 2. The infrared spectrum of Ac-Ala$_2$-NHMe in DMSO-d$_6$ at room temperature.

TFE is a good hydrogen bond donor and promotes the formation of bifurcated hydrogen bonds (one carbonyl group accepting two hydrogens) or hydrogen bonds between the amide groups and solvent molecules [5]. The Raman spectrum of alanine tripeptide in TFE shows the upshift of amide I frequency that corresponds to the intensity increase of the band at 1678 cm$^{-1}$ due to the free or weakly shielded carbonyls. The band at 1662 cm$^{-1}$ represents solvent exposed amide carbonyls. The third component at 1640 cm$^{-1}$ is assigned to a vibration of carbonyls involved in intermolecular hydrogen bonds with the solvent (Figure 3). The corresponding band in the amide III region can be found near 1235 cm$^{-1}$. Such low frequency amide III bands are also indicative of the formation of intermolecular hydrogen bonds.

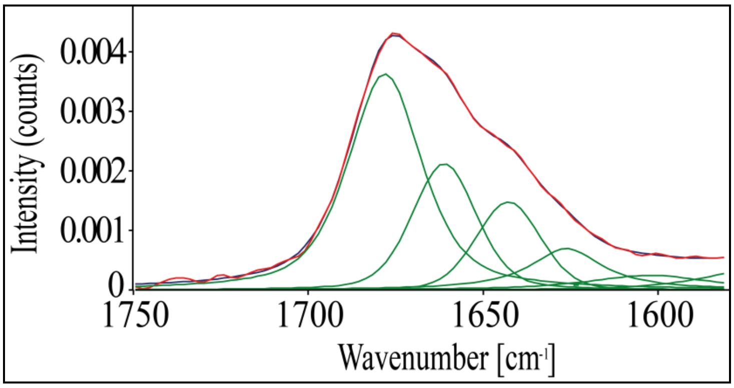

Figure 3. The Raman spectrum of Ac-Ala$_2$-NHMe in TFE-d$_2$ at room temperature.

The vibrational circular dichroism (VCD) provides the bandshape variability of CD with the frequency resolution of IR where the bandshape and its frequency position predict the dominant secondary structural type in peptides and proteins [7]. Alanine tripeptide in water has a symmetrical coupled amide I band with the negative band at 1628 cm$^{-1}$ and the positive one at 1658 cm$^{-1}$. The low frequency band is indicative of a strong intramolecular hydrogen bond. The similar band shape and band frequencies are reported for the C$_7$ hydrogen bonded inverse γ-turn of cyclic tetrapeptides [8].

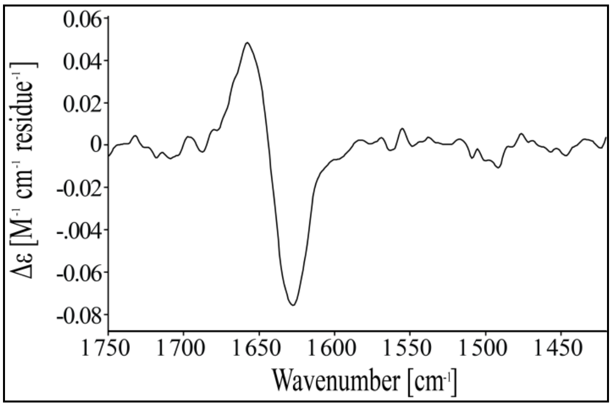

Figure 3. The VCD spectrum of Ac-Ala$_2$-NHMe in D$_2$O at a concentration of 0.2 M at room temperature.

## Conclusions

The Raman, infrared and VCD spectroscopic techniques were employed for the characterization of different conformational populations of alanine tripeptide in water, DMSO and TFE. Beside the population of conformations found in alanine dipeptide, alanine tripeptide possesses an additional conformation stabilized with an intramolecular hydrogen bond which is indicative of the $C_7$ conformation. By changing solvent with DMSO, which is known as a proton acceptor solvent, no intramolecular hydrogen bonds were observed. All carbonyl groups in alanine tripeptide in DMSO are nearly free or weakly shielded by the formation of the intermolecular hydrogen bond between NH groups and solvent molecules. TFE is a proton donor solvent, which intensively interacts with carbonyl groups from alanine tripeptide. Thus, it competes with the intramolecular donor amino group. On the basis of infrared spectra it is indicative that alanine tripeptide solved in TFE contains mainly intermolecular hydrogen bonds with the solvent.

## References

[1]J. Grdadolnik, V. Mohacek-Grosev, R.L. Baldwin, F. Avbelj. Populations of the three major backbone conformations in 19 amino acid dipeptides. *Proc Natl Acad Sci U S A*, 108:1794-1798, 2011.

[2]V. Madison, K.D. Kopple. Solvent-dependent conformational distributions of some dipeptides. *Journal of the American Chemical Society*, 102:4855-4863, 1980.

[3]E. Vass, M. Kurz, R.K. Konat, M. Hollosi. FTIR and CD spectroscopic studies on cyclic penta- and hexa-peptides. Detailed examination of hydrogen bonding in beta- and gamma-turns determined by NMR. *Spectrochimica Acta Part A: Molecular and Biomolecular Spectroscopy*, 54:773-786, 1998.

[4]C. Di Bello, M. Simonetti, M. Dettin, L. Paolillo, G. D'Aurla, L. Falcigno, M. Saviano, A. Scatturin, G. Vertuani, P. Cohen. Conformational studies on synthetic peptides reproducing the dibasic processing site of pro-ocytocin-neurophysin. *J Pept Sci*, 1:251-265, 1995.

[5]E. Vass, M. Hollosi, F. Besson, R. Buchet. Vibrational spectroscopic detection of beta- and gamma-turns in synthetic and natural peptides and proteins. *Chemical reviews*, 103:1917-1954, 2003.

[6]G. Pohl, A. Perczel, E. Vass, G. Magyarfalvi, G. Tarczay. A matrix isolation study on Ac-Gly-NHMe and Ac-l-Ala-NHMe, the simplest chiral and achiral building blocks of peptides and proteins. *Phys Chem Chem Phys*, 9:4698-4708, 2007.

[7]T.A. Keiderling, R.A.G.D. Silva, G. Yoder, R.K. Dukor. Vibrational circular dichroism spectroscopy of selected oligopeptide conformations. *Bioorganic & Medicinal Chemistry*, 7:133-141, 1999.

[8]E. Vass, Z. Majer, K. Kőhalmy, M. Hollósi. Vibrational and chiroptical spectroscopic characterization of γ-turn model cyclic tetrapeptides containing two β-Ala residues. *Chirality*, 22:762-771, 2010.

## Za širši interes

Naše raziskovalno delo vključuje konformacijske analize kratkih peptidov, katerih namen je razumevanje vseh sil in interakcij znotraj peptida, ki bi pomagale razumeti začetno stopnjo proteinskega zvitja in vlogo konformacijskih preferenc aminokislin. Ramanska in infrardeča vibracijska spektroskopija ter vibracijski cirkularni dihroizem omogočajo natančno analizo konformacij posameznega proteina in peptida z razčlenitvijo posameznih konformacijsko odvisnih regij v spektru. Primerjali smo porazdelitev konformacij alanin dipeptida in alanin tripeptida v vodi. Alanin dipeptid je pretežno v PII konformaciji in delno v □ konformaciji. Delež □R konformacije je majhen. Alanin tripeptid pa poleg omenjenih konformacij vsebuje še znaten delež C7 konformacije, ki je stabilizirana z intramolekularno vodikovo vezjo. Z zamenjavo topila smo pokazali, da se lahko ta vez prekine, pri čemer molekula zavzame bolj odprto, topilu dostopnejšo strukturo.

# Basic study of relaxors: Materials for high technological devices

**Nikola Novak**[1,2] and **Zdravko Kutnjak**[1,2]

[1] Department of Condensed Matter, Jožef Stefan Institute, Ljubljana, Slovenia

[2] Jožef Stefan International Postgraduate School, Ljubljana, Slovenia

nikola.novak@ijs.si

**Abstract.** Ferroelectric relaxors belong to a subgroup of ferroelectric materials. Relaxors are characterised by unique dielectric, polarization, electromechanical and electro-optical properties. These extraordinary properties make them suitable for high technological electronic devices such as sensors, actuators, electro or elasto-optic and photorefractive elements. Understanding the origin of these properties and physical background is a key for useful applications. In this paper we show the investigation of the nature of the relaxor ground state which is one of the unresolved enigmas of relaxors. We will interpret the high-resolution calorimetric measurements of the electric field induced ferroelectric phase transition of the ferroelectric relaxor $Pb(Mg_{1/3}Nb_{2/3})O_3$ single crystal oriented in the [110] direction.

**Keywords**: critical point, relaxor ferroelectric, latent heat.

## 1 Introduction

Relaxor ferroelectric materials or relaxors offer a wide range of useful properties which make them attractive for various high technological applications. These include ferroelectric hysteresis (used in non-volatile memories), high permittivity (used in capacitors), high piezoelectric effects (used in sensors, actuators and resonant wave devices such as radio-frequency filters), high pyroelectric coefficients (used in infra-red detectors), strong electro-optic effects (used in optical switches) and anomalous temperature coefficients of the resistivity (used in electric-motor overload protection circuits). The largest and most important relaxor ferroelectric family is a perovskite structured group. It was shown that the origin of relaxor properties is due to the charge and site disorder of the perovskite structure caused by the substitution of cations with a different valence [1]. To improve or to make them suitable for useful applications we have to understand the physical background of these complex perovskite compounds.

Ferroelectric relaxor $Pb(Mg_{1/3}Nb_{2/3})O_3$ (abbreviated as PMN) is known for more than five decades and is still in the focus of the research as a prototypical example of relaxors. In contrast to ordinary ferroelectrics, relaxors like PMN show some unusual responses like: (i) a broad frequency dispersion in a complex dielectric response exhibiting maximum at $T_m$, (ii) the logarithmic decay of the polarization which persists even above $T_m$, (iii) absence of the spontaneous polarization in zero external electric field, (iv) a slim hysteresis loop at $T_m$ and (v) slowing dynamics [1-4]. One of the key features of relaxors is the absence of a long range ordered ferroelectric phase in zero electric field at any temperature [3, 5]. It is believed that the origin of all these properties lies in an intrinsic inhomogeneity. The chemical disorder in relaxors is a basis for the formation of dipolar entities at very high temperatures. On cooling the system bellow the so-called Burns temperature [6] these dipolar entities form polar nanoregions which are randomly oriented and form in the ergodic relaxor state in a way similar to that of dipolar glasses [1, 3, 7]. By cooling the system below freezing temperature the relaxor state undergoes the transition into the non-ergodic dipolar glass state with randomly frozen polar nanoregions. This glassy state can be converted into a ferroelectric phase by application of the electric field higher than the critical electric field, $E \geq E_C$. Besides this widely accepted physical picture of the relaxor ground state, there are other possible models, such as for instance a random field (RF) mechanism [8]. The RF mechanism proposes that the relaxor state is a ferroelectric state broken up under the constraint of quenched random electric fields. It proposes also that these random fields destroy the long range ferroelectric order which can be established by applying a high enough electric field at which nanodomains align along the field. In order to understand relaxor properties the question of the relaxor ground state is one of the important issues which has to be resolved.

In the past it was shown that the polarization measurements do not provide a clear answer because the results can be interpreted in favour of both suggested models. Here, we report the results of high-resolution calorimetric measurements of the

PMN single crystal oriented in the [110] direction. The calorimetric measurements should provide the information about the presence of the latent heat at the ferroelectric transition line. The presence of the latent heat will prove that the ground state of relaxors is a state which is thermodynamically different from the ferroelectric state, i.e., the dipolar glass state is by applying $E_c$ transformed into the long range ferroelectric state. In the case of the RF mechanism, the ferroelectric state is proposed to be established already at some higher temperature and so no significant change of the enthalpy as well as the latent heat should be observed between the low and high electric field states, because the local ferroelectric symmetry is preserved.

## 2 Experiments and discussion

High-resolution calorimetric measurements were performed in the ac and relaxation mode (see details in Ref. [9]) in such a way that either electric field or temperature was constant. In the former case the temperature was changed in the ac mode with 2 K/h at the constant field to measure continuous variation of enthalpy. Relaxation mode, however, is sensible also to the latent heat and so the total enthalpy change can be measured. We modify the calorimeter in such a way that it was possible to perform isothermal relaxation measurements in which the electric field was linearly ramped between ±10 kV/cm.

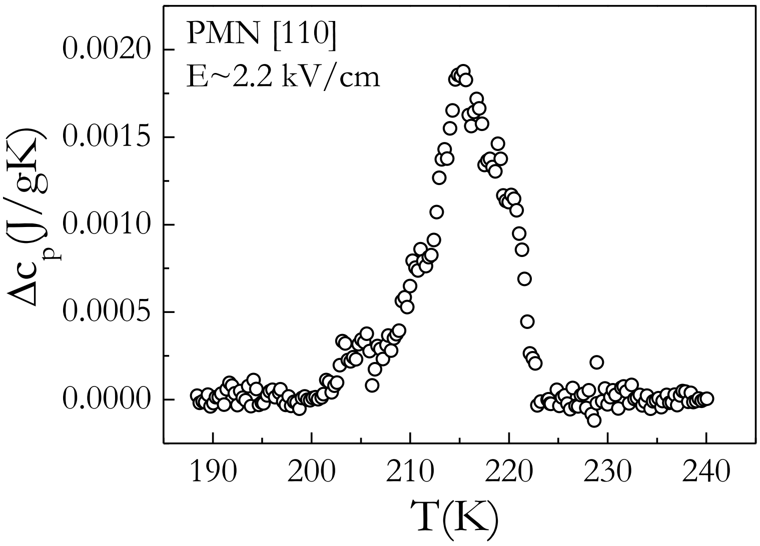

**Figure 1:** The temperature dependence of the excess heat capacity data obtained in the ac mode at the isofield condition.

In order to detect enthalpy changes at the ferroelectric transition the ac and relaxation measurements of the heat capacity were conducted. The temperature dependence of the excess heat capacity obtained from the ac measurement in PMN [110] single crystal is displayed in Figure 1. The excess of the heat capacity can be observed only if $E \geq E_C$. By increasing the electric field above 8 kV/cm, the excess heat capacity got suppressed and smeared out. Similar behaviour of the excess heat capacity was observed at the cubic to tetragonal (C-T) phase transition in PMN-PT system where the first order transition line separates paraelectric cubic and ferroelectric tetragonal phases and terminates in the critical point [10, 11].

To get a clear answer about the transition between the relaxor and ferroelectric state in PMN we utilized modified relaxation measurements. In the isothermal experiment we monitor the sample temperature when linearly ramped electric field was applied. At $E = E_C$, a sharp increase of the sample temperature was clearly visible (see Fig. 2). The increase of the sample temperature is directly related to the released latent heat at the electric field induced ferroelectric transition.

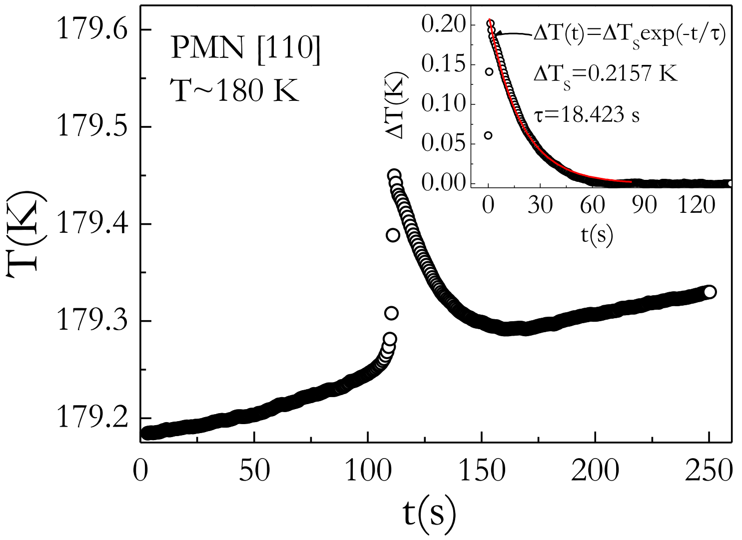

**Figure 2:** The change of the sample temperature for the PMN [110] single crystal as a consequence of the released latent heat at the field induced ferroelectric transition, at 180 K. The inset shows a fit to the simple exponential decay ansatz which reveals the amplitude of the sample temperature change and thus the latent heat.

To determinate the released latent heat in the first approximation we fit the dissipated latent heat into the surrounding by the simple exponential decay ansatz as shown in the inset of Fig. 2. The obtained amplitude of the sample temperature change, $\Delta T_S$=0.2157 K, can be used to calculate corresponding latent heat. With further measurements it was shown that the amplitude of the sample temperature change decreases with increasing temperature and electric field. The presence and diminishing of the latent heat prove the existence of the first order transition line between the relaxor and ferroelectric phases which terminates at the critical point.

## 3 Conclusion

High-resolution heat capacity measurements were employed to investigate the nature of the electric field induced ferroelectric transition of the ferroelectric relaxor PMN single crystal oriented in [110]. The ac measurements display an excess of the heat capacity at $E \geq E_C$. At a much higher electric field the heat capacity anomaly is suppressed indicating the supercritical behaviour. The detected latent heat confirms the existence of a real phase transition line between the zero-field ground state and ferroelectric long range order. The calorimetric measurements reveal a similar behaviour as observed at the C-T phase transition in the PMN-PT system. The presence of the latent heat supports the idea of the dipolar glass like ground state of relaxors rather than the RF frozen ferroelectric state broken up into nanodomains.

## References:

[1] L. E. Cross. Relaxor ferroelectrics. *Ferroelectrics,* 76:241-267, 1987.

[2] D. Viehland, S. J. Jang, L. E. Cross, M. Wuttig. Deviation from Curie-Weiss behaviour in relaxor ferroelectrics. *Physical Review B,* 46:8003, 1992.

[3] V. E. Colla, E. Y. Koroleva, N. M. Okuneva, S. B. Vakhrushev. Long-Time Relaxation of the Dielectric Response in Lead Magnoniobate. *Physiscal Review Letters,* 74:1681, 1995.

[4] A. Levstik, Z. Kutnjak, C. Filipič, R. Pirc. Glassy freezing in relaxor ferroelectric lead magnesium niobate. *Physical Review B,* 57:11204, 1998.

[5] G. Schmidt, H. Arndt, G. Borchhardt, J. von Cieminski, T. Petzsche, K. Borman, A. Sternberg, A. Zirnite, V. A. Isupov. Induced Phase Transitions in Ferroelectrics with Diffuse Phase Transition. *Physica Status Solid*, 63:501, 1981.

[6] G. Burns, F. H. Dacol. Crystalline ferroelectrics with glassy polarization behavior. *Physical Review B* 28:2527, 1983.

[7] R. Pirc, R. Blinc. Spherical random-bond-random-field model of relaxor ferroelectrics. *Physical Review B*, 60:13470, 1999.

[8] V. Westphal, W. Kleemann, M. D. Glinchuk. Diffuse Phase Transition and Random-Field-Induced Domain States of the “Relaxor” Ferroelectric $PbMg_{1/3}Nb_{2/3}O_3$. *Physical Review Letters*, 68:847, 1992.

[9] H. Yao, K. Ema, C.W. Garland. Nonadiabatic scanning calorimeter. *Review of Scientific Instruments*, 69:172, 1998.

[10] Z. Kutnjak, J. Petzelt, R. Blinc. The giant electromechanical response in ferroelectric relaxors as a critical phenomenon. *Nature,* 441:956-959, 2006.

[11] Z. Kutnjak, R. Blinc, Y. Ishibashi. Electric field induced critical points and polarization rotations in relaxor ferroelectrics. *Physical Review B,* 76:104102,2007.

## For wider interest

Relaxor ferroelectric materials represent a subgroup of ferroelectrics. $Pb(Mg_{1/3}Nb_{2/3})O_3$ is one of the most famous and widely studied relaxor. Relaxor materials are known for their unusual properties which are useful for various applications in high technological devices. Relaxors exhibit high permittivity (used in capacitors), ferroelectric hysteresis (used in non-volatile memories), high piezoelectric effects (used in sensors, actuators and resonant wave devices such as the radio-frequency filters, scanning probe microscopy, ink jet printer, adaptive optics, micromotors, vibration sensors/attenuators, Hubble telescope correction), high pyroelectric coefficients (used in infra-red detectors), strong electro-optic effects (used in optical switches, segmented displays, modulators, image storage, holographic data storage) and anomalous temperature coefficients of the resistivity (used in electric-motor overload protection circuits). Our work is dedicated to understanding the ordering process in this material which is of a fundamental importance for the further application progress as well as engineering new materials with enhanced properties.

In this work we represent the study of the glass-ferroelectric phase transition that addresses also the long standing question about the ground state of relaxors in zero electric field. The isofield and isothermal measurements of the heat capacity reveal an excess of the heat capacity as well as released latent heat at the field induced ferroelectric transition. The detected latent heat confirms the existence of the real ferroelectric phase transition and support the physical picture of the dipolar glass like ground state of relaxors.

# Morfotropna fazna meja v $(Na_{1-x}K_x)_{0,5}Bi_{0,5}TiO_3$ piezoelektrični keramiki

**Mojca Otoničar**[1,2]

[1] Odsek za raziskave sodobnih materialov, Institut Jožef Stefan, Ljubljana, Slovenija
[2] Mednarodna podiplomska šola Jožefa Stefana, Ljubljana, Slovenija
mojca.otonicar@ijs.si

**Mentor: doc. dr. Srečo D. Škapin**

Razvoj piezoelektrikov je pretežno usmerjen v optimizacijo strukture materialov, saj so v območju morfotropne fazne meje (MPB) piezoelektrični odzivi občutno povišani. Keramikam na osnovi sistema $(Na_{1-x}K_x)_{0,5}Bi_{0,5}TiO_3$, kjer se tvori trdna topnost v območju sestav $0 \leq x \leq 1$, sem določila strukturne značilnosti in izvedla meritve elektromehanskih lastnosti. Določila sem sestave z MPB (pri $x = 0{,}2$ in 0,22), kjer soobstojata romboedrična in tetragonalna struktura. Prisotnost MPB potrjujejo tudi rezultati električnih meritev; vzorec s sestavo $x = 0{,}2$ izkazuje najvišje vrednosti dielektrične konstante, remanentne polarizacije in piezoelektričnega koeficienta. Analiza s presevnim elektronskim mikroskopom (TEM) je pokazala, da v MPB prevladuje tetragonalna domenska zgradba, superstrukturni ukloni v elektronskih difrakcijah pa potrjujejo obstoj P4bm tetragonalne strukture. Rezultati TEM analize ne sovpadajo z rezultati rentgenske praškovne difrakcije (RTG), ki pri sestavi $x = 0{,}2$ kažejo pretežno romboedrično strukturo. In-situ TEM meritve s segrevanjem do 500°C so potrdile, da se po ohlajanju tetragonalna domenska zgradba ne vzpostavi ponovno. Tako lahko sklepamo, da je tetragonalna struktura sprožena z mehanskim obremenjevanjem med pripravo vzorcev za TEM, kar ustreza visoki polarizabilnosti ter strukturni 'prilagodljivosti' MPB materialov.

**Ključne besede**: piezoelektrik, morfotropna fazna meja, presevna elektronska mikroskopija (TEM)

## 1 Uvod

Piezoelektrični materiali se uporabljajo kot sestavne komponente predvsem v elektronski industriji kot senzorji, pretvorniki ali aktuatorji. Tako različne naprave izkoriščajo piezoelektrično lastnost materialov, da se polarizirajo oziroma deformirajo pod vplivom električnega polja, ali da generirajo električno napetost kot posledico mehanske obremenitve. Težnja pri razvoju novih piezoelektričnih materialov je v izboljšanju piezoelektričnega odziva, kar prispeva k izboljšavi učinkovitosti komponent in k miniaturizaciji elektronskih naprav. Zato je študij poteka sprememb v materialu, kot na primer spremembe strukture zaradi sestave ali zaradi sekundarno vnesenih napetosti pri obremenitvah materiala, ali pa premikanje domenskih sten pod vplivom polja, izrednega pomena za nadaljnji razvoj piezomaterialov.

Najpogosteje uporabljeni piezoelektrični materiali vsebujejo svinec ($PbZr_xTi_{1-x}O_3$), ki je strupen tako za človeka kot za okolje. Zato je cilj razvoja novih piezomaterialov priprava materialov brez ali z manj vsebnosti svinca. Med najprimernejše piezomateriale, ki bi potencialno lahko zamenjali materiale na osnovi svinca, sodijo sistemi trdnih raztopin s perovskitno strukturo v območju morfotropne fazne meje (MPB), kjer soobstojata dve različni strukturi. [1-6] V tem območju namreč piezoelektrični materiali izkazujejo močnejšo elektromehansko sklopitev in s tem povišane vrednosti piezoelektričnega odziva. [1,2]

Na podlagi predhodnih študij smo se odločili za raziskave keramik iz sistema $Na_{0,5}Bi_{0,5}TiO_3$-$K_{0,5}Bi_{0,5}TiO_3$ (NBT-KBT), ki v določenem razmerju kationov tvorijo MPB med tetragonalno in romboedrično strukturo. Tako sem določila sestavo, pri kateri se pojavlja MPB, ovrednotila elektromehanske lastnosti trdnih raztopin in podrobno analizirala kristalno in domensko strukturo keramik.

## 2 Eksperimentalni del

Keramične vzorce v obliki trdnih raztopin z različnimi deleži NBT in KBT sem pripravila po postopku sinteze v trdnem. Fazno sestavo in kristaliničnost vzorcev sem preverila z rentgensko praškovno difrakcijo (RTG) s pomočjo difraktometra Bruker AXS D4 Endeavor. Za detajlne raziskave lokalne kristalne in domenske strukture sem vzorce v obliki tanke folije analizirala s presevnim elektronskim mikroskopom (TEM; JEM-2100, Jeol Ltd., Tokyo, Japan).

## 3 Rezultati in diskusija

### 3.1 Rentgenska praškovna difrakcija (RTG)

Z rentgensko praškovno difrakcijo sem določila kristalno strukturo trdnih raztopin NBT-KBT. Iz difraktogramov je razvidno, da se lege posameznih uklonov zvezno zamaknejo s spreminjajočo se sestavo, kar sovpada z večanjem osnovne celice od NBT proti KBT. Natančni RTG posnetki sestav $x$ = 0,2 in 0,22 v ($Na_{1-}$

$_{x}K_{x})_{0,5}Bi_{0,5}TiO_3$ so pokazali, da se hkrati pojavljajo ukloni obeh struktur, romboedrične in tetragonalne, torej gre za sestavo z MPB. Pri sestavi $x = 0,2$ prevladuje romboedrična struktura in je intenziteta uklonov tetragonalne strukture manjša, pri sestavi $x = 0,22$ pa je prevladujoča tetragonalna struktura.

### 3.2 Električne meritve

Električne meritve vzorcev, t.j. meritve dielektrične konstante, remanentne polarizacije (Slika 1) in piezoelektričnega koeficienta izkazujejo najvišje vrednosti pri MPB sestavi z vrednostjo $x = 0,2$ ($\varepsilon_r = 1140$; $P_r = 40\mu C/cm^2$; $d_{33} = 134 pC/N$). Takšen rezultat lahko pripišemo višjemu številu možnih smeri polarizacije zaradi soobstoja več kot ene anizotropne kristalne strukture; 6 <100> smeri pri tetragonalni in 8 <111> smeri pri romboedrični strukturi. Tako MPB struktura omogoča dipolnim momentom, da se učinkoviteje usmerijo skladno z zunanjim poljem, kar se odraža v višji polarizabilnosti materiala.

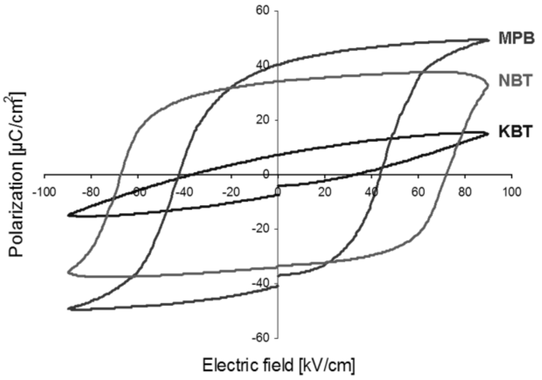

**Slika 1:** Histereze odvisnosti polarizacije od električnega polja vzorcev NBT, MPB in KBT.

### 3.3 Presevna elektronska mikroskopija (TEM)

Lokalno domensko in kristalno strukturo trdnih raztopin NBT-KBT sem podrobno preučila s pomočjo presevne elektronske mikroskopije (TEM) (Slika 2). Iz cepitev uklonov v elektronskih difrakcijah (ED) in na podlagi značilnih domenskih vzorcev sem ločila tetragonalne domene od romboedričnih. Kristalno strukturo s pripadajočo prostorsko skupino sem določila na podlagi superstrukturnih uklonov v izbranih kristalografskih conah ED, ki določajo sisteme nagibov kisikovih oktaedrov v kristalni mreži. Keramike na osnovi enofaznega KBT in trdnih raztopin do sestave MPB sestavljajo 90°-tetragonalne domene, medtem ko so za NBT in ostale sestave do MPB značilne 71/109° romboedrične domene. Za MPB vzorec z deležem $x = 0,2$ sem ugotovila, da je domenska zgradba značilno tetragonalna, z jasnimi in ravnimi lamelami, ki so medsebojno orientirane pod kotom 90°, ter z značilno tetragonalno cepitvijo uklonov v ED. Pri vzorcu KBT ni superstrukturnih uklonov v nobeni kristalografski coni, tako da lahko strukturo opišemo s prostorsko skupino P4mm. Superstrukturni ukloni pri NBT se pojavljajo le v <011> conah, tako da je struktura določena z romboedrično R3c prostorsko skupino z anti-fazno usmerjenimi oktaedri. V MPB vzorcu z $x = 0,2$ in v bližnjih tetragonalnih sestavah se pojavljajo superstrukturni ukloni v <001> in <111> kristalografskih conah, iz česar sem, tudi zaradi prisotne tetragonalne domenske zgradbe in predhodnih študij na visoko temperaturnih modifikacijah NBT, določila, da gre za tetragonalno P4bm strukturo z $a^0a^0c^+$ sistemom rotacije oktaedrov. S študijo domenske morfologije in superstrukturnih uklonov še ostalih NBT-KBT sestav sem lahko ugotovila, da se kristalna mreža postopno spreminja s sestavo, torej od tetragonalne P4mm strukture pri KBT, preko tetragonalne P4bm strukture proti romboedrični R3c strukturi NBT keramike.

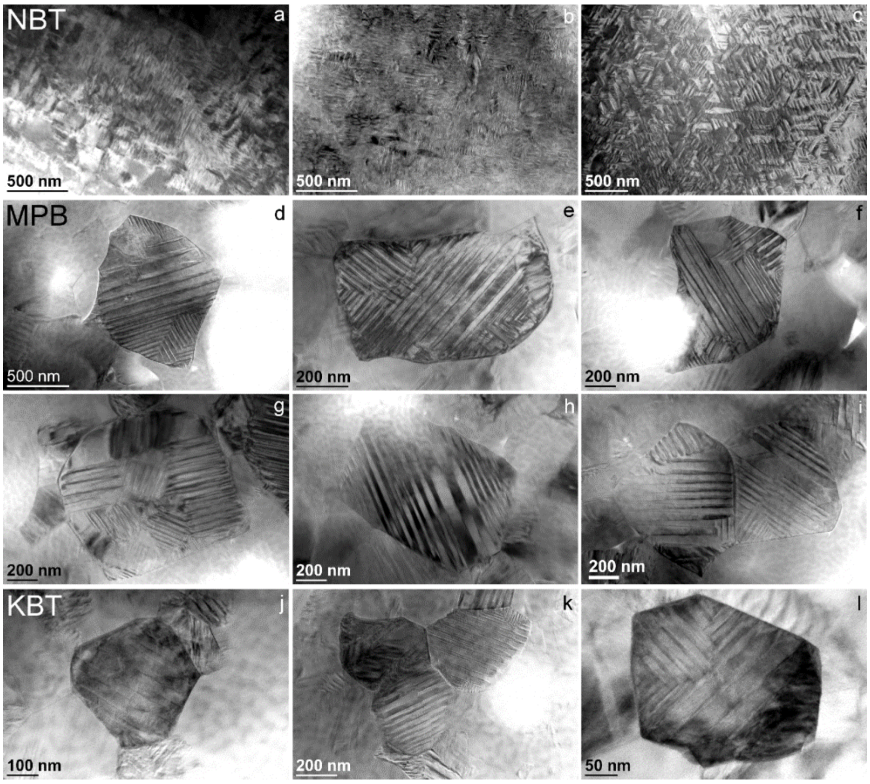

**Slika 2:** Domenska struktura sedmih različnih vzorcev: slike a-c predstavljajo NBT keramiko z lamelno do igličasto domensko zgradbo; slike d-i prikazujejo zrna MPB vzorca z lamelno domensko zgradbo, značilno za tetragonalno strukturo; na slikah j-l vidimo zrna KBT keramike, prav tako z značilno tetragonalno lamelno domensko strukturo.

In-situ TEM analiza s segrevanjem vzorcev nad temperaturo depolarizacije je pri MPB sestavi pokazala, da feroelektrične tetragonalne domene izginejo in se ne vzpostavijo ponovno. Superstrukturni ukloni, značilni za P4bm tetragonalno strukturo z oktaedri zasukanimi proti kristalografski osi, pa ostajajo tudi po segrevanju do 500°C in so torej neodvisni od feroelektrične faze.

## 4 Zaključek

Iz pojava tetragonalne P4bm strukture v MPB vzorcu, katerega difraktogram kaže na morfotropno fazno sestavo s soobstojem romboedrične in tetragonalne strukture, ter iz in-situ TEM meritev, kjer se po ohlajanju tetragonalna domenska zgradba ni obnovila, sem zaključila, da je prišlo do sprememb v strukturi zaradi mehanske obdelave vzorca za TEM. Ker vemo, da so vzorci z MPB dovzetni za tovrstne strukturne spremembe zaradi visoke polarizabilnosti, kar jih tudi odlikuje, ta pojav ni nenavaden. Za potrditev slednje trditve pa moramo opraviti še nadaljne raziskave.

## Literatura:

[1] B. Jaffe, W. R. Cook and H. Jaffe. *Piezoelectric ceramics*. Academic press, London, 1971.

[2] R. E. Cohen. Theory of ferroelectrics: a vision for the next decade and beyond. *J. Phys. Chem. Solids*, 61: 139–146, 2000.

[3] T. R. Shrout and S. J. Zhang. Lead-free piezoelectric ceramics: Alternatives for PZT? *J. Electroceram.*, 19: 111–124, 2007.

[4] T. Takenaka, H. Nagata and Y. Hiruma. Current developments and prospective of lead-free piezoelectric ceramics. *Jpn. J. Appl. Phys.*, 47: 3787–3801, 2008.

[5] Y. Saito, H. Takao, T. Tani, T. Nonoyama, K. Takatori, T. Homma, T. Nagaya and M. Nakamura. Lead-free piezoceramics. *Nature*, 432: 84-87, 2004.

[6] J. Rödel, W. Jo, K. T. P. Seifert, E.-M. Anton, T. Granzow and D. Damjanovic. Perspective on the Development of Lead-free Piezoceramics. *J. Am. Ceram. Soc.*, 92(6): 1153-1177, 2009.

## Za širši interes

Novi piezoelektrični materiali brez vsebnosti svinca, ki v določenem območju sestav izkazujejo močno povišane vrednosti elektromehanske sklopitve, se raziskujejo zaradi njihove potencialne uporabe v elektroniki. Pri trdnih raztopinah s povišanimi piezoelektričnimi lastnostmi se namreč pojavi soobstoj dveh kristalnih struktur – območje imenujemo morfotropna fazna meja - zaradi česar se material enostavneje polarizira. Dejansko stanje kristalne strukture MPB je težko ovrednotiti, saj so metode ugotavljanja strukture posredne, povprečne ali invazivne, kar botruje številnim nesoglasjem stroke o realnem stanju strukture materiala. Naše raziskave so potekale na sistemu trdnih raztopin $(Na_{1-x}K_x)_{0,5}Bi_{0,5}TiO_3$, za katere smo določili strukturne in električne lastnosti piezokeramik. Detajlne analize kristalne in domenske zgradbe so potekale s pomočjo presevne elektronske mikroskopije v kombinaciji z rentgensko praškovno difrakcijo.

# The peak base as a characteristic feature of the Auger electron spectra

**Besnik Poniku**[1,2], **Igor Belič**[1], **Monika Jenko**[1]

[1] Institute of Metals and Technology, Ljubljana, Slovenia

[2] Jožef Stefan International Postgraduate School, Ljubljana, Slovenia

besnik.poniku@imt.si

**Abstract.** The background in Auger spectra has always been regarded as nuisance. Its removal presents a real challenge when processing data from Auger spectra in order to extract from them the required information. This task becomes even more immediate and unavoidable when one thinks of automating the retrieval of qualitative and quantitative information from the Auger spectra. For this reason different approaches have been developed from various researchers to overcome this problem. On the other hand we should not disregard the fact that the background also carries information. For this reason the removed background should be saved for reference when necessary.

**Keywords**: Auger spectra, automation, background, peak base.

## 1 Introduction

Ideally, when recording Auger spectra, we should see on the plot only the characteristic peaks coming from the elements present in the sample. In such a case the intensity represented by the area under the peaks would be strictly defined. But when obtaining real spectra from samples the characteristic peaks are always situated on a top of the background [1].

## 2 Contributors to the background

The signal that forms the background of the Auger spectra is generated from three principal sources: the backscattered electrons, the secondary electrons, and the inelastically scattered Auger electrons [2]. The backscattered electrons are electrons of the primary beam which come back at the surface of the sample and reach the detector after having penetrated the sample. Authors like Jousset and Langeron [3] worked on defining the inelastically scattered primary electron spectrum. They proposed a model which predicts in a wide energy range, from about 0.2 to 0.75 $E_p$ (energy of the primary beam), an exponential law for the contribution of backscattered primary electrons to the spectrum in the integral form [the *N(E)* spectrum]. Equation (1) [2] gives the relationship in a simplified form:

$$n_B(E) \approx \exp(E / E_1), \tag{1}$$

where $n_B$ represents the number of backscattered primary electrons leaving the surface at energies $E$, whereas $E_1$ corresponds to a minimum loss which is a fixed value for a certain energy of the primary beam.

Secondary electrons are considered in general as those electrons which are created as a result of the primary beam electrons interaction with the sample. Sickafus' work describes the contribution of the secondary electrons to the spectrum [4, 5]. The contribution of the secondary electrons could be written as [6]:

$$B(E) = AE^{-m}, \tag{2}$$

where *B(E)* is the number distribution of secondary electrons emitted with the kinetic energy $E$ from a solid sample, $A$ and $m$ are constants characteristic of the material, but $A$ also depends upon the energy of the primary beam.

Sickafus also studied the Auger emission from the sample, describing it in two parts, namely as the elastic Auger emission coming from the surface, and the scattered Auger emission coming from the subsurface of the sample (Fig. 1) [4, 5].

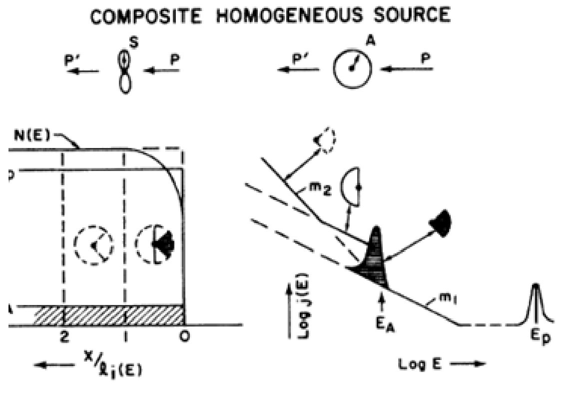

**Figure 1:** Emissions from the surface and subsurface and their effect on the spectrum.[5]

While the elastic Auger emission from the surface of the sample accounts for the signal which forms the visible Auger peak in the spectrum, the scattered Auger emission coming from the subsurface consists of the signal which creates in the spectrum the feature of the background that we refer to as the peak base.

Since the background interferes especially in the quantitative evaluation of Auger spectra, different approaches presented by various researchers to define and remove the background have been developed. Our group has employed neural networks to deal with the problem of background definition.

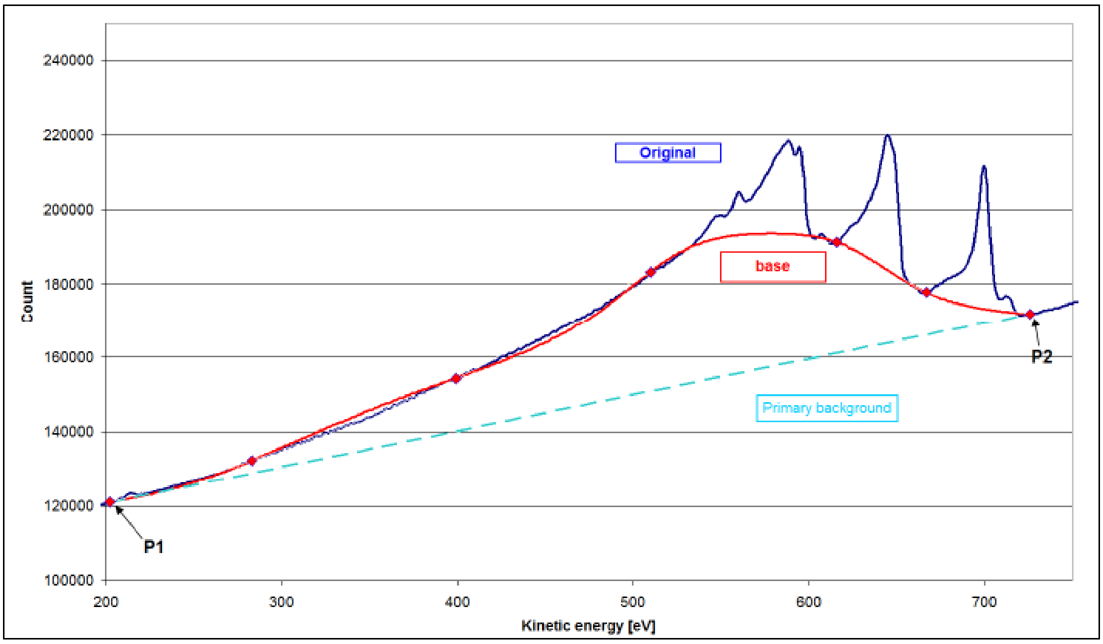

**Figure 2:** Elements of the Auger spectrum (in this case the Auger spectrum of Fe).

This enables a visual representation of the background approximated on the basis of the experimental data which the neural network is fed with.

In our work we have sectioned the spectrum in three main elements, namely the primary background, the peak base, and the peaks (Fig. 2). When inspecting more closely the more complete spectrum of iron (Fig. 3), the dashed line in Figure 2 looks like a natural continuation of the primary background where the secondary electrons and the backscattered electrons have the largest influence.

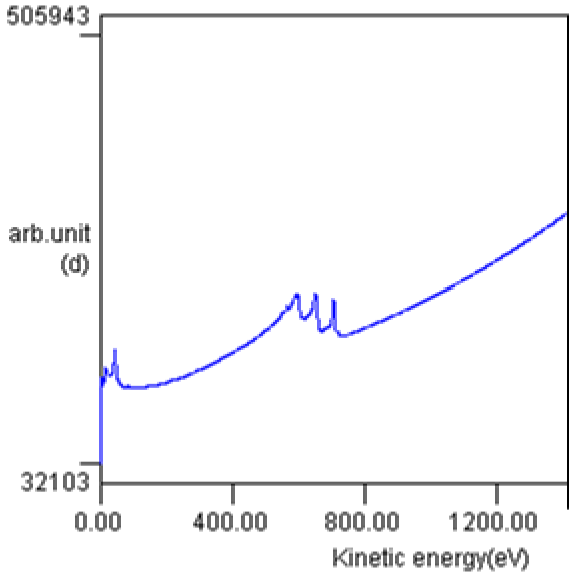

**Figure 3:** The spectrum of elementary iron [7].

## 3 The peak base

By feeding the neural network further with data from the remaining background, but not the peaks, the element which we named the peak base ("base" line in Figure 2) becomes apparent. We think that the attenuated Auger electrons that come from slightly deeper layers (the subsurface) and that have lost their characteristic energies are the main contributors to this feature. This claim is supported by further investigating the Auger spectrum of a TiNi alloy (Fig. 4).

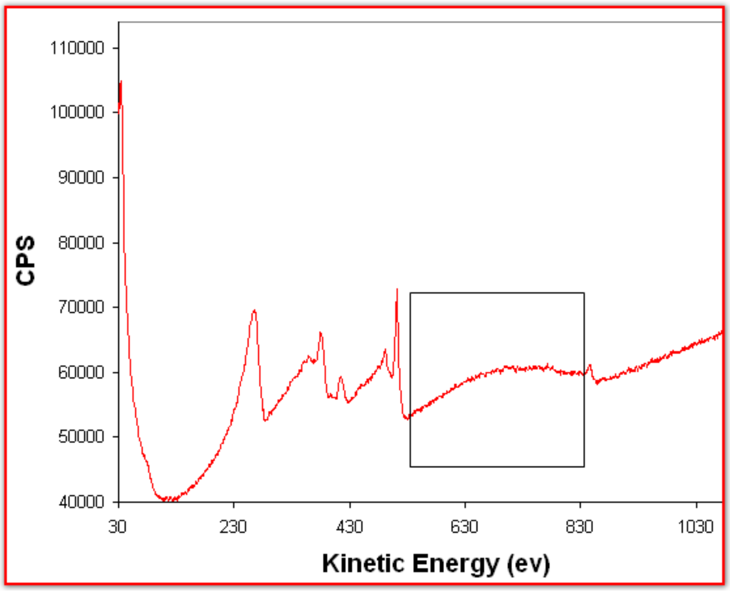

**Figure 4**: The spectrum of a TiNi alloy.

In this case the Ni was slightly buried under the Ti oxide that was formed on the surface and the contaminating carbon, whose peaks (Ti, O, and C) are clearly observable in the spectrum. Therefore, the signal coming from Ni was slightly attenuated, and instead of clear peaks in the area encompassed by the square in Figure 4 we observe a "bump". From the knowledge of the sample used in this case, and the energy interval where this feature appears, we come to the conclusion that it is largely influenced by the Auger signal of Ni present in the subsurface. Since it is very obvious that this feature very much resembles the peak base described in Figure 2, we also come to the conclusion that the part of the background under the respective peaks comes as a result of the attenuation of the Auger electrons which are generated in the subsurface.

In instances like the one presented in Figure 4, where the signal is not strong enough to form clear peaks, the peak base feature of the background may be used to detect the presence of the element in question. This fact that the background may contain information regarding the investigated sample should be kept in mind during the background removal operations, and the removed background should be saved for reference if necessary.

## References:

[1] Auger Electron Spectroscopy. Queen Mary, University of London. http://www.chem.qmul.ac.uk/surfaces/scc/scat5_2.htm, 2012.

[2] M.P. Seah, I. S. Glimore. High Resolution Digital Auger Database of true spectra for Auger elenctron spectroscopy intensities. *Journal of Vacuum Science and Technology A*, 14(3): 1401-1407, 1996.

[3] D. Jousset, J. P. Langeron. Energy distribution of primary backscattered electrons in Auger electron spectroscopy. *Journal of Vacuum Science and Technology A*, 5(4): 989-995, 1987.

[4] E. N. Sickafus. Linearized secondary – electron cascades from the surfaces of metals. I. Clean surfaces of homogeneous specimens. *Physical Review B*, 16(4): 1436-1447, 1977.

[5] E. N. Sickafus. Linearized secondary – electron cascades from the surfaces of metals. II. Surface and subsurface sources. *Physical Review B*, 16(4): 1448-1458, 1977.

[6] J. C. Greenwood, M. Prutton, and R. H. Roberts. Atomic – number dependence of the secondary – electron cascade from solids. *Physical Review B*, 49(18):12485-12495, 1994.

[7] COMPRO 10 - Common Data Processing System Version 10. http://www.sasj.jp/COMPRO/, 2012.

## For wider interest

The long term goal of our group is to automate the interpretation of spectra in Auger Electron Spectroscopy. To automate the interpretation of the quantitative and qualitative results obtained from the Auger spectra, in other words to enable the software to automatically tell us which elements are present in the surface of the sample and how much of each element is there, among other things, we must prepare the data by removing the background. The background interferes when we attempt to analyze how much of a specific element is presented in the sample. Even though the idea is straightforward, simply just to remove the background, the actual work of its removal is quite a challenge. Different researchers have taken different approaches to overcome the problem of how to define the background for its later proper removal. Our group has used neural networks for this purpose, modelling the background by feeding the neural network with the data that were obtained experimentally.

By visually inspecting the different approximated (modelled) parts of the background, a feature which we termed “the peak base” became apparent. We investigated further and found out that most of the researchers in the previous work on the topic of background definition and its later removal had treated this as an integral part of the feature that we termed “the primary background”. But unlike the primary background, the peak base is actually formed from characteristic Auger electrons which normally would form the main peak, but are slowed down and lose slightly their characteristic energy since the electrons forming the peak base are generated deeper in the sample surface (the subsurface) and thus travel further and overcome additional obstacles on their way to the detector. Thus, the background that would normally be removed and hence its signal would be lost, actually carries information about our sample and can be used to detect elements when clear peaks are absent.

Through this work we attempt to bring the automation of Auger spectra interpretation one step closer. This on the one hand will make the analysis much easier for anyone involved in the study of metals and other materials through Auger spectroscopy, and on the other hand the proposed advanced treatment of the background part of Auger spectra will contribute to more reliable results about the elements present in the samples studied.

# Underwater electromagnetic remote sensing

**Uroš Puc**[1], **Andreja Abina**[1], **Anton Jeglič**[3], **Pavel Cevc**[2], **Aleksander Zidanšek**[1,2]

[1] Jožef Stefan International Postgraduate School, Ljubljana, Slovenia

[2] Department of Condensed Matter Physics, Jožef Stefan Institute, Ljubljana, Slovenia

[3] Faculty of Electical Engineering, University of Ljubljana, Tržaška 14, Ljubljana, Slovenia

uros.puc@mps.si

## Abstract

Utilization of non-destructive and non-invasive methods for the real-time underwater remote sensing is one of the challenging and desired tasks in the maritime security and safety as well as the harbour surveillance. Our aim was to develop and verify advanced electromagnetic sensors for a seabed objects detection and inspection. The seabed is a complex environment often covered with the sand, dense aquatic vegetation and rocks. Hence, it is difficult to investigate the seabed by only one conventional method. Usually a combination of the sonar and video system is used for the detection and classification of underwater targets. In this paper, we verified the operation and efficiency of two EM imaging sensors, a ground penetrating radar (GPR) and an electromagnetic continuous wave sensor (CWEMS).

**Keywords**: electromagnetic sensors, GPR, remote sensing, underwater detection.

## 1 Introduction

The underwater remote sensing technology plays a key role in investigations of the underwater environment and detection of unknown objects. Nowadays, several techniques (Fig. 1) exist in this field; the most important among them are acoustic, electromagnetic and optical devices [1-6]. Electromagnetic (EM) sensors have long been recognized as a useful tool for the geophysical exploration and remote sensing. However, no system currently available on the market is capable to accurately survey and map the location of objects buried under the bottom sediments or vegetation. The technology that we selected includes an adapted version of the ground penetrating radar (GPR) and the continuous wave electromagnetic sensor (CWEMS) which are competing tools against the SONAR (sound navigation and ranging) and metal detector. The preliminary results achieved by these two EM sensing methods are presented in this paper.

## 2 EM sensing methods

The EM propagation in water is very different from the propagation through air due to the high permittivity and electrical conductivity of water. In freshwater the conductivity is 0.1 - 10 mS/m, whereas in sea water this value is around 4 S/m. Another difference is a greater attenuation loss of the propagation pulses in water. It depends on the selected frequency and salinity of water. Hence, for the freshwater and sea water the attenuation loss at 100 MHz is 0.1 $dBm^{-1}$ and 100 $dBm^{-1}$, respectively, whereas at 1 GHz it increases to 1 $dBm^{-1}$ and 1000 $dBm^{-1}$, respectively. Furthermore, the propagation velocity and corresponding wavelength in water decrease by a factor of about 10 in comparison to the velocity and wavelength in air [1-3].

### 1.1 Ground penetrating radar

The ground penetrating radar or GPR is a non-destructive geophysical method based on the propagation of high frequency electromagnetic waves. The GPR method images structures in the ground that are related to changes in the dielectric properties [1]. If a very short EM pulse is transmitted by an electric dipole into the medium, it propagates in the subsurface with a velocity depending on the electrical properties of the medium. For a layered subsurface with contrasting electrical properties, a part of the EM energy is reflected back to the surface where it is detected by a receiver dipole and recorded. Synchronization between the transmitter and the receiver systems allows the determination of the time taken for the EM pulse to be reflected back. In our case, several candidate sites were surveyed to find out a test area with the desired water depth for the underwater GPR investigation. We selected the lake Podpeč, a location near the city of Ljubljana. The lake is located in the Karst region and it is the deepest lake in Slovenia with a depth of 47 m.  The experimental work was conducted using a commercial GPR system equipped with a 250 MHz and 50 MHz antenna. The design of the 250 MHz antenna ensured that the transmitted radar energy is emitted only from the bottom of the antenna housing and protects the receiver element from an external noise. The antenna was placed in a rubber dinghy on the water surface. The experiment with a 50 MHz antenna was performed from the wooden pier at the lake shore. The 50 MHz antenna with a flexible "snake"-like design allows easy manoeuvring and provides optimum results in difficult environments as well as a deeper signal penetration into the medium.

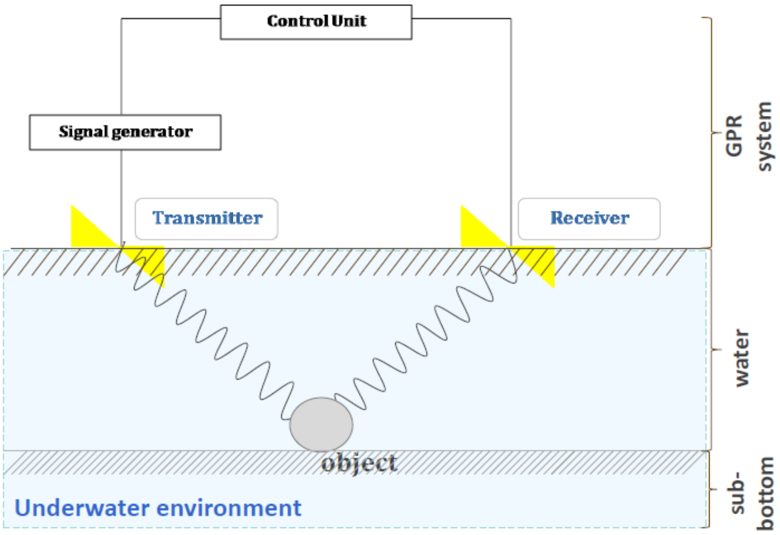

**Figure 1**: The GPR system for underwater measurements.

## 1.2 Continuous wave electromagnetic sensor

In the CWEMS method, the primary magnetic field produced by the transmitter coil is changed in such a way that a higher density of magnetic flux lines occurs due to the presence of metallic objects [5]. The modified magnetic field is detected by a receiver coil. Additionally, eddy currents occur which originate from metallic objects and have an important effect on the induction of the receiver coil field. The CWEMS sensor has proven to be very effective in detecting both ferromagnetic and nonmagnetic metallic targets lying on the sea bottom or buried in the seabed. The scenario for CWEMS monitoring was comprised of the CWEMS sensor composed of eight probes mounted on a wooden pole (Fig. 2). Moreover, the constructed CWEMS sensor was moving on a quadratic holder made from wood to reduce destructive interferences from other objects. For the investigation purposes, samples with simple circular and rectangular cross sections were selected.

The samples were located on the wooden plate with the constant distance from the sensor which was in the range of a few centimetres. The investigated area was limited with dimensions of 45 cm by 90 cm. A special software was prepared to acquire signals from all eight probes simultaneously. The raw signals in a matrix form were imported in the Matlab programming environment. In order to obtain a more realistic circular or rectangular cross section of the detected objects, the 2-D interpolation between the data in matrix was applied. Furthermore, the obtained plots were smoothed using a MatLab built-in cubic interpolation function. The final results were visualized as an intensity plot.

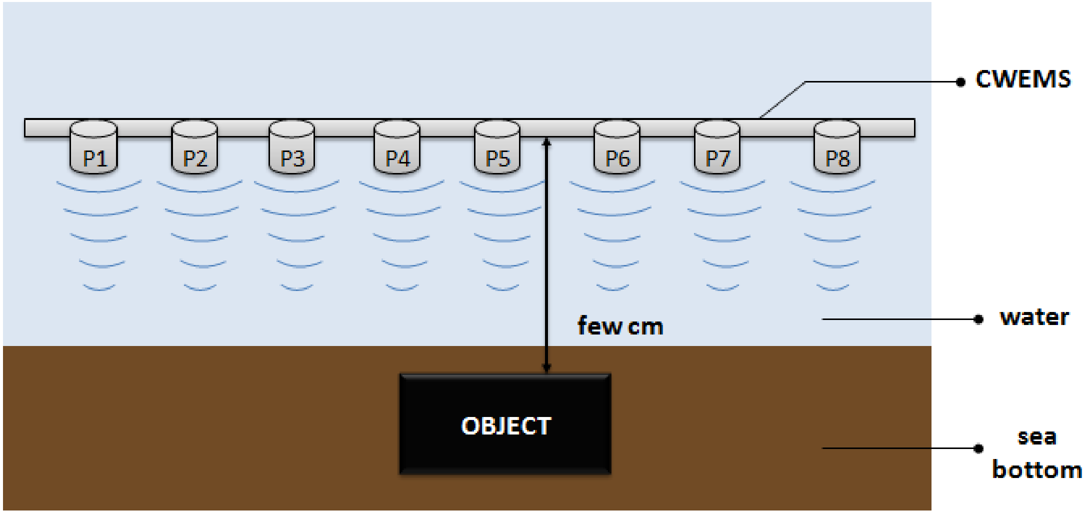

**Figure 2**: The CWEMS sensor adapted for underwater operation.

## 3 Results and discussion

The calculated GPR profile with a 50 MHz antenna shows that we reached a penetration depth of more than 3 m (Fig. 3, right). A distinct subsurface layer with a depth close to 1 m is also visible in addition to a rather homogenous layer observed up to at least 5 m in depth and possibly even lower. Namely, in the Fig. 3 the depth scale is given in the left-hand scale as the double time needed for the calculation of the electromagnetic waves to travel the distance from the transmitting antenna to the observed object or structure and back to the receiving antenna. In the right-hand scale, this double time is transformed to the real underwater depth, using the velocity of the transmission of electromagnetic waves through the water layer, which is about ten times lower than in the air. For the subsurface layer, the velocity of the transmission of electromagnetic waves is much larger than in the water, usually three or four times. The size of the homogeneous subsurface layer is therefore much larger than depicted from the scale, and can be estimated to be at least 10 m.

From the GPR profile with a 250 MHz antenna the results are similar (Fig. 3, left). While the penetration depth is not as deep as with the 50 MHz antenna, the resolution is better, so it is possible to see a more detailed structure of the first meter of the subsurface layer. From Fig 3 it is clear that both selected frequencies are useful for the investigation of the subsurface below the lake bottom. The low frequency 50 MHz antenna provides the deep penetration of more than 10 m, and the higher frequency 250 MHz antenna provides a higher resolution of the observed region closer to the surface.

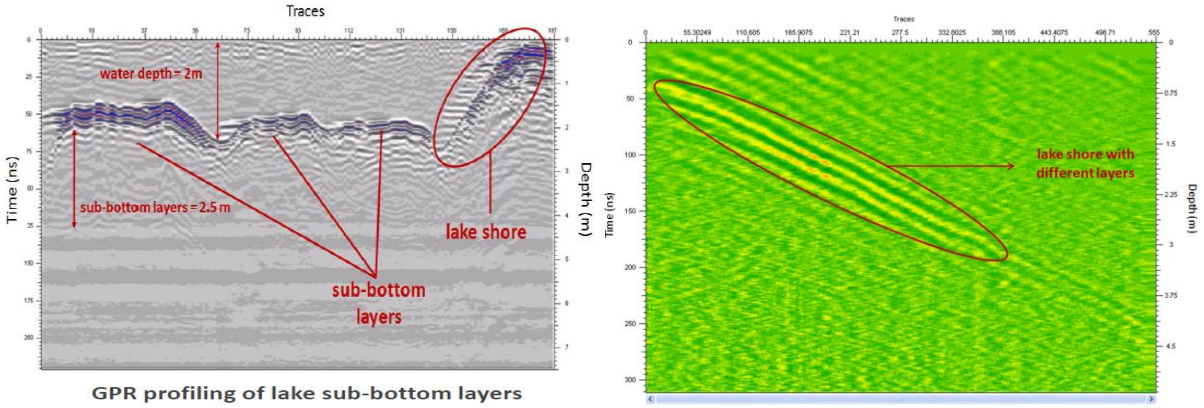

**Figure 3**: 250 MHz (left) and 50 MHz (right) lake profiling with the GPR.

The CWEMS method is used to characterize whether the material within the sensor range is metallic or not. Apart from this, we found out that different metallic objects give the various responses. The probes in Fig. 2 are equidistantly positioned on a wooden pole. In this case, we investigated objects with different dimensions and shapes. The raw EM responses were recorded in a matrix form. With the basic imaging method based on cubic interpolation, 2-D images were obtained (Fig. 4). From these images one can notice that not only the shape and orientation of the objects could be detected, but also some information regarding the metal material characterization could be defined. In Fig. 4 there is a major difference in EM responses between aluminium and iron objects, due to the eddy currents which originate in metallic objects and they are particularly expressed in the case of conductor materials such as aluminium and not as much in the case of the ferro-magnetic materials such as iron.

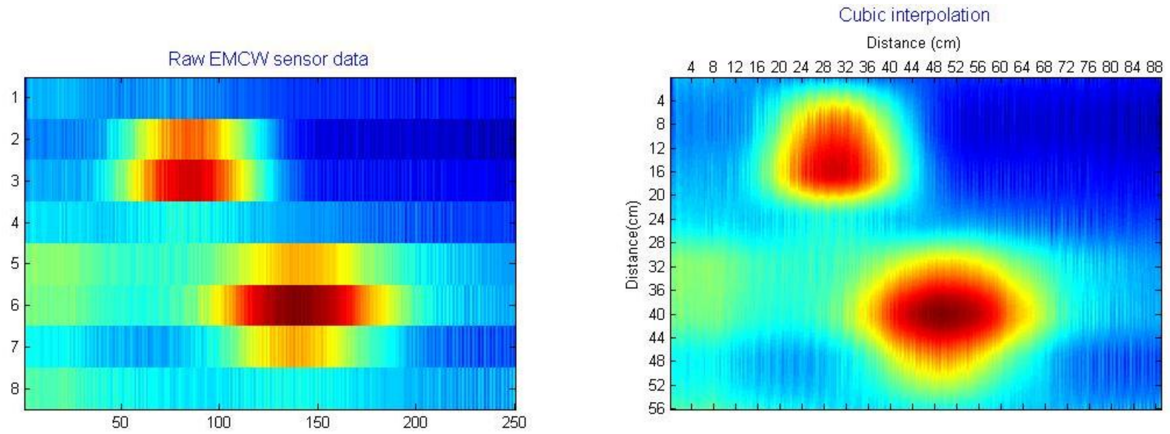

**Figure 4**: CWEMS imaging.

## 4 Conclusions

We measured the structure of the lake subsurface with a commercial GPR at frequencies of 50 MHz and 250 MHz, respectively. The used GPR system is capable to observe the subsurface below 10 m and through more than 3 m of water with the 50 MHz antenna. However, a more detailed structure can be obtained with a higher frequency 250 MHz antenna at the expense of a lower penetration depth. The GPR method has several potential applications in the general exploration and security of the underwater environment as well as in the oil and gas industry. In addition, we measured and imaged several metal objects of different sizes and shapes with the CWEMS sensor. The discrimination between various metallic object is possible, which makes the sensor appropriate for the underwater security imaging.

## References:

[1] D. J. Daniels, Ground Penetrating Radar, 2nd ed., UK: The Institute of Electrical Engineers, 2004, pp. 1-352.
[2] M. J. Harry, Ground Penetrating Radar: Theory and Applications, 1st ed., The Netherlands: Elsevier Science, 2009, pp. 1-176.
[3] D. Margetis, Pulse propagation in sea water: the modulated pulse, Progress In Electromagnetics Research, vol. 26, pp. 89-110, 2000.
[4] Annan, A. P. GPR Methods for Hydrogeological Studies, In: Hydrogeophysics, edited by. Y.Rubin and S.S. Hubbard, Springer, Netherlands, 2005, pp. 185-213.
[5] I. J. Won, D. A. Keiswetter, and T. H. Bell, Electromagnetic induction spectroscopy for clearing landmines, Geoscience and Remote Sensing, IEEE Transactions on, vol. 39, pp. 703-709, 2001.
[6] T. Lasri, D. Glay, L. Achraït, A. Mamouni, and Y. Leroy, Microwave Methods and Systems for Nondestructive Control, Subsurface Sensing Technologies and Applications, vol. 1, pp. 141-160, 2000.

# For wider interest

The underwater remote sensing technology plays a key role in underwater investigation and unknown objects detection. Electromagnetic (EM) principles have long been recognized as a useful tool for the geophysical exploration and remote sensing. The technology that we selected includes an adapted version of the ground penetrating radar (GPR) and the continuous wave electromagnetic sensor (CWEMS), which are competing methods against the SONAR (sound navigation and ranging) and metal detector. The ground penetrating radar or GPR is a non-destructive geophysical method, which is based on the propagation of high frequency electromagnetic waves. The GPR method images structures in the ground that are related to changes in the dielectric properties. In addition, the CWEMS sensor has proven to be very effective in detecting both, ferromagnetic and nonmagnetic metallic targets, lying on the sea bottom or buried in the seabed. We measured the structure of the lake subsurface with a commercial GPR at frequencies of 50 MHz and 250 MHz, respectively. The used GPR system is capable to observe the subsurface below 10 m and through more than 3 m of the water layer with the 50 MHz antenna. However, a more detailed structure can be obtained with a higher frequency 250 MHz antenna at the expense of a lower penetration depth. The GPR method has several potential applications in the general exploration and security of the underwater environment as well as in the oil and gas industry. In addition, we measured and imaged several metal objects of different sizes and shapes with the CWEMS sensor. The discrimination between various metallic objects is possible, which makes the sensor appropriate for the underwater security imaging.

# Estimating the size of the maximum inclusion in a large sample area of steel

**Nuša Pukšič**[1,2], **Monika Jenko**[1]

[1] Institute of Metals and Technology, Ljubljana, Slovenia

[2] Jožef Stefan International Postgraduate School, Ljubljana, Slovenia

nusa.puksic@imt.si

**Abstract.** Non-metallic inclusions influence the properties of steel and finished steel products. The methods relating to statistics of extremes are effective for the purpose of predicting the size of the maximum inclusion, which is an important parameter in the quality control and lifetime estimation. A steel sample with two types of inclusions is used to demonstrate the use of the extreme value theory in practice. The results of the general extreme value method are compared to the results of the mixture and the competing risk models. The competing risk model gives the best fit to data, and predicts the largest inclusions.

**Keywords**: steel; inclusions; statistics of extremes; GEV; mixture; competing risk; model

## 1 Introduction

Non-metallic inclusions, formed during the steel production process, have a great impact on the properties of steel and finished steel products. The detection and estimation of the size of the largest inclusions is an important consideration in quality control and lifetime estimation of steel and steel products.

The size distribution of inclusions in steels is found to have a log-normal form [1,2,3]. The standard method of fitting the log-normal distribution requires a quantitative measurement of inclusion sizes right across the size range to obtain a good fit. Measurements of small inclusions with sizes smaller than 3 μm are unreliable. On the other hand, the statistic of large inclusions is affected by their low occurrence rate.

When using prediction methods based on the extreme value theory, only measurements of the maximum inclusions in randomly chosen areas are needed. The general extreme value (GEV) statistics method can be used to estimate the maximum size of inclusions in a large amount of steel.

The estimation of the sizes of extreme inclusions is affected by the presence of multiple types of inclusions in a single steel grade. When the presence of multiple types of inclusions is obvious and the types can be distinguished by their shapes, it is good practice to apply the method to each type of inclusions separately. This will also enable one to consider each set of inclusions in connection with its harmfulness [4]. Unfortunately, this approach prolongs the manual analysis and it is difficult to implement it in an automatic image analysis. The mixture and the competing risk models were suggested, where the diversity of the inclusions is taken into account statistically [4,5].

In this paper, an overview of the statistical approach is given, followed by the results of the analyses of the data obtained by the automatic image analysis from a spring steel sample.

## 2 Overview of statistical methods

### 2.1 The general extreme value (GEV) method

For distributions decreasing exponentially at upper tails, the distribution of the largest values can be described by Gumbel distribution. If the distribution decreases following a power law, the distribution of the largest values is either Fréchet- or Weibull-like. The GEV distribution groups the three types:

$$P(x) = \exp\left\{ -\left(1+\xi\left(\frac{x-\lambda}{\alpha}\right)\right)^{-1/\xi} \right\}, \tag{1}$$

where *P(x)* is the cumulative probability, $\lambda$ and $\alpha$ are the location and scale parameters, and $\xi$ is the tail index. The tail index determines the type of the distribution: a Fréchet distribution for $\xi > 0$, a Weibull distribution for $\xi < 0$, and a Gumbel distribution for $\xi \rightarrow 0$.

A standard inspection area $S_0$ is defined. The area of the maximum inclusion in $S_0$ is measured in $N$ such areas. Then, the square root of the area of each measured inclusion is calculated, $z = \sqrt{area_{\max}}$. The cumulative probability $G(z_i)$ of the $i$-th largest measured inclusion size $z_i$ can be calculated by:

$$G(z_i) = \frac{z_i}{N+1} = \exp\left\{-\exp\left(-\frac{z_i-\lambda}{\alpha}\right)\right\}, \tag{2}$$

where $z_i$ is the $i$-th in the series of $\sqrt{area_{\max,i}}$ ordered by size. The probability plot of $-\ln(-\ln(G(z_i)))$ versus $z_i$ can then be used for the basic diagnostic [1].

For the estimation of the extreme inclusions size in a large examined area of steel $S$, the return period is defined as $T = S/S_0$. The characteristic size of the maximum inclusion, denoted by $z_S$, expected to be exceeded exactly once in an area $S$, can be defined by solving the equation $G(z_S) = 1 - 1/T$ to give:

$$z_S = \lambda - \frac{\alpha}{\xi}\left(1 - \left(-\ln\left(1-\frac{1}{T}\right)\right)^{-\xi}\right). \tag{3}$$

### 2.2 The mixture model and the competing risk model

The mixture model assumes multiple types of inclusions and the Gumbel distribution for the maximum inclusions of each type. When we have two types of inclusions, the areas are then also of two kinds: containing inclusions of the type 1 and of the type 2, the proportion of the second kind being $p$. The observation process is such that the kind of area being measured remains unknown (as in automatic image analysis, where sizes of inclusions are recorded, but not types) [4]. The distribution function is then of the form:

$$F_{mix}(x) = (1-p)G_1(x) + pG_2(x), \tag{4}$$

where $G_i$ are Gumbel distribution functions for $i = 1, 2$ and $0<p<1$.

The more natural assumption is that inclusions of both types are present throughout the material and the measuring process detects the inclusion that happens to be the largest in a given area. The competing risks model assumes, that the sizes of the largest inclusions of different types follow independent Gumbel distributions $G_1$ and $G_2$ [4]. The distribution function is then of the form:

$$F_{risk}(x) = G_1(x)G_2(x)\,. \tag{5}$$

## 3 Results and discussion

To obtain the data, 544 sample areas, each of 0.27 mm$^2$, from a single steel slab were investigated. The area of each inclusion larger than 3 μm$^2$ was measured using automatic image analysis. The results of the GEV analysis are given first, followed by the results of the mixture and the competing risk models.

The fit of the GEV model to the data gives the estimates for the parameters of the distribution, Table 1. With the estimated parameters, the size of the largest inclusions can be calculated (Eq. 3) as a function of the number of sample areas $S_0$ to be investigated. Results are shown in Figure 1.

Manually inspecting the samples, we see two types of inclusions contributing to the set of maximum inclusions. The parameter values obtained by fitting both models to the data are gathered in Table 1. The fit of both models to data and estimated inclusion sizes are shown in Figure 2.

Predictions of the three models show appreciable discrepancies. The competing risk model, which seems to best capture the underlying features and also gives a good fit to the data, predicts the largest inclusions.

**Table 1:** Estimated parameter values for the GEV model, the mixture model and the competing risk model.

| GEV | | Mixture model | | Competing risk model | |
|---|---|---|---|---|---|
| Parameter | Value | Parameter | Value | Parameter | Value |
| $\alpha$ | 1.96 | $\alpha_1$ | 26.4 | $\alpha_1$ | 3.39 |
| $\lambda$ | 6.37 | $\lambda_1$ | 41.6 | $\lambda_1$ | 2.23 |
| $\xi$ | –0.0089 | $\alpha_2$ | -0.97 | $\alpha_2$ | 58.8 |
| | | $\lambda_2$ | -0.98 | $\lambda_2$ | 90.3 |
| | | $p$ | 0.501 | | |

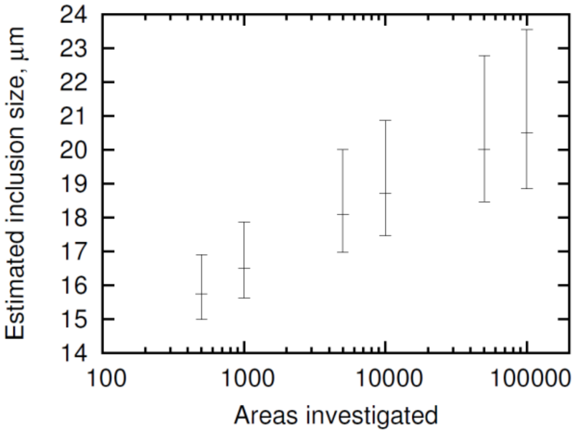

**Figure 1:** The maximum inclusion size estimated from the parameters of the GEV model with 95% confidence intervals.

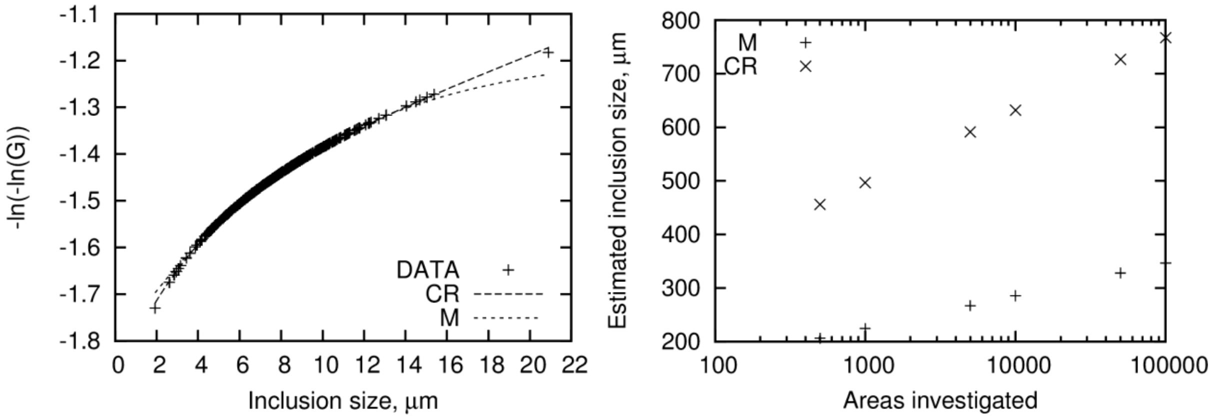

**Figure 2:** The Gumbel probability plot with a comparison of the mixture model (M) and the competing risks model (CR) fits to the data, left. The estimated inclusion size for the largest inclusions in each model, right.

## References:

[1]C. W. Anderson, G. Shi, H.V. Atkinson, and C.M. Sellars. The precision of methods using the statistics of extremes for the estimation of the maximum size of inclusions in clean steels. *Acta Materialia,* 48:4235–4246, 2000.

[2]H.V. Atkinson, and G. Shi. Characterization of inclusions in clean steels: a review including the statistics of extremes methods. *Progress in Materials Science,* 48:457–520, 2003.

[3]Y. Murakami. *Metal Fatigue: Effects of Small Defects and Nonmetallic Inclusions.* Elsevier, 2002.

[4]S. Beretta, C. Anderson, and Y. Murakami. Extreme value models for the assessment of steels containing multiple types of inclusion. *Acta Materialia,* 54:2277–2289, 2006

[5]C.W. Anderson, G. Shi, H.V. Atkinson, C.M. Sellars, and J.R. Yates. Interrelationship between statistical methods for estimating the size of the maximum inclusion in clean steels. *Acta Materialia*, 51:2331–2343, 2003.

## For wider interest

The properties of steel and finished steel products are affected by non-metallic inclusions, formed during the steel production process. The detection and estimation of the size of the largest inclusions can be an important parameter in the quality control and lifetime estimation of steel and steel products. Statistical methods can be helpful, since they can provide an additional insight not necessarily apparent from the raw data. There are a few options that allow us to estimate the size of the largest inclusion to be expected. Unfortunately, there can be great discrepancies in the predictions from different models. Care should be taken when choosing a method and a model to investigate and analyse your product. Any of the models presented in this paper, on the other hand, can be used as a means of comparing different grades of steels or to define bounds, within which the quality of a given grade of steel is still acceptable.

# Solvent capabilities of liquid and supercritical xenon

**Kristian Radan, Boris Žemva**

Department of Inorganic Chemistry and Technology, Jamova 39, Jožef Stefan Institute, Ljubljana, Slovenia

Jožef Stefan International Postgraduate School, Ljubljana, Slovenia

kristian.radan@ijs.si

**Abstract.** A great majority of "interesting" compounds in fluorine and noble gas chemistry are thermodynamically unstable, highly oxidative and thus hard to isolate and characterize materials. Since the ultimate characterization - structural determination is very often related to a route to crystalline products, the aforementioned unique properties severely restrict the choice of a solvent for these compounds to a few inorganic ($BrF_5$, $IF_5$, $SF_6$, anhydrous HF, SOClF, etc.) and in some cases organic solvents ($CH_3CN$, fluorotrichloromethane, etc.). However, several coordination complexes with noble gas fluorides for example, especially those with large polyionic units [1], remain insoluble in solvents mentioned above. In this work we report some preliminary results of three experiments made in order to investigate the solvent potential of liquid and near-supercritical xenon on these systems.

**Keywords**: inorganic fluorides, compounds of noble gases, liquid xenon, supercritical xenon.

## 1 Introduction

The idea of using liquid xenon as a solvent is not new. The experimental evidence was presented by Rentzepis and Douglass in 1981 in the form of UV, visible, IR and NMR spectra which showed that liquid Xe can be used as a fluid solvent for several biological and organic molecules at temperatures ranging from near room temperature to about –100 °C [2].

Xenon is particularly useful among the noble gases because its liquid phase occurs in the fairly convenient conditions of ~16 °C and 58 atm, so that solution studies can be carried out near room temperature (Fig. 1). Xenon also possesses a polarizability of $4.01 \cdot 10^{-24}$ $cm^3$ [3] which is relatively large when compared to the other rare gases [2], thereby Xe may be expected to have significant, but not chemically or structurally disruptive, interactions with solutes: Xe should approach the behaviour of an ideal inert solvent. Because of its optical transparency in most of the vacuum UV and all of the UV, visible and IR spectral regions, spectra may be recorded with Xe over a very wide spectral range, leaving the character of the molecular environment intact. Moreover, a change in spectral features arising from an environmental change, solvent fluorescence or spectral interference, is also avoided. Thus, spectra are often sufficiently well resolved and intense to permit vibrational assignments and kinetic studies with visible, UV, Raman and NMR spectroscopies even at low solubility. Soon after the discovery of solvent properties of liquid xenon, many experiments were done to determine the solubility of various organic substances in liquid [4] and supercritical Xe ($T_c$ = 16 °C) [5], covering the pressure range of 60–95 atm at temperatures from 0 °C to 40 °C for liquid and 100–225 atm in a 34.9–45 °C range for supercritical conditions. Authors reported that the large organic neutral species dissolved readily, while attempts to dissolve ion pairs or free ions failed. In addition, the other research groups used liquid [6–9] and supercritical Xe [6] as a solvent for chemical reactions.

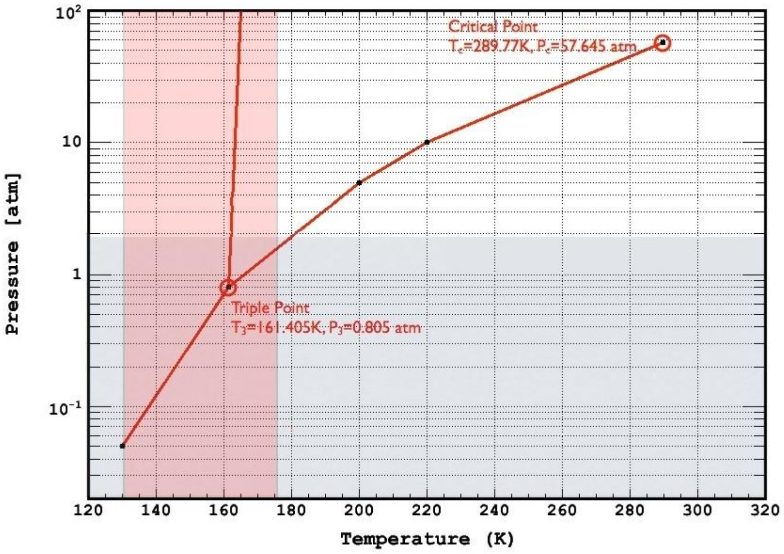

**Figure 1 :** Xenon phase diagram. Adapted from Solid Xenon R&D Project by Jonghee Yoo (FERMILAB) [10].

However, despite some cryospectroscopic investigations of binary noble gas fluorides in liquid Xe by Nabiev and co-workers [11], we have not been able to find any reports of liquid nor supercritical xenon used as a solvent for any kind of inorganic compounds. Some papers [12, 13] describe reactions with liquefied Xe, in terms of a reactant - reducing agent or complex ligand and without mentioning any solvent effects. Hereby, we present some preliminary results of the first investigations on the solubility of the compound $XeF_2 \cdot 2SnF_4$ in liquid and near-critical Xe. Its chemical inertness, high density and relative high polarizability combined with low temperature conditions make xenon an attractive candidate as a solvent for this kind of coordination compounds.

## 2 Materials and methods

*Reagents.* Xenon (Messer Griesheim, 99.997 %) was used as purchased. $SnF_4$ was synthesized by fluorination of $SnF_2$ (Aldrich, 99%) with excess $F_2$ (Solvay Fluor, 98–99% by volume) at room temperature in anhydrous HF (aHF; Fluka, purum), which was treated with $K_2NiF_6$ (Ozark-Mahoning, 99%) for several days prior to use. The purity of $SnF_4$ was checked by the Raman spectroscopy. Xenon difluoride was prepared by photochemical reaction between Xe and $F_2$ at room temperature [14]. $XeF_2 \cdot 2SnF_4$ was synthesized from $SnF_4$ and excess $XeF_2$ in aHF. After decantation of a $XeF_2$ rich supernatant, the compound was isolated by pumping off volatiles at 0 °C on a vacuum line.

*Apparatus and techniques.* A Teflon and FEP reaction line and nickel vacuum system were used as described previously [15]. For the experiment with xenon in near supercritical conditions argon arc welded nickel pressure and weighing vessel (Fig. 2A), equipped with a nickel valve was constructed and used. The volume of the reaction vessel was 5.8 ml and was tested up to 110 atm. For solubility experiments with Xe between its melting (–112 °C) and boiling point (–108 °C), a reaction vessel was made of a 16 mm i.d. (19 mm o.d.) FEP (fluorinated ethylene propylene) tubing and equipped with a Teflon valve and a Teflon-coated stirring bar. The volume of this vessel was 64 ml, which allowed 7.7 mmol of Xe to expand to ~3.5 bar at room temperature. A smaller reaction vessel was made of a 3 mm i.d. (6 mm o.d.) FEP tubing equipped with the same Teflon valve (Fig. 2B). This vessel (working volume 0.74 ml), tested up to 45.4 atm, allowed experiments with liquid xenon in a temperature range from –112 °C to –19 °C with a maximum pressure of 25 atm.

All solids were stored and handled in an argon atmosphere in a glovebox with maximum water content of less than 0.5 ppm (LABstar, MBRAUN, Garching, Germany). Transfer of all volatiles (aHF, Xe) was carried out by condensation under static vacuum at –196 °C. All reaction vessels were passivated with $F_2$ prior to use.

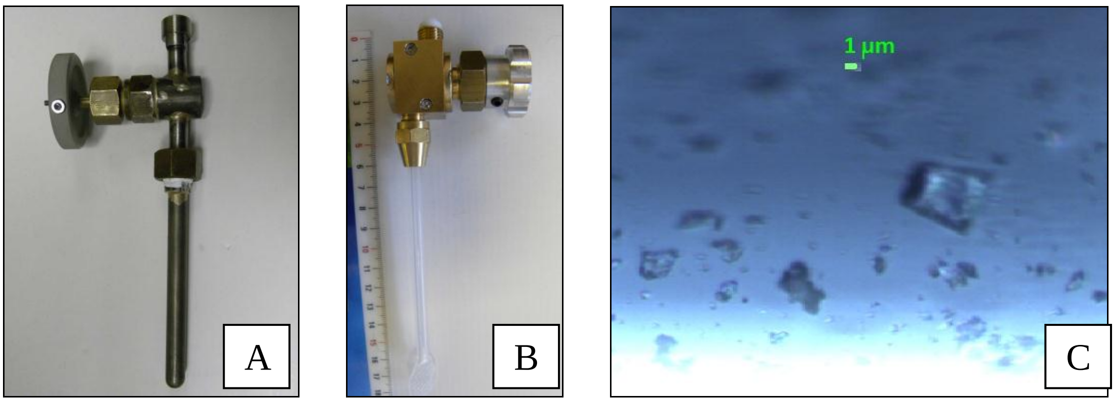

**Figure 2**: A – Nickel vessel for experiments with supercritical xenon. B – Thick walled FEP reaction vessel. C – Crystals of an undefined composition $aXeF_2{\cdot}bSnF_4$ grown from liquid xenon.

## 3 Experimental procedure and results

*Near supercritical conditions.* On 17 mg of amorphous white solid $XeF_2{\cdot}2SnF_4$, 6.2 g of Xe was condensed reaching the solvent density of 1.07 g/cm$^3$ ($\varrho_c$ = 1.11 g/cm$^3$) and approximately 90 atm of pressure at room temperature. After 79 days, Xe was slowly pumped off at –20 °C and the reaction vessel was opened in the glovebox. A white, slightly crystalline material was accumulated on the top of the vessel and inside the valve. Attempts to isolate a suitable crystal for the X-ray structural analysis were unsuccessful. The Raman spectrum of this material confirmed the unchanged compound $XeF_2{\cdot}2SnF_4$.

*Liquid xenon.* First, the process of liquefying was studied at low temperatures and pressures in an ordinary FEP reaction vessel in order to obtain a general impression of the behavior of Xe near its melting and boiling point in these systems (expansion, amounts, liquefying and boiling rate, possible interactions with $XeF_2{\cdot}2SnF_4$ or FEP walls, etc.). Using liquid nitrogen, the known amount of Xe from this vessel was then quantitatively condensed into a smaller thick-walled FEP reaction vessel, so that liquid xenon reached half of its height as the temperature was raised to –19 °C. A mixture of $XeF_2$ (15 mg) and $SnF_4$ (25 mg) was added in the vessel prior to the experiment. The reaction vessel was held overnight in the cryostat at –25 °C. The following day, a few crystals appeared on the liquid-gas interface, but were lost during slow removal of Xe on the vacuum line. However, some crystalline material was found under a microscope magnification (Fig. 2C) and the Raman spectroscopy showed (Fig. 3) that reaction between $XeF_2$ and $SnF_4$ in liquid xenon occurred, producing an unknown adduct $aXeF_2{\cdot}bSnF_4$. Further investigations on this product are still in progress.

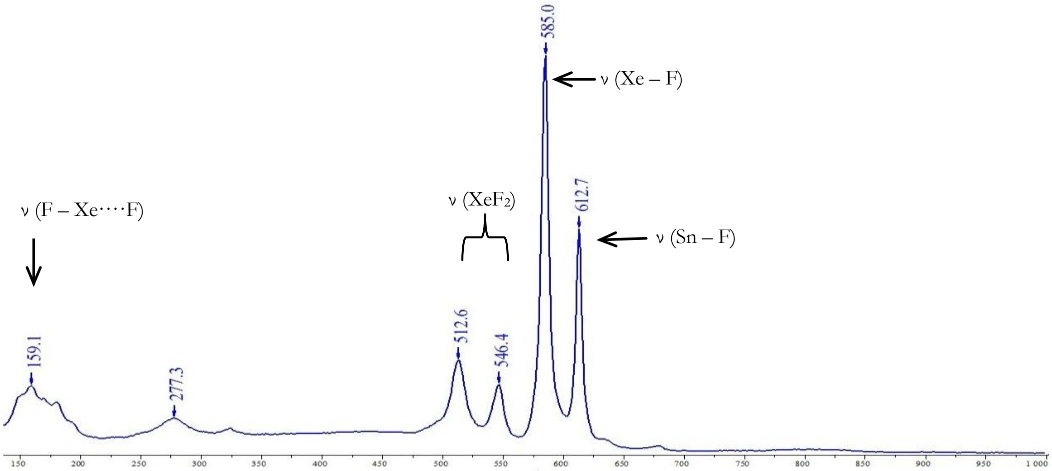

**Figure 3:** The Raman spectrum and tentative assignments of the undefined crystalline product $aXeF_2{\cdot}bSnF_4$.

## References:

[1]L. Graham, O. Graudejus, N. K. Jha, N. Bartlett. Concerning the nature of $XePtF_6$. *Coordination Chemistry Reviews,* 197:321-334, 2000.

[2]P. M. Rentzepis, D. C. Douglass. Xenon as a solvent. *Nature*, 293:165-166, 1981.

[3]G. W. Castellan. *Physical Chemistry, 2nd Edition.* Addison-Wesley, Reading MA, 1971.

[4]D. B. Marshall, F. Strohbusch, E. M. Eyring. Solubility of organic substances in liquid xenon. *Journal of Chemical & Engineering Data,* 26: 333-334, 1981.

[5]V. J. Krukonis, M. A. McHugh, A. J. Seckner. Xenon as a Supercritical Solvent. Journal of Physical Chemistry, 88(13): 2687-2689, 1984

[6]R. K. Upmacis, M. Poliakoff, J. J. Turner. Structure and thermal reactions of dihydrogen complexes: The IR characterization of $M(CO)_5(H_2)$ (M = Cr, Mo, and W) and cis-$Cr(CO)_4(H_2)_2$ in liquid xenon solution and the formation of HD during exchange of $H_2$ and $D_2$. *Journal of the American Chemical Society*, 108(13):3645-3651, 1986.

[7]M. B. Sponsler, B. H. Weiller, P. O. Stoutland, R. G. Bergman. Liquid Xenon: An effective inert solvent for C–H oxidative addition reactions. *Journal of the American Chemical Society*, 111(17):6841-6843, 1989.

[8]P. A. Hamley, S. G. Kazarian, M. Poliakoff. Hydrogen-Bonding and Photochemistry of Organometallics in Liquid Xenon Solution in the Presence of Proton Donors: A Low Temperature Infrared Study of the Interaction of $(CF_3)_3COH$ with $(C_5Me_5)M(CO)_2L$ (M = Mn and Re; L = CO, $N_2$, and $H_2$) and with $(C_5Me_5)V(CO)_4$. *Organometallics*, 13(5):1767-1774, 1994.

[9]A. A. Bengali, B. A. Arndtsen, P. M. Burger, R. H. Schultz, B. H. Weiller, K. R. Kyle, C. B. Moore and R. G. Bergman. Activation of carbon-hydrogen bonds in alkanes and other organic molecules by Ir(I), Rh(I) and Ir(III) complexes. *Pure and Applied Chemistry,* 67(2):281-288, 1995.

[10] Jonghee Yoo. Solid Xenon project at Fermilab. In *Dark Matter 2010 Presentations,* Ninth UCLA Symposium on Sources and Detection of Dark Matter and Dark Energy in the Universe, Marina del Rey, California, USA, 2010.

[11] Sh.Sh. Nablev, V.D. Klimov, B.S. Khodiev. Cryospectroscopic analysis of individual xenon fluorides. *Journal of Fluorine Chemistry*, 58(2-3):293, 1992.

[12] C. T. Goetschel, K. R. Loos. Reaction of xenon with dioxygenyl tetrafluoroborate. Preparation of FXe-$BF_2$. *Journal of the American Chemical Society*, 94(9):3018-3021, 1972.

[13] S. Seidel, K. Seppelt, C. van Wüllen, X. Y. Sun. The Blue $Xe_4^+$ Cation: Experimental Detection and Theoretical Characterization. *Angewandte Chemie International Edition*, 46(35):6717-6720, 2007.

[14] A. Šmalc, K. Lutar. *Inorganic Syntheses*, *Vol. 29*. R. N. Grimes, 1992.

[15] H. Borrmann, K. Lutar, B. Žemva. Manganese(II) Hexafluoroarsenate: Unusually High Coordination of Manganese(II) in a Fluorine Environment. *Inorganic Chemistry*, 36(5):880–882, 1997.

## For wider interest

The single crystal X-ray diffraction is a very powerful tool to get structural information on chemical compounds. Crystals are usually grown from solutions of these compounds and here the choice of a solvent plays a crucial role. Our research field involves syntheses and characterizations of new coordination compounds with binary fluorides as ligands ($XeF_2$, $XeF_4$, $KrF_2$, $AsF_3$, HF, etc.), as well as preparations of new binary and ternary fluorine compounds. Because of their high reactivity and/or low solubility in classical inorganic solvents, finding a suitable solvent and optimal crystallization conditions very often represents a difficult challenge. In addition, research on solvents and solutions has again become a topic of interest because many of the solvents commonly used in laboratories and in the chemical industry are considered as unsafe for reasons of the environmental protection, mainly because they are often used in huge amounts and because they are volatile liquids that are difficult to contain. An introduction of cleaner technologies has become a major concern throughout both the academia and industry. This includes the development of environmentally benign new solvents, sometimes called neoteric solvents (neoteric - recent, new, modern), constituting a class of novel solvents with desirable, less hazardous properties. This term covers supercritical fluids, ionic liquids, and also perfluorohydrocarbons. Despite its high price, liquid xenon's good solvating properties, optical transparency, very convenient critical properties, high density near critical conditions and inertness, makes it a promising solvent useful in the fundamental as well as applied research by opening a new possibility for high quality products.

# A chemometric approach towards transmembrane region prediction of protein sequences

**Amrita Roy Choudhury**[1,2], **Marjana Novič**[1]

[1] Laboratory of Chemometrics, National Institute of Chemistry, Ljubljana, Slovenia

[2] Jožef Stefan International Postgraduate School, Ljubljana, Slovenia

amrita.roychoudhury@ki.si

**Abstract.** Transmembrane proteins play vital roles in maintaining the normal cell physiology. They are also important as potential drug targets. Therefore, there is an immense academic and pharmaceutical interest in these proteins. In our lab, we have tried to use chemometric approach along with other computational and experimental methods towards elucidation of transmembrane protein structures and functional mechanisms. Here we present a data-driven chemometric classification model based on mathematical descriptors to discriminate between transmembrane and non-transmembrane regions of protein sequences. The model is then utilized to predict the transmembrane regions of specific proteins, and also to differentiate between transmembrane and globular proteins.

**Keywords**: chemometric model, transmembrane region prediction tool, amino acid adjacency matrix, mathematical descriptors.

## 1 Introduction

Transmembrane proteins play crucial roles acting as transporters, receptors, helping in cell signalling etc., and thus help to maintain the normal cell functioning. They are also of interest for the pharmaceutical industry with more than a half of the drugs currently available on the market targeting the transmembrane proteins [1]. However, the structures and functional mechanisms of a very few of these proteins are known down to date owing to experimental difficulties. Although, around 25% of the Open Reading Frames code for transmembrane proteins, they account for only ~2% of the Protein Data Bank (PDB) structures [2]. A vast majority of these proteins, therefore, remain unexplored and present challenges to both computational and experimental procedures. Our aim is to utilize different chemometric approaches in coordination with experimental and other computational methods towards working in this direction.

The first step towards the elucidation of structures and functional mechanisms of transmembrane proteins is to know the exact number and position of their transmembrane regions. For this purpose, we have developed a transmembrane region prediction algorithm, based on mathematical descriptors and neural networks. The advantage of our algorithm over other existing ones is that it uses mathematical descriptors derived from the sequence information alone, and is independent of physiochemical property indices and evolutionary information. The algorithm is able to well discriminate between the transmembrane and the non-transmembrane regions of the α-transmembrane proteins. The developed model is then used to predict the transmembrane regions of unknown protein sequences [3].

## 2 Methodology

### 2.1 Dataset used

We collect α-transmembrane protein sequences and information from databases PDB and Protein Data Bank of Transmembrane Proteins (PDBTM) [2], [4]. The sequences are checked for redundancy and low-resolution data. Each sequence is then segmented into its transmembrane and non-transmembrane regions. The final dataset contains 552 protein chains, divided into 2545 transmembrane and 3255 non-transmembrane segments.

### 2.2 Amino acid adjacency matrix

In building the chemometric classification model, we have used mathematical descriptors derived from amino acid adjacency matrices to characterize the protein segments. The amino acid adjacency matrix is a 20×20 matrix with the rows and columns labelled with the 20 amino acids [5]. Each position in the matrix denotes the number of times the corresponding amino acids occur as neighbours in the sequence (Fig. 1). The 20-element rowsum vector of the amino acid adjacency matrix is used as the descriptor set to represent the protein segments in our model. All the transmembrane and non-transmembrane regions of the protein sequences are encoded accordingly into the mathematical descriptors. The advantage of the descriptors is that they are dependent only on the sequence information.

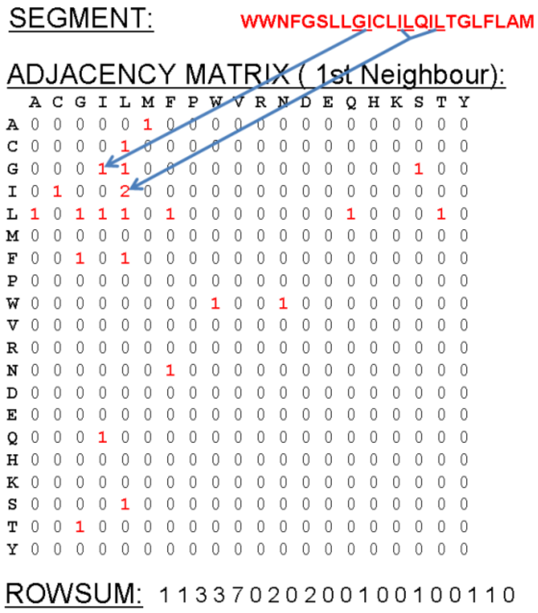

SEGMENT: WWNFGSLLGICLILQILTGLFLAM

ADJACENCY MATRIX ( 1st Neighbour):

| | A | C | G | I | L | M | F | P | W | V | R | N | D | E | Q | H | K | S | T | Y |
|---|---|---|---|---|---|---|---|---|---|---|---|---|---|---|---|---|---|---|---|---|
| A | 0 | 0 | 0 | 0 | 0 | 1 | 0 | 0 | 0 | 0 | 0 | 0 | 0 | 0 | 0 | 0 | 0 | 0 | 0 | 0 |
| C | 0 | 0 | 0 | 0 | 1 | 0 | 0 | 0 | 0 | 0 | 0 | 0 | 0 | 0 | 0 | 0 | 0 | 0 | 0 | 0 |
| G | 0 | 0 | 0 | 1 | 1 | 0 | 0 | 0 | 0 | 0 | 0 | 0 | 0 | 0 | 0 | 0 | 0 | 1 | 0 | 0 |
| I | 0 | 1 | 0 | 0 | 2 | 0 | 0 | 0 | 0 | 0 | 0 | 0 | 0 | 0 | 0 | 0 | 0 | 0 | 0 | 0 |
| L | 1 | 0 | 1 | 1 | 1 | 0 | 1 | 0 | 0 | 0 | 0 | 0 | 0 | 0 | 1 | 0 | 0 | 0 | 1 | 0 |
| M | 0 | 0 | 0 | 0 | 0 | 0 | 0 | 0 | 0 | 0 | 0 | 0 | 0 | 0 | 0 | 0 | 0 | 0 | 0 | 0 |
| F | 0 | 0 | 1 | 0 | 1 | 0 | 0 | 0 | 0 | 0 | 0 | 0 | 0 | 0 | 0 | 0 | 0 | 0 | 0 | 0 |
| P | 0 | 0 | 0 | 0 | 0 | 0 | 0 | 0 | 0 | 0 | 0 | 0 | 0 | 0 | 0 | 0 | 0 | 0 | 0 | 0 |
| W | 0 | 0 | 0 | 0 | 0 | 0 | 0 | 0 | 1 | 0 | 0 | 1 | 0 | 0 | 0 | 0 | 0 | 0 | 0 | 0 |
| V | 0 | 0 | 0 | 0 | 0 | 0 | 0 | 0 | 0 | 0 | 0 | 0 | 0 | 0 | 0 | 0 | 0 | 0 | 0 | 0 |
| R | 0 | 0 | 0 | 0 | 0 | 0 | 0 | 0 | 0 | 0 | 0 | 0 | 0 | 0 | 0 | 0 | 0 | 0 | 0 | 0 |
| N | 0 | 0 | 0 | 0 | 0 | 0 | 1 | 0 | 0 | 0 | 0 | 0 | 0 | 0 | 0 | 0 | 0 | 0 | 0 | 0 |
| D | 0 | 0 | 0 | 0 | 0 | 0 | 0 | 0 | 0 | 0 | 0 | 0 | 0 | 0 | 0 | 0 | 0 | 0 | 0 | 0 |
| E | 0 | 0 | 0 | 0 | 0 | 0 | 0 | 0 | 0 | 0 | 0 | 0 | 0 | 0 | 0 | 0 | 0 | 0 | 0 | 0 |
| Q | 0 | 0 | 0 | 1 | 0 | 0 | 0 | 0 | 0 | 0 | 0 | 0 | 0 | 0 | 0 | 0 | 0 | 0 | 0 | 0 |
| H | 0 | 0 | 0 | 0 | 0 | 0 | 0 | 0 | 0 | 0 | 0 | 0 | 0 | 0 | 0 | 0 | 0 | 0 | 0 | 0 |
| K | 0 | 0 | 0 | 0 | 0 | 0 | 0 | 0 | 0 | 0 | 0 | 0 | 0 | 0 | 0 | 0 | 0 | 0 | 0 | 0 |
| S | 0 | 0 | 0 | 0 | 1 | 0 | 0 | 0 | 0 | 0 | 0 | 0 | 0 | 0 | 0 | 0 | 0 | 0 | 0 | 0 |
| T | 0 | 0 | 1 | 0 | 0 | 0 | 0 | 0 | 0 | 0 | 0 | 0 | 0 | 0 | 0 | 0 | 0 | 0 | 0 | 0 |
| Y | 0 | 0 | 0 | 0 | 0 | 0 | 0 | 0 | 0 | 0 | 0 | 0 | 0 | 0 | 0 | 0 | 0 | 0 | 0 | 0 |

ROWSUM: 1 1 3 3 7 0 2 0 2 0 0 1 0 0 1 0 0 1 1 0

**Figure 1:** The amino acid adjacency matrix and 20-element rowsum vector of the given protein sequence.

## 2.3 Classification model

The mathematically encoded transmembrane and non-transmembrane segments are divided into training, test and external validation sets using the Kohonnen network. We use the non-linear modelling method the Counter Propagation Neural network (CPNN) to build the classification model [6]. The model is trained and optimized using the training and test sets with varying network parameters. The optimized network, i.e., the one with a minimum error in recall and prediction abilities, is then challenged with the external validation set that is not used in any of the previous model optimization steps.

## 2.4 Transmembrane region prediction tool

The developed classification model is used for the transmembrane region prediction of unknown protein sequences [3]. For this purpose, a sliding window approach is used with the window size of 20 residues for the α-transmembrane proteins. Each window segment is then fed into the classification model for its prediction as transmembrane or non-transmembrane. As the segments are overlapping, the central residues covered by 10 or more consecutive overlapping segments predicted as transmembrane is reported as the final transmembrane region.

# 3 Results

## 3.1 Classification model

The optimized classification model uses the following network parameters: network size - 40×40, number of epochs – 500, maximum correction factor – 0.9. The model shows a 95.67% recall ability, and a 91.33% prediction ability. During the external validation, 90.75% of the segments are predicted correctly [3].

## 3.2 Transmembrane region prediction of unknown proteins

We challenge the model with 6 α-transmembrane protein sequences for which the transmembrane regions are known. The predicted transmembrane regions are compared with the experimental results (Table 1). The model is also challenged with the protein bilitranslocase with unknown transmembrane regions. Four transmembrane regions for bilitranslocase (24-48, 75-94, 220-238, 254-276) are predicted that are in accordance with the observations and hypothesis from antibody studies [3].

**Table 1**. Transmembrane region prediction of unknown proteins

| PDB Id | Experimental | Predicted | False Positive | False Negative |
|---|---|---|---|---|
| 2npk | 11 | 9 | 0 | 2 |
| 1bha | 2 | 2 | 0 | 0 |
| 1otu | 10 | 8 | 2 | 2 |
| 2bhw | 3 | 3 | 0 | 0 |
| 2ahy | 2 | 2 | 0 | 0 |
| 3c9m | 7 | 7 | 0 | 0 |

## 3.3 Testing the model with globular proteins

The model is challenged with globular proteins to check its discriminating capability between the transmembrane and globular α-helices. Of the 7 globular proteins tested with 117 globular helices, only 2 globular helices were wrongly predicted as transmembrane helices (Table 2).

**Table 2**. Discriminating between globular and transmembrane helices

| PDB Id | Helices present | Predicted helices |
|---|---|---|
| 3gak | 14 | 0 |
| 3h9e | 13 | 1 (106-117) |
| 3b97 | 21 | 0 |
| 3cls | 10 | 0 |
| 3h1v | 19 | 0 |
| 2wu8 | 31 | 1 (318-333) |
| 1i7y | 9 | 0 |

## 4 Conclusion

We have successfully implemented a chemometric model in the classification and prediction of transmembrane and non-transmembrane regions of protein sequences. The mathematical descriptors used to represent the protein segments in the model are based on the sequence information alone, and are independent of evolutionary data. The model shows a prediction accuracy of 90.75%. When tested with unknown protein sequences, the model predicts their transmembrane regions successfully. It is also able to distinguish and separate the globular proteins from the transmembrane ones.

## References:

[1]A. Elofsson, G. von Heijene. Membrane protein structure:prediction versus reality. *Annual Review of Biochemistry*, 76:125-140, 2007.

[2]H.M. Berman *et al.* The protein data bank. *Nucleic Acids Research*, 28:235-242, 2000.

[3]A. Roy Choudhury, M. Novič. Data-driven model for the prediction of protein transmembrane regions. *SAR QSAR in Environmental Research*, 20:741-754, 2009.

[4]G.E. Tusnady, Z. Dosztanyi, I. Simon. Transmembrane proteins in the protein data bank: Identification and classification, *Bioinformatics*, 20:2964-2972, 2004.

[5]M. Randić, M. Novič, M. Vračko. On novel representation of proteins based on amino acid adjacency matrix. *SAR QSAR in Environmental Research*, 19:339-349, 2008.

[6]R. Hecht-Nielsen. Counterpropagation networks. *Applied Optics*, 26:4979-4984, 1987.

## For wider interest

Transmembrane proteins are membrane proteins spanning the whole biological membrane, acting both as barriers and communication channels between the intracellular and the extracellular spaces. They play crucial roles in the cell functioning acting as the transporters and receptors of various ligands, helping in the cell signalling etc. In addition, they are important as drug targets. However, the transmembrane proteins remain vastly unexplored due to experimental difficulties. Most of these proteins have unknown structures, and those with known structures often remain poorly annotated. Several interdisciplinary computational approaches along with experimental ones are therefore used to gain insights into the transmembrane proteins. Our lab expertizes: (i) the development and applications of standard and modern chemometrics techniques (clustering, classification, modelling, neural networks, genetic algorithms); (ii) handling of large amounts of multivariate data: transformations, projections, reductions, selection of variables and optimization of the data-representation for different modelling approaches; (iii) modelling using linear or non-linear methods – case studies in (Quantitative Structure-Activity Relationship) QSAR (modelling of biological properties), in analytical chemistry, determination of 3D molecular structures, calculation of descriptors and structure representations; validation of QSAR models. Our aim is to utilize this expertise for the characterization of transmembrane proteins using different chemometric methods for their structural elucidation. In the first step reported here, we have successfully developed a novel transmembrane region prediction algorithm. It is based on mathematical descriptors and neural networks. The prediction method, based on the sequence information, is independent of evolutionary data and physiochemical properties. The model is able to both predict successfully the transmembrane regions of unknown protein sequences and distinguish them from globular proteins. In the future, our aim is to utilize the data obtained from the inhibition studies applying chemometric tools, along with other computational and experimental methods, to study and predict the transport function of specific transmembrane proteins; and we are currently already working on these items. The chemometric methods along with other computational and experimental procedures, can be a very powerful aid to elucidate the structures and functional mechanisms of various transmembrane proteins.

# Vpliv legirnih elementov na lomno žilavost vzmetnega jekla 51CrV4

**Bojan Senčič**[1,2]
**Vojteh Leskovšek**[3]
[1] ŠTORE STEEL d.o.o., Železarska cesta 3, Štore, Slovenija
[2] Mednarodna podiplomska šola Jožefa Stefana, Jamova 39, Ljubljana, Slovenija
[3] Inštitut za kovinske materiale in tehnologije, Lepi pot 11, Ljubljana, Slovenija
bojan.sencic@store-steel.si

**Povzetek.** Za izdelavo listnatih vzmeti se večinoma uporablja vzmetno jeklo 51CrV4. Ker je v avtomobilski industriji prisoten stalen trend po zmanjševanju mase komponent, potrebujejo proizvajalci vzmeti jekla z izrednimi mehanskimi lastnostmi, med katerimi je zaradi želene visoke trajne dinamične trdnosti še posebej pomembna lomna žilavost $\boldsymbol{K}_{\mathrm{Ic}}$. Izdelano je bilo več jekel z različnimi dodatki Nb, Mo, C, Al in Ca. Z nestandardnim postopkom preizkušanja lomne žilavosti s cilindričnim nateznim preizkušancem z zarezo po obodu in utrujenostno razpoko v dnu zareze smo raziskali vpliv legirnih elementov na lomno žilavost pri enaki trdoti Rockwell-C vakuumsko toplotno obdelanega vzmetnega jekla.
Ugotovili smo, da določen dodatek legiranih elementov pozitivno vpliva na lomno žilavost $\boldsymbol{K}_{\mathrm{Ic}}$.

**Ključne besede:** lomna žilavost, vzmetno jeklo, legirni elementi, diagram popuščanja.

## 1 Uvod

V avtomobilski industriji se za izdelavo listnatih vzmeti uporablja predvsem vzmetno jeklo 51CrV4. Zaradi stalnega trenda po zmanjševanju mase vozil tudi proizvajalci vzmeti težijo k zmanjševanju mase vzmeti. Zato potrebujejo jekla z boljšimi mehanskimi lastnostmi, med katerimi pa je še posebej pomembna lomna žilavost $\boldsymbol{K}_{\mathrm{Ic}}$. Namen raziskovalne naloge je bil, da raziščemo vpliv dodatka različnih legirnih elementov na lomno žilavost, ki smo jo merili z nestandardnim postopkom preizkušanja lomne žilavosti, s cilindričnim nateznim preizkušancem z zarezo po obodu in utrujenostno razpoko v dnu zareze preizkušanca, ki je bil vakuumsko toplotno obdelan [1].

## 2 Eksperimentalni del

V Štore Steel d.o.o. smo izdelali štiri različne šarže vzmetnega jekla. Prva šarža z oznako A je bila klasična. Kemijska sestava in mikrostruktura je ustrezala jeklu 51CrV4 (po DIN 17221 in DIN 17222). Drugi šarži z oznako B smo dodali 0,075 ut.% Nb, pri tretji šarži z oznako C smo zmanjšali dodatek Al za 0,007 ut.% in Ca za 0,0013 ut.%, pri četrti šarži z oznako D smo dodali 0,18 ut.% Mo in 0,03 ut. % C.

Vzorce za preiskavo smo izrezali iz kontinuirno litega vzmetnega jekla, ki je bil dobavljen v obliki vroče valjanih mehko žarjenih palic, dimenzij 100 mm x 25 mm x 6000 mm.

Cilindrične natezne preizkušance z zarezo po obodu v prečni smeri in utrujenostno razpoko v dnu zareze ($\boldsymbol{K}_{\mathrm{Ic}}$ - preizkušanci) smo izrezali iz sredine palic v smeri valjanja (Slika 1).

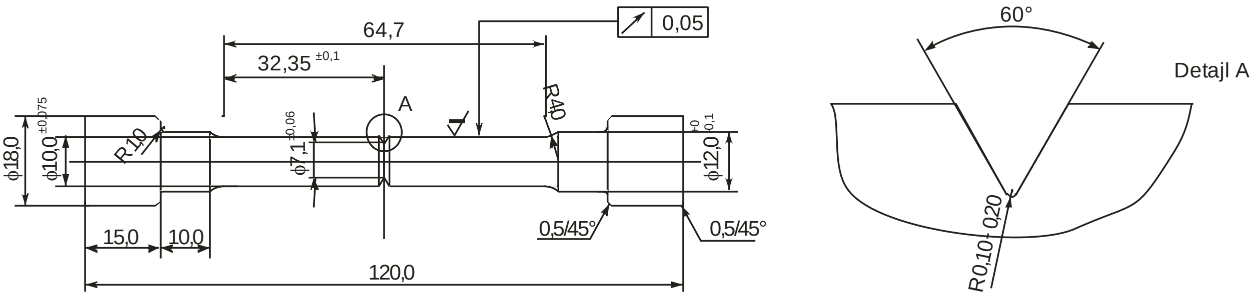

**Slika 1:** $\boldsymbol{K}_{\mathrm{Ic}}$ – preizkušanec.

Preizkušance smo toplotno obdelali v horizontalni enokomorni vakuumski peči IPSEN VTTC-324R s homogenim ohlajanjem v toku $N_2$ pod tlakom 5 bar. Vzorci so bili po prvem predgrevanju (650°C) ogreti s hitrostjo 10°C/min do temperature avstenitizacije (870°C), zadržani na temperaturi avstenitizacije 10 minut, in nato kaljeni do temperature 100°C v toku $N_2$ pod tlakom 5 bar ($\lambda_{800\text{-}500} = 0.42$). Temu je sledilo enkratno enourno popuščanje pri temperaturah 425°C in 475°C. Pri vsaki temperaturi popuščanja smo toplotno obdelali po osem $\boldsymbol{K}_{\mathrm{Ic}}$ - preizkušancev iz vsake šarže raziskovanih vzmetnih jekel.

Merjenje lomne žilavosti smo opravili z univerzalnim nateznim elektro-hidravličnim strojem tipa Instron 1255, in sicer s hitrostjo odmikanja glav stroja 1 mm/min, ki je značilna za standardni natezni preizkus pri preizkusni dolžini 100 mm. Uporabili smo posebej v ta namen izdelani kardansko vpeti glavi, ki jamčita popolno aksialnost natezne obremenitve. Pri preizkusu smo zasledovali odvisnost med natezno obremenitvijo in pomikom vse do loma preizkušanca. Značilen zapis, dobljen med kvazi-statičnim natezanjem toplotno obdelanih $\boldsymbol{K}_{\mathrm{Ic}}$ -preizkušancev do porušitve, je prikazan na Sliki 2.

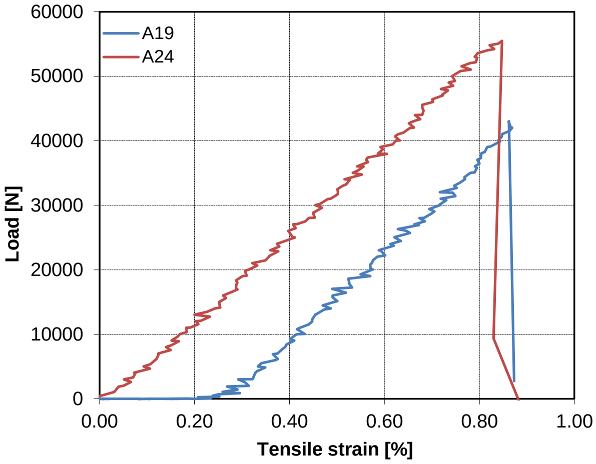

**Slika 2:** Natezni preizkus

Ta odvisnost je bila v vseh primerih linearna (vedno je bilo doseženo ravninsko deformacijsko stanje), kar pomeni, da je bila zaradi linearno-elastičnega vedenja $\boldsymbol{K}_{\mathrm{Ic}}$-preizkušancev enačba (1) za izračun lomne žilavosti vseskozi veljavna.

Na osnovi meritev kritične natezne obremenitve in meritev »utrujenostnega premera« v x in y smeri, izvedenih na obeh polovicah $\boldsymbol{K}_{\mathrm{Ic}}$ - preizkušanca (Slika 3) smo z uporabo enačbe (1) izračunali lomno žilavost $\boldsymbol{K}_{\mathrm{Ic}}$.

$$K_{Ic} = \frac{P}{D^{3/2}}\left(-1{,}27 + 1{,}72\frac{D}{d}\right) \tag{1}$$

pri čemer je $d$ takoimenovani povprečni »utrujenostni premer«, to je premer ligamenta ob razpoki, $D$ premer preizkušanca, $P$ pa natezna obremenitev pri lomu preizkušanca. Odvisnost (1) velja za razmerje $0{,}5 < d/D < 0{,}8$ [2].

Trdoto HRc (Rockwell-C) smo merili po nateznem preizkusu na obeh polovicah $\boldsymbol{K}_{\mathrm{Ic}}$ - preizkušanca. Trdoto HRc smo na vsaki polovici $\boldsymbol{K}_{\mathrm{Ic}}$ - preizkušanca izmerili 3x, in sicer po tri v razmiku po 120°, na delu s premerom 12 mm [3].

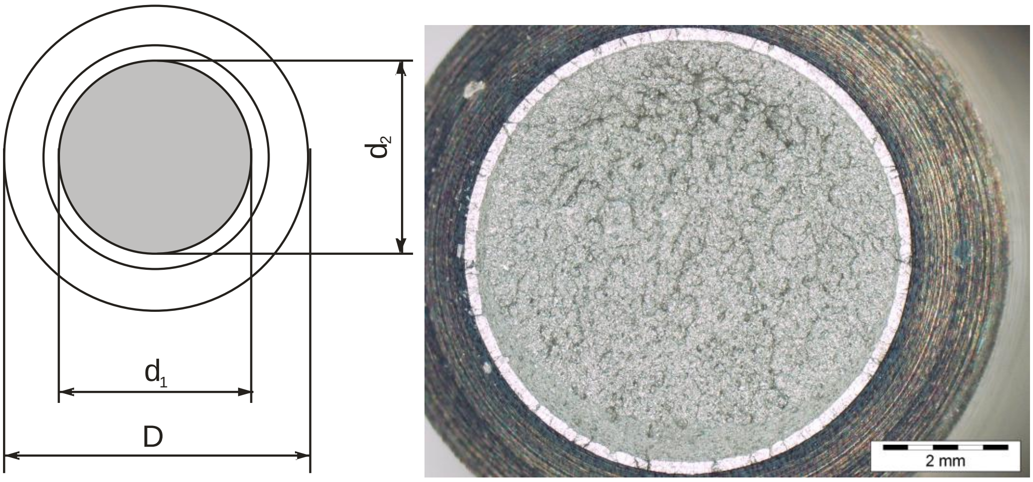

**Slika 3:** Prikaz merjenja ligamenta in izgled prelomne površine $\boldsymbol{K}_{\mathrm{Ic}}$ – preizkušanca.

## 3 Rezultati in diskusija

Rezultati meritev lomne žilavosti $\boldsymbol{K}_{\mathrm{Ic}}$ in trdote HRc so predstavljeni v obliki diagrama, ki prikazuje vpliv temperature popuščanja na razmerje $\boldsymbol{K}_{\mathrm{Ic}}$/HRc in na trdoto HRc za štiri različne šarže vzmetnega jekla (Slika 4).

Iz diagrama je razvidno, da je za izbrani temperaturi popuščanja razlika v trdoti pri vseh štirih šaržah raziskovanega vzmetnega jekla minimalna. Razlika med najvišjo in najnižjo trdoto pri posamezni temperaturi popuščanja je le 1,4 HRc, kar je lahko posledica merilne negotovosti in nehomogenosti jekla. Iz diagrama je razvidno, da z višanjem temperature popuščanja, trdota HRc pada.

Obratno velja za lomno žilavost $\boldsymbol{K}_{\mathrm{Ic}}$ in razmerje $\boldsymbol{K}_{\mathrm{Ic}}$/HRc, ki raste s temperaturo popuščanja. Pri temperaturi popuščanja 475°C je lomna žilavost jekla skoraj dvakrat višja kot pri temperaturi popuščanja 425°C. Pri obeh temperaturah popuščanja je razvidno, da ima šarža A (klasično vzmetno jeklo 51CrV4) najnižjo lomno žilavost, medtem ko je lomna žilavost preostalih šarž na enakem nivoju. Rezultati kažejo, da nam je uspelo izboljšati lomno žilavost za ~10% že z majhnim dodatkom legirnih elementov (šarža B - 0,075 ut.% Nb) oziroma z zmanjšanjem njihove vsebnosti (šarža C - 0,007 ut.% Al in 0,0013 ut.% Ca). Pri šarži D, kjer smo dodali 0,18 ut.% Mo in 0,03 ut % C je bil učinek podoben kot pri šaržah B in C. Glede na to, da so lomne žilavosti šarž B, C in D za približno 10% višje kot pri klasični šarži A, lahko sklepamo, da je za proizvajalca jekla najprimernejša šarža C, kjer že z zmanjšanjem vsebnosti Al in Ca dosežemo izboljšanje lomne žilavosti.

V okviru nadaljnih raziskav bomo poskušali ugotoviti kakšna je najprimernejša količina legirnih elementov, ki pri doseganju enakih trdot omogočajo še nadaljnje povečanje lomne žilavosti.

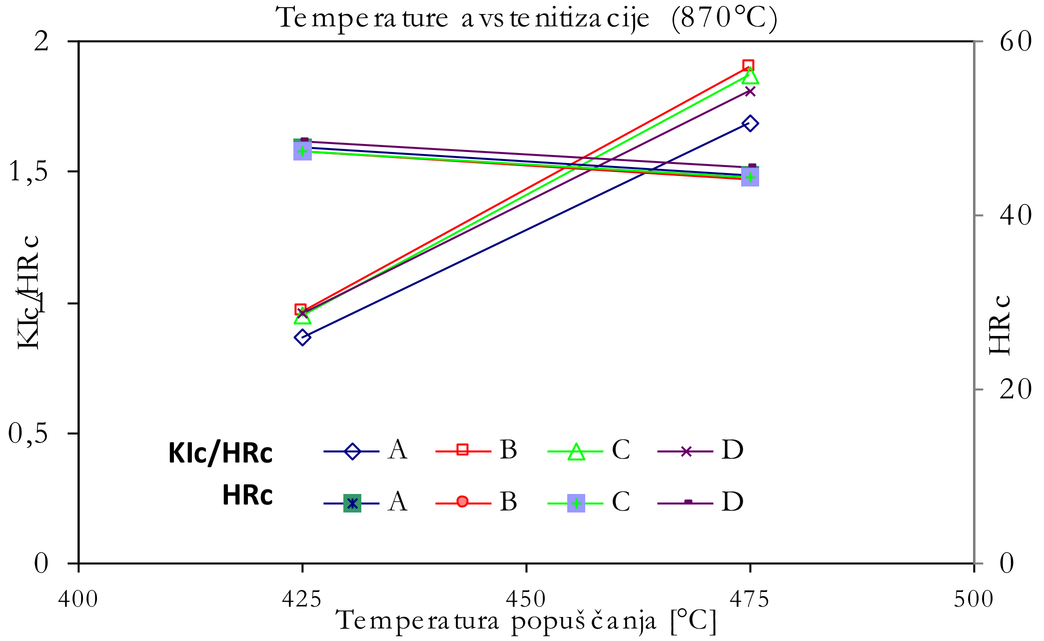

**Slika4 :** Diagram popuščanja za 4 šarže vzmetnega jekla.

## 4 Zaključki

Z nestandardnim postopkom preizkušanja lomne žilavosti s cilindričnim nateznim preizkušancem z zarezo po obodu in utrujenostno razpoko v dnu zareze lahko uspešno merimo lomno žilavost vakuumsko toplotno obdelanega vzmetnega jekla. S preliminarnimi raziskavami smo ugotovili, da lahko pri enaki trdoti Rockwell-C povečamo lomno žilavost konvencionalnega vzmetnega jekla za 10%, in sicer z mikrolegiranjem elementov (Nb, Al, Ca, C in Mo). Enaka ali večja duktilnost in lomna žilavost pri večji trdnosti pa proizvajalcu vzmeti omogoča zmanjšanje mase vzmeti in hkrati povečanje njihove vzdržljivosti v eksploataciji.

## Literatura:

[1]B. Senčič in V. Leskovšek. Fracture toughness of the vaccum-heat-treated spring steel 51CrV4. Materials and technology, 45(1): 67-73, 2011.

[2]Wei S. et al.. Fracture toughness measurement by cylindrical specimen with ring-shaped crack. Engineering Fracture Mechanics, 16(1): 69-92, 1982.

[3]B.Podgornik. Tempering diagrams and bending resistance of four high strength spring steels. IMT-LMP-ML-02, 2012.

## Za širši interes

V avtomobilski industriji se za izdelavo listnatih vzmeti uporablja predvsem vzmetno jeklo 51CrV4. Zaradi stalnega trenda po zmanjševanju mase komponent potrebujejo proizvajalci vzmeti jekla z izrednimi mehanskimi lastnostmi, med katerimi je zaradi želene dolge življenjske dobe vzmeti še posebej pomembna lomna žilavost.

Namen raziskovalne naloge je bil, da raziščemo vpliv vsebnosti različnih legirnih elementov na lomno žilavost vzmetnega jekla 51CrV, ki smo jo merili z nestandardnim postopkom preizkušanja lomne žilavosti s cilindričnim nateznim preizkušancem z zarezo po obodu in utrujenostno razpoko v dnu zareze preizkušanca, ki je bil vakuumsko toplotno obdelan.

Izdelano je bilo več vzmetnih jekel z različnimi dodatki Nb, Mo, C, Al in Ca.

Na osnovi meritev lomne žilavosti in izdelanega diagrama popuščanja smo ugotovili, da lahko izboljšamo lomno žilavost klasičnega vzmetnega jekla za 10% že z majhnimi spremembami vsebnosti legirnih elementov (dodatek 0,075 ut.% Nb ali zmanjšanje vsebnosti Al za 0,007 ut.% in Ca za 0,0013 ut.%).

# Dielectric and ferroelectric properties of sol-gel-derived $Na_{0.5}Bi_{0.5}TiO_3$ thin films

**Tina Šetinc**[1,2], Matjaž Spreitzer[1], Špela Kunej[1], Danilo Suvorov[1,2]

[1] Advanced Materials Department, Jožef Stefan Institute, Ljubljana, Slovenia

[2] Jožef Stefan International Postgraduate School, Ljubljana, Slovenia

tina.setinc@ijs.si

**Abstract.** $Na_{0.5}Bi_{0.5}TiO_3$ thin films were fabricated on Pt/Ti/$SiO_2$/Si substrates using a chemical solution deposition (CSD). The decomposition behaviour of the precursors, the phase formation and the film morphologies were investigated by means of the thermogravimetric and differential thermal analysis (TG/DTA) coupled with an online evolved-gas analysis (EGA), X-ray powder diffraction (XRD), field-emission scanning electron microscopy (FEG-SEM) and atomic force microscopy (AFM), respectively. The prepared thin films were single phase with a polycrystalline structure. The measured room-temperature dielectric constant at 100 kHz was 680, with a corresponding dielectric loss of 0.06. The temperature dependence of the dielectric properties showed a steady increase of the permittivity with increasing temperature, reaching a value of 940 at 200°C.

**Keywords**: sodium bismuth titanate, chemical solution deposition, thin films, dielectric properties

## 1. Introduction

In recent decades much attention has been given to perovskite materials, from both the theoretical and application points of view, because of their interesting electrical properties. The dielectric, ferroelectric, piezoelectric, and pyroelectric properties of these materials were investigated for the corresponding electronic applications, such as electromechanical devices, transducers, capacitors, actuators, high-k dielectrics, dynamic random-access memories, field-effect transistors, and logic circuitry. Ferroelectric thin films, in particular, received a considerable interest due to their potential integration with microelectronic circuits, offering low operating voltages, high switching speeds and a possible integration with the existing semiconductor technology [1-8].

Sodium bismuth titanate $Na_{0.5}Bi_{0.5}TiO_3$ (abbreviated as NBT) is a complex perovskite with a relaxor ferroelectric behaviour. NBT bulk ceramics exhibit strong ferroelectric properties with a large remanent polarization, Pr = 38 $\mu C/cm^3$, and a relatively high temperature of the dielectric maximum, $T_m$ = 320 °C. In addition, NBT was investigated as one of the key end-members of binary and ternary compounds exhibiting impressive piezoelectric properties [10]. Regarding the NBT thin-film preparation, several studies have been performed using different deposition techniques. Among them, the chemical solution deposition (CSD) (e.g., the sol-gel, metallo-organic deposition) represents a relatively low-cost method offering a high compositional control and uniform deposition, and is thus employed by the industry for the fabrication of commercial devices. Furthermore, CSD offers the advantage of being able to tailor the solution chemistry, which enables adjustment of the physico-chemical properties of the precursors, the development of new compositions, the control of the microstructure and the physical properties of the crystalline film [11, 12]. Regarding the sol-gel-derived NBT thin films, the investigations of their dielectric properties indicated rather different values for the measured dielectric constants. Some of the reported dielectric characteristics can be briefly summarized as follows: Tang et al. [13] reported a dielectric constant of 171 (tanδ 0.024) at 100 kH, Yu et al. [14] reported a dielectric constant of 270 (tanδ 0.05) at 1 MHz and Xu [15] reported a dielectric constant of 440 (tanδ 0.05) at 1 MHz. The observed variation in the dielectric properties is a result of the different solution synthesis and processing conditions, ultimately defining the microstructural characteristics of the prepared thin films. In addition, the sol-gel method as a solution technique is rather prone to introducing a large number of defects into the structure, which may additionally deteriorate the dielectric properties. Thus, the improvement of the dielectric characteristics of the sol-gel-derived NBT films is still a matter for further studies. Furthermore, the high conductivity and large coercive field of the un-doped NBT bulk ceramics typically causes difficulties in their poling and a significant deterioration in the polarization properties. These phenomena are expected to be even more pronounced in the thin-film form due to the size effect and the lattice mismatch between the film and the substrate. Employing multilayered thin films or interposing a dielectric layer of a paraelectric material between the ferroelectric layer and the bottom as well as the top electrode offers the possibility to overcome these difficulties. However, in order to systematically investigate the dielectric and ferroelectric properties of multilayers, some preliminary research on pure NBT thin films is required. Thus, the object of our research work was to fabricate NBT thin films via the CSD method and to investigate their morphological, dielectric and ferroelectric properties. The obtained results would be subsequently used to estimate the properties of multilayers in relation to pure NBT thin films.

## 2. Experimental

Bismuth acetate $[Bi(CH_3CO_2)_3]$, sodium acetate $[Na(CH_3COO)]$, and titanium butoxide $[Ti(OC_4H_{9)4}]$ were used as the starting materials. 2-methoxyethanol and glacial acetic acid were selected as the solvent and the pH-value adjusting reagent, respectively. To compensate for the losses during the annealing treatment, a 10% molar excess of sodium and a 5% molar excess of bismuth were added with respect to the stoichiometry of the NBT. First, the titanium butoxide was stabilized in the 2-methoxyethanol solvent by the addition of acetylacetone in an equimolar ratio, followed by the addition of bismuth acetate, sodium acetate and acetic acid under stirring. The mixture was first refluxed at 80°C for 1 h and further partially distilled. The concentration of the final solution was adjusted to 0.3 M by the addition of 2-methoxyethanol. Prior to deposition, 4 vol. % of formamide was added in order to control the rate of pyrolysis and to minimize the formation of cracks during the thermal annealing. The spin-coating technique was employed to deposit the films onto $Pt/TiO_2/SiO_2/Si$ substrates using a spinning rate of 3000 rpm for 20 s. The as-deposited NBT thin films were dried on a hot-plate at 230°C for 3 min and pyrolyzed at 460°C for 10 min. The films were finally annealed at 600-700°C for 0.5 h in air to enable a complete perovskite phase formation.

To determine the decomposition and crystallization behavior, the NBT xerogel was investigated by thermogravimetric (TG) and differential thermal analysis (DTA) (Jupiter STA 449 C/6/G & 403C Aëoloss, Netzch) in an $O_2$ flow with a heating rate of 5°C/min. The crystal structure was investigated with an X-ray diffractometer (Bruker AXS D4 Endeavor, wavelength of $CuK_\alpha$ radiation = 1.5406 Å). The X-ray powder-diffraction data were recorded in the $2\theta$ ranges 20°-35° and 45°-60° with a step of 0.02° and a counting time of 6 seconds. The surfaces and cross-sections of the films were investigated by the atomic force microscopy (AFM, Veeco Dimension 3100) and field-emission-gun scanning electron microscopy

(FEG-SEM, Jeol F7600). The electrical measurements were carried out using the metal-insulator-metal, parallel-plate, capacitor configuration. For the dielectric characterization, Au electrodes (diameter of 200 μm) were sputtered onto the film surface through a designed mask. The dielectric properties were characterized in the frequency range from 1 kHz to 1 MHz using an ac voltage of 1V and an LCR meter (Agilent 4284A) connected to a Probe Station Cascade Summit 1200 AP. The out-of-plane dielectric constant was calculated from the capacitance, $C=\varepsilon_0\varepsilon_r A/d$, where $d$ is the film thickness estimated from the cross-section FEG-SEM images. The polarization-electric field (*P-E*) hysteresis curves were measured at room temperature using a radiant precision workstation based on a standard Sawyer-Tower circuit at 10 Hz.

## 3. Results and discussion

The thermal decomposition of the NBT xerogel was studied in order to roughly determine the appropriate temperatures for the thermal treatment of the wet films. From the corresponding TG/DTA curves, shown in Figure 1, a strong exothermic peak was observed at a temperature of 329°C, which is related to the formation of the carboxylate-alkoxide network. The second, relatively weak, exothermic peak at 472°C was ascribed to the crystallization of the NBT. The low temperature of the decomposition and nucleation was previously observed for NBT films prepared via the 2-methoxyethanol route. According to the results of the thermal analysis, the temperature of the drying and the thermolysis were set to 230°C and 460°C, respectively.

For a complete crystallization to the perovskite phase the films were further annealed at 600°C and 700°C for 0.5 h and the corresponding diffraction patterns are shown in Figure 2. Within the measurement precision of the XRD, a single NBT perovskite phase was determined. The rhombohedral structure of the NBT can be represented as a pseudo-cubic lattice for simplicity and in such a way it was possible to index the XRD patterns. The diffraction patterns indicate the polycrystalline nature of the prepared films with a slight (100) preferential orientation observed with respect to the reference PDF card (No. 89-3109) [27]. The comparable intensity of the films annealed at different temperatures indicates that the NBT films are already well crystallized at 600°C.

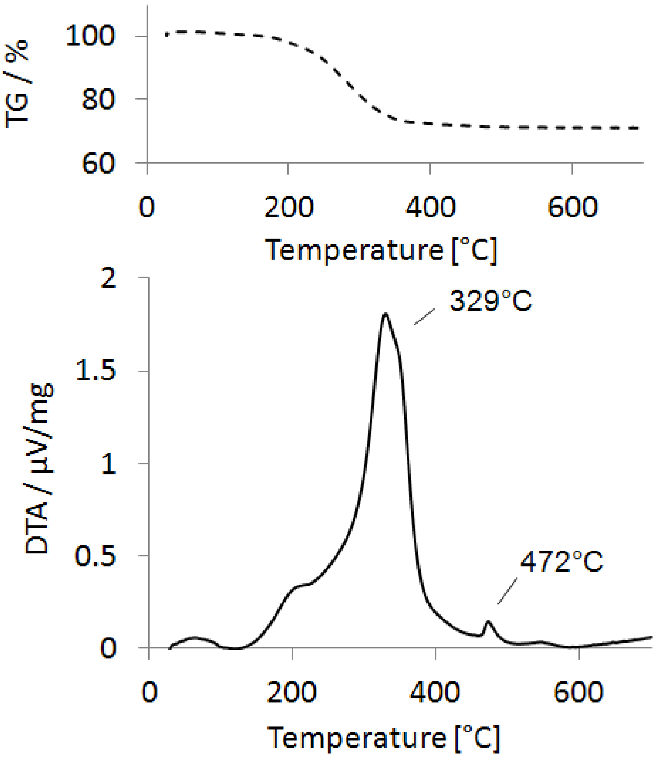

**Figure 1:** DTA/TG curve of the NBT xerogel.

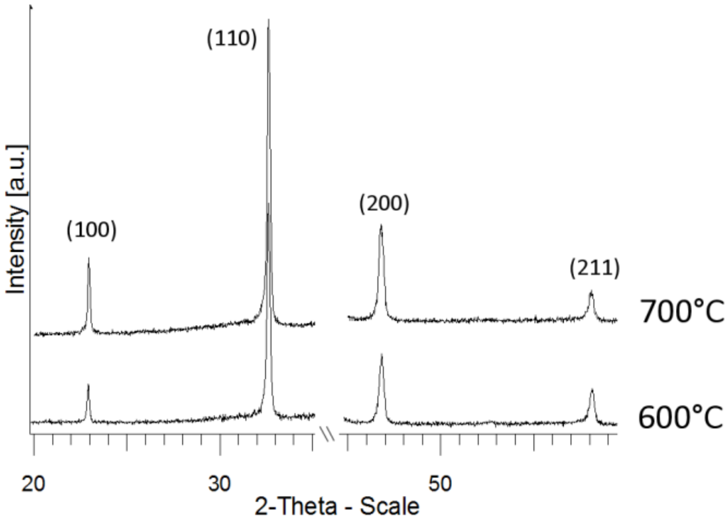

**Figure 2:** XRD patterns of the NBT thin films annealed at 600°C and 700°C for 0.5 h.

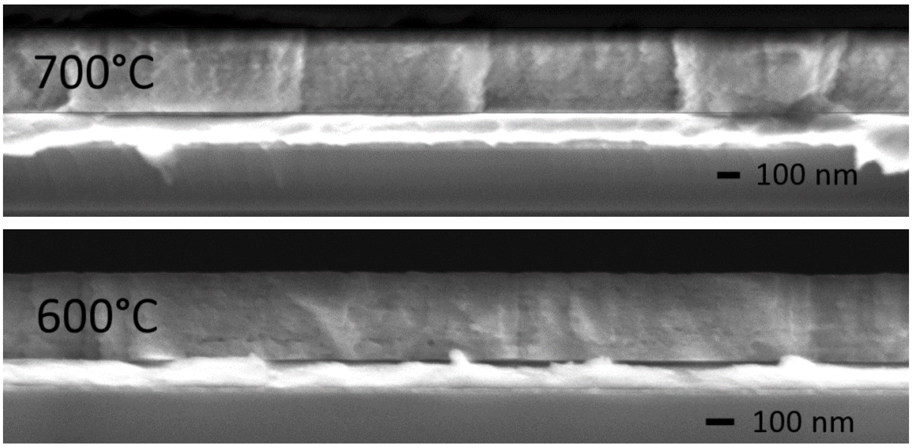

**Figure 3:** The SEM cross-section images of the films annealed at 600°C and 700°C.

Figure 3 shows the cross-sections of the prepared thin films with estimated thicknesses of between 370 nm and 380 nm for the samples annealed at 600°C and 700°C, respectively. The surface morphology of the thin films was investigated by means of the AFM, and the corresponding 2D and 3D surface-profile images are shown in Figure 4.

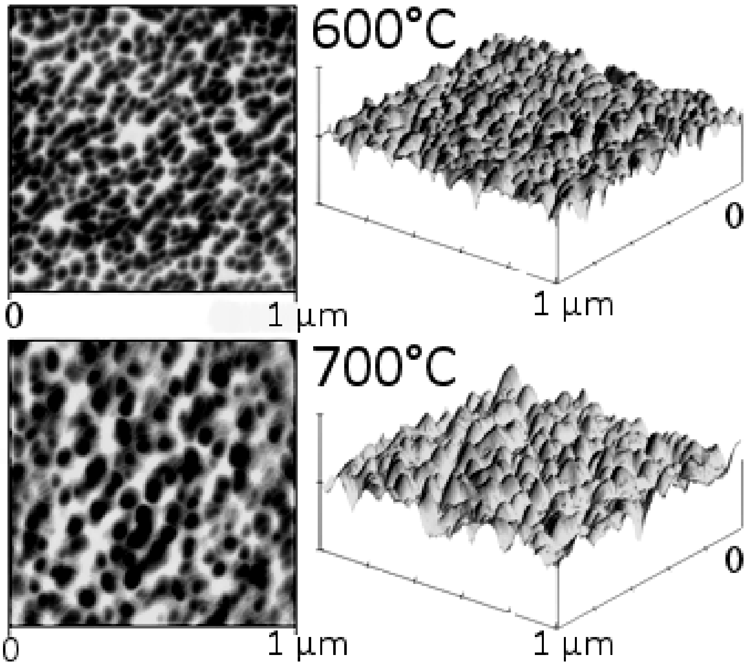

**Figure 4:** The AFM 2D and 3D surface-profile images of the films annealed at 600°C and 700°C.

The prepared NBT thin films exhibited a fine-grained morphology with average grain sizes of 52 and 60 nm and estimated root-mean-square (RMS) values of the surface roughness of 1.3 nm and 2.5 nm for the films annealed at 600°C and 700°C, respectively.

The frequency dispersions of the dielectric constant for the NBT thin films are shown in Figure 5. The measured dielectric constants for the films annealed at 600°C and 700°C were 680 and 530, respectively, at 100 kHz, with corresponding losses of ~0.06 for both samples. The observed differences in the dielectric constant for the thin films annealed at different temperatures might be ascribed to the volatility of Bi and Na at higher annealing temperatures, causing changes in the chemical stoichiometry, which consequently affect the structure and the physical properties of the material. A previous study of the bismuth-deficiency effect on the dielectric properties showed a substantial decrease in the permittivity with a decreasing bismuth content in the low-temperature region [17]. However, additional investigations would be required in order to completely confirm this assumption.

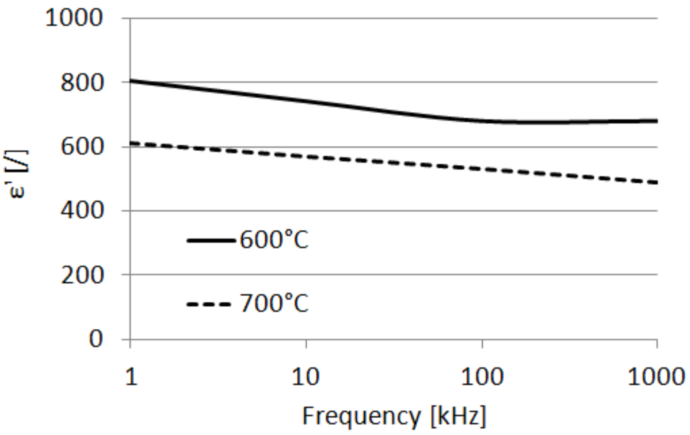

**Figure 5:** The frequency dispersion of the dielectric constant measured at room temperature for thin films annealed at 600°C and 700°C.

Furthermore, the observed dispersion of the dielectric constant over the measured frequency range may be attributed to the existence of surface-charge layers at the electrode-film interface and the grain boundaries. It is well established that imperfections, defects, depletion and other extrinsic effects can be responsible for the frequency dependence and may greatly affect the dielectric behaviour, particularly for fine-grained ceramics in a thin-film form with the geometry imposing additional boundary conditions [18].

Figure 6 presents a typical temperature dependence of the dielectric constant, here shown for the film annealed at 600°C. In the temperature range between -50°C and 200°C the dielectric permittivity gradually increases for all the measured frequencies. The increase in permittivity is related to the appearance of the dielectric maximum, which in the bulk NBT ceramics occurs at around 320°C. Furthermore, a weak dielectric hump was observed in the permittivity curve around 150°C. Some authors suggest that an antiferroelectric state occurs in this temperature range; however, a neutron and Raman scattering and other measurements contradict this hypothesis. Another explanation for the formation of the dielectric hump is based on the contribution of the polar nano-regions prevailing over the dielectric dynamic of the rhombohedral domains. This dielectric anomaly is accompanied by the frequency dispersion of the dielectric losses, which was also clearly observed for our NBT films (shown in Figure 7), and previously ascribed to the dipole relaxation [19].

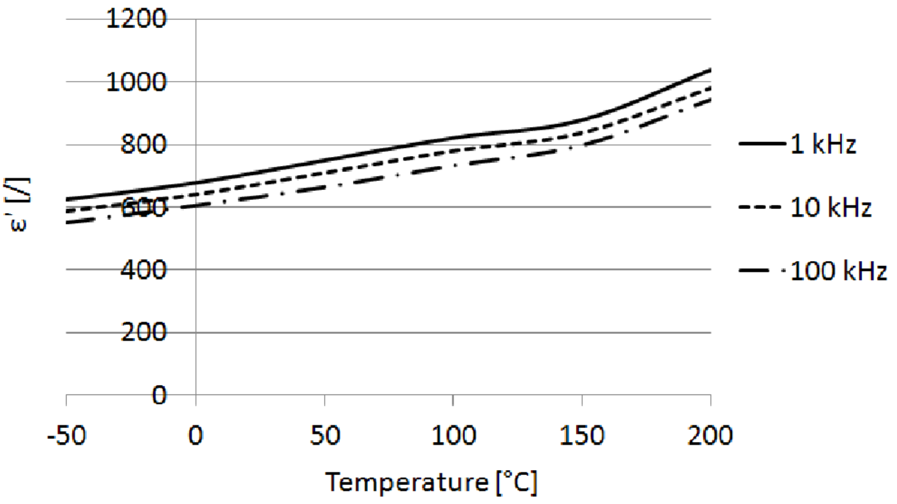

**Figure 6:** The temperature dependence of the dielectric constant measured at various frequencies for a thin film annealed at 600°C.

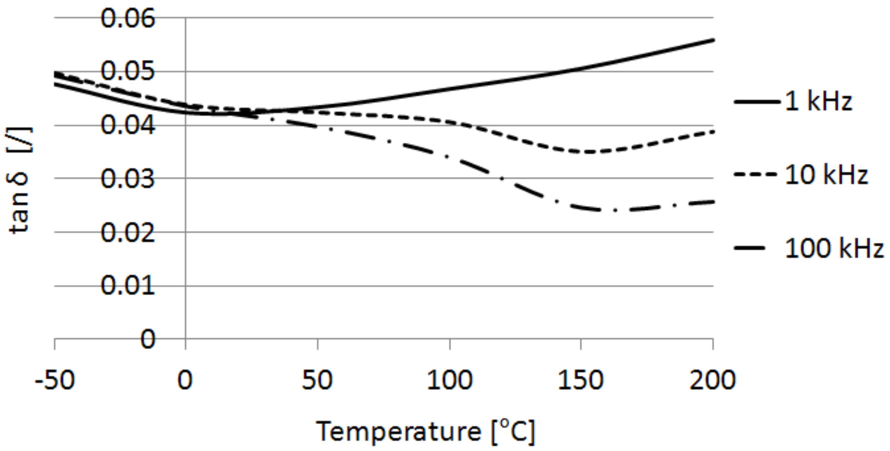

**Figure 7:** Temperature dependence of loss tang measured at various frequencies for a thin film annealed at 600°C.

The *P-E* measurements carried out at 10 Hz and under an applied electric field of 7 V are shown in Figure 8. The obtained hysteresis loops indicate the ferroelectric character of the prepared NBT thin films. Better ferroelectric properties were exhibited by films annealed at higher temperatures, i.e., 700°C. The maximum remanent polarization of 6.7 μC/cm$^2$ was determined under an electric field of 9 V for a sample prepared at 700°C with a corresponding coercive field of 50 kV/cm. The low breakdown fields of the prepared NBT films were observed, regardless of the annealing conditions, and caused difficulties with saturating the *P-E* hysteresis.

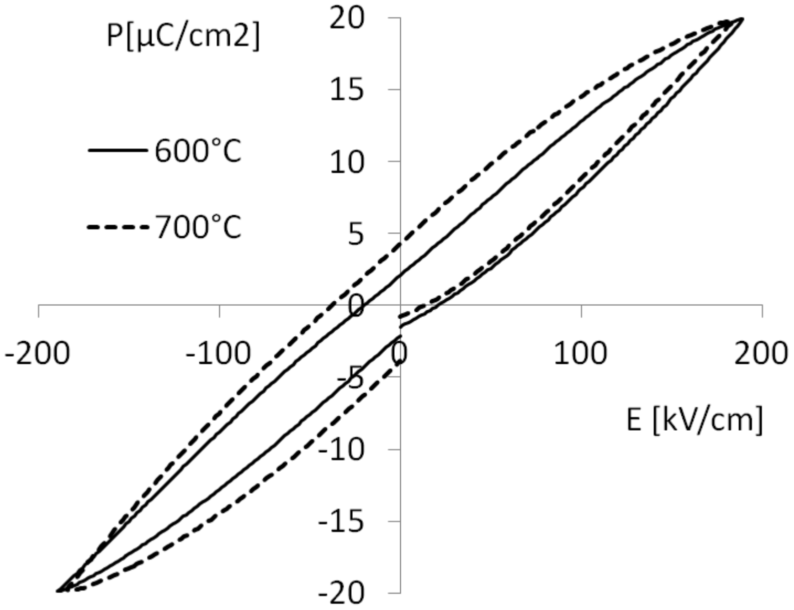

**Figure 8:** The observed room temperature *P-E* hysteresis loops for the NBT thin films annealed at 600°C and 700°C under an applied electric field of 7 V.

## 4. Conclusions

Polycrystalline NBT thin films were prepared on $Pt/Ti/SiO_2/Si$ substrates using the sol-gel method. The NBT thin films exhibited a fine-grained microstructure with average grain sizes of 52 and 60 nm, and a surface roughness of 1.3 nm and 2.5 nm, for the films annealed at 600°C and 700°C, respectively. In the measured frequency range from 1 kHz to 1 MHz, the dielectric permittivity ranged from 800 to 630 for the film annealed at 600°C and from 610 to 490 when annealing at 700°C. In the temperature range between -50°C and 200°C the dielectric permittivity gradually increases for all the measured frequencies, reaching a value of 940 at 200°C for a film annealed at 600°C. Better ferroelectric properties were measured for the NBT films annealed at 700°C, with a measured remanent polarization and coercive field of 6.7 $\mu C/cm^2$ and 50 kV/cm, respectively. The low breakdown field caused difficulties with obtaining a well-saturated *P-E* hysteresis for the prepared NBT thin films, which might be improved by employing multilayered thin films. This issue will be addressed in our future studies.

## References

[1] Hill, N. A. *J. Phys. Chem. B* 2000, *104*, 6694.
[2] Scott, J. F. *Ferroelectr. Rev.* 1998, *1*, 1.
[3] Millis, A. J. *Nature* 1998, *392*, 147.
[4] Chandler, C. D.; Roger, C.; Hampden-Smith, M. J. *Chem. Rev.* 1993, *93*, 1205.
[5] Schrott, A. G.; Misewich, J. A.; Nagarajan, V.; Ramesh, R. *Appl. Phys. Lett.* 2003, *82*, 4770.
[6] Tao, S.; Irvine, J. T. S. *Nat. Mater.* 2003, *2*, 320.
[7] G.V. Belokopytov, *Ferroelectrics*, 168,69 (1995).
[8] S. Gevorgian and E. Kollberg, IEEE Trans. Microwave Theory Tech. 49, 2117 (2001).
[9] A. Safari and M. Abazari, 'Lead-free Piezoceramic ceramics and Thin Films,' *IEEE Trans. Ultrason. Ferroelectr. Freq. Control*, 57 [10], 2165-2176 (2010).
[14] S.B. Krupanidhi, H. Hu and V. Kumar, J. Appl. Phys. 71 (1992) 376.
[15] L.H. Parker and A.F. Tasch, IEEE Circ. Dev. Mag. 1 (1990) 17.
[16] A. Mansingh, Ferroelectrics 102 (1990) 69.
[17] R. W. Schwartz, T. Schneller, and R. Waser, "Chemical Solution Deposition of Electronic Oxide Films," *Chimie* 7 [5] 433–61 (2004).
[18] L. G. Hubert-Pfalzgraf, "Some Trends in the Design of Homo- and Heterometallic Molecular Precursors of High-Tech Oxides," *Inorg. Chem. Com.*, 6, 102–20 (2003).
[19] K. Kato, K. Suzuki, D. S. Fu, K. Nishizawa, and T. Miki, "Chemical Approach Using Tailored Liquid Sources for Traditional and Novel Ferroelectric Thin Films," *Jpn. J. Appl. Phys., Part 1*, 41 [11B] 6829–35 (2002).
[20] M. L. Calzada, I. Bretos, R. Jiménez, H. Guillon, and L. Pardo, "Low-Temperature Processing of Ferroelectric Thin Films Compatible with Silicon Integrated Circuit Technology," *Adv. Mater.*, 18 [16] 1620–4 (2004).

[21] I. Bretos, R. Jiménez, J. García-López, L. Pardo, and M. L. Calzada, "Photochemical Solution Deposition of Lead-Based Ferroelectric Films: Avoiding the PbO-Excess Addition at Last," *Chem. Mater.*, 20, 5731–3 (2008).

[22] Tang et al., *Chem. Mater.*, Vol 16, No. 25, 2004

[23] C.Y. Kim, *J. Sol-Gel Sci. Tech.* (2010), 55:306-310

[24] T. Yu, *Thin Solid Films* (2007) Volume: 515, Issue: 7-8, Pages: 3563-3566

[25] J. Xu, *J. Appl. Phys.* 104, 116101 (2008)

[26] Yang CH, *Journal of Crystal Growth*, Volume 284, Issues 1–2, 15 October 2005, Pages 136–141

[27] A.I. Agranovskaya, Izv. *Akad. Nauk* SSSR, Ser. Fiz., 24, 1275 (1960)

[28] J. Suchanicz, The low-frequency dielectric relaxation Na0.5Bi0.5TiO3 ceramics, *Materials Science and Engineering: B* Vol. 55, Issues 1–2, 14 August 1998, Pages 114–118

[29] Q. Xu, Y.H. Huang, M.Chen, B.H. Kim, B.K. Ahn, *J. Phys. And Chem. Of Solids* 69 (2008) 1996-2003

[30] D. Damjanovic, Ferroelectric, dielectric and piezoelectric properties of ferroelectric thin films and ceramics, *Rep- Prog. Phys.* 61 (1998) 1267-1324

## For wider interest

Perovskite materials have attracted a lot of attention over recent decades owing to their many interesting properties, especially from the application point of view. The uses of these materials are based on their intrinsic dielectric, ferroelectric, piezoelectric, and pyroelectric properties in the corresponding electronic devices, such as micro-electromechanical systems (MEMS), transducers, capacitors, actuators, high-k dielectrics, dynamic random-access memories, field-effect transistors, and logic circuitry. Furthermore, a considerable amount of interest in ferroelectric thin films has resulted from the possibility of integrating them with existing semiconductor technology, low operating voltages and high switching. Among the different film-deposition techniques, chemical solution deposition (CSD) methods (e.g., sol-gel, metallo-organic deposition) are low-cost techniques that provide high compositional control and uniform deposition, used in industry for the fabrication of commercial devices with a planar configuration.

The relaxor ferroelectric $Na_{0.5}Bi_{0.5}TiO_3$ (abbreviated as NBT) has attracted increasing interest as a member of the dielectric perovskites with intriguing piezoelectric and ferroelectric properties. The distorted NBT structure exhibits good ferroelectric properties, with a large remanent polarization, $Pr = 38\ \mu C/cm^3$, and a relatively high temperature of the dielectric maximum, $T_m = 320$ °C, and was widely investigated as one of the key end-member compounds for lead-free piezoelectric ceramics. The main drawbacks of pure NBT are a large coercive field and a high conductivity, which causes problems in the process of poling. These phenomena are expected to be even more pronounced in the thin-film form due to the size effect and the lattice mismatch between the film and the substrate. Employing multilayered thin films or interposing a dielectric layer of a para-electric material between the ferroelectric layer and the bottom as well as top electrode offers a possibility to overcome these difficulties. However, in order to systematically investigate the dielectric and ferroelectric properties of multilayers some preliminary research on pure NBT thin films is required. Thus, the object of our research work was to fabricate the NBT thin films via the CSD method, and to investigate their morphological, dielectric and ferroelectric properties. The obtained results would be subsequently used for critically estimating the properties of multilayers in relation to pure NBT thin films.

# Synthesis and characterization of calcium phosphate coatings on $ZrO_2$ ceramics for bone implant applications

**Martin Štefanič**[1], **Kristoffer Krnel**[1], **Tomaž Kosmač**[1,2]

[1] Engineering Ceramics Department, Jožef Stefan Institute, Ljubljana, Slovenia

[2] Center of Excellence Namaste, Ljubljana, Slovenia

martin.stefanic@ijs.si

**Abstract.** Calcium phosphate (Ca-P) coatings on zirconia bone implants have a great potential to improve the osseointegration of already existing ceramic implants, owing to their bone-bonding ability and high osteoconductive characteristics. In our study, we have prepared three different kinds of Ca-P coatings, namely the octacalcium phosphate (OCP), hydroxyapatite (HAp) and β-tricalcium phosphate (β-TCP) coatings. The OCP coatings were prepared by utilizing a simple wet-chemical biomimetic procedure, which included immersion of the implant material in a solution with a similar composition as the human blood plasma and at physiological conditions. Further heat treatment of the OCP coatings at 600 °C and 800 °C resulted in the formation of HAp and β-TCP coating, respectively. Beside the changes in the morphology and crystal structure, the heat treatment also improved the adhesion of the coating to the ceramic substrate.

**Keywords**: Zirconia ceramics, bone implant, calcium phosphates, bioactive coating

## Introduction

Zirconia implants are becoming increasingly important in the field of dental medicine because of their good mechanical properties, biocompatibility, and for aesthetic reasons [1]. However, zirconia is bioinert and this can lead to a poor fixation of the ceramic implant in the bone [2]. A promising approach to circumvent this problem is to coat the implants with the thin layers of calcium phosphates (Ca-P), which are known to be bioactive and osteoconductive, i.e., they show a good bone-bonding ability and support the bone-tissue ingrowth [2]. A very promising approach for the preparation of coatings is the so-called biomimetic method, which includes the immersion of the implant into a supersaturated Ca-P solution under physiological conditions. This method allows the synthesis of homogenous coatings with a good surface coverage of materials with complex shapes. Nevertheless, the drawbacks of the method are the long time of the synthesis, poor reproducibility and, in particular, poor adhesion of the coating to the substrate [3]. In this work, we report on the use of a simple wet-chemical biomimetic process for the deposition of an OCP coating on zirconia ceramics and on the further thermal processing to produce HAp and b-TCP coatings with an improved attachment to the substrate.

## Materials and Methods

Clean zirconia substrates (Y-TZP) in the form of discs were used as substrates for the preparation of Ca-P coatings. For the coating process, two different Ca-P solutions were used: Solution 1 and Solution 2. Their compositions are given in the Table 1.

Table 1. The ionic composition of the CPS1 and CPS2 in mM

| | $Na^+$ | $Ca^{2+}$ | $Cl^-$ | $PO_4^{3-}$ | pH | buffer |
|---|---|---|---|---|---|---|
| Solution-1 | 7.5 | 2.5 | 5.0 | 2.5 | 7.4 | HCl/TRIS |
| Solution-2 | 7.5 | 2.5 | 5.0 | 2.5 | 7.0 | HCl/TRIS |

The synthesis procedure included two steps. In the first step, the zirconia substrate was soaked in a plastic beaker filled with 30 ml of the Solution-1 for 1h at 37 °C. In the second step, the substrate was transferred from the Solution-1 into the beaker filled with the Solution-2 at 37 °C for 11 hours. At the end of the synthesis the coated substrates were dried under ambient conditions. Some of the coated specimens were subsequently fired in a furnace at 600 °C or 800 °C for 1h in air. The heating rate was 10 °C/min. The samples were characterized by the scanning electronic microscopy (SEM, JEOL JSM-7600F, Japan) and X-ray diffraction (XRD; PANalytical, Holland). The bond strength of the coatings was determined according to the standardised ISO 4624 test. For the test, a miniaturized measuring device on a universal testing machine Zwick Z100 was used and the HTK ULTRA BOND® glue was chosen as an adhesive (Germany). Precipitation of the glue took place at 190 °C for 35 min. The test speed was set to 0.5 mm/min.

## Results and discussion

During the immersion of the zirconia substrates in the reaction solutions, an approximately 10-µm-thick coating with a lamellar structure was deposited on the substrates (Figure 1). The XRD analysis showed that the coating is composed of OCP (JCPDS-26-1056) (Fig. 1).

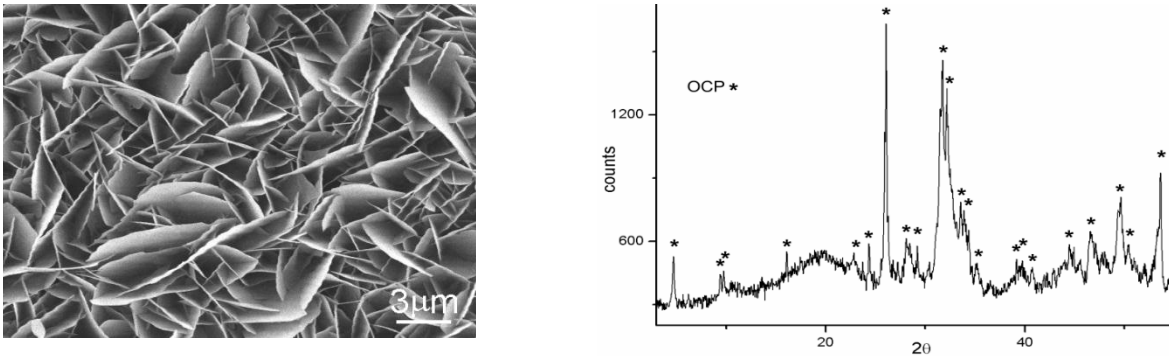

Figure 1. The SEM image of the OCP coating after 11 hours of immersion in the Solution-2 (left) and its corresponding XRD pattern (right).

The bond strength of the coating was 1.8 MPa. Some of the coated substrates were then fired at 600 °C or 800°C. The samples fired at 600 °C preserved the lamellar structure of the initial coating, while the XRD profile corresponded to the apatitic structure (JCPDS-09-0432), indicating that the OCP phase transformed to HAp during the heat treatment (Fig. 2). The bond strength of such HAp coatings was improved to 3.2 MPa.

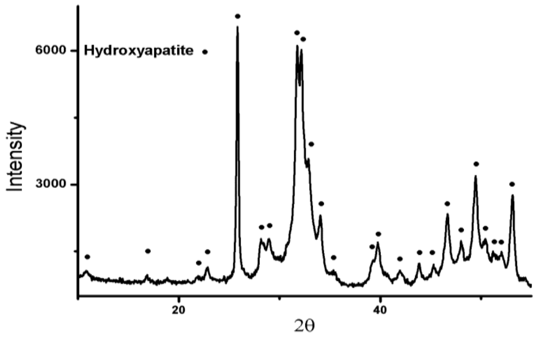

Figure 2. The XRD profile of the apatite coating after heat treatment at 600 °C.

In contrast, a change in the structure of the coating was observed when the samples were fired at 800 °C. The individual lamellas that constitute the coating became porous (Figure 3). The XRD spectrum of the coating matched that of the β-TCP crystal structure (β-TCP, JCPDS-09-0169) (Fig. 3).

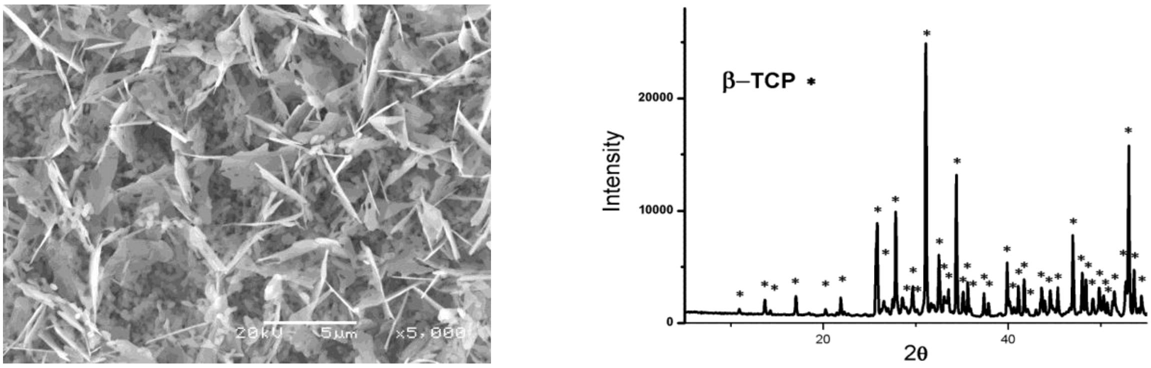

Figure 3. The SEM image of the β-TCP coating after a heat treatment at 800 ºC (left) and its corresponding XRD pattern (right).

Moreover, the coating lost its integrity, such that by applying a small force, for example, the sonification in a water bath, a majority of the coating could be easily removed, except for the thin Ca-P coating remaining on the zirconia surface (Fig. 4). Its XRD diffractogram also corresponded to the β-TCP phase (Fig. 4).

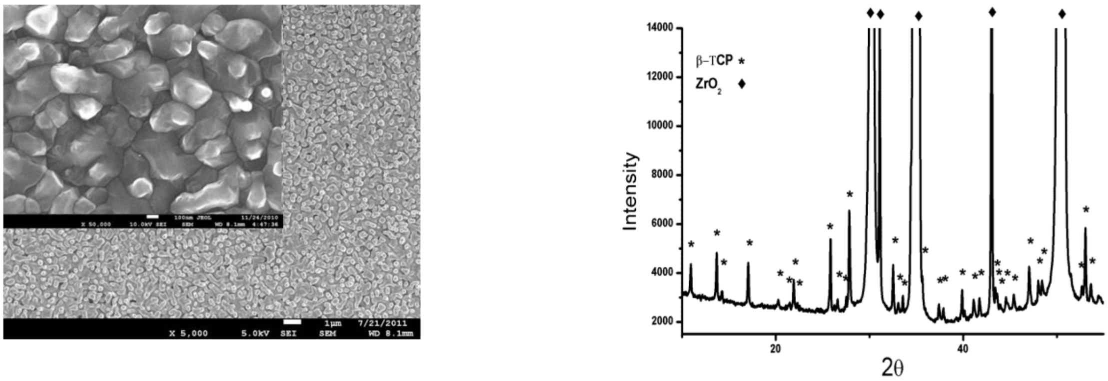

Figure 4. The SEM image of the β-TCP coating after a heat treatment at 800 °C and short ultra-sonic treatment (left) and its corresponding XRD pattern (right).

The mean bond strength of such coatings was 29 MPa. Morever, with our pull-off bond test the coating could not be detached from the substrate (Fig. 5), indicating that the failure occurred at the adhesive-coating interface. In contrast, both the OCP and the HAp coatings were detached from the substrate with the test.

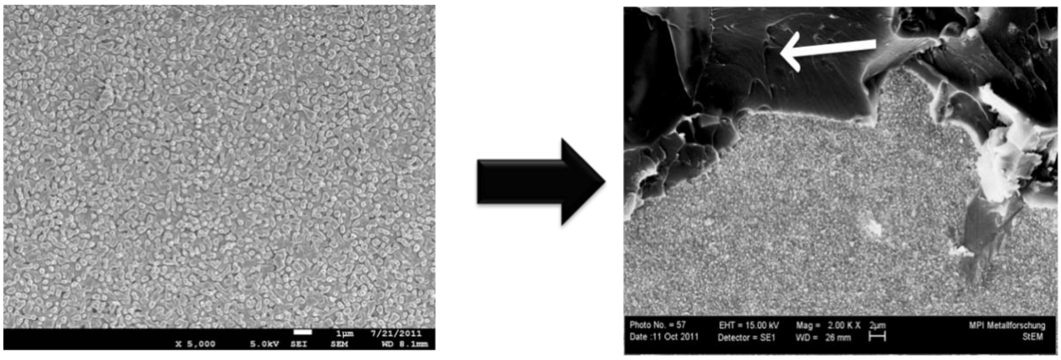

Figure 5. The SEM image of the β-TCP coating before (left) and after (right) the pull-off test. On the right figure, the remaining of the adhesive appear as a dark coloured area and marked with a white arrow. As can be seen on the right figure, coatings could not be detached from the substrate with the pull-off test.

Thermal treatments of the OCP coatings resulted in the changes of the crystal structure, morphology and adhesion of the coatings. Bond strength values for all the prepared coatings are collected in the Table 2. As it can be seen from the table, the bond strength values of the Ca-P coatings could be significantly improved with thermal treatments.

Table 2. The bond strength values of prepared coatings on the zirconia substrates

| Sample | Bond strength (MPa) |
|---|---|
| OCP | 1.8 ± 0.3 |
| HAp<br>(600 °C) | 3.2 ± 0.6 |
| β-TCP<br>(800 °C & sonification) | 29.3 ± 6.4 |

## Conclusions

A simple wet-chemical biomimetic method was employed for the rapid deposition of lamellar OCP coatings on zirconia (Y-TZP) ceramics. An additional thermal processing of the coatings at 600 °C and 800 °C resulted in the phase transformation from OCP to Hap and β-TCP. Moreover, thermal treatments also caused changes in the morphology and adhesion strength of the coatings to the substrate. The bond strength of the coating could be improved from the initial 2 MPa up to the value of 29 MPa.

## References

[1] C. Piconi, G. Maccauro. Zirconia as a ceramic biomaterial. *Biomaterials* 1999;20(1):1-25.

[2] L. L. Hench, J. Wilson. *An introduction to bioceramics*. London: World Scientific; 1999.

[3] B. León, J. Jansen. *Thin Calcium Phosphate Coatings for Medical Implants*; Springer, 2009.

## Za širši interes

Naše raziskovalno delo obsega razvoj metod za pripravo bioaktivnih kalcijevih fosfatnih (Ca-P) prevlek na keramičnih kostnih implantatih, kot so npr. dentalni, kolčni in kolenski implantati. Intrinzična lastnost obstoječih implantoloških materialov je, da se slabo vežejo s kostjo, kar lahko posledično vodi do slabe fiksacije implantata v kosti, njegovega majanja in izpada. Ca-P imajo edinstveno lastnost, da v telesu reagirajo s kostjo in se z njo s kemijskimi vezmi čvrsto povežejo. Tako lahko z nanosom Ca-P prevleke na površino implantata izboljšamo njegovo fiksacijo v kosti in osteointegracijo. Naša raziskovalna skupina je razvila preprosto in poceni metodo za sintezo Ca-P prevlek na implantatih. Prevleke imajo dobre mehanske lastnosti, poleg tega pa nam metoda daje možnost, da kontroliramo sestavo in morfologijo prevlek. Dodatna prednost našega sinteznega postopka je, da lahko poteka pri milih pogojih, ki omogoča vključevanje zdravil v prevleke. Ker so post-operacijske infekcije pogost vzrok za neuspešnost implantacij, imajo prevleke z vključenimi antibiotiki potencial za izboljšanje uspešnosti kostnih implantatov.

# Photocatalytic discoloration of the azo dye methylene blue in the presence of irradiated $TiO_2$/Pt nano-composite

**Vojka Žunič**[1,2]

[1] Advanced Materials Department, Jožef Stefan Institute, Ljubljana, Slovenia
[2] Jožef Stefan International Postgraduate School, Ljubljana, Slovenia
vojka.zunic@ijs.si

**Abstract.** An efficient photocatalytic material $TiO_2$/Pt was prepared via the sonochemical synthesis followed by the thermal treatment. The $TiO_2$/Pt nano-composite was able to photocatalytically degrade the azo dye methylene blue (MB) under UV (ultraviolet) and Vis (visible) irradiation. The enhanced photocatalytic activity of Pt/$TiO_2$ for methylene blue degradation is attributed to the following factors; to the presence of Pt particles which store photogenerated electron thus contribute to an efficient charge carrier's separation and to the adsorption of the dye on the surface of the composite, which acts as a photosensitizer.

**Keywords**: $TiO_2$ nano-powders, $TiO_2$/Pt nano-composites, photocatalytic discoloration, methylene blue

## 1 Introduction

Waste waters originating from industrial discharges represent a global problem which demands the development of an effective, economic, and environmental friendly water treatment technology [1]. A high environmental impact has the textile industry since its discharge waters contain large amounts of non-fixed dyes among which are also the azo dyes [2]. It is well known that some of azo dyes and their degradation products such as aromatic amines are highly carcinogenic [3]. Chemical methods which are able to mineralize organic pollutants to carbon dioxide, water and inorganics or, at least, transform them into harmless products are the "advanced oxidation processes" (AOP) [1, 4]. One of the AOP is the heterogeneous photocatalysis, which is based on the generation of highly reactive and oxidizing hydroxyl radicals in the presence of an irradiated semiconductor metal oxide [1]. The most interesting semiconductor for the photocatalytic applications is titanium dioxide ($TiO_2$). However, the most active $TiO_2$ crystal form anatase is active only when it is irradiated with UV light [1]. Since the sunlight contains only a small part of the UV light, many efforts have been made to improve the photocatalytic activity of $TiO_2$ in the near UV and Vis portion, as well as to shift the $TiO_2$ anatase absorption edge to the Vis part. Among the different methods for the improvement of the $TiO_2$ photocatalytic efficiency is the attachment of $TiO_2$ with noble metals, such as platinum (Pt), gold (Au) and silver (Ag) [5]. If the work function ($\Phi_{SB}$) of the metal is higher than that of $TiO_2$, the photogenerated conduction band electrons are removed from the $TiO_2$ in the vicinity of the metal particle (Fig. 1). As a consequence, a Schottky barrier occurs at the contact metal-semiconductor, which leads to a decrease in the electron-hole recombination as well as to an efficient charge separation [1, 6]. Therefore the $TiO_2$ photocatalytic efficiency should be significantly improved.

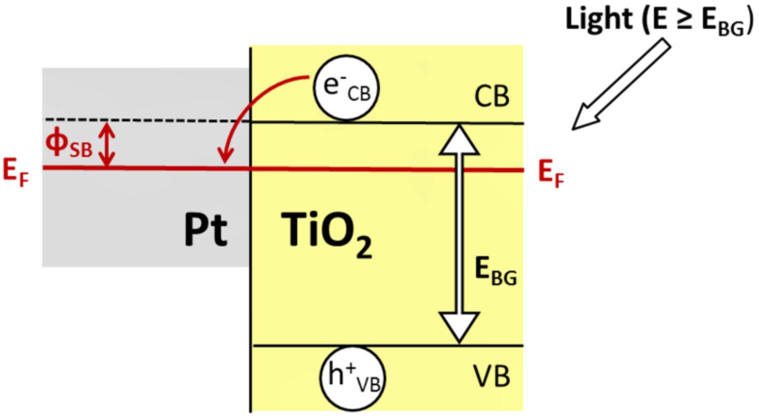

**Figure 1.** A schematic representation of the photoinduced electron transfer between $TiO_2$ and Pt particles.

The highest Schottky barrier is produced with Pt [1]. Therefore, to improve the photocatalytic activity under UV irradiation, we choose to attach the $TiO_2$ particles with the Pt particles. For the photocatalytic activity test the organic azo dye methylene blue was used. Since the dye absorbs Vis light, we expected that the photosensitization effect that would be caused with the $TiO_2$ surface adsorbed dye would induce a Vis light performance.

## 2 Experimental

2.1. Synthesis of $TiO_2$/Pt

The $TiO_2$ nano-powders and $TiO_2$/Pt nano-composites were prepared by using an alkoxide Ti precursor. Titanium(IV) n-butoxide (TNB; $TiO_4H_{36}C_{16}$, 98%) was dissolved in 1-Bultanol ($C_4H_9OH$, 99%) to form a Solution 1. Nitric acid ($HNO_3$, 65%) was diluted in ultrapure water to a form Solution 2. Afterwards a Solution 2 was added dropwise to the Solution 1. A transparent Solution 3 (pH=1) was formed. The Pt precursor chloroplatinic acid hexahydrate ($H_2PtCl_6 \cdot 6H_2O$) was dissolved in ultrapure water and added to the Solution 3, which was transferred into a Suslick reactor and heated to the temperature 80°C. Afterwards the sonication was initiated. The following parameters were used: time of sonication t=3h, pulse on:off = 02:01 s, amplitude 80%, power P=600W and frequency f=20 kHz. The formed precipitates were separated with centrifugation, dried and thermally treated in a reducing atmosphere ($Ar/H_2$=96/4) at 400°C for 3h.

2.2. Characterization techniques

The phase composition and the average crystallite size were evaluated utilizing the X-ray powder diffraction analysis. The specific surface area ($s_{BET}$) was measured by the Brunauer-Emmett-Teller method and the morphological characteristics were analyzed with the transmission electron microscopy (TEM, HRTEM, SAED). UV-Vis spectra were recorded using a UV-Vis-NIR in which the $BaSO_4$ standard was used as the reference spectrum. The photocatalytic activity was evaluated in an aqueous methylene blue solution. A 7.5 ml of the dye solution ($2.67 \cdot 10^{-5}$ M; 10mg/l) and 15 mg of the $TiO_2$ powder (2g/l) were tested under UV and Vis irradiation. The change in the absorbance of the dye solution was measured utilizing the UV-Vis-NIR spectrometer (Shimadzu UV-Vis-NIR 3600).

## 3 Results and discussion

The phase composition analysis of the $TiO_2$ nano-powder and $TiO_2$/Pt nano-composite before the thermal treatment revealed that the materials were a semi-crystalline $TiO_2$ anatase. The following thermal step led to an improvement of $TiO_2$ crystallinity and to the oxidation state reduction of Pt particles deposited on the $TiO_2$ surface. The crystallinity and phase composition were also confirmed with the selected area electron diffraction (SAED) analysis (Fig. 2).

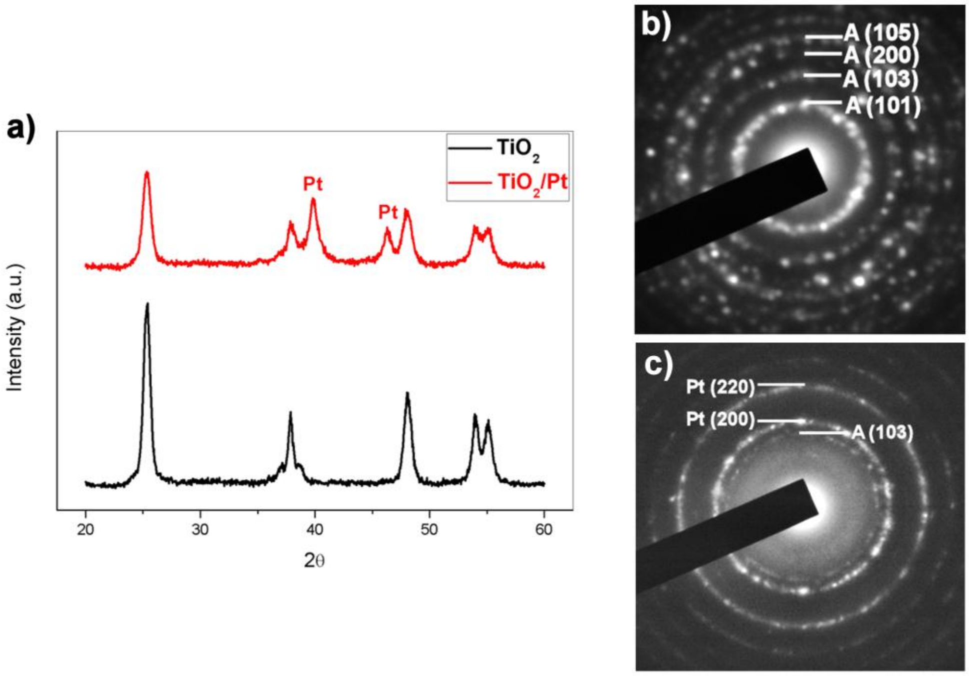

**Figure 2.** The phase composition of thermally treated $TiO_2$ and $TiO_2$/Pt obtained with a) X-ray analysis and with the SAED analysis for b) $TiO_2$ and c) $TiO_2$/Pt.

The average size of $TiO_2$ particles calculated from the X-ray patterns was 7 nm for the $TiO_2$ and 10 nm for the $TiO_2$/Pt. Since the $TiO_2$ nano-powders consisted of smaller particles than the $TiO_2$/Pt nano-composites, they exhibited a higher specific surface. The measured specific surface area was 87 $m^2$/g for the $TiO_2$ nano-powders and 54 $m^2$/g for the $TiO_2$/Pt nano-composites.

Morphologically, the sonication method followed by the thermal treatment resulted in the formation of uniformly sized sphere-like $TiO_2$ nano-particles which tended to agglomerate (Fig. 3). The ultrasound induced agglomeration of $TiO_2$ could be due to the collision of two particles which caused melting at the point of impact resulting in the agglomeration [7]. The observed $TiO_2$ particle size was in agreement with the calculated one. The formed Pt nanostructures in the $TiO_2$/Pt nano-composites were present in the form of sphere-like (up to 5 nm) and polyhedral (up to 25 nm) particles (Fig. 4).

The formed $TiO_2$/Pt nano-composites exhibited a blue shift of the fundamental absorption edge as analyzed with the diffuse reflectance spectroscopy (Fig. 5). Such a blue shift of the fundamental absorption edge is usually observed with $TiO_2$ nano-materials which consist of particles from 5 to 10 nm due to the quantum size effect [1]. Since the formed $TiO_2$/Pt material consisted of larger particles than the $TiO_2$, we believe that the addition of chloroplatinic ions led to changes in the electronic band structures of the $TiO_2$/Pt nano-composites.

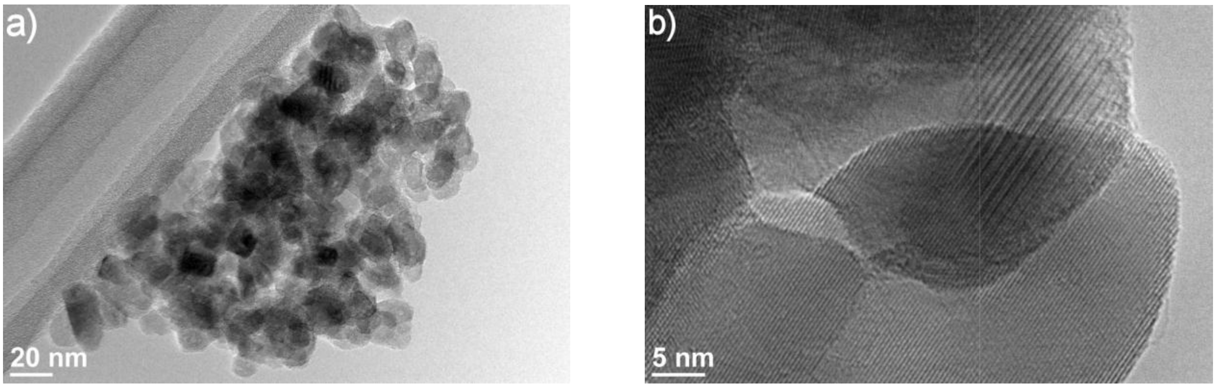

**Figure 3.** The TEM image (a) and the HRTEM image (b) of the $TiO_2$ nano-powder.

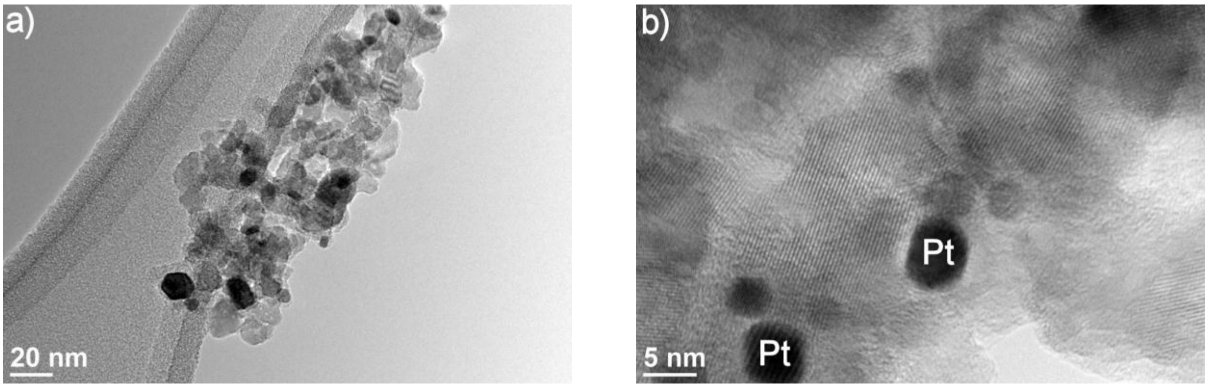

**Figure 4.** The TEM image a) and the HRTEM (b) of the $TiO_2$/Pt nano-composite.

The kinetics of the photocatalytic discoloration of the model organic pollutant, the azo dye methylene blue, follows an apparent first order reaction mechanism (Eq. 1) which is in agreement with the generally observed Langmuir-Hinshelwood model [8]:

$$lnC = ln(C_0) - k_{app}t, \tag{1}$$

where $C_0$ and $C$ are the initial concentrations of the dye at time zero and at time t, respectively, and $k_{app}$ is the apparent first-order reaction constant. The degradation reaction constants were determined based on this apparent first-order kinetic mechanism (Table 1).

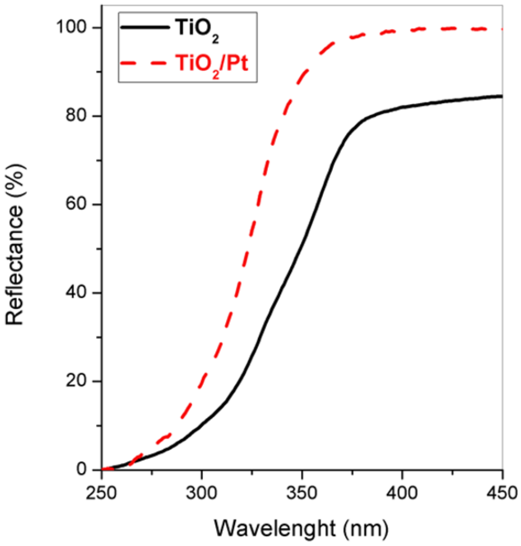

**Figure 5.** The Diffuse reflectance spectra of the prepared materials $TiO_2$ and $TiO_2$/Pt.

The photocatalytic activity measurements showed that the prepared $TiO_2$/Pt nanocomposites were characterized with an improved photocatalytic efficiency when compared to bare $TiO_2$. The efficiency of $TiO_2$/Pt under UV irradiation was two times higher than that of $TiO_2$. Under Vis irradiation bare $TiO_2$ was not able to degrade the methylene blue. However, after the $TiO_2$ particles were attached with Pt particles there was a noticeable degradation of the dye under Vis irradiation.

**Table 1**

The UV and Vis first-order reaction constants $k_{app}$ ($min^{-1}$) for $TiO_2$ and $TiO_2$/Pt

| Sample | $k_{app}$ ($min^{-1}$) UV x $10^3$ | $k_{app}$ ($min^{-1}$) Vis x $10^3$ |
|---|---|---|
| $TiO_2$ | 10 | 0.3 |
| $TiO_2$/Pt | 23 | 7 |

The enhancement of the UV photocatalytic activity of the prepared $TiO_2$/Pt composite, when compared to bare $TiO_2$ could, be ascribed to the presence of the $TiO_2$ surface attached Pt particles which acted as the an electron storage [5] thus contributing to better separation of charge carriers'. On the contrary, we believe that the Vis induced photocatalytic activity was caused with the surface adsorbed dye methylene blue. Since methylene blue absorbs Vis light, it can be excited by the Vis light irradiation thus acting as a photosensitizer [9]. The excited dye injects an electron to the $TiO_2$ conduction band, where it is scavenged by preadsorbed oxygen ($O_2$), forming and forms oxygen radicals which are able to drive the photodegradation or mineralization [9]. We believe that this phenomenon is responsible for a Vis light photocatalytic activity of the $TiO_2$/Pt nano-composites.

## 4 Conclusions

The $TiO_2$/Pt nano-composites which consisted of Pt particles (up to 25 nm) and $TiO_2$ particles in the anatase crystal form (up to 10 nm) were synthesized via the sonochemical method. Such materials are shown to be an efficient photocatalytic material for the discoloration of the azo dye methylene blue under UV and Vis irradiation. The $TiO_2$ surface attachment with the Pt particles led to the significant improvement of the UV photocatalytic activity and the Vis light photocatalytic activity was induced with $TiO_2$ surface adsorbed dye.

## References:

[1]O. Carp, C.L. Huisman, A. Reller. Photoinduced reactivity of titanium dioxide. *Progress in Solid State Chemistry,* 32: 33-177, 2004.

[2]N. Tüfekci, N. Sivti, İ. Toroz. Pollutants of textile industry wastewater and assessment of its discharge limits by water quality standards. *Turkish Journal of Fisheries and Aquatic Science,* 7: 97-103, 2007.

[3]H. Lachheb, E. Puzenat, A. Houas, M.Ksibi, E. Elaloui, C. Guillard, J.-M. Herrmann. Photocatalytic degradation of various types of dyes (Alizarin S, Crocein Orange G, Methyl Red, Congo Red, Methylene Blue) in water by UV-irradiated titania. *Applied Catalysis B: Environmental,* 39: 75-90, 2002.

[4]R. Andreozzi, V. Caprio, A. Insola, R. Marotta. Advanced oxidation processes (AOP) for water purification and recovery. *Catalysis Today,* 53: 51-59, 1999.

[5]H. Tada, T. Kiyonaga, S. Naya. Rational design and applications of highly efficient reaction systems Photocatalyzed by noble metal nanoparticle-loaded titanium(IV) dioxide. *Chemical Society Reviews,* 38: 1849 (2009).

[6]B. Kreaeutler, A.J. Bard. Heterogeneous photocatalytic preparation of supported catalysts. Photodeposition of platinum on $TiO_2$ powder and other substrates. *Journal of the American chemical society,* 100(13): 4317, 1978.

[7]T. Prozorov, R. Prozorov, K.S. Suslick. High velocity interparticle collisions driven by ultrasound. *Journal of American chemical society,* 126: 13890 (2004).

[8]R.W. Matthews. Photocatalytic oxidation and adsorption of methylene blue on thin films of near-ultraviolet-illuminated $TiO_2$. *Journal of the Chemical Society, Faraday Transactions,* 85(6): 1291 (1989).

[9]T. Wu, T. Lin, J. Zhao, H. Hidaka, N. Serpone. TiO2-assisted photodegradation of dyes. 9. Photooxidation of a squarylium cyanine dye in aqueous dispersion under visible light irradiation. Environmental Sciences and Technology, 33: 1379 (1999).

## For wider interest

It is well know that $TiO_2$ is characterized with photocatalytic properties by utilizing UV (ultraviolet) light. This phenomena is already been used for commercial applications such as self-cleaning concrete (Italcement Group) in building facades (Jubilee Church (also known as the Dives in Misericordia) in Rome) and pavements (Municipal District of Bergamo, Italy – Borgo Palazzo Street), self-cleaning windows (Pilkington), ect. Another field, in which the photocatalytic properties of $TiO_2$ can be of advantage, is the water purification. Water contamination due to the industrial wastewaters which contain organic dyes has become a global problem. About 1-20% of organic dyes are lost during the industrial dyeing processes and released into the environment. The dyes itself and their degradation products represent toxic substances which cause diverse effects on animal and human health. Therefore, the purification and remediation of discharged waters generated from industrial processes is a necessity. Having in mind such problems, the idea of this work was to prepare $TiO_2$ which could be used for azo dyes degradation in water. Since the UV light represents only a small part of the sunlight (only 2-3%) the goal of our work was to synthesize a $TiO_2$ which exhibits improved photocatalytic properties under UV irradiation and also is active under Vis (visible) light irradiation. Since such $TiO_2$ is able to degraded organic dyes utilizing solar energy (UV and Vis) it represents an economic and efficient method for water purification. We prepared such photocatalyst by forming a $TiO_2$/Pt nano-composite which is able to effectively photocatalytically degraded the azo dye methylene blue under UV and Vis irradiation.

# LIFE TIME ASSESSMENT OF REAL COMPONENTS EXPOSED TO HIGH TEMPERATURES AND PRESURES

**Borut Žužek[1,2], Bojan Podgornik[1], Monika Jenko[1]**

[1] Institute of Metals and Technology, Ljubljana, Slovenia

[2] Jožef Stefan International Postgraduate School, Ljubljana, Slovenia

borut.zuzek@imt.si

**Abstract.** Components in the industry are often exposed to elevated temperatures and high pressures. These conditions cause changes in the microstructure and thermo-mechanical properties of steel components. With the aim to determine the properties of steels after a certain period of operation, thermo-mechanical investigations and microstructure characterization can be made and the results of this investigation can serve for the remaining lifetime assessment of components. From the economic and technological point of view this is a very important information.

Creep is one of the major mechanisms which cause the deformation and degradation of steels at elevated temperatures. The creep can occur in local areas due to an increased load or due to a microstructural degradation during the operation at elevated temperatures. The microstructure degradation of the steels can be defined by microstructural investigations on metallographic samples or replicas. The aim of this work is to present some methods for the microstructure characterization of steels used in the Slovenian thermal power plants.

**Keywords**: lifetime assessment, creep, microstructural degradation, elevated temperatures

## 1 Introduction

Elevated temperatures and high pressures are present in a lot of different industrial applications. High temperatures and pressures accelerate a lot of thermodynamic processes in steel which cause the degradation of steel. Mechanical properties of steel are deteriorated trough the thermal degradation of steel with the microstructural changes, thinning of the wall thickness due to corrosion processes, damages because of the creep deformation, thermal fatigue, corrosion damage and high temperature oxidation. The life time expectancy (remaining life time) of such components depends on the state of the microstructure and their mechanical properties. The good condition and awareness of the degradation of crucial components is important for the safe operation and for the undisturbed production, i.e. for the undisturbed electrical power supply in thermal power plants. To estimate the remaining service life of such components, different investigations methods can be used. The non-destructive testing is essential to assess the current status of components, because the component integrity is preserved. Sometimes destructive methods have to be used, for a more detailed inspection.

The observation of microstructure change is the most sensitive method for monitoring the condition of the steel components. In the present work a few different possibilities for the microstructure analyses will be presented and their advantages and disadvantages discussed.

## 2 Methods for the microstructure evaluation

For analyzing the microstructure of a component used in industry, there are a few different methods that can be used. In general we have three options: we can take a sample of the component, we can perform analyses on the field, or we can take a replica and perform analyses in the laboratory.

### 2.1 Cut out the sample from a component and examine it in the laboratory

Cutting out the sample from the component, is a destructive method and is not always possible, because if we cut out the sample, we damage the integrity of the component (Fig. 1A). On the other hand, if we can take out the sample of a material, we can perform more detailed analyses and make different investigations with the results being more accurate and reliable.

### 2.2 The on field examination

The on field examination is a non-destructive method, where the microstructure evaluation is performed on the field, using a portable microscope (Fig. 1B). The method is relatively quick and not so complicated to perform. Disadvantage of this method is that portable microscopes have a low magnification (100x) and sometimes this magnification is not sufficient for a precise and reliable evaluation of the microstructure.

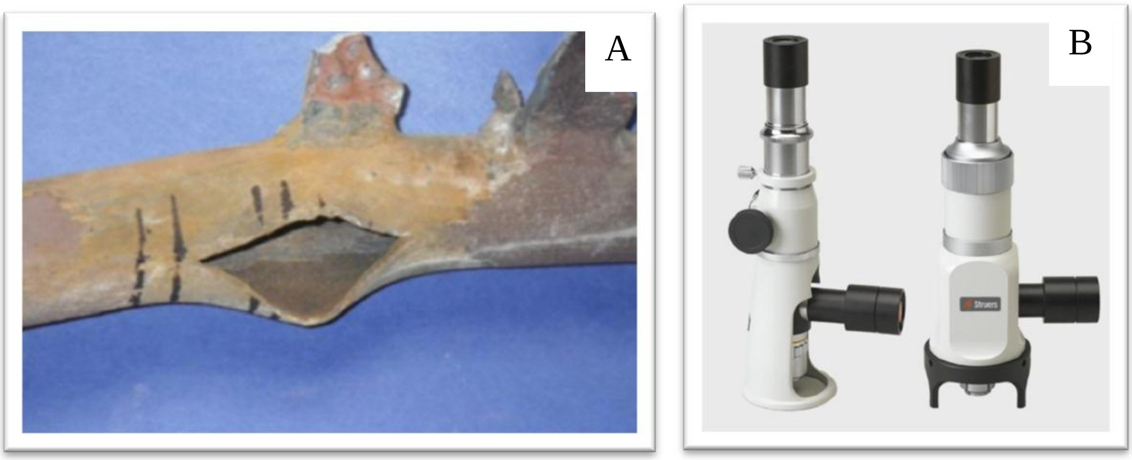

**Figure 1**: A) A steel pipe ready for cutting after a failure during the operation, B) portable microscopes [1], [3].

### 2.3 Taking a metallurgical replica

Method, where we can combine some advantages of both previously mentioned methods is when we take a replica from the material of the component (Fig. 2A). This method is a non-destructive method, and the microstructure of the material is analyzed in the laboratory. The disadvantage of this method is that it is hard to prepare a good replica, because the surface of the material must be very clean what is hard to achieve in industry (Fig. 2B).

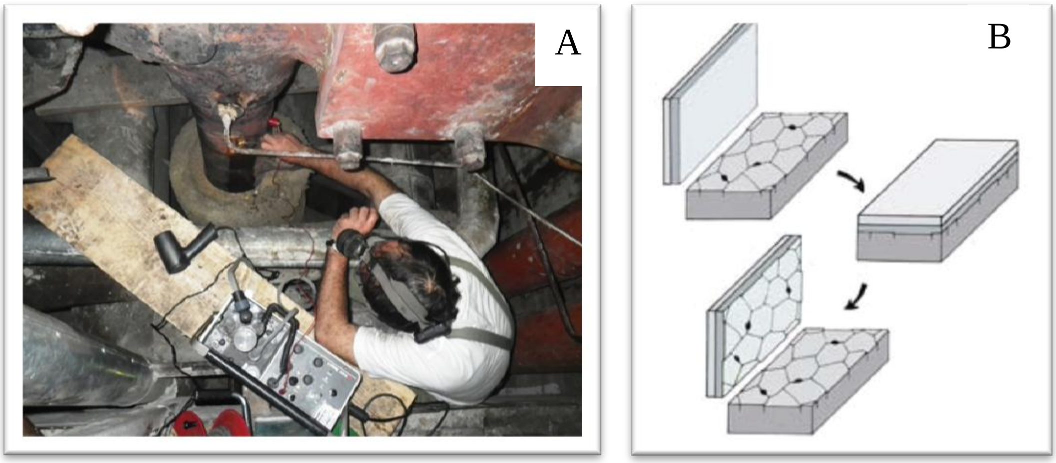

**Figure 2**: A) An example of taking the replica from a weld between the tube and valve in a power plant, B) Steps of taking replicas [2], [3].

## 3 Results of microstructure analyses

A typical creep curve of steel which shows the strain of steel versus time at a constant stress and constant elevated temperature is shown on Figure 3. On this creep curve, points where typical signs of the microstructure degradation start to appear are marked. Independently of the method used for microstructure analyses, we are looking for the signs of the microstructure degradation in steel during the operation (Fig. 4). These signs are: a spheroidisation of the microstructure, the precipitation of carbides in ferrite, the formation of cavities and micro porosities or micro cracks, etc. Levels of the degradation, types of the damage and recommended actions are shown in Table 1.

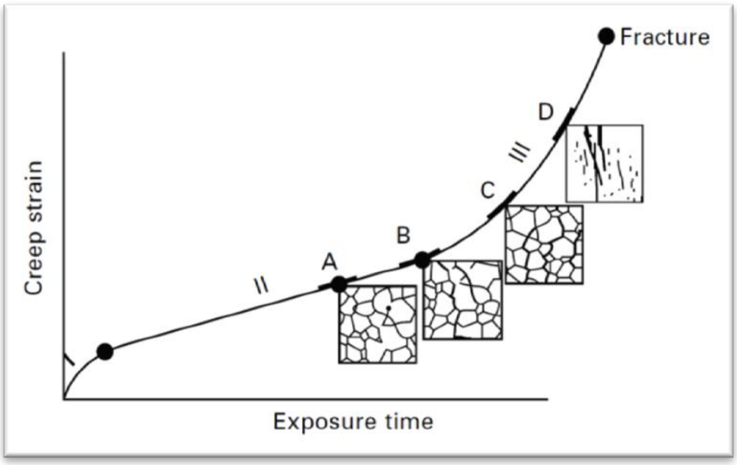

**Figure 3**: The creep curve with specific microctructure damages caused by the creep deformation.

**Table 1**: Damages of the microstructure in different stages of the creep curve and recommended actions

| Level of degradation | Evolution of cavities | Actions |
|---|---|---|
| A | Isolated cavities | Planed examinations |
| B | Oriented cavities | Examination with replicas in planed intervals |
| C | Linked cavities (microcracks) | Limited operation until recondition |
| D | Macrocracks | Immediate recondition |

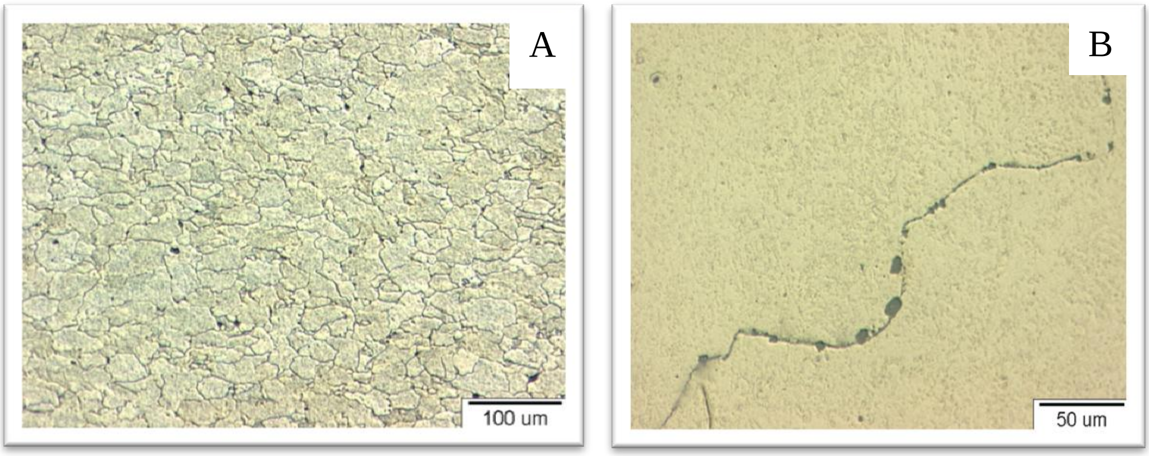

**Figure 4**: A) Individual micro porosities in the microstructure of ferrite and bainite, B) Micro porosities linked in a micro crack [1], [2].

## 4 Conclusions

Changes of the microstructure are the first step in a degradation of steel during the operation of steel at elevated temperatures. The observation of the microstructure degradation is the most sensitive method for monitoring the condition of the steel components. Different methods can be used for a microstructure evaluation, with the sample cutting being the most accurate but destructive one and taking the replica preserves a component with the satisfactory precision. However, a combination of more of them gives the best results. Based on the microstructure evaluation, the decision for the replacement a specific component exposed to high temperatures and pressures could be made before a catastrophic failure occurs.

## References:

[1] Žužek, Borut, in drugi. *Poročilo o preiskavi poškodovanih parovodnih cevi iz pregrevalnika bloka 4.* Ljubljana: Inštitut za kovinske materiale in tehnologije, 2011.

[2] Žužek, Borut, in drugi. *Preiskave na elementih kotla bloka 5, remont 2011.* Ljubljana: Inštitut za kovinske materiale in tehnologije, 2011.

[3] Struers. *Struers.com.* Struers A/S, 2012. [citet: 3. 4 2012.] http://www.struers-ndt.com/.

## Za širši interes

V proizvodnih industrijskih obratih je mnogo komponent pogosto izpostavljenih delu pri visokih temperaturah in delu pod tlakom. Visoka temperatura in povišan tlak pospešujeta poslabšanje mehanskih lastnosti jekla. Zaradi slabšanja mehanskih lastnosti jekla med obratovanjem lahko po določenem času pride do nepričakovane odpovedi kakšne od komponent. Poškodba komponente, ki deluje v okolju visokih temperatur in tlakov, pa je velikokrat podobna eksploziji bombe.

Zavedanje neprestanega slabšanja mehanskih lastnosti tako izpostavljenih komponent je iz ekonomskega in tehničnega vidika zelo pomembno. Odpoved takšne komponente povzroči ustavitev proizvodnje, nedoseganje zastavljenih ciljev in izpad dohodka, lahko pa tudi nevarnost ogrožanja življenja zaposlenih.

Stanje takšnih komponent lahko preverimo z različnimi metodami metalografske analize, kjer se pod mikroskopom preveri stanje mikrostrukture jekla. Metalografske preiskave lahko dopolnimo tudi z drugimi neporušitvenimi preiskavami, kot so ultrazvočne meritve, preiskave s tekočimi penetranti, meritve trdote, itd.

Na podlagi teh preiskav lahko ocenimo preostalo življenjsko dobo takšnih komponent in podamo mnenje o primernosti njihovega nadaljnjega varnega obratovanja.

## Organizator

MEDNARODNA PODIPLOMSKA ŠOLA JOŽEFA STEFANA
SLOVENIJA
LJUBLJANA
2004

## V sodelovanju z

Nanocenter

Center odličnosti nanoznanosti
in nanotehnologije

cipkebip
Centre of excellence for integrated approaches
in chemistry and biology of proteins

Center odličnosti Napredni nekovinski
materiali s tehnologijami prihodnosti

NAMASTE

Center odličnosti za integrirane pristope v
kemiji in biotehnologiji proteinov

# Ustanovitelji in partnerji MPŠ

Institut "Jožef Stefan", Ljubljana, Slovenija

B/S/H/

COSYLAB

DOMEL

ETI

gorenje

HYB
emotional electronics

iMT

JUTEKS

KOLEKTOR

LTH Castings

LUKA KOPER

mik
CELJE

PREMOGOVNIK
VELENJE

SALONIT
ANHOVO

SLOVENSKO ZAVAROVALNO ZDRUŽENJE
Slovenian Insurance Association

ŠTORE STEEL

TALUM

TelekomSlovenije

tes

Trimo

UNIOR

POTI MIRU V POSOČJU
FUNDACIJA